

Design of a Solar Array Drive Mechanism for CubeSats

Rahul Ravi Ravichandran

Design of a Solar Array Drive Mechanism for CubeSats

A scalable, modular and reliable SADM for CubeSats in Low-Earth orbit

by

Rahul Ravi Ravichandran

in partial fulfilment of the requirements to obtain the degree of

Master of Science

in Aerospace Engineering at the Delft University of Technology,

to be defended publicly on Friday, September 30, 2022 at 8:30 AM.

Student Number: 5054206

Project duration: May 20, 2021 - September 30, 2022

Thesis committee:

Dr. Stefano Speretta,	TU Delft, Supervisor
Dr. Bert Monna,	AAC Hyperion Technologies, Supervisor
Dr. Angelo Cervone,	TU Delft, Chair of assessment committee
Dr. Ron Noomen,	TU Delft, External Examiner

An electronic version of this thesis is available at: <http://repository.tudelft.nl/>.

Acknowledgement

This report is the documentation of the Master thesis carried out by Rahul Ravi Ravichandran. This is the last step in completion of my Master's in Space engineering at Delft. The thesis was aimed at designing a Solar Array Drive Mechanism for CubeSats. The thesis starts by finding why a SADM is needed in the SmallSat industry followed by designing the SADM to mitigate tribological failures, modular and scalable to different CubeSat sizes. The thesis has resulted in designing the smallest SADM in the market with a novel power and data transfer mechanism. This thesis subject was undertaken due to my keen interest in space mechanisms after I was introduced to the field in my Bachelor's student Team Rudra. This journey turned out to be way different than I had imagined it would be initially with a global pandemic, health, career and financial surprises. In spite of all the ups and downs, I am grateful to have learnt a great deal over the past three years.

I would like to firstly thank my parents Ravichandran, Tamilselvi and the rest of my family for supporting me throughout this journey. I am indebted to both of you. I wish I had spent more time with you thatha. Nextly, I would like to thank my mentors and supervisors Dr Stefano Speretta and Dr Bert Monna to have provided their expertise whenever I needed it, for pulling me back whenever I got lost in details and for pushing me in the right direction when I got stuck. I do not think I would have come so far if not for my family and support system in Delft (Kavin, Prakash, Venkatraman, Karthik, Lokesh, Sadhna, Swati, Nishu, Anusha, Shivesh, Gary, Adhil, Aayushi, Cedric, Adithya, Vishwa). You have made Delft a home far away from home. It would be incomplete to not thank my wonderful colleagues at Hyperion (Alisa, Suman, Egor, Lisette, Johaan, Taavishe, Steven, Ali, Julian & Manav) for their fun discussions, spicy gossips, motherly advice, torturous KiCad demonstrations, polar-bearing support, coffee machine conversations, technical discussions, fun outings and everything in between. Work would have been monotonous if not for you guys.

Lastly, I am grateful to everyone else who have been a direct or indirect part of this journey. An aspiration is now a milestone.

*Rahul Ravi Ravichandran
Delft, September 2022*

Abstract

CubeSats have rose to popularity since its first launch in the year 2003. The low mass, lower launch cost, lower development cost, possibility for piggy-back with larger satellites and lower development time involved compared to larger satellites have opened them to be commercialised by private companies. In contrast to being used for educational, research and technology demonstration purposes in their early years, they are now being used for varied applications such as communications, Earth observation, military surveillance, in-orbit manufacturing, asteroid exploration, Internet-of-things and interplanetary exploration missions. Their lucrative features make them favourable over their larger counterparts, and as a result are predicted to launch in higher numbers in the coming years considering preference for missions involving constellations or distributed space systems. This trend of increasing demand for CubeSats and their application in advanced missions requires more electrical power for their operation. The increased demand for electrical power can be solved by using a Solar Array Drive Mechanism. The SADM allows relative rotary motion of the solar arrays with respect to the satellite structure so that the solar panels are always perpendicularly positioned to the Sun independent of the payload pointing requirements. They are able to produce up to 185% more power than the panels being just deployed in case of a 3U CubeSat. Only a handful of six such SADM products were found in the commercial market and four of them had a very similar design that drove two solar arrays and could be used in limited panel mounting configurations. A need in the commercial market for a SADM system that is modular and scalable was identified. Space mechanisms such as the SADM were found to be one of the major causes of mission failure after communications and unknown causes. It was found that tribological elements were the prominent root cause of such space mechanism failure. A research gap was identified to find the root causes of tribological failure in space mechanisms and design a SADM system that minimises failure caused due to tribological elements. This thesis has succeeded in designing a SADM that is scalable to multiple sizes of CubeSats (3U to 12U), applicable to more than three panel mounting configurations that were possible with the existing SADM and minimising failure chances due to tribological elements. The current SADM has minimised the chances of failure due to common tribological elements such as roller bearings and sliprings by eliminating the cause of failure. This includes eliminating rolling elements, liquid lubricants and metals in the case of bearings and a novel power and data transfer mechanism alternative to sliprings called "*Flex-wrap*" has been designed in this project. The current SADM is the smallest in the market in terms of dimensions ($70 \times 50 \times 6.9$ mm) and is applicable to 5 different solar array mounting configurations.

List of Abbreviations

ADCS	Attitude Determination & Control System
AC	Alternating Current
AIT	Assembly, Integration and Testing
AWG	American Wire Gauge
AGMA	American Gear Manufacturers Association
AI	Artificial Intelligence
BOL	Begin Of Life
BAPTA	Bearing and Power Transfer Assembly
COTS	Commercial Off The Shelf
CFRP	Carbon Fiber Reinforced Plastic
CMG	Control Moment Gyro
CVCM	Collected Volatile Condensable Material
CCD	Charge Coupled Device
CDH	Command and Data Handling
CAD	Computer Aided Design
CNC	Computer Numerical Control
DOF	Degree of Freedom
DC	Direct Current
EOL	End Of Life
ESA	European Space Agency
EPS	Electrical Power System
ECSS	European Cooperation For Space Standardization
ERBS	Earth Radiation Budget Satellite
EMI	Electro Magnetic Induction
ETFE	Ethylene tetrafluoroethylene
ESD	Electro Static Discharge
FPC	Flexible Printed Circuit
FFC	Flat Flexible Cable
GEO	Geostationary Earth orbit
GCR	Galactic cosmic rays

ISS	International Space Station
ISARA	Integrated Solar Array & Reflectarray Antenna
LEO	Low Earth Orbit
MCU	Micro-Controller Unit
MLT	Mission Life Time
HDRM	Hold-Down and Release Mechanism
MPPT	Maximum Power Point Tracker
NASA	National Aeronautics and Space Administration
OBC	On-Board Computer
PV	Photo-Voltaic
PCB	Printed Circuit Board
PDTM	Power and Data Transfer Mechanism
PVDF	Polyvinylidene Fluoride
PTFE	Polytetrafluoroethylene
PEEK	Poly Ethyl Ether Ketone
POM	Polyoxymethylene
RMS	Root Mean Square
RPM	Revolutions Per Minute
RAMS	Reliability, Availability, Maintainability & Safety
SADA	Solar Array Deployment Assembly
SPDM	Solar Panel Deployment Mechanism
STEM	Storable Tubular Extendable Member
SADM	Solar Array Drive Mechanism
SMA	Shape Memory Alloy
SSO	Sun Synchronous Orbit
SPE	Solar Particle Events
SAA	South Atlantic Anomaly
SARA	Solar Array Rotary Actuator
SEE	Single Event Effects
TBD	To Be Determined
TRL	Technology Readiness Level
TID	Total Ionizing Dose
TVAC	Thermal Vacuum Chamber
TTC	Telemetry, Tracking & Command
USD	United States Dollar

Nomenclature

α_{SA}	angular acceleration of solar array
α_{sa}	angular acceleration rate of the solar arrays
$\ddot{\theta}_m$	Angular acceleration of motor
ΔI_{mp}	Co-efficient of change in current at maximum power point per unit change in temperature
ΔV_{mp}	Co-efficient of change in voltage at maximum power point per unit change in temperature
$\dot{\theta}_m$	Angular velocity of motor
$\frac{N_m}{N_l}$	Mass moment of Inertia reflected to the motor
μ_d	Dynamic friction co-efficient
μ_s	static co-efficient of friction of journal bearing
ω	Rotational speed
ω_0	initial angular velocity of solar array
ω_{ecl}	rotation rate of solar panels in the eclipse phase
ω_{ecl}	rotation rate of solar panels in the eclipse phase
ω_f	final angular velocity of solar array
ω_{sun}	rotation rate of solar panels in the sunlight phase
ω_{tt}	rotation rate of solar panels in target tracking phase
ρ_{cov}	density of cover-glass
ρ_{ins}	density of insulation
ρ_{sub}	density of substrate
τ	Torque required to rotate solar arrays
τ	Torque
τ_D	Inertial resistance torque caused by worst-case acceleration
τ_{fd}	Torque due to dynamic friction force
τ_{fs}	torque due to static friction
τ_I	Inertial torque applied to a mechanism subjected to acceleration in an inertial frame of reference
τ_L	Deliverable output torque
τ_S	Spring torque
θ_i	incidence angle of Sun
θ_{rot}	Rotation angle of FPC
θ_{sun}	angle of orbit spent in eclipse

θ_{sun}	angle of orbit spent in sunlight
A_{cell}	Area of PV cell
B_l	Damping co-efficient of motor
B_m	Gear ratio of motor to load
c	Distance of layer from neutral axis at which stress is calculated
D	Diameter of bearing
D_i	Inner diameter of spiral
D_o	Outer diameter of spiral
d_s	distance travelled by satellite in one second
E_B	Amount of copper deformation allowable (0.3% for dynamic flex applications)
E_{Cu}	Young's modulus of copper
E_{Kp}	Young's modulus of Kapton
F_{max}	Maximum force on bearing surface (N)
F_{Cu}	Force due to copper layer
f_d	Dynamic frictional force
F_{Kp}	Force due to Kapton layer
F_R	Worst case friction torque
f_s	static friction
GR_i	Internal gear ratio of motor
GR_{opt}	Optimum gear ratio
H_A	Harness and other torque or force resistances
H_D	Adhesion torque
H_m	Motor magnetic losses
H_Y	Hysteresis torque
I_{max}	Maximum current
I_{Cu}	Moment of inertia of Copper layer cross-section
I_{Kp}	Moment of inertia of insulation layer cross-section
I_{sa}	Inertia of the solar arrays
I_{xx}	Inertia of solar array along x axis
I_{yy}	Inertia of solar array along y axis
J_C	Inertia of coupling
J_D	Inertia of drive system (ball-screw/belt/rack-&-pinion)
J_E	Inertia of external load (solar array)
J_G	Inertia of gearbox

J_l	Mass moment of Inertia of the load
J_m	Mass moment of Inertia of the motor's rotor
J_{sc}	Saturation current density
k_{SB}	Stephan-Boltzmann constant
L	Length of bearing
l_{array}	Length of solar array
l_{cell}	length of PV cell
L_d	Life time degradation
l_{panel}	length of solar panel
L_{spiral}	Length of spiral
L_{Sun}	Fraction of sun intensity
M	Moment
M	Moment
M_{array}	Mass of solar array
M_{cell}	Mass of one PV cell
$M_{cov_{panel}}$	Mass of cover-glass per panel
$M_{ins_{panel}}$	Mass of insulation per panel
M_{panel}	Mass of one solar panel
$M_{PV_{cell_{panel}}}$	Mass of PV cells per panel
m_{SA}	Mass of solar array
$M_{sub_{panel}}$	Mass of substrate material per panel
N	normal force on bearing
n	Number of electrons
N_{bolts}	Number of bolts
$N_{cell-rows_{wid-wise-gap}}$	Number of PV cell rows that can be fit in the gap remaining along the width of the panel
$N_{cell-rows_{wid-wise-gap}}$	Number of PV cell rows that can be fit within remaining gap in width direction of panel
$N_{cell_{len-wise}}$	Number of PV cells along length of solar panel
$N_{cell_{panel}}$	Number of PV cells per panel
$N_{cell_{panel}}$	Number of PV cells per panel
$N_{cell_{wid-wise-gap}}$	Number of PV cells that can be fit in each row of the gap remaining along the width of the panel
$N_{cell_{wid-wise-gap}}$	Number of PV cells that can be fit within remaining gap in the width direction of panel
$N_{cell_{wid-wise}}$	Number of PV cells along width of solar panel
$N_{cells-per-string}$	Number of PV cells per string
N_{panels}	Number of solar panels

$N_{strings}$	Number of strings connected in parallel
N_{tr}	Number of traces
N_{turn}	Number of turns in spiral
P_0	Initial power output
P_f	Final power output
P_{mech}	Mechanical power
P_{SP}	Surface pressure (N/mm)
q	Charge of an electron
r	radius of shaft or inner radius of journal bearing
R_{bend}	Bending radius of FPC (μm)
RD	rate of degradation per year (in %)
T	Time period of orbit
t	time required to accelerate solar arrays from initial to final angular acceleration
T_{amb}	Ambient temperature
T_{ecl}	Time spent in eclipse
T_m	Motor torque
T_{SA}	Temperature of solar array
T_{sun}	Time spent in sunlight
th_{Adh}	Thickness of adhesive in FPC
th_{cov}	thickness of cover-glass
th_{cov}	thickness of cover-glass
th_{Cu}	Thickness of copper (μm)
th_D	Dielectric thickness (μm)
Th_{FPC}	Total thickness of FPC
th_{Ins}	Thickness of insulator layer in FPC
th_{ins}	thickness of insulation
th_{panel}	Thickness of solar panel
th_{panel}	thickness of panel
th_{sub}	thickness of substrate
V_{max}	Maximum voltage
V_{peak}	Peak voltage in trace
w_{cell}	width of PV cell
w_{edge}	Gap on edges of the FPC
W_{FPC}	Total width of FPC

Nomenclature

w_{gap}	Gap between traces
w_{panel}	Breadth of solar panel
w_{panel}	width of solar panel
w_{tr}	Width of each trace
I_p	Current in primary coil
I_s	Current in secondary coil
N_p	Number of turns in primary coil
N_s	Number of turns in secondary coil
V_p	Voltage in primary coil
V_s	Voltage in secondary coil
r	Gear ratio

List of Tables

2.1	Classification of satellites based on mass	5
2.2	Commercial SADMs for CubeSats	15
2.3	Issues in current SADMs and their common elements	18
3.1	Functional Requirements	20
3.2	Performance Requirements	21
3.3	Interface Requirements	22
3.4	Environmental Requirements	23
3.5	Reliability, Availability, Maintainability and Safety Requirements	23
3.6	Design requirements	24
4.1	Summary of angular rotational speed calculations	34
4.2	Number of PV cells that can fit in a panel	38
4.3	Summary of inertia & mass calculations	39
4.4	Summary of angular acceleration calculations	40
4.5	Summary of torque calculations	40
4.6	Summary of mechanical power calculations	40
4.7	Summary of maximum torque, speed & power required calculations	41
4.8	Voltage, current and power calculations for PV cell connection configuration-2	46
4.9	Voltage, current and power calculations for PV cell connection configuration-3	46
4.10	Voltage, current and power calculations for PV cell connection configuration-4	47
4.11	Voltage, current and power calculations for PV cell connection configuration-5	48
4.12	Maximum current, voltage, wires & power	48
4.13	Environmental loads [108] [14]	50
4.14	Launch force on shaft for different hold-down point placement	57
4.15	Summary of preliminary design calculations	58
5.1	Housing requirements	60
5.2	List of SEE and their description	64
5.3	Summary of material thicknesses required for TID less than 10krad in different orbits	66
5.4	Stepper versus piezo motor technology trade-off	72
5.5	Faulhaber v/s Micro-motion trade-off	73
5.6	Optimum external gear ratio for different internal gearbox ratios and axis of rotation	79
5.7	Optimum external gear ratios required for different internal gearbox ratios for rotational speed matching	80
5.8	Optimum external gear ratios required for different internal gearbox ratios for maximum power point matching	81
5.9	Optimal gear ratio	81
5.10	Gear types and their useful gear ratio range[111, 192]	83
5.11	Optimal gear ratio	84
5.12	Gear parameters for pinion and driven gears	86
5.13	Material selection for gears	88
5.14	Power and data transfer mechanism requirements	90
5.15	Bolt preload for different sizes	92
5.16	Selected power and data interface [67] [57]	93
5.17	Power and data transfer mechanism requirements	96
5.18	Gooseneck and cable-wrap trade-off	100
5.19	Conductor carrier options trade-off	100
5.20	Wire sizes for current rating	103

5.21 Trace and FPC specifications for different current and voltage values	106
5.22 Length and forces of FPC spiral	110
5.23 Bearing requirements	113
5.24 COTS-bearing-selection	122
5.25 Summary of bearing friction calculation for two Z-type sliding bearings	124
6.1 Requirements verified by inspection and CAD	135
6.2 Verification approach for requirements needing demonstration and testing	137
7.1 Comparison of COTS CubeSat SADMs	142
A.1 Commercially available single axis articulation SADM for Mini/Micro-satellites	ii
A.2 Aluminium thickness required for different radiation doses in orbit with SAA passover	vii
A.3 Titanium thickness required for different radiation doses in orbit with SAA passover	vii
A.4 Iron thickness required for different radiation doses in orbit with SAA passover	viii
A.5 Tantalum thickness required for different radiation doses in orbit with SAA passover	viii
A.6 Aluminium thickness required for different radiation doses in a LEO Heliosynchronous orbit	x
A.7 Titanium thickness required for different radiation doses in a LEO Heliosynchronous orbit	x
A.8 Iron thickness required for different radiation doses in a LEO Heliosynchronous orbit	xi
A.9 Tantalum thickness required for different radiation doses in a LEO Heliosynchronous orbit	xi
A.10 Aluminium thickness required for different radiation doses in a LEO polar orbit	xiii
A.11 Titanium thickness required for different radiation doses in a LEO polar orbit	xiii
A.12 Iron thickness required for different radiation doses in a LEO polar orbit	xiv
A.13 Tantalum thickness required for different radiation doses in a LEO polar orbit	xiv
A.14 Motor selection trade-off	xv
A.15 Formulas for gear sizing [81, 185]	xxi

List of Figures

1.1	CubeSats and deployers	1
1.2	Breakdown of the SADM into elements and their respective functions	3
2.1	Evolution of satellites with time	6
2.2	Total number of nano-satellites & CubeSats launched from 1998 to 2021 [66]	7
2.3	Percentage of Nanosats and CubeSats compared to Other class of satellites [52]	8
2.4	Applicability of CubeSats for advanced missions	8
2.5	Operational status of Small-satellites	9
2.6	Causes of CubeSat mission failure (1999-2013) [119]	10
2.7	Deployable mechanisms failure per year 1961-2020 [172]	10
2.8	Type and insurance claims of deployable mechanisms by type[172]	11
2.9	Deployable mechanism anomalies by cause [172]	12
2.10	SADMs for Mini and MicroSats	14
2.11	Commercially available Solar Array Drive Mechanisms (SADMs) for CubeSats	16
2.12	Various panel mounting configurations for CubeSats of different mission profiles	17
3.1	12U CubeSat dimensions & deployer imposed volume limits [32]	24
4.1	Satellite in sunlight and eclipse	27
4.2	Common pointing modes a) Nadir pointing b) Target tracking c) Inertial pointing with Sun tracking phase	28
4.3	Basic operating modes of the SADM	29
4.4	Angular rotation rate of target tracking satellite	33
4.5	A typical 12U solar array & its axes	35
4.6	Cut-section of a typical solar panel [68]	35
4.7	PV cells alignment configurations	36
4.8	PV cell layout	37
4.9	Typical I-V curve of a PV cell [42]	41
4.10	Cosine relation between power produced & incidence angle	42
4.11	PV cell connection configurations a) parallel b) series	43
4.12	Variation of electrical characteristics of PV cell	44
4.13	PV cell connection configuration-1	45
4.14	PV cell connection configuration-2	45
4.15	PV cell connection configuration-3	46
4.16	PV cell connection configuration-4	47
4.17	PV cell connection configuration-5	47
4.18	Launch loads classification	49
4.19	Launch loads acting on satellite shaft	51
4.20	Structural simplification of the satellite with a hinge	52
4.21	Free body diagram of solar panel under launch loads with hold down point at the end of panel	52
4.22	Beam splitting for case-1	53
4.23	Free body diagram of solar panel under launch loads with hold down at midpoint	54
4.24	Beam splitting for case-2	54
4.25	Free body diagram of solar panel under launch loads with 2 hold down points	55
4.26	Beam splitting for case-3	56
5.1	Housing design concepts trade-off	61
5.2	Trapped radiation belt around Earth [54]	62
5.3	Different effects of radiation on electronics	64

5.4	Radiation mitigation strategies at different levels of design	65
5.5	Preliminary housing design	68
5.6	Actuator design options	69
5.7	Motor technology design option	71
5.8	Difference between torque v/s speed of motor and load (solar arrays)	74
5.9	Comparison of the torque and speed curves of the motor and the solar arrays	74
5.10	Common gear nomenclature [104] [111]	76
5.11	Types of gear trains	77
5.12	Power versus RPM curve of the actuator	80
5.13	Gear design options	82
5.14	Non-intersecting axis gear configurations[89]	84
5.15	Worm gear configurations	85
5.16	Motor with parallel axis gear	86
5.17	Gear material options	87
5.18	System interface diagram	89
5.19	Nomenclature & forces of a bolt joint	91
5.20	Power and data transfer mechanism design options	96
5.21	Failure mechanisms of sliprings [133]	97
5.22	Conductor carrier options & the mechanisms they are used in	99
5.23	Flex-wrap conductor arrangement configurations	101
5.24	Optimal cable arrangement around shaft	103
5.25	Cross-section of the FPC	104
5.26	Plotting spiral shape of the Flex-wrap for different turns	108
5.27	Shape of the FPC in uncoiled state	111
5.28	Classification of bearings	114
5.29	Working and lubrication regimes of Journal bearing [111]	115
5.30	Bearing nomenclature and clearance	115
5.31	Bearing preload methods [48, 197]	116
5.32	Roller-bearing failure mechanisms causes and effects [34, 37, 39, 48]	117
5.33	Shaft trajectory of sleeve bearing in different failure mechanisms [200]	119
5.34	Friction co-efficient versus surface speed of Z-type plain bearing A.22	123
6.1	The SADM and its components labelled	130
6.2	Two parts of the shaft	131
6.3	Electrical connection methods	133
6.4	The SADM fitted to a 12U CubeSat	134
6.5	Scalability of the SADM to 3U and 6U CubeSats	134
6.6	Scalability of the SADM to 8U CubeSat	135
7.1	Final SADM design	139
A.1	Qualification random vibration loads from NASA GEVS [108]	iii
A.2	ISIS 12 U data sheet [32]	iv
A.3	ISIS all structures dimensions [33]	v
A.4	Simulation parameters of orbit through SAA (referred from [20])	vi
A.5	Ground track of orbit through SAA	vi
A.6	Simulation parameters of heliosynchronous orbit (referred from [186])	ix
A.7	Ground track of heliosynchronous orbit	ix
A.8	Simulation parameters of polar orbit	xii
A.9	Ground track of polar orbit	xii
A.10	DM0620-datasheet	xvii
A.11	DM0620-datasheet	xviii
A.12	DM0620-gearbox-datasheet	xx
A.13	FFC-datasheet-1 [79]	xxiii
A.14	FFC-datasheet-2 [79]	xxiv
A.15	FFC-datasheet-3 [79]	xxv
A.16	PCB Way's FPC stackup for different trace thicknesses [41]	xxvi

A.17 Bending radius of FPC [83]	xxvii
A.18 Flex-wrap schematic with 3 spiral turns	xxvii
A.19 Iglidur service life [59]	xxviii
A.20 Z material bearing data-sheet - 1 [61]	xxix
A.21 Z material bearing data-sheet - 2 [61]	xxx
A.22 Z material bearing data-sheet - 3 [61]	xxxi
A.23 Z material bearing data-sheet - 4 [61]	xxxii
A.24 Z material bearing data-sheet - 5 [61]	xxxiii
A.25 Nut factors[103] [185]	xxxiv
A.26 Space saving bolt tightening torque values [64]	xxxiv
A.27 Omnetics Micro-D 9 pin connector	xxxv
A.28 Omnetics Nano-D 25 pin connector	xxxvi

Contents

Acknowledgement	i
Abstract	ii
List of Abbreviations	iii
List of Tables	x
List of Figures	xii
1 Introduction	1
1.1 Background	1
1.2 Research questions	3
1.3 Thesis outline	4
2 Motivation	5
2.1 History and evolution of satellites.	5
2.2 Present & future of Small-Sats.	7
2.3 Success rate of Small-Sats.	9
2.4 Survey of Solar Array Drive Mechanisms	12
2.5 Summary	18
3 System requirements & constraints	19
3.1 System requirements	19
3.2 Design constraints	24
4 Preliminary design calculations	26
4.1 Common mission scenarios.	26
4.2 System Architecture & Operating modes	28
4.3 Design calculations	30
4.4 Chapter summary.	58
5 Detailed system design	59
5.1 Housing design	59
5.2 Rotary actuator selection and sizing	69
5.3 Mechanical power transmission element design	74
5.4 Interface selection & sizing	89
5.5 Power and data transfer mechanism design.	95
5.6 Bearing selection	113
5.7 Position sensing.	126
5.8 Chapter summary.	127
6 System integration	129
6.1 Design description	129
6.2 Mechanical integration	131
6.3 Electrical integration	132
6.4 Modularity	133
6.5 Scalability.	134
6.6 Verification	135
6.7 Summary	137
7 Conclusions	138
7.1 Results and Discussion	138
7.2 Future recommendations	143

Bibliography	145
A Appendix	ii
A.1 COTS SADA for Mini & MicroSats	ii
A.2 CubeSat structure standard data-sheets.	iii
A.3 SPENVIS Radiation simulation results	vi
A.4 Rotary actuator	xv
A.5 Gearbox datasheet	xx
A.6 Bevel gear calculation formulas	xxi
A.7 Flat flexible cable datasheet.xxiii
A.8 Sleeve bearing service life & datasheetxxviii
A.9 Interfacesxxxiv

Introduction

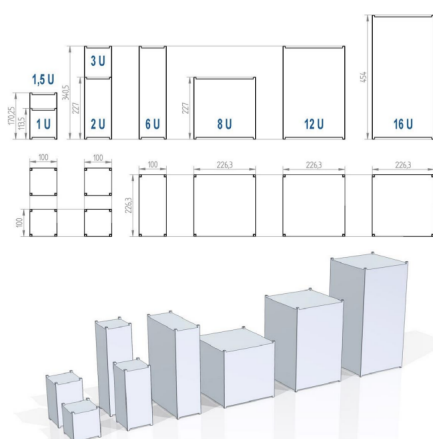
This chapter introduces the Solar Array Drive Mechanism system by detailing its purpose, functions and constituent sub-systems. This is followed by formulating the research questions of the project and concludes by giving an outline of the thesis.

1.1. Background

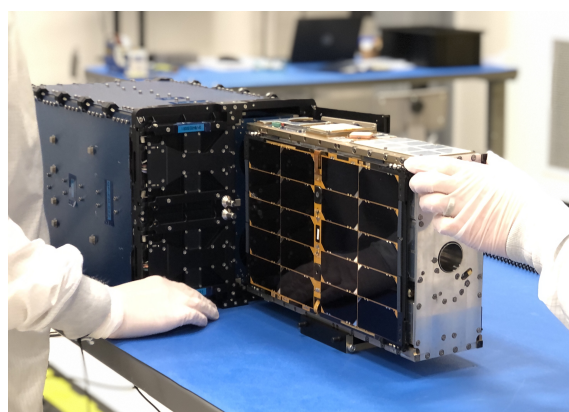
This section will begin by introducing the concept of a CubeSat followed by defining the terms, system, sub-system and elements as they will be used throughout this report. The section then introduces the SADM and its constituents by briefly describing its function, purpose, constituent elements and the design criteria that are considered to design such a sub-system.

1.1.1. CubeSats

Cube-satellites are abbreviated as CubeSats, which are a class of small-satellites that fall within the category of satellites having mass lower than 500 kg. CubeSats are built by combining the basic building blocks which is one unit (U) and has a dimension of $10 \times 10 \times 11$ cm and weigh roughly around 1.3 kgs. These structures are sold commercially in sizes 1U, 1.5U, 2U, 3U, 6U, 8U, 12U, 16U and 36U as shown in Figure (1.1a). CubeSats with size less than 12U usually have a mass less than 10 kgs and fall under the category of nano-satellites. In the year 2000, Prof. Jordi Puig Suari and Prof Bob Twigs [135] are credited for introducing the concept of CubeSats and for pioneering the Newspace industry that thrives on small satellites with low cost and less development times. These CubeSats are fit inside deployers as shown in Figure 1.1b and deployed in orbit.



(a) Different CubeSat sizes [194]



(b) CubeSat being fit inside a deployer

Figure 1.1: CubeSats and deployers

1.1.2. System, sub-system & elements

According to ECSS-S-ST-00-01C [21], a system is a set of interrelated or interacting functions to achieve a specified objective. An example of a satellite system will be the Attitude Determination & Control System (ADCS) [157]. A sub-system is a set of independent elements combined to achieve a given objective by performing a specific function. The star-tracker will be an example of a sub-system constituting the ADCS. An element is a combination of integrated equipment, components and parts. Equipment is an integrated combination of parts and components that perform a specific function. They are self-contained and can be manufactured separately. An example of equipment will be a Printed Circuit Board (PCB). A component or a part is a device which performs a single electronic, mechanical, electrical or electro-mechanical function and cannot normally be disassembled without destruction. The term "part" is used for mechanical devices, and the term "component" is used for electronic devices. The fasteners like bolts and nuts are parts, and circuit elements like transistors, resistors, capacitors, etc, are components that make up the sub-system. In the current application, the SADM is the sub-system of the structures and mechanisms system of the satellite.

1.1.3. Purpose of the SADM

The Solar Array Drive Mechanism is a sub-system responsible for deploying the panels in orbit, rotating the solar arrays to the desired position and transferring the generated power to the CubeSat EPS for the entire duration of the mission. The Solar Array Drive Mechanism system has been given various other names and acronyms like Bearing and Power Transfer Assembly (BAPTA), Solar Array Rotary Actuator (SARA), Solar Array Deployment Assembly (SADA) and Solar Panel Deployment Mechanism (SPDM). In this project, this sub-system would be referred as SADM, henceforth. Some missions would require the constant positioning and alignment of the solar arrays with respect to the sun to capture maximum sunlight and generate maximum power. In this case, the position of the panels has to be constantly adjusted relative to the position of the Sun. By generating more power, advanced mission capabilities that require more power can be accomplished.

1.1.4. Functions of the SADM

The SADM is mainly required for five main functions:

- To transfer the generated power from the solar panels to the satellite bus.
- To maintain the solar arrays in stowed position during launch without damaging them.
- To deploy the arrays to the required final position and position them relative to the sun.
- To transfer the data from sensors mounted on the solar panel to the satellite body.
- Maintaining the position of the solar arrays at the desired position and preventing them from wobbling or waving.

1.1.5. SADM elements

The SADM is an assembly of elements within the satellite. These elements assembled together form the SADM and enable it to achieve its functions. These elements themselves have sub-functions that they must perform to enable the SADM to achieve complete functionality. The SADM can be broken down into five such elements as shown in Figure (1.2). The rotary actuator is responsible for rotating the solar arrays. The sensors measure physical quantities which are required for control, monitoring and error detection. The interfaces form most of the elements in the SADM. They can be classified as electrical and mechanical interfaces. Electrical interfaces allow electrical connections between the elements of the SADM and also between the SADM and other CubeSat systems. Electrical interfaces allow the SADM to achieve its functionality of transferring power and data from the solar arrays to the CubeSat mounted systems. Electrical interfaces include wires, power & data transfer mechanism like sliprings, connectors, etc. Mechanical interfaces allow the transfer of mechanical power and loads within the SADM elements and from the SADM to other systems and elements of the CubeSat. These include mechanical power transfer elements, couplings, springs and fasteners (bolts, nut, screw, rivets, etc.). As most of the mechanical elements move and as some of them are in contact with each other, tribology comes under effect. Tribological elements ensure to reduce friction between these interacting surfaces to mitigate mechanism failure. These include bearings and lubricants to name a few. Control

electronics bring together all the elements by controlling and commanding them in order to enable the SADM to achieve its objectives.

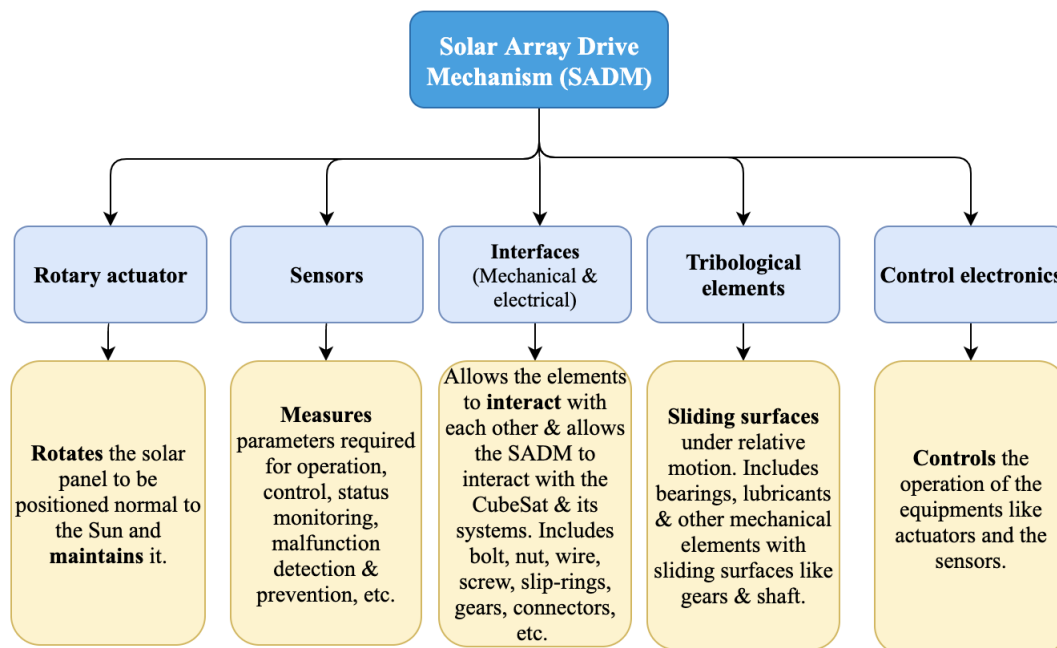


Figure 1.2: Breakdown of the SADM into elements and their respective functions

1.1.6. Design considerations & significance

The design of the SADM depends on the mission profile (orbit type, sun availability, sun angle, etc.), size of the satellite and requirements (power, performance, interface, etc.). Therefore, it is not a single design suitable for all missions. This is a critical system in the satellite because failure to deploy the solar panels would cause inadequate or no power production. Without power, none of the sub-systems would be able to function, and the satellite would not be able to fulfil its mission requirements. This would mean that the satellite would just be another costly debris in space if the SADM fails. Given that it is a combination of elements combined to form a mechanism assembly, eliminating a single point of failure is important. Also, as it is required to be continually in operation over the mission lifetime in the extreme space environment, having high reliability is also important for this system.

1.2. Research questions

As the title of the thesis states, the main aim of the thesis is to design a SADM for CubeSats. To achieve this goal, three main research questions and sub-questions were formulated as stated below. The rest of this report aims to elucidate the process of finding answers to these research questions. Each of these research questions will be answered in each chapter and each of their sub-questions will be answered within the sections of each chapter.

1. Why design a SADM for CubeSats?

- (a) What causes space mechanism failure?
- (b) What is lacking in the existing state-of-the-art products?

2. How to design a SADM system for CubeSats that is reliable (less failure scenarios and probability of its occurrence)?

- (a) How to design or select an actuator that can rotate the solar arrays?
- (b) How to design a power & data transfer arrangement capable of transferring the maximum power with the least degradation over its lifetime as opposed to such shortcomings of conventional sliprings?

- (c) What causes the failure-causing components in space mechanisms susceptible to failure and how can they be designed to have lower chances of failure through their lifetime?
 - (d) How to design interfaces that can survive the environmental loads and be reliable through their lifetime?
3. **How to verify the system's proper functioning and survival in a space environment for a given mission lifetime?**
- (a) How to verify if the system is capable of surviving environmental conditions (ground, launch and space)?
 - (b) How can the system be validated?

1.3. Thesis outline

This report is split into seven chapters. The current chapter is the first and introduces the SADM by exploring its functions and elements. Followed by this, the research questions for this project were formulated.

Chapter 2 It explores the motivation for this work by exploring the demand for SADMs for CubeSats, space mission failures due to mechanisms and the state-of-the-art technology existing and their drawbacks.

Chapter 3 describes the systems engineering involved in the project by arriving at the requirements and constraints that applied to the SADM sub-system's design.

Chapter 4 dives into the SADM design by exploring the mission scenarios that the SADM would experience in orbit and then describes the system level working of the SADM by describing its architecture and operating modes. Based on the operating environments and the requirements established for the sub-system, preliminary calculations of the mechanical power required, electrical power that the SADM has to handle and design loads that the SADM has to survive will be calculated so that the constituent elements can be designed accordingly.

Chapter 5 dives deeper into the SADM design by exploring each element's design step-by-step by firstly highlighting its purpose, followed by the element's requirements translated from the SADM's requirements, followed by a trade-off for technology selection based on the requirements and finally describes its design and the rationale. The housing design is described first as it sets the envelope for the rest of the enclosed elements. This is followed by a section detailing the selection process of the rotary actuator used in this project to rotate the solar panels. This section is further followed by the mechanical power transmission design that transfers the mechanical power from the actuator to the solar panel. The next section describes the electrical power transfer element that allows relative rotation of the solar array and the CubeSat. This is then followed by a section detailing the selection of the most critical tribological element of the system - bearings. The next section describes the position sensor's selection process that monitors the shaft's position. The chapter ends by describing the selection and sizing of the electrical and mechanical interfaces that connect the SADM to other systems of the CubeSat.

Chapter 6 describes the verification and integration process of the SADM that was carried out to verify its requirements.

The report culminates in the last chapter 7, where the project results are described along with the answers to the research questions formulated at the beginning of this project. This chapter also suggests recommendations for continuing this project to achieve a space-qualified product which could not be achieved during the stipulated time period.

2

Motivation

This chapter will attempt to find an answer to research question 1a. This chapter will investigate the need for a SADM for CubeSats. The first research question has two sub-questions - 1a & 1b. In order to answer these questions, this chapter firstly introduces satellites, followed by a brief overview of their history and evolution. The chapter then explores the trends in the growth of the industry and the missions they are utilised in. This is then followed by a section 2.3 that investigates missions that failed due to mechanisms and the lessons learned from such missions. This section aims to answer research question 1a. The chapter then explores the history of SADMs from their application in MicroSats and their evolution over time. The next section is aimed at finding an answer to research question 1b. Section 2.4 details a review of the state-of-the-art SADMs, followed by a critique of their drawbacks and future demands. The chapter culminates with section 2.5 that gives an account of the summary briefing on the research gap and the dire need in the industry for such a product which serves as the motivation for this project.

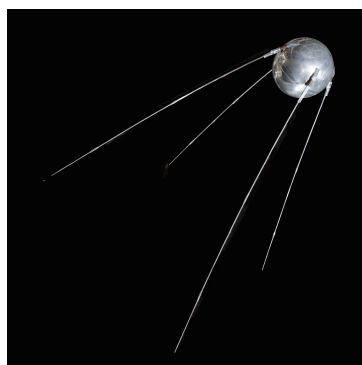
2.1. History and evolution of satellites

Planets have natural satellites that orbit around them, and these planets are in turn satellites for the star that they revolve around. The Moon is the Earth's natural satellite and the Earth is the Sun's satellite. Similarly artificial satellites have been launched into space made by humans to revolve Earth and get a bird's eye view of the Earth or to enable communication or explore rest of the solar system and its planets. These artificial satellites can be categorised based on their size or purpose. Artificial satellites are mostly launched for purposes like communication, observing Earth, observing other planets, exploring extra-terrestrial environments, measuring scientific data, meteorology, navigation, in-orbit demonstration of new technology and in-orbit manufacturing. Satellites are advantageous for Earth-based applications because they can overcome terrain imposed hindrances in communication and they can cover large parts of the Earth in a single go which is beneficial for observation. They are advantageous for extra-terrestrial applications as they overcome the atmosphere-induced hindrances in imaging and as they are machines they can be operational for years. Based on mass, satellites are classified as shown in the Table 2.1 below:

Category	Mass (kgs)
Extra heavy	> 7001
Heavy	5400 to 7000
Large	4200 to 5400
Intermediate	2500 to 4200
Medium	1200 to 2500
Small	600 to 1200
Mini-satellite	200 to 600
Micro-satellite	10 to 200
Nano-satellite	1 to 10
Pico-satellite	0.1 to 1
Femto-satellite	< 0.1

Table 2.1: Classification of satellites based on mass

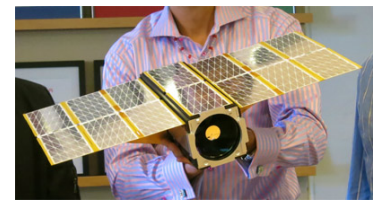
Since the launch of Sputnik-1 in 1957 (refer Figure 2.1a), thousands of satellites have been launched into space to date and are continuing to be launched. The design of these satellites has changed over the years, from their size to the technology they use and their purposes. The first satellites used batteries to power their systems and were mostly radio-based communication satellites. These early satellites were small but they required large and expensive ground stations that needed constant maintenance by large manpower. Satellites were recognized for their potential and more such missions were promoted. As the development in electronics technology led to more transistors being implemented per chip, the size and complexity of the satellites increased compared to the initial satellites to enable the satellite to be applicable for more varied applications and missions such as remote sensing, mass communication, navigation and reconnaissance for military applications. This trend was observed for four decades from the 1960s to the 2000s. One such extra-heavy category satellite launched during this era is the EnviSat as shown in Figure 2.1b, which was an European remote sensing satellite equipped with various scientific payloads (spectrometer, radiometer, altimeter & Synthetic Aperture Radar) to observe Earth. The satellite systems also changed to cope with this varied applicability. The power systems now included much larger solar arrays that could be stowed, deployed and constantly pointed at the Sun, the communication systems included large antennas to achieve concentrated beams and reuse spectrum multiple times and the ADCS systems changed to allow three-axis stabilization and higher pointing accuracy to point at the ground station. The development in electronics led to an inversion of size in ground support systems as they grew smaller compared to their earlier variants and required low manpower for maintenance.



(a) Sputnik-1: launched 1957



(b) EnviSat spacecraft: launched 2002



(c) A 3U Dove CubeSat with a human for scale: launched 2013

Figure 2.1: Evolution of satellites with time

By the end of 20th century as the computer industry and internet saw a great spike in expansion, as a result the micro-electronics industry experienced a huge development and the electronics could be miniaturised much more than ever. Towards the end of the 20th century, the satellite industry went through a complete change in approach. Before this period space missions and space engineering were limited only to national space agencies of the country and the companies supplying them with their products. By the end of the 20th century, space travel and space missions had inspired many people around the world thus drawing more learners to the subject, especially at the university level. This spike in interest led to the advent of CubeSats. In the year 2000 the concept of CubeSats was introduced by Dr. Jordi Puig and Dr. Bob Twiggs [135], the satellite industry saw new entrants like universities, commercial companies and start-ups. The first CubeSat was launched in the year 2000 by California Polytechnic University in collaboration with Stanford University [144]. The idea of smaller satellites became popular mainly to cater to student missions whose sole aim was for educational purposes. These missions had a low budget, lower development times and fewer mission objectives to be achieved as a result these missions needed small instruments and consequently smaller supporting sub-systems. Also, as these satellites are small they could piggyback on larger spacecraft and thus do not have to wait for long periods to be launched into space. Prof. Jordi Puig-Suari & Prof. Bob Twiggs introduced the concept of CubeSats and their standard sizes for catering to various applications. The standard CubeSat sizes are defined based on units (U) where 1U is a cuboid of dimensions - 10 x 10 x 11 cm and weighs around 1.3kgs. The standard CubeSat frame sizes that are commercially available are - 1U, 1.5U, 2U, 3U, 6U, 8U, 12U, 16U, 27U and 36U as shown in Figure A.3. All these advantages initiated entrepreneurship and many start-ups entered the space industry. Small-satellites became popular due to educational institutes but very

soon they were being used for commercial, military, technology demonstration and scientific purposes. This trend still continues until today (2022). It is predicted that SmallSats have a brighter future in the upcoming years as they are planned to be launched in large numbers (as constellations and formation flying missions), planned for use in inter-planetary missions, asteroid imaging missions, private companies using constellations for Earth-imaging and internet service, and the possibilities just keep growing. Planet Labs was one of the early companies to take advantage of CubeSats for commercial purposes. Planet Labs had launched a constellation of 3U satellites called Doves as shown in Figure 2.1c, that were equipped with high resolution camera and was aimed covering the entire Earth to track changes over time. Planet Labs is one of many such companies that made use of the SmallSat's advantages to become a successful enterprise. Few other such companies include AAC Clyde, Surrey Satellite Technology Limited and One Web to name a few.

2.2. Present & future of Small-Sats

The last section described the inception and rise to popularity of SmallSats. This section is aimed at diving deeper to understand the trends in their growth and their future to be applicable to advanced missions.

2.2.1. Trends in growth of the SmallSat industry

Around 8950 satellites in total have been launched into space from 1957 to 2021 [69]. Out of which only 3372 (37.676%) satellites are operational as of now [55]. As seen in Figure 2.2, the number of small satellites launched over the years have seen exponential growth.

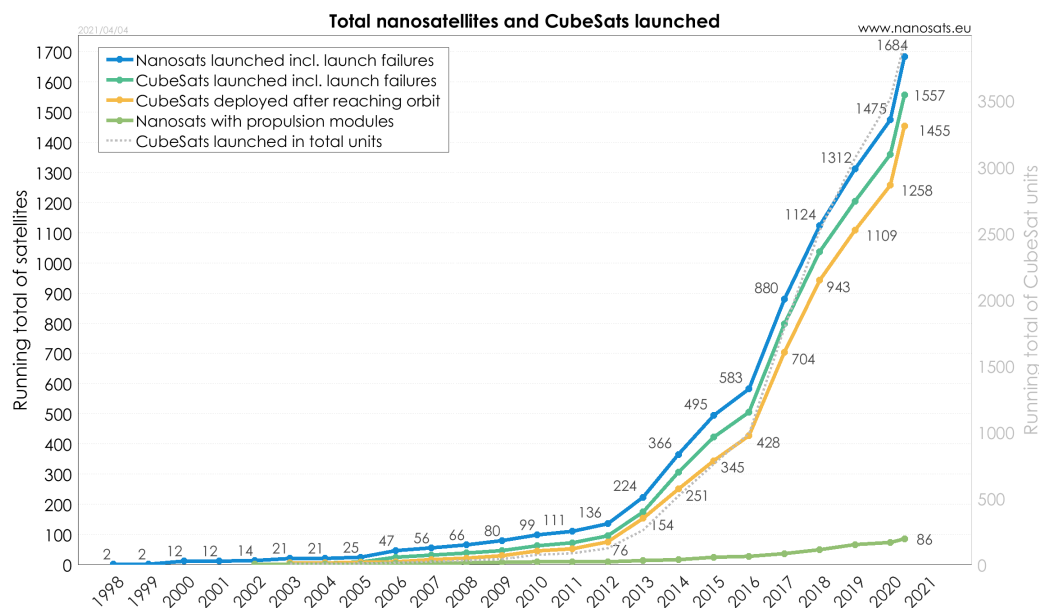


Figure 2.2: Total number of nano-satellites & CubeSats launched from 1998 to 2021 [66]

From 2000 until March 2021, around 1684 Nano-satellites (mass from 1-10 kg) have been launched into space. This includes 1553 CubeSats missions which have been launched to date [66] including two inter-planetary CubeSats to Mars [52]. Figure 2.3 shows the percentage of the number of NanoSats and CubeSats compared to other classes of satellites (Mini-satellites, medium-satellites & Large-satellites) launched from 1957 until 2021. It can be inferred from the Figures 2.2 & 2.3 that NanoSats and CubeSats are forming a significant percentage of the total number of satellites, even though they had gained popularity only over the last two decades. The reason behind this trend has been detailed in section (2.4.2). This growth trend is expected to continue over the coming years as around 990 SmallSats are expected to launch each year till 2028 [25]. This would mean that around 2,400 nano/micro-satellites are expected to launch in the next five years [70].

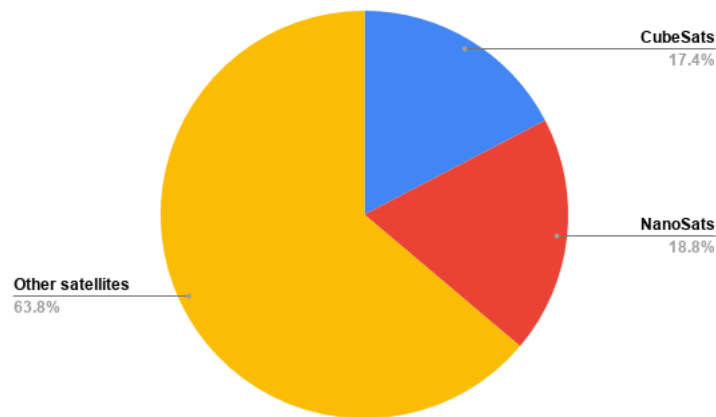
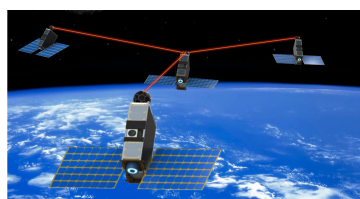


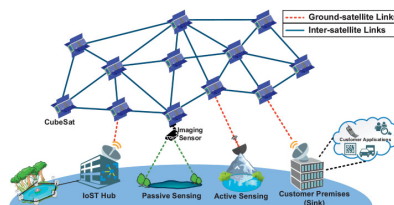
Figure 2.3: Percentage of Nanosats and CubeSats compared to Other class of satellites [52]

2.2.2. Advanced missions for Small-Sats

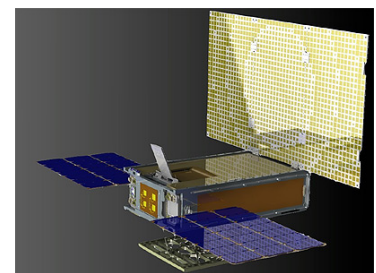
Initially SmallSats were launched for student research missions to collect data and for Earth observation by imaging. This is the major purpose that the SmallSats are used for until recent times. As the technology has matured over time, CubeSats are being used for advanced missions like communication, especially laser communication, radar altimetry, ship tracking, interplanetary missions, AI-based on-board data processing, in-orbit manufacturing and supporting 5G services. 5G is the communication technology that is being heavily tested and implemented globally. Once the technology is fully operational it would support a whole array of terrestrial applications like autonomous cars, Internet-Of-Things, Over-the-Top media services and data networking to name a few applications. LEO SmallSat constellations could support bigger satellites in covering more ground space more frequently. Compared to conventional Earth imaging applications, these missions would require higher electrical power as they have to process huge amounts of data at faster rates. As an example, AAC Clyde Space's imager IM200 [29] consumes a peak power of 1W whereas the laser communication terminal CubeCAT [56] made by the same company consumes a peak power of 15W. This results in two consequences on the satellite system - faster processing systems and communication systems with high bandwidth and high speed (transmission and receiving). In order to support these systems, the power system must be capable of providing higher electrical power.



(a) CubeSats for laser communication [195]



(b) CubeSats for Internet-of-Things [93]



(c) MARCO - Interplanetary CubeSat mission to Mars [63]

Figure 2.4: Applicability of CubeSats for advanced missions

Higher electrical power demand in CubeSats can be met in three ways - by improving the PV cell efficiency, increasing the number of PV cells or maintaining optimal conditions for power production of the PV cells. These methods can also be combined together, ideally, all three methods would have to be combined to achieve maximum power generation. Triple-junction solar cells are the most commonly available commercial PV cells for space applications and have a maximum efficiency of around 32%. Four junction PV cells are just coming into the terrestrial market and have an efficiency of around 48%. No such PV cell was commercially available for space application at the time of writing this report. Such a high efficiency PV cell will definitely boost the power production capability per unit area of the solar panel. The number of PV cells can be increased by fitting as many cells in a panel or by having a very large solar array. Using a large solar

array is not favourable because it increases the mass of the satellite and moreover there is limited space in the SmallSat deployers, which means there is a limited number of panels that can be used. The third option is to maintain optimal conditions to maximize power generation from the PV cells. The power produced by PV cells depends on their temperature, relative angle of sunlight and intensity of the radiation. The power produced deteriorates with increase in temperature, so low temperature is preferable for power production. As the satellite revolves around the Sun, the temperature of the solar panels are bound to increase this can be controlled to an extent using active or passive thermal control methods but cannot be completely eliminated. The intensity of radiation is dependent on the distance from the Sun, as most satellites in LEO do not change this distance, the intensity of radiation is not going to change. The power generated by the PV cells is related to the angle between the normal to the solar cell and the sun rays by a cosine relation. As the power generated is related by a cosine function, maximum power is generated when the angle between the PV cell and the sunlight is zero. As the satellite rotates around the Earth and as different missions require different pointing requirements, the orientation of the satellite changes with time and position of the orbit. This causes different relative position of PV cells with respect to the Sun and leads to lower than maximum power generation. This issue can be solved by allowing relative rotation of the solar arrays with respect to the satellite structure. This is where the SADM comes handy and solves this need for constant orientation by allowing relative rotation of the solar arrays with respect to the satellite structure.

2.3. Success rate of Small-Sats

Even though the SmallSats have gained popularity over the years, they have also been known for their high infant mortality rates and low success rate. This is evident in the Figure (2.5a & 2.8b). It can be seen that only 329 missions out of the 1145 CubeSat missions have completed their entire mission completely. Also the fact that 124 CubeSats arrived dead on-orbit and 63 CubeSats having failed early highlights the infant mortality issue of Small-Satellites. The low success rate can be attributed to multiple causes but the most compelling reason was suggested by Decker, who indicated that the majority of missions failed because the integrated testing was not carried out due to time and budget constraints of the educational institutes [119]. It is also important to note that the success rate has been improving over the years [52]. This can be attributed to the fact that most of these failed SmallSat missions are launched by educational institutions and Hobbyists who become better at developing the technology with experience. A similar trend can also be observed in the case of Nano-satellites, which is depicted in Figure (2.5a). Overall it can be stated that the technology has matured enough to witness lower failure rates and is ready to be extended to a wide range of applications.

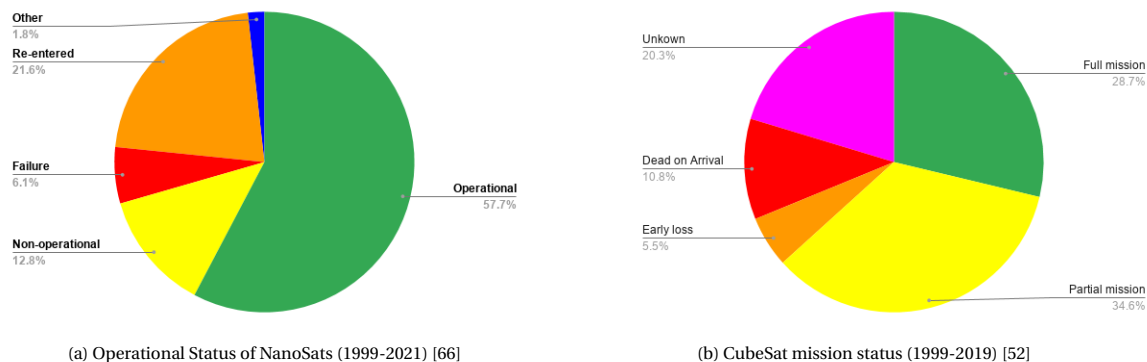


Figure 2.5: Operational status of Small-satellites

2.3.1. Missions affected by mechanisms

Diving a bit deeper to find out the other causes behind the high failure rate of the Small-satellites, a graphical representation has been presented in Figure 2.6. From this pie-chart, it can be observed that communication and power systems are the major cause of failure (17% each), followed by the mechanical system [119]. This observation is further validated by Guo et al., who have found through statistical methods that Mechanisms, Telemetry, Tracking & Command (TTC) and the Thermal Control systems have the lowest reliability among all the other systems and consequently are the main causes of early failure of CubeSats [131].

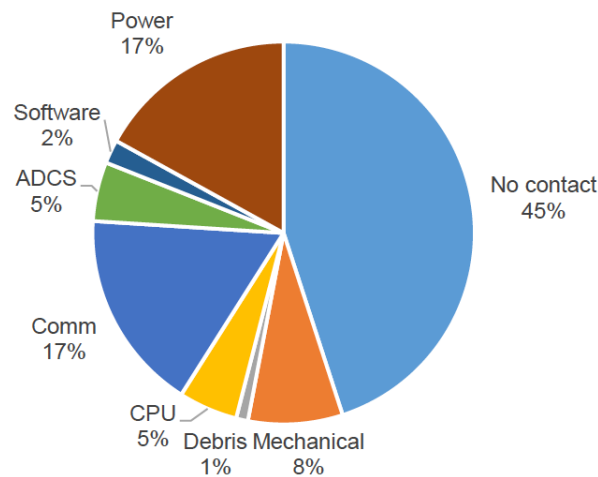


Figure 2.6: Causes of CubeSat mission failure (1999-2013) [119]

Not only in recent SmallSat missions, but many earlier satellite missions have suffered due to failure of such spacecraft mechanisms. A detailed review of about 30 such missions from 1964 to 1967 that suffered due to mechanisms malfunctioning or failure has been reported by Shapiro et al. [184]. Among the various affected missions, most notable ones are the Voyager (1977), SeaSat (1978), Apple (1981), Magellan (1989), Galileo (1989) and the Hubble space telescope (1990) [127]. A very recent study conducted by Rivera [172] dives deeper into the space missions from 1964 to 2020 that were affected due to failure of deployable mechanisms, their cause and their impact on the mission in terms of cost and severity. It has to be noted that this study has not considered CubeSat missions. Around 54 spacecraft missions were surveyed in this study and it was stated that on average at least one spacecraft has been affected every year from 1961 to 2020. The graph showing the number of space missions affected each year due to the failure of deployable mechanisms has been shown in Figure 2.7.

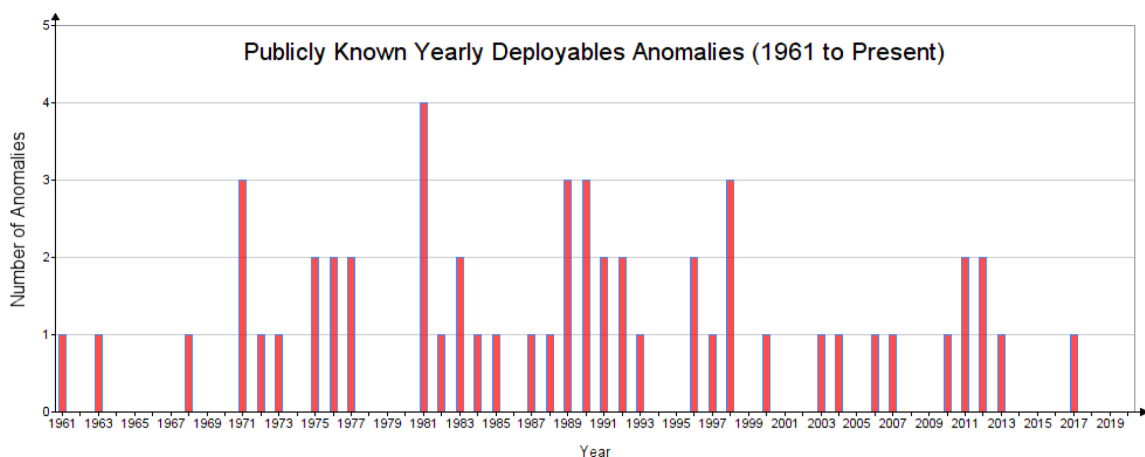


Figure 2.7: Deployable mechanisms failure per year 1961-2020 [172]

The scan platform gearbox of Voyager seized because of lubricant failure. The SeaSat failed because of short circuit due to slip-ring debris between power and ground disc. ArabSat-1A [13] and Thaicom-3 [53] also faced short circuit in sliprings which caused permanent loss of transponders and temporary outages respectively. The solar arrays of the Apple satellite failed to deploy because of the deployment device failure. The Magellan satellite failed to latch at the end position because of the micro-switch maladjustment. The instrument cover and the antenna cover of Galileo failed to deploy because of thermal binding. The solar array booms of the Hubble telescope experienced jitter because of thermal gradient in the deployable boom. A couple of missions also faced disruptions due to lubricants. The Earth Radiation Budget Satellite (ERBS) [22] and INTELSAT-V [62] are two such missions whose mechanisms failed due to lubricants. The whole

SADM system has failed in a couple of missions like the LandSat 5 [38], Eutelsat W5 [26] and HELIOS[181]. In some missions like the PIONEER 11 [44] and the GOES 10 [28] missions the SADM failed due to radiation induced malfunction and gear damage respectively.

The study conducted by Rivera classified the deployable anomalies by type and cost of insurance claimed for the damage to mission as shown in Figure (2.8). As shown in the figure (2.8a), it can be observed that solar array deployable mechanisms contribute to majority (29 out of 54) of the deployable anomalies as compared to deployable booms, antennas and tethers[172]. The solar array deployable mechanisms also contribute to the majority of the insurance claims (close to 800 million USD) as compared to deployable antennas. This highlights the significance and magnitude of impact the solar array deployable systems have on the entire spacecraft and the mission.

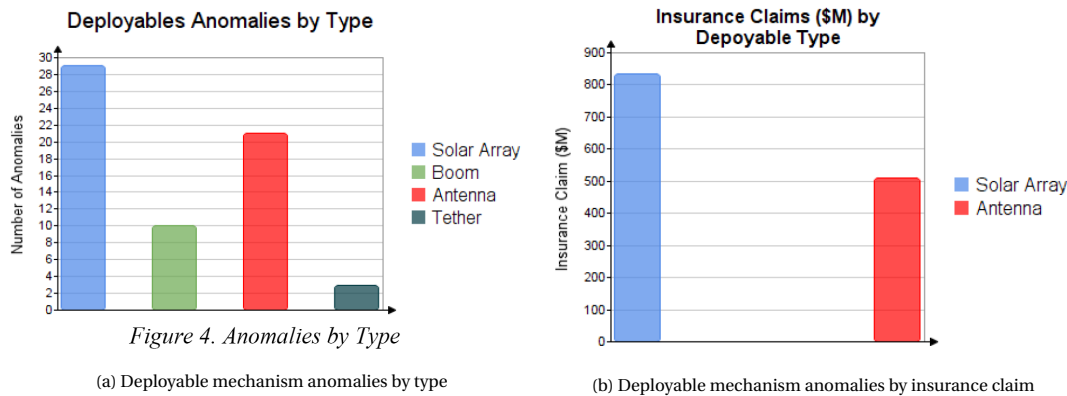


Figure 2.8: Type and insurance claims of deployable mechanisms by type[172]

2.3.2. Lessons learned from space mechanisms failure

The lessons learned through developing and testing mechanisms for various missions have been documented by NASA. The lessons learned from experience with space mechanisms have been divided into three categories: deployable appendages and rotating & oscillating systems. The most common cause of failure in all of these sub-systems and their components were found to be lubrication issues (early depletion or over-lubrication issues), vibration-induced unexpected behaviour (like deployment), ball-bearing damage, and other unexpected effects caused by thermal gradients [181]. Furthermore, the study suggested that Hold-Down and Release Mechanism (HDRM), bearings and slings were found to be very critical components as they had high chances of failure. The study by Rivera has categorized the space mission failures due to deployable mechanisms based on the cause as shown in Figure (2.9). Most of the reasons for anomaly were unknown as the failure occurs in space. But the most prominent causes of failure were found to be caused by tribological elements, followed by thermal and mechanical interfaces. It can be summarized from these studies that **tribological elements (bearings, lubricants, gears, etc.) and interfaces (electrical & mechanical) are the most crucial components** of the solar array deployable mechanisms.

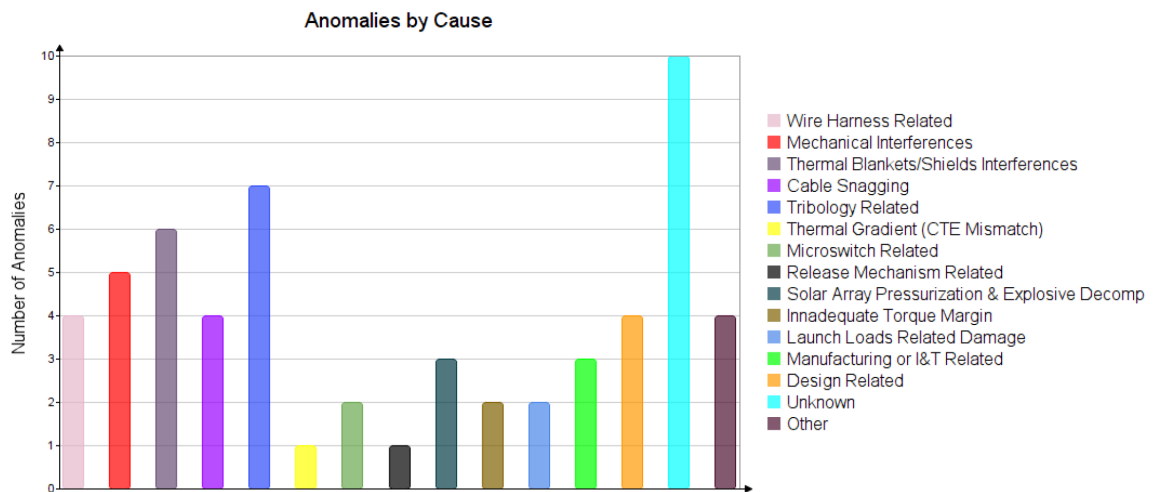


Figure 2.9: Deployable mechanism anomalies by cause [172]

2.3.3. Overview

In this section, it was found that SmallSats are increasing in the number of launches compared to bigger satellites, and this trend is expected to continue through the current decade too. Moreover, it was found that SmallSats are becoming potential candidates for advanced missions and this in turn requires higher power. Through analysis of the previous satellite missions, deployable mechanisms are less reliable and have been a significant cause of mission failure in both SmallSats and the bigger class of satellites. Furthermore, the tribological elements were identified as critical components in mechanisms. From this section, the need and significance of the SADM system in a satellite has been understood and the need for a highly reliable system was found.

2.4. Survey of Solar Array Drive Mechanisms

In the previous section, the significance of the SADM systems was understood. This section is aimed at diving a little more deeper to find out the past, present and future of the SADM systems used in satellites. The section is split in to two sub-sections namely the SADM for Micro, Mini-satellites and the Small-satellites. This section also discusses how the system design differs with respect to the size of the satellite and explores the commercially available products and their respective drawbacks. More significance will be provided to SmallSats as they are the focus of this project. But the lessons learned from the SADMs used in both of these class of satellites will be utilized.

2.4.1. SADMs for Mini/Micro-satellites

History of SADMs for Microsats

Mini-satellites are satellites having mass in the range of 100-500 kg, whereas micro-satellites are satellites having mass in the range of 10-100 kgs. Sputnik-1 was the first micro-satellite to be launched and it used batteries to power its systems. Vanguard-1 which was launched in 1958 was the first satellite to make use of solar cells to generate power, it made use of body mounted solar cells [7]. Explorer-6 was the first micro-satellite (64.4 kg) to use deployable solar panels for power generation [6]. As the satellite was spin stabilized, the solar panels were deployed using moment generated by the satellite spin. Currently, this class of satellites are usually launched in low numbers as compared to smaller satellites (Like CubeSats & Nanosats) because they have a longer development time and higher development cost. As a result of higher development cost and times, only space agencies and big companies are mostly involved in the development and launch of this class of satellites, educational institutions do not participate much. Thus, Mini & MicroSats mostly find their usage in commercial, military and large scientific applications.

Need of SADMs for Microsats

These are significantly bigger satellites and have bigger instruments and longer mission duration. Thus, they have higher power demands as well, usually in the range of Kilo-Watts. Consequently it follows that this type of satellite would have larger solar panels and higher power and data transmission requirements. The SADM systems for such satellites are accordingly designed to handle large amounts of power. This is the design aspect that differentiates the SmallSat SADM from the bigger ones. These class of satellites usually use sliprings for power transfer and data transfer. Also, satellites of this class make use of multi-DOF actuation mechanisms rather than just body-mounted panels as they have high power requirements and steerable panels provide higher power generation capability. Also, as these class of satellites are bigger, they have less strict volume and mass constraints when compared to smaller satellites which is also another reason for using bigger components like sliprings and motors.

Trends in research and state-of-the-art technology

One of the earliest SADM systems from the 1970's have been described by Rees et al. for the ESA's communication satellite missions around that time [171]. It weighed around 4.2 kilograms and was capable of transferring 4.5 kW of power. The design made use of gold-plated sliprings for power transfer, sun-sensors for pointing, brushed DC motors for actuation, pyrotechnic pins for stowage and release, dry lubricants and Silver / Molybdenum-di-sulphide (Ag/MoS₂) brushes in the slip ring. This design was attained after testing for 2 years on an initial model.

Many of the later designs of SADM that followed made use of a similar design but with slightly different variations and modifications. In an attempt to eliminate discontinuities in angular momentum, improve operating torque margins and to eliminate stalling and back-driving Jones and Roger describe a constant speed solar array drive mechanism. To achieve constant speed motion with the stepper motor they have used the concepts of mini-stepping, reduction gearing and open loop control [145]. The SADM designed for the German DFS-Kopernikus satellite also made use of a stepper motor for actuation but used a quartz oscillator for controlling speed and direction, pancake-type slip-ring with the same (Ag/MoS₂) brushes and an optoelectronic zero position sensor [96]. Around the same time, NASA as well made use of stepper motors for actuating its SADM systems for the XTE and the Tropical Rainfall Measurement missions [125]. But this design made use of a cable wrap for power and data transfer and thus had limited rotation capability of ± 175 degrees. Other notable features of the design used were the spring loaded hinges to provide kick-back force, spherical bearings for correcting misalignment, viscous damper for slow speed deployment and rotary potentiometer for position telemetry of the shaft.

The SADM technology for mini-satellites and bigger satellites had matured by the end of the 20th century as most of the satellites were using similar SADM systems as described above with minor changes as required by the mission. Around the start of the 21st century, research on improving the performance of these systems were prevalent. Rajagopal et al. designed the hybrid stepper motor so as to attain a constant torque operation irrespective of changes in the voltage or operating temperature [169]. This was achieved by modifying the stator winding and the permanent magnet operating point of the hybrid motor to attain torque saturation. Following this work, Devasahayam et al. found that material saturation limited the torque capability of the stepper motor. A power efficient and higher torque capabilities were obtained by removing the material saturation in the pole stem and yoke and also by increasing the rotor permanent magnet excitation [120].

Later in to the 21st century, in recent times (2003-2017) most of the research has been focused on designing and developing compact versions of the SADM. During this period, multiple private organizations stepped into space engineering research and thus it can be observed that most of these research were aimed at developing a modular design in order to be used for various mission geometries (LEO, GEO, MEO, etc.) which had the drawback of being over-designed in some cases [98]. As the size of the SADM had been reduced and the power specifications remained almost same or increased in some cases, the thermal issues and the electrical noise were observed to be the most challenging issue to tackle in the designing phase [92, 98, 151]. These SADM systems were not much different from the earlier systems, some of them made use of planetary gears [128] or spur gears for micro-stepping and cable wraps for power transfer so as to achieve a compact and modular design. Remaining designs made use of the previously established designs like gold-on-gold brushes for the slip-ring, optical encoders for position measurement and Commercial Off The Shelf (COTS) stepper motors for actuation, etc with minor improvements. Apart from these single-axis deployable systems, an unique bi-axial SADM was described by Scheidegger et al. which included a track axis (± 360 deg) for tracking sun and a trim axis (± 60 deg) for compensating satellite's attitude changes due to disturbances [175]. This was designed for advanced Low-Earth orbit missions of mini and micro-satellites which had higher power demands

and frequent eclipse periods. The basic principles and mechanisms behind this bi-axial SADM was taken from imager focus mechanisms and antenna pointing mechanisms already used in imaging satellites. This bi-axial SADM also used stepper motors for actuation, spur gear transmission, duplex bearings, deployment locking mechanism and a slip-ring. It weighed around 6 kgs and was capable of handling up to 60 circuits at 1.5 A.

COTS SADMS for Mini & Micro-Sats

The various commercially available single degree articulated Solar Array Drive Mechanism products are as listed in Table A.1 [1–5]. Few of the SADMs used in Micro and MiniSats are shown in Figure 2.10. As visible in the pictures, these SADMs were big and weighed in the range of 3 to 5 kilograms each. It was observed that most of these products were designed in such a way so that they can be easily modified to have a different number of power and data transfer rings in the slipring, step angles and other such performance parameters. Apart from the single axis articulated mechanisms as listed in the Table A.1, various 2-DOF gimbals are commercially produced by companies like Sierra Nevada Corporation, Honeybee Robotics and RUAG Space.

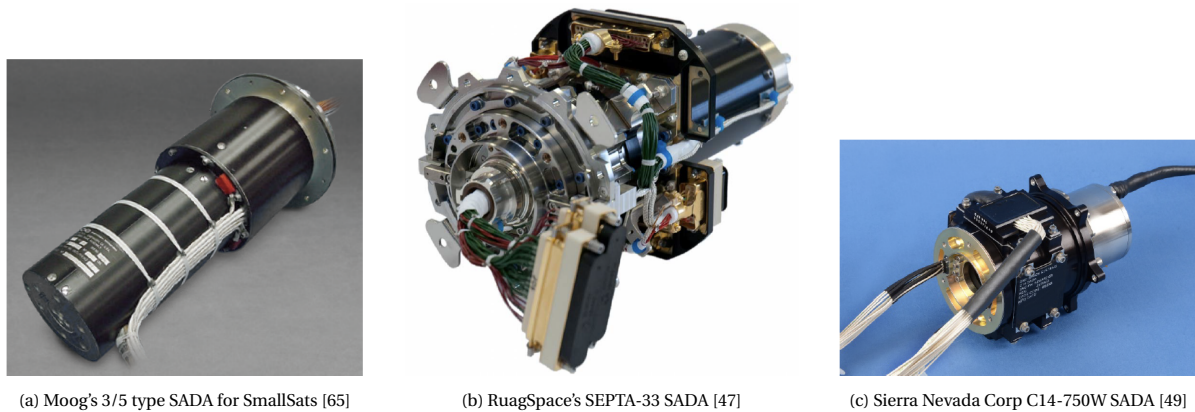


Figure 2.10: SADMs for Mini and MicroSats

2.4.2. SADMs for SmallSats

This sub-section will explore the SADMs for SmallSats by exploring their need in such a system, and trends in research and culminates with a survey of COTS products and a critique of their drawbacks.

Need of SADM for SmallSats

CubeSats need electrical power to function, and this demand is solved by using solar cells. Solar cells could be either body-mounted or deployable. The small satellite is usually launched by a deployer which is cubical, this means that the deployable structures must be folded, and the satellite must be stowed into the deployer for launch. The HDRM come in use for this purpose, to hold the deployable solar panels in stowed position during launch and deploy them at the right time once in orbit. It is different from the SADMs used in bigger satellites as they should be smaller due to the mass constraints, volume constraints, and clearance requirements set by the deployer [144]. As stated earlier in the sub-section (2.2.2), different missions require different pointing modes of the payload, and the solar cells need perpendicular positioning with respect to the sunlight to generate maximum electrical power. Satellites with fixed deployable panels usually have a specific Sun-pointing mode where the satellite is oriented towards the Sun for maximum power generation. The problem of the difference in pointing requirements of the payload and the solar cells is solved using the SADM. This is the main reason to use a SADM in a SmallSat, to decouple the payload and solar panel pointing requirements so that both have optimal pointing. Another important reason for using steerable solar panels over body-mounted panels is the increased power-producing capability. It was found that articulation of the panels around a single axis for a 3U CubeSat in LEO could provide from 496 W/m^2 up to 817 W/m^2 as compared to just 286 W/m^2 power density capable by a body-mounted solar panel [137]. Considering the increased power demand by the current and future CubeSats for advanced missions, deployable panels are the most desired option over body-mounted panels, thus requiring a SADM for such systems.

Trends in research and state-of-the-art technology:

Various papers have been published over the past two decades describing the design, development, manufacturing and testing of the CubeSat SADM systems. The earliest CubeSat made use of body-mounted solar panels as the power demand was very small [168]. CUTE-1 and QuakeSat were one of the first CubeSats to use deployable solar panels in 2003. CUTE-1 used a DC motor to remove a stopper and allowed the panel to be deployed by the restoration force of the hinge's spring [161]. QuakeSat made use of a spring-loaded hinge to deploy its solar panel and had a deployable boom mounted with high sensitivity magnetometer [152]. One of the first deployed tracked SADM systems was designed by Honeybee robotics in 2010, which used a bipolar stepper motor and an intra-bank barrier to achieve autonomous sun-tracking [163]. In the same year multiple papers were published on different designs of SADM systems for CubeSats like spring actuated hinges for deploying & damping the panels and pyrotechnics for burning the hold-down nylon wire [122], scissor-joint based deployment mechanism described by Senatore et al. [180], articulation using a micro-stepper motor [137], deployable booms for solar sails [162, 190] and Hoberman mechanism based deployment system [124]. After this, various CubeSats started utilizing the existing technology with minor improvements. Especially many CubeSats made use of the spring actuated hinge mechanism for solar panel deployment along with a nichrome burn wire HDRM like Walsh [198], Santoni et al. [174], Mahdi et al. have detailed a similar SADM for nano-satellites [154] and Solís-Santomé et al. have described a similar design but have incorporated a latch to the hinge in order to lock and maintain the panel at the final desired position [189]. Also MARCO, the first CubeSat to Mars made use of the similar spring loaded hinge for deployment and nylon burn wire for hold-down and release [136]. Apart from the spring-actuated hinge mechanism, the Shape Memory Alloy based deployment mechanism and the micro-stepper motors were the most researched and worked upon deployment methods. Santoni et al. [173] and Marino et al. [156] have detailed the design, fabrication and testing of the micro-stepper motors to deploy and actuate the solar panels of a 3U CubeSat. Recently, Guzik and Benafan from NASA have designed a SMA based HDRM and hinge for usage in CubeSats [132].

In summary, it can be inferred from the existing literature that spring deployed hinges are the most used SADM system for CubeSats and nano-sats having fixed deployed position as they are simple and reliable. Micro-stepper motors are prevalently used for systems requiring 1-DOF articulation. SMA based solutions are being moderately used for actuation and being researched as they can only provide two shapes and have a complicated manufacturing and training process.

Commercially available SADMs for SmallSats

A handful of SADMs are available as off-the-shelf products for CubeSats as shown in Figure 2.11. This subsection will describe these SADMs and their performance specifications. The CubeSat SADM by Honeybee Robotics is one of the most popular commercially available integrated SADM systems for CubeSats. This was one of the first products to be launched in its category. This product uses two micro-stepper motors to actuate two solar arrays and slip rings for power transfer. It is capable of ± 180 degrees tracking motion, it can accommodate a peak power transfer of 18 Watts per wing and it is just 6.5mm thick making it a very convenient option [11, 202]. This system is currently being used in the One-Web satellite constellation [10].

Commercial SADM for CubeSats	IMT SRL μ -SADA [30]	HoneyBee nanoTrack	Tethers Unlimited Cobra HPX [9]	RevolvSpace SARA [46]
CubeSat sizes applicable	6U & 12U	3U	-	3U & 6U
Dimensions	0.15 U (100x88x15 mm)	0.065U (100x100x6.5 mm)	0.37U (113x113x29.2 mm)	0.15 U (96x96x15 mm)
Possible panel mounting positions	2	2	6	2
Pointing accuracy	± 0.3 deg	-	± 0.077 deg	± 0.1 deg
Special features	Well suited for interplanetary missions	Smallest in market	3-DOF	Drag based attitude control

Table 2.2: Commercial SADMs for CubeSats

Tethers Unlimited Inc is the only company in the world to have designed a 3-DOF gimbal positioning, and pointing mechanism for CubeSats - the COBRA-UHPX and the COBRA-HPX [9]. It uses the Canfield joint design and doesn't use slings or cable wraps for power transfer. It can position and point the panels or

antennas within a complete hemisphere at a high resolution of ± 0.077 degrees. The newest entrant in this category of products is the RevolvSpace SARA. The design of this system is very similar to the HoneyBee Robotic's nanoTrack SADM. The only difference being, this SADM has a higher height and higher pointing accuracy than the HoneyBee robotics SADM. This SADM is also different in the aspect that it is applicable to fit with 3U and 6U CubeSats, whereas the HoneyBee Robotics SADM is applicable to 3U CubeSat. The specifications of the SADM are compared in Table 2.2. DHV Technology in Spain is also developing a SADM for CubeSats called MicroSADA [18], but no specifications have been made public yet.

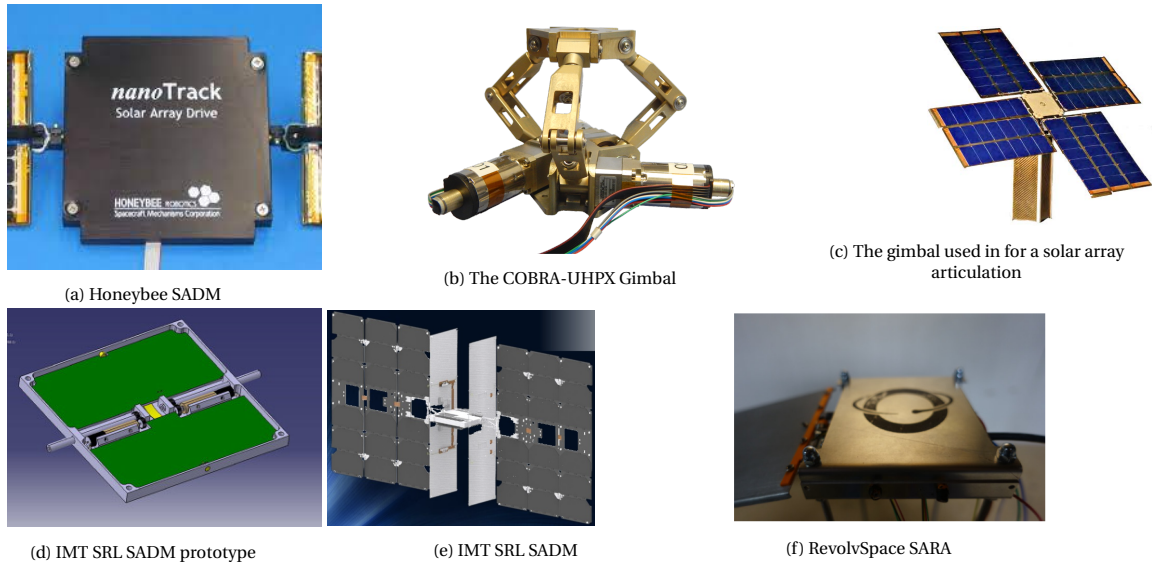


Figure 2.11: Commercially available SADMs for CubeSats

IMT (Ingegneria Marketing Tecnologia) in collaboration with University of Roma have designed a SADM very similar to the Honeybee Robotics system, which is capable of driving two solar panels about one DOF [173]. GomSpace, a Denmark based company sells two systems for deploying panels where one of them is a spring actuated hinge [8] with 2 possible deployment angles and an one-DOF tracked solar panels [8] whose specifications have been kept confidential.

Drawbacks of existing solutions & future demands

Firstly, the very fact that only a handful of products exist for solar panel articulation of SmallSats and most of them have the similar design highlights the need for a better and improved SADM in the market. With the increasing amount of CubeSats (2.2.1) that are going to be launched in the upcoming years for varied mission applications. Thus, it is high time that a new SADM product enters the SmallSat industry that is simple, reliable and efficient enough to meet all these demands.

Currently most CubeSats are in LEO that is why single axis steerable panels are used in most missions or as observed in many cases, a simple spring-loaded hinge is used for fixed position deployable solar panels. But after a few CubeSat demonstration missions to Mars (MarCO) and asteroid exploration missions (Hera mission), many such missions beyond LEO are planned in the near future [100]. Such advanced missions have limited exposure to sun and carry lot of solar panels to meet their power demand, but articulation of solar panels at least about one DOF would significantly reduce the number of panels and improve the power produced per panel. Thus increasing the application of CubeSats for various types of missions like interplanetary missions, asteroid exploration, technology demonstration, inter-satellite communication, etc.

The current products do have drawbacks which make them less favourable for these advanced applications. The gimbal designed by Tether Unlimited is bulky and over-designed for usage in CubeSat solar panel deployment. Moreover the effectiveness of the hemispherical rotation mechanism in terms of power generation is not verified yet in any scientific publication. The Honeybee Robotics and the IMT SRL's SADM suits the need comparatively better, as it is compact, provides one DOF to the solar panels and designed to be compatible with any CubeSat size. This product still has a drawback that it can only drive two panels, where four panels can be deployed (one from each edge of a face). And also, they are suitable for use only in one particular panel mounting configuration. But there are many other panel configurations (as shown in Figure (2.12))

which are applicable for varied missions and pointing requirements where the usage of this product is not possible. This is also one of the reasons why many CubeSats that have varied mission profiles use a simple spring-loaded hinge and more solar panels to generate the same power that could be generated by lesser panels with at least one Degree of Freedom (DOF).

These systems are very small and simple in terms of their working principle, which simply involves heating a tie-down element (the most commonly used method). Given the simplicity and function of this sub-system, it would be very advantageous to the end-user if the HDRM sub-system were also integrated with the SADM system. Also the fact that the commonly used burn-wire mechanisms require proper tie-down for every use makes them vulnerable to human errors and a time-taking process. Thus, a research gap still exists to find an alternative HDRM mechanism that is easily reusable and can be integrated with the SADM system.

Thus, it can be said that the SmallSat industry would benefit significantly with the advent of a SADM product that incorporates all these design features of being modular enough to be usable in more than one-panel mounting configuration, has an integrated HDRM that is reliable and testable many times on-ground and capable of maintaining power transfer capabilities over its mission lifetime.

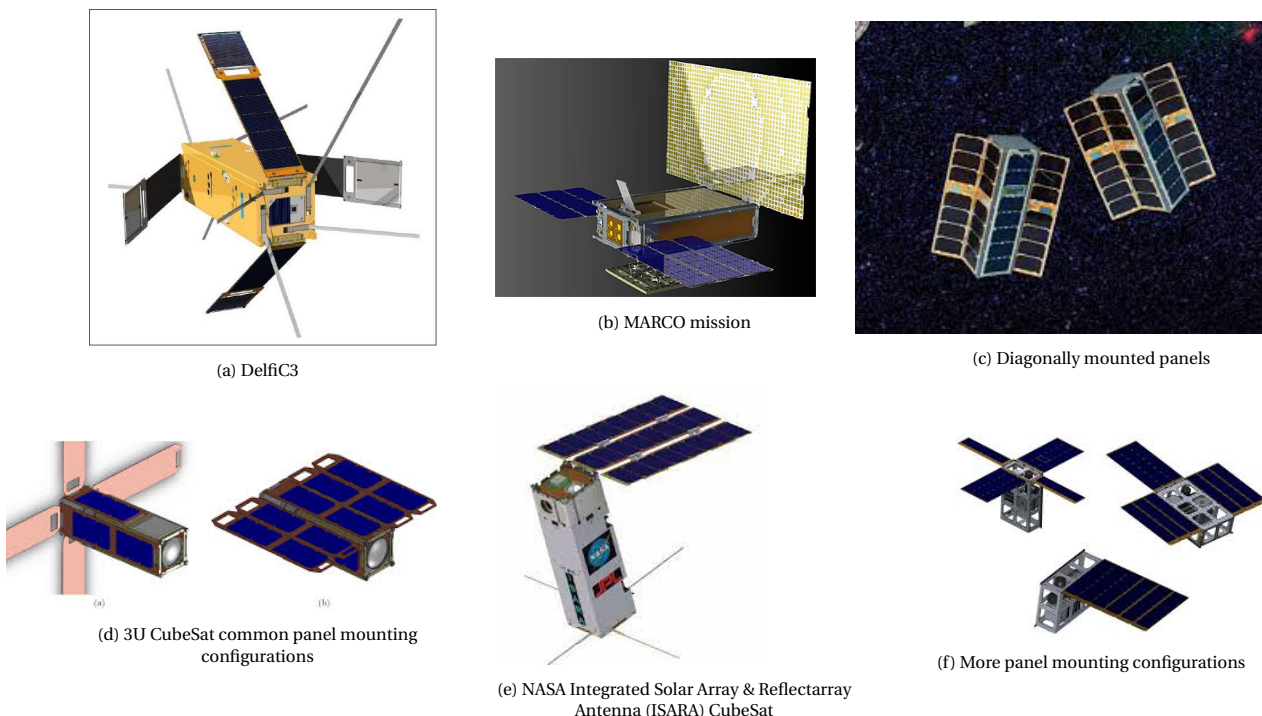


Figure 2.12: Various panel mounting configurations for CubeSats of different mission profiles

Issues with SADM & their elements

From the literature review of the SADM system that has been conducted so far, multiple issues and research gaps have been found in the SADM system and its elements. These issues and gaps were stated in detail in the earlier sections. This sub-section aims to collect all these issues and summarize them so that they can be addressed and avoided in the scope of the current project.

Firstly, most of the COTS SADMs have a similar design that can drive two solar arrays and are limited to application in a few panel mounting configurations. It was also found that multiple space mechanisms, such as the SADM, failed due to tribological elements and interfaces such as slippers and bearings. These tribological elements failed due to debris and friction caused by various mechanisms, such as under-lubrication, erosion, corrosion and surface irregularities. The Table 2.3 below briefly points out the issues and gaps in the SADM and its elements, along with references to scientific publications that explore these issues in detail. This table summarizes the findings from the literature review and the motivation for the current work.

Components	Issues	References
COTS SADM	Applicable to limited panel mounting configurations 3 of the 5 SADMs are similar in design Not scalable for use in multiple CubeSat sizes Tethers Unlimited product is voluminous IMT SRL's μ -SADA occupies internal volume	-
Power and data transfer mechanism	Issues with sliprings Material erosion (Abrasive & arcing) Debris generation Heat dissipated due to friction Short circuit Arcing at high voltage <hr/> Issues with wireless power transfer Active electronics exposed to space radiation Low Technology Readiness Level (TRL) Difficulties in miniaturisation High power loss transmission	[115, 206] [113] [130] [121] [112] [97] - [167] [208] [109]
Bearings	Wear of ball and contacting surfaces Vibration Irregular torque variations Right preloading Maintaining preload Gap formation	[34] [159] [102] [150] [197]
Tribology	Selection of right lubricant Maintenance of lubricant levels Under-lubrication causes friction Over-lubrication causes leakage Surface reaction Creep Volatility Oxidation	[105, 106, 126]
Overall system design	Thermal control Minimisation of micro-vibrations Reliability Scalability Integration and compatibility with other systems	[182, 183, 205]

Table 2.3: Issues in current SADMs and their common elements

2.5. Summary

In this section the past, current research trends and the future demands of the Micro-, Mini- and Small-satellites were explored. The main takeaways from this section are:

- There is an increase in the number of CubeSats launched per year with increased power demand due to advanced payloads and mission capabilities. SADMs are required to allow independent pointing of payload and increase the power generation of PV cells by normal positioning with respect to the Sun.
- Current COTS CubeSat SADMs are voluminous and not modular (scalable for use in multiple CubeSat sizes & configurable for use in multiple panel mounting configurations). Thus, there is a gap in the CubeSat market for a modular SADM that is scalable for use in CubeSats of different sizes.
- Failures in space missions have occurred due to the failure of mechanisms. This can be attributed to the problems in the sub-system's common elements as summarized in Table 2.3.

A SADM system with a low volume, applicable for multiple panel mounting configurations and scalable for use in CubeSats of different sizes, was needed in the industry. Now, that the need and the drawbacks have been identified, upcoming sections will aim to address these demands and avoid the pitfalls.

3

System requirements & constraints

This chapter will set the requirements and constraints for this project. Requirements are verifiable criteria for the system. The requirements are set by the stakeholders of the project which include - the author, AAC Hyperion, and TU Delft's project supervisor. Constraints are restrictions imposed on the system by its operational environments. This is defined in the beginning so that the system can be designed in conformance to these criteria & conditions. Most of the design decisions in the later sections will be based on these requirements and constraints, making them an important stepping stone for the project. The requirements are usually defined at a system level, which later flows down to the component level as child requirements. This is in a way, a top-down approach. This chapter has three sections, it begins by defining the different kinds of requirements in section (3.1) for the system along with their rationale and verification and followed by a section (3.2) on constraints imposed on the system by its operational environment.

3.1. System requirements

System requirements are the guidelines to design the system and are usually formulated at the beginning of the project based on the research questions and agreed upon in consultation with the stakeholders. They are crucial because they drive design decisions. The requirements in this project have been divided into categories such as functional, performance, interface, environmental, Reliability, Availability, Maintainability & Safety (RAMS) & Design.

There are four methods to verify the requirements, which include Testing (T), Analysis (A), Demonstration (D) & Inspection (I). Testing using a prototype requires the operation of a part or complete system under controlled conditions to verify if a quantitative requirement has been met. It requires test equipment & instrumentation for measuring. Verification by inspection includes a visual inspection of drawings, data, the system itself and its physical attributes (weight, dimensions, colour, marking) or documentation. Verification by analysis includes evaluation of data generated by statistical analysis, qualitative analysis and/or simulations. Verification by demonstration includes observing and recording the system's functional operation to determine its conformance to requirements without using test equipment or instrumentation.

Functional requirements

Functional requirements are the key functionalities that the system shall be capable of performing. Simply stated, the SADM system has to rotate the solar arrays and transfer the electrical power generated by the PV cells along with the data generated by the panel-mounted sensors. These requirements are usually verified by demonstration because these are basic functionalities of the system and do not require special equipment to test; these requirements cannot be verified by analysis or inspection as they need an integrated working system.

Among the various sizes of CubeSats available, AAC Hyperion required the SADM to be designed specifically for a 12U CubeSat as that was the structure part of their product portfolio. It was later required to be desirable to have the product scalable to multiple sizes. Therefore, the current project will be aimed at designing the SADM specifically for a 12U CubeSat but the scalability to other sizes would be a secondary priority or rather a design consideration rather than a stringent requirement. This explains the functional and performance

requirements framed to be specific for a 12U CubeSat. The solar panel size has been fixed to 326×210 mm which is lower than the dimensions of a 12U CubeSat's face (340×226 mm as shown in Figure A.2). This is because, part of the solar panel's area will be used for hinges, wire routes and sensors. This reduced dimensions of the solar panel was referred from similar products [19].

Identifier	Requirement	Rationale	Verification			
			T	A	D	I
SADM-FUN-001	The system shall be able to rotate an array consisting of 3 rigid solar panels of 12 U size (326×210 mm) each along one axis throughout 360 degrees in space & ground.	The system should be able to orient the solar panels normal to the Sun rays for maximum power generation and the satellite is constantly changing position throughout the orbit.	.	.	✓	.
SADM-FUN-002	The system shall deploy and stabilize the solar arrays after release from stowed position.	This is because the solar panels should be rigid once deployed so that it doesn't impart unnecessary disturbance torque to the satellite.	.	.	✓	.
SADM-FUN-003	The system shall allow the transfer of electrical power generated from three 12 U sized (326×210 mm) solar panels to the CubeSat bus.	Because the solar panels are rotating with respect to the satellite and due to this relative motion, the power generated by the panels should be transferred through the SADM. The maximum power generated should be considered because this is the worst case scenario.	.	.	✓	.
SADM-FUN-004	The system shall allow the transfer of data generated by the panel-mounted sensors to the CubeSat mounted systems.	Because the systems on-board of the satellite would use the data generated by these sensors for various purposes.	.	.	✓	.
SADM-FUN-005	The system shall communicate the deployment status of the solar panels to the satellite OBC	Deployment status telemetry is mandatory for space mechanisms according to Section 4.7.5.4.2 of ECSS-E-ST-33-01C Rev.1 [179]	.	.	✓	.

Table 3.1: Functional Requirements

Performance requirements

Performance requirements are performance specifications that the SADM system should meet, they state how well the system must perform the functions. This kind of requirement usually specify a value that the system can be tested against to be verified, which is why they are usually verified by testing.

Identifier	Requirement	Rationale	Verification			
			T	A	D	I
SADM-PER-001	The system shall point the solar panels with an accuracy of atleast ± 8 degree (3σ 99.7% confidence) with respect to the solar incident angle (or beta angle).	The power produced by the panels is a function of cosine of the angle between the sun and the normal of the solar panel, the power drops by 1% with an 8 degree deviation of panel from the Sun.	✓	.	.	.
SADM-PER-002	The system shall give the position of the solar panels at any point during operation with an accuracy of TBD degrees.	The solar panel position knowledge is necessary in situations where the system undergoes a reboot and the relative position of the Sun with respect to satellite has changed. The accuracy can be determined with reference to a pointing error budget for this application which could not be carried out.	.	.	✓	.
SADM-PER-003	The system shall have an in-orbit duty of at least 29200 cycles in LEO.	29200 = 16 orbits per day @ 160 km LEO x 365 days x 5 years. Refer SADM-ENV-001 for mission life.	✓	.	.	.
SADM-PER-004	The system shall have 29200 on-ground working cycles.	The system is usually life tested on ground and mostly not in a vacuum chamber.	.	.	✓	.

Table 3.2: Performance Requirements

Interface requirements

Interface requirements define how the system should interact with the external environment or how the subsystem interacts with other components within the system. It defines how the system should exchange energy, mass, etc. It can be further spilt into mechanical interface, electrical interface, data, interfaces, etc.

Identifier	Requirement	Rationale	Verification			
			T	A	D	I
SADM-INT-001	The system shall be compatible to fit on the external surface of a CubeSat of standard size 12 U.	Set partly by AAC Hyperion & author.	.	.	.	✓
SADM-INT-002	The system shall be stowed in the defined volume envelope specified for a standard 12U CubeSat deployer.	Because the system should be fit into a standard deployer in order to be launched.	.	.	.	✓
SADM-INT-003	The system shall provide mechanical connection interface between solar panels and satellite.	The system has to be mounted to the CubeSat structure to be mechanically stable & constrained.	.	.	✓	.

SADM-INT-004	The system shall provide electrical connection interface between solar panels and satellite power bus.	Needed to transfer the power to the EPS.	.	.	✓	.
SADM-INT-005	The system shall provide data interface between panel-mounted sensors and satellite data bus.	Only then the data can be transferred.	.	.	✓	.

Table 3.3: Interface Requirements

Environmental requirements

This system is supposed to be operational in ground and space environments along with surviving launch vehicle imposed loads. These are the environment-imposed requirements on the system, and the system is designed to operate or survive these conditions. Therefore, these requirements apply to all the components of the system. Some of these requirements are stated in the Table (3.4) below. Most of these requirements require a test bed to simulate the environmental factors and measuring equipment to measure the system's response in order to be verified, therefore they are verified by testing. Ariane-5 rocket was chosen to gain representative launch loads. There are multiple other launchers such as the PSLV, Falcon, Atlas, etc. It was not necessary to find the launcher imposing maximum launch loads because the maximum random vibration load was specified by NASA-GEVS-7000A [108] which is the maximum launch load that would act on the CubeSat. Other launch forces are stated to gain an overview of the launch environment.

Identifier	Requirement	Rationale	Verification			
			T	A	D	I
SADM-ENV-001	The system shall be designed for 5 years in Low Earth orbit.	Standard CubeSat hardware design life as observed with other commercially available sub-systems.	✓	.	.	.
SADM-ENV-002	The system shall have an operating temperature between -40 C to 80 C.	Referred from similar systems. [30] [46]	✓	.	.	.
SADM-ENV-003	The system shall survive temperatures between -65 C to + 125 C.	Referred from NASA GEVS [108] & NASA Environmental conditions for space flight hardware survey. [165]	✓	.	.	.
SADM-ENV-004	The system shall withstand a lateral acceleration of 0.6 g.	Referred from Ariane launcher manual.[14] Requirement will be verified by test because it needs vibration test equipment.	✓	.	.	.
SADM-ENV-005	The system shall withstand a longitudinal acceleration of 10 g.	Referred from Ariane launcher manual.[14]	✓	.	.	.
SADM-ENV-006	The system shall withstand a maximum dynamic load factor of $\pm 3.2g$	Referred from NASA GEVS.[108]	✓	.	.	.
SADM-ENV-007	The system shall withstand random vibration loads of 14.1 G_{RMS} .	Referred from NASA GEVS. A.1 [108]	✓	.	.	.
SADM-ENV-008	The system shall withstand a sine load of $\pm 3.2g$	Referred from NASA GEVS.[108]	✓	.	.	.

3.1. System requirements

SADM-ENV-009	The system shall withstand shock loads in the range of 100 Hz & 10g to 10000Hz & 132g.	Referred from NASA GEVS.[108]	✓	.	.	.
SADM-ENV-010	The system shall withstand a maximum depressurization rate of 4.5 kPa/s.	Referred from Ariane launcher manual.[14]	✓	.	.	.
SADM-ENV-011	The system shall function in vacuum as well as atmospheric conditions.	Referred from NASA GEVS.[108] Shall be verified by functional test in Thermal Vacuum Chamber (TVAC).	✓	.	.	.

Table 3.4: Environmental Requirements

Reliability, Availability, Maintainability & Safety requirements

These requirements are set to improve the reliability of the system by specifying margins and setting restrictions. These requirements can be verified by inspection of design documentation where it can be verified if the margins and restrictions have been considered while designing.

Identifier	Requirement	Rationale	Verification			
			T	A	D	I
SADM-RAMS-001	The system shall be designed with a load safety factor of 1.25 for qualification and acceptance.	Defined according to limit mentioned in Table 4-3 of ECSS-E-ST-32-10C Rev.1. [178]	.	.	.	✓
SADM-RAMS-002	The system should not use volatile fluids.	Necessary steps would be taken to avoid volatile fluids, but in some cases, it is unavoidable, like sealed bearings.	.	.	.	✓
SADM-RAMS-003	The materials used in the system shall adhere to low out-gassing criterion such that they have a Total Mass Loss < 1 % and Collected Volatile Condensable Material (CVCN) < 0.1 %. [191]	Out-gassing compounds must be avoided so as to prevent volatile substances to deposit on other materials and cause malfunction.	.	.	.	✓

Table 3.5: Reliability, Availability, Maintainability and Safety Requirements

Design requirements

Design requirements apply to the system design, these are usually set by the stakeholders. These requirements are verified by inspection because the design is usually verified by review of design or by review of documentation.

Identifier	Requirement	Rationale	Verification			
			T	A	D	I
SADM-DES-001	The system shall use COTS components as & whenever possible.	To improve ease of procurement and reduce cost of production.	.	.	.	✓
SADM-DES-002	The design of the system should be scalable to be usable in 3-12 U CubeSats.	AAC Hyperion's requirement to maximise application range or scalability.	.	.	.	✓

SADM-DES-003	The design of the system should be such that it can be applied for more than a panel mounting configuration.	Author's suggestion to improve modularity of product.	.	.	.	✓
SADM-DES-004	The system shall not extend beyond one plane.	AAC Hyperion's requirement.	.	.	.	✓

Table 3.6: Design requirements

3.2. Design constraints

Considering the requirements SADM-INT-001, SADM-INT-002 & SADM-DES-002; the dimensional limits within which this system should fit can be obtained. Setting the dimensional limits would be one of the first steps, as it sets the limits for all the other components within the system.

The first interface requirement states that the system should be compatible to fit on the external surface of a 12U CubeSat. The dimensions of a typical 12U CubeSat are shown in Figure (3.1) below; for a detailed data sheet that contains the detailed dimensions of the CubeSat and the deployer imposed volume limits, refer to A.2. Looking at the dimensions of the 12U CubeSat structure (Top and side view given on left side of figure), it is evident that the SADM can be fit in the volume on the top face of the CubeSat after excluding the space occupied by the rails on all four corners. This would result in a volume limit of 209.3 x 209.3 x 7 mm on the top face.

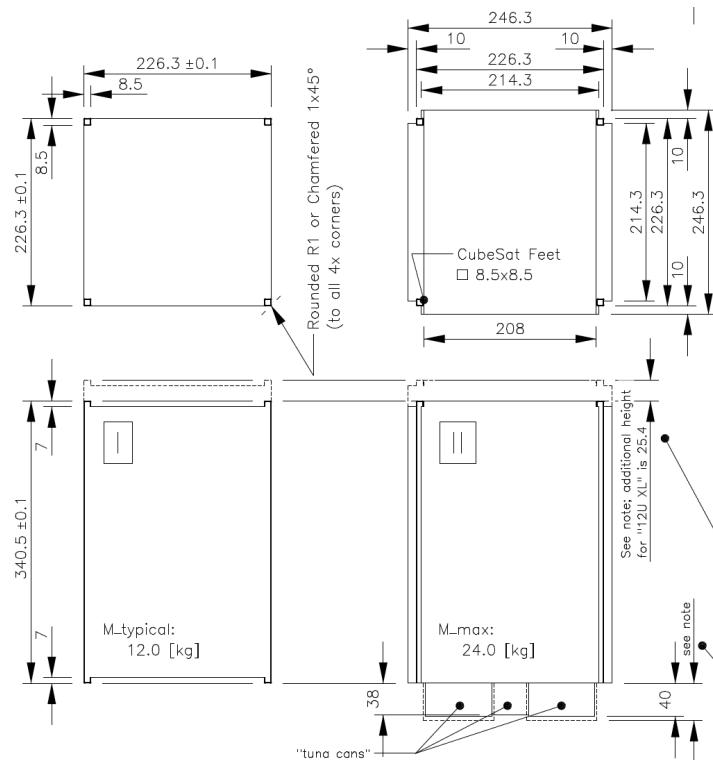


Figure 3.1: 12U CubeSat dimensions & deployer imposed volume limits [32]

The second interface requirement SADM-INT-002 states that the SADM shall fit within the volume limits of the deployer, whose limits are mentioned in the two pictures on the right side of Figure (3.1). It can be inferred that the deployer allows up to 18.5 mm height on the side faces of the CubeSat and up to 25.4 mm height clearance on the top face of the CubeSat, as depicted on the top and bottom pictures on the right side of Figure (3.1) respectively. It is important to note that the 25.4 mm clearance on the top surface is only pos-

sible with the XL version of the deployer (refer Figure 3.1). It would remain 7 mm for a normal deployer. The height clearances on the side would also have to include the solar panels. For the SADM to not be in direct contact with the deployer, the SADM must have a clearance height lower than the allowable dimensions. The direct contact between the SADM and the deployer has to be avoided to prevent the direct transfer of launch loads to the SADM. By providing a clearance, the rails would take up most of the launch loads without transferring it to the SADM. A clearance of 0.1 mm is enough to prevent contact between the two surfaces. This is an assumption made at this initial stage of the design based on comparison with systems of similar design and mounting [31]. The ISIS deployable antenna is also mounted on the external surface of a 3U CubeSat and has dimensions of $98 \times 98 \times 7$ mm. Moreover, multiple manufacturers state that CNC machine tolerance ranges from 0.127 to 0.0254 mm, which is close to the assumed clearance value. As the material used for the housing is selected, the clearance value can be revisited for other considerations such as thermal expansion. Hence a height of 6.9 mm would suffice for now. Thus the volume limits are now: $209.3 \times 209.3 \times 6.9$ mm.

The third requirement on the dimensional limits, as stated by the design requirement SADM-DES-002 says that the system should fit on 3U - 16 U satellites. Even though this is very broad and dimensionally restrictive at the same time, an estimate of the volume required to satisfy this requirement shall be made for now and shall be attempted to achieve, if not successful, the previous dimensional envelope ($209.3 \times 209.3 \times 6.9$ mm) considering the two interface requirements shall be utilized. The volume limit shall be obtained by considering the dimensions of the 3U CubeSat as it is the smallest of the satellites mentioned in the requirement. The dimensions available on the top face of a 3U CubeSat, excluding the rails as referred from Figure (A.3) are $83 \times 83 \times 7$ mm. Again, considering the clearance of 0.1 mm between the deployer and the SADM a **design dimensional envelope** of $83 \times 83 \times 6.9$ mm is obtained. The system shall be aimed to fit within this dimensional limit.

4

Preliminary design calculations

The requirements & constraints of the SADM were set in the previous chapter. In order to start designing and selecting components for the SADM, these requirements must be converted to values and specifications that the SADM sub-system and its elements must satisfy. Until now, the report has only detailed the basic functionality of the SADM. As the SADM is to be designed for a wide range of missions, its working in different conditions and environments must be understood in order to start designing the SADM. Which is why in this chapter, firstly the common mission scenarios that occur for satellites in Low Earth Orbit (LEO) would be explored in section 4.1 to understand the SADM's functioning in different scenarios that it may face during operation. This will be followed by a section 4.2 on basic operating modes design for the SADM. The purpose of these sections is to understand the operation modes of the SADM to find worst case operation scenarios. As it was defined earlier that the SADM's main function is to rotate the solar arrays and transfer the power generated by the solar cells, this would mean that the rotary actuator and the power & data transfer mechanism would be the most crucial elements for designing the SADM. The maximum mechanical power required to rotate the solar array and the maximum electrical power generated by the solar array have to be calculated so that the rotary actuator and the power transfer mechanism can be selected and sized based on these specifications later. Therefore, sub-sections 4.3.1 & 4.3.2 will be focused on calculating the mechanical and electrical power respectively. The other crucial requirement applying to the SADM apart from the two functions is the fact that it has to withstand the environmental conditions defined in Table 3.4 throughout its operational lifetime. The most detrimental environment for the survival of the SADM is the launch environment. The SADM must survive the worst-case launch load that can act on it in order to be operational. Sub-section 4.3.3 is aimed at finding the worst case launch load and translates this to the SADM to calculate the worst case launch force that the SADM's structural elements must be designed to sustain. The chapter culminates in section 4.4 with a brief summary of the results obtained from these preliminary design calculations.

4.1. Common mission scenarios

Common mission scenarios of CubeSats in LEO can be classified based on various categories like mission operational phases (launch, deployment, detumble, deploy appendages, mission operations, decommission & disposal), payload functional phase, pointing modes & energy generation phases. But for designing the SADM, the most appropriate design case is the mission scenarios based on energy generation and pointing modes because they will determine various design parameters for the SADM like the rotational speed and the angle by which the panel has to be rotated which would be calculated in a later section. These mission scenarios will be explored in this section along with their relevance to the current application.

4.1.1. Scenarios based on energy generation

Most of the satellites in LEO experience a period of sunlight and eclipse when rotating around the Sun because of the shadow cast by the Earth. The sunlight and eclipse region are shown in the Figure (4.1) below. The solar panels can generate electrical energy only in the sunlit region and cannot generate any electrical energy in the eclipse region. This means that the SADM has to track the Sun when orbiting in the sunlight

region, which is one of its main functional requirement SADM-FUN-001 & SADM-PER-001. Based on energy generation there are 2 main mission scenarios:

- Sunlight phase - Energy generation by solar cells
- Eclipse phase - No energy generation

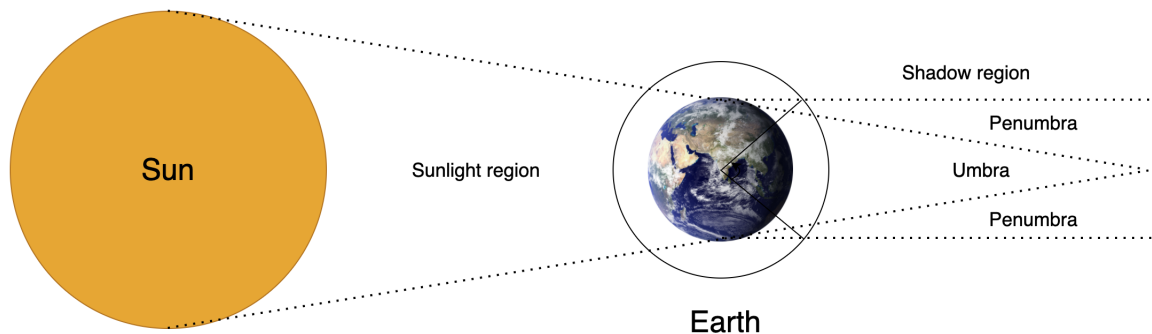


Figure 4.1: Satellite in sunlight and eclipse

4.1.2. Scenarios based on attitude pointing modes

Satellites in LEO have different attitude pointing modes in order to point the payload at different directions based on mission requirements. The most common attitude pointing modes [176] include but are not limited to :

- **De-tumbling mode:** Used to dampen the rotational moment of the satellite. Usually used when the satellite is just released from the deployer and is tumbling. The solar panels would not have been deployed at this stage, thus this mode is not applicable for this application's design.
- **Sun pointing mode:** Satellites that have fixed deployable solar panels would require the satellite to be oriented towards the Sun for charging the battery. This can be done in 2 ways, orient the satellite towards the Sun while keeping the attitude inertial fixed or by rotating the satellite about the viewing axis or yaw axis while maintaining pointing towards the Sun. By utilizing a SADM that allows relative positioning of the solar panels with respect to the CubeSat, this mode would not be required.
- **Inertial pointing mode:** This is a pointing mode where the satellite is pointed towards a star or another heavenly body like the Moon while maintaining a zero rotational rate of the satellite with respect to the pitch axis.
- **Nadir pointing mode:** Also called as Earth pointing mode. The satellite is continually pointed toward the nadir or center of the Earth which is optimal for Earth observation missions. In this mode, the solar panels would continually track the Sun with the same velocity as the orbital velocity of the satellite.
- **Target tracking mode:** Target tracking mode is the mode where the satellite is rotated about the pitch axis to continually track a point on the ground. This would mean that for a particular phase of the orbit, the satellite would rotate faster than the nominal orbital speed in order to track the point on ground.
- **Maneuvers:** This mode is required for changing the satellite's pointing attitude from one orientation to a different one. This mode would require the solar panels to be re-oriented by the same angle as the manoeuvre in addition to the angle subtended by the satellite over the period of manoeuvre.

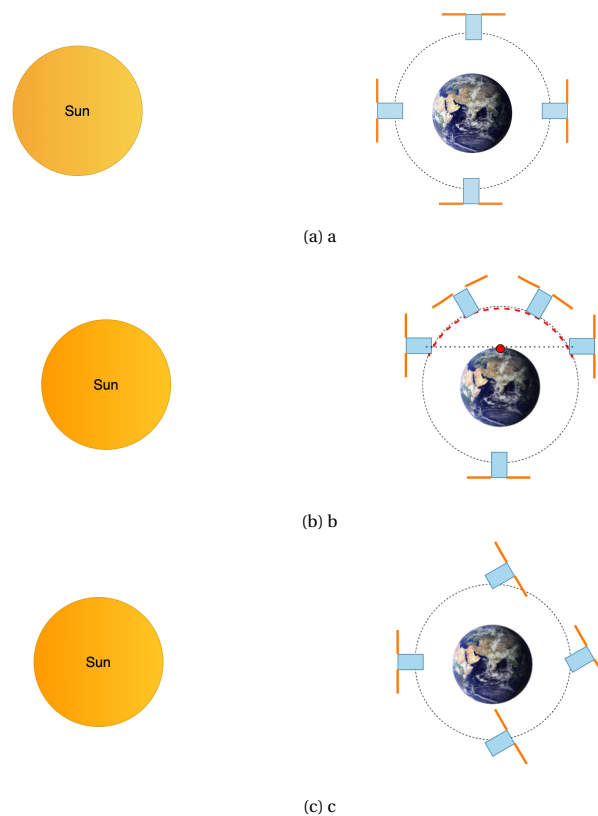


Figure 4.2: Common pointing modes a) Nadir pointing b) Target tracking c) Inertial pointing with Sun tracking phase

4.2. System Architecture & Operating modes

The SADM is designed for application in LEO as stated in SADM-ENV-001. There are many scenarios and pointing modes that are possible in LEO as discussed in the previous section. It would be desirable to design the SADM to be applicable to all mission scenarios that are possible in LEO. This design requirement is advantageous from a commercial point of view but, each mission would require a specific operational cycle or profile from the SADM that is suited to the mission profile. This requirement of broad applicability would make it hard to design the SADM at this initial stage. Thus, the approach followed in this project would be to design the SADM with operating modes that would cater to operation of common phases of most missions but would also be designed for a worst case scenario (in terms of Revolutions Per Minute (RPM)) so that it can be inclusive to be applicable over a broad range of applications. This section will describe the basic operational flow of the SADM.

The basic operational modes of the SADM are graphically presented in Figure 4.3. Initially, the solar arrays are stowed during launch and are deployed once in orbit. The springs in the hinge would slowly unfurl the solar panels in the array until they are stabilised, this is the deployment phase. The SADM would not have to perform any functions during this phase. As soon as the deployment phase is completed, the SADM enters idle mode. In this mode, the system is powered, sensors data acquisition is active and the power generated by the panels are transferred but the motor is not functional; therefore, the panels are not rotated. After the idle mode, the SADM enters the test mode. As the name suggests, this mode is designed to make the SADM perform basic functions such as moving clockwise for a defined number of steps and anti-clockwise for a defined number of steps. The position sensor and actuator status data are used to monitor the functional status of the SADM. The actuator's status can be monitored by measuring the current and voltage flowing to drive the actuator or the temperature can be monitored to detect overheating. The position sensor would measure the position of the solar panels, which would be compared with the actuator's functional status. If there is an apparent difference between the two then that would indicate a malfunction or error in the SADM. The number of steps in test mode shall be predefined with reference to the home position so that the result is an expected value and the SADM's functional status can be decided by comparing the actual value with the expected value. This mode will help find if the SADM has arrived dead or detect a failure at any point of

operation of the SADM. If no abnormalities were detected, the SADM then moves to the Sun detection mode, where the SADM detects the relative position of the Sun with respect to the satellite so that it can point the solar panels accordingly. This can be done in multiple ways. The relative position can be calculated based on the attitude knowledge of the satellite and the Sun that can be retrieved from the ADCS and its elements (Sun-sensor, horizon sensor, etc.). The relative position can also be found independent of the ADCS by rotating the solar arrays through the entire 360 degrees, and the position corresponding to maximum power generation could be found using the Maximum Power Point Tracker (MPPT). After the approximate position of the Sun is known, the SADM then enters the Sun tracking mode, where it rotates the solar array to be normal to the incident sunlight. The Sun's position relative to the satellite changes with its position in orbit. The solar arrays can be rotated to continuously track the Sun or intermittently. The SADM under consideration shall also be designed to have two tracking modes - Continuous & Sporadic Sun tracking modes. The SADM shall enter either of these modes based on the customer's choice. The Sporadic Sun tracking mode has a constant angle or fixed rotation rate mode. In the constant angle mode, the solar panel is rotated at a fixed angle for every period of a set time interval. In the fixed rotation rate mode, a fixed angular rotation rate is maintained throughout the orbit. For example, this can be calculated to match the satellite's orbital speed. The SADM returns to the idle mode if any fault is detected or if any abnormality in operation is detected by the SADM's MCU. The failure scenarios must be defined while implementing the software, which is out of this project's scope. Common error detection and recovery methods in such embedded systems are Interrupts and Watchdog timers. Watchdog timers are electronic hardware that restarts the system if the system has not communicated within a specified time period. Interrupts are hardware-triggered events that lead to a software routine once activated. If a fault has been detected, the system reboots or executes a fault recovery method appropriate for the fault scenario. If the fault has not been resolved after multiple reboots, other fault recovery methods can be used, such as switching to a redundant MCU or just maintaining the solar panels at a fixed position that is optimal for power generation throughout the orbit. If no fault is detected after reboot, the system returns to test mode and repeats the rest of the flow process.

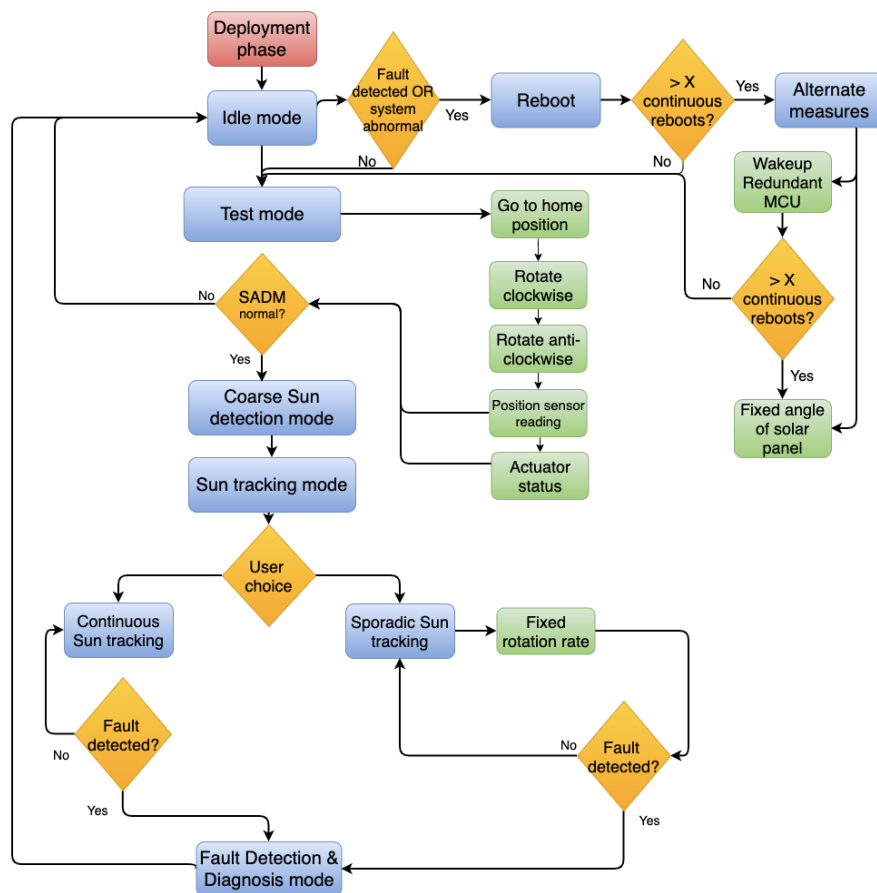


Figure 4.3: Basic operating modes of the SADM

A brief description of these modes have been stated below:

- **Deployment phase**

Occurs after detumbling and attitude stabilization. The solar panels are released from stowed position and move from 0 to 90 degrees. The restoration force is provided by the spring in the hinge. Deployment is initiated by the HDRM release. It happens only one time in orbit, because the panel has to be reset back to its initial position manually.

- **Idle mode**

In this mode, the system is powered but the motor is not functional. So the panels are not rotating. This is the default mode right after deployment, fault detection and reset mode. Sensors are not active in this mode.

- **Sun detection mode**

The SADM enters this mode after reboot and after the idle mode. This mode is functional during the orbit in the sunlit phase. The relative position of the Sun with respect to the solar arrays is determined in this mode. This can be determined by rotating the solar arrays through its rotation range or by using the attitude knowledge provided by the ADCS. The SADM enters this mode after reboot because the satellite would have moved by some distance while restarting the SADM and it would be beneficial to know the changed position and position the solar panels accordingly.

- **Continuous Sun tracking mode**

In this mode, the SADM continuously rotates the solar arrays to position it normal to the Sun. This mode is preferable for nominal operation and maximum power generation.

- **Sporadic Sun tracking mode**

In this mode, the SADM positions the solar arrays intermittently. The tracking and power generation would not be as efficient as the continuous Sun tracking mode. This mode is designed so that if some unexpected malfunction happens with the software or sensors, the system would still have basic functionality. This mode has two sub-operative mode options:

- **Reboot**

In this mode, the power to the SADM is switched on and off. This is sort of a fault recovery method that prevents the SADM from failing catastrophically and allows safe failing. After reboot, the SADM goes back to the test mode and Sun detection mode. The number of reboots are kept account of so that the SADM does not go into an endless loop of reboots. After a particular number of continuous reboots, if the SADM does not return to normal functioning, alternate measures are taken to keep the SADM operational. These alternate measures include but are not limited to using a redundant MCU. If this second level of safety measure of switching MCU also fails, the SADM will maintain the solar array at an optimal fixed position throughout the orbit.

- **Fault detection & diagnosis mode**

The MCU enters this mode when an error is detected. The error or failure scenario is logged by the MCU and sent to the satellite OBC for keeping and account. The MCU then detects and classifies the fault based on previously defined scenarios. The MCU then performs the fault response method specific to the fault scenario identified.

4.3. Design calculations

The requirements for designing the system and the operational environments have been defined in previous sections. In this section, the system design requirements and the environment-imposed design conditions will be translated into numerical specifications of the system. These specifications would serve as the stepping stone to sizing, selecting components and driving design choices in the detailed design phase. These numerical specifications mainly include the mechanical power required for rotating the solar panels, launch forces that the system will experience, and the electrical power it has to transfer. In order to answer research question 2a, the mechanical power that the actuator must provide should be known. For answering research question 2b, the maximum electrical power characteristics (current & voltage) must be known. Research questions 2d and 3a can be answered only if the launch loads are known. This section will therefore be split into three sub-sections - 4.3.1, 4.3.2, & 4.3.3 that calculate the mechanical power, electrical power and launch loads respectively.

4.3.1. Mechanical power calculations

One of the main functions of the SADM, as stated in SADM-FUN-001, is that the system shall rotate a solar array consisting of three solar 12-U size solar panels. A certain magnitude of mechanical power would be required to rotate the solar panels, this power would have to be provided by the rotary actuator. The mechanical power is essential to size and select the rotary actuator technology. This is why the mechanical power is calculated initially to provide boundary conditions for the actuator selection & sizing. Mechanical power is composed of two factors - torque & speed, as shown in the formula below.

$$P_{mech} = \tau \omega \quad (4.1)$$

Therefore, the rotational speed and the torque required for this application during various mission scenarios will be calculated in the subsequent sub-sections, and the worst case among them in terms of the power required (maximum power demanding case) will be used for selecting and sizing the rotary actuator in later sections.

Rotational speed calculation

To calculate the rotational speed required, 3 different mission scenarios were considered among the various mission scenarios explored in section (4.1):

- **Speed in continuous Sun-tracking phase:** This operational mode (4.2) is considered because the SADM has to continually track the Sun in this phase.
- **Speed in eclipse phase:** The solar panels could be rotated to a desirable position during the eclipse period. This desirable position would be an angle where maximum power is produced by the satellite just at the beginning of the sunlight phase.
- **Speed in ground tracking:** Among the various attitude pointing modes explored in subsection (4.1.2), it was found that the maximum relative rotational speed between the solar panels and the Sun vector occurs during the ground tracking mode, where the satellite had to be continuously pointed towards the ground station over a part of the orbit where the satellite was in line of sight of the ground station.

An orbital altitude of 200 km will be considered for calculations because the SADM is designed to be operational in LEO (160-1000 km) as stated in SADM-ENV-001 and the lowest altitude is selected for calculations because the number of revolutions per orbit would be higher which would mean the orbital speed would also be higher compared to higher altitude orbits. As stated earlier, it is favourable to design the system for the worst case scenario. The altitude of 200 km is considered rather than 160 km because the atmosphere is much denser at 160 km, and not many CubeSats are launched into that altitude as they would de-orbit quickly due to drag.

The time period of a 160km altitude orbit:

$$T = 2\pi \sqrt{\frac{(R_E + R_{sat})^3}{\mu}} \quad (4.2)$$

$$T = 2\pi \sqrt{\frac{(200 + 6371)^3}{6.987 \times 10^{14}}} \Rightarrow 5300 \text{ seconds} \quad (4.3)$$

At 160km orbit altitude, the orbital speed of the satellite would be 5252.4 seconds which is not far off from the calculated value for 200km altitude.

Angular rotation rate in sunlight

Time spent in sunlight is calculated using the formula below:

$$T_{sun} = \frac{\pi + 2\alpha}{2\pi} \times T \quad (4.4)$$

$$\alpha = \cos^{-1}\left(\frac{R_E}{R_{sat}}\right) \quad (4.5)$$

$$\alpha = \cos^{-1}\left(\frac{6371}{200}\right) = 0.9$$

$$T_{sun} = \frac{\pi + 2\alpha}{2\pi} \times T \quad (4.6)$$

$$T_{sun} = \frac{\pi + 2(0.9)}{2\pi} \times 5300 = 3068 \text{ seconds}$$

The total angle of orbit spent in sunlight:

$$\theta_{sun} = \frac{\pi + 2\alpha}{2\pi} \quad (4.7)$$

$$\theta_{sun} = \frac{\pi + 2 \times 0.9}{2\pi} = 283 \text{ degrees}$$

The angular rotation rate of solar panels in the sunlight phase:

$$\omega_{sun} = \frac{283}{3068} = 0.09 \frac{\text{deg}}{s} = 1.6 \times 10^{-3} \frac{\text{rad}}{s} = 5.4 \frac{\text{deg}}{\text{min}} \quad (4.8)$$

Angular rotation rate in eclipse

Time spent in eclipse is calculated using the formula below:

$$T_{ecl} = \frac{\pi - 2\alpha}{2\pi} \times T \quad (4.9)$$

$$\alpha = \cos^{-1}\left(\frac{R_E}{R_{sat}}\right) \quad (4.10)$$

$$\alpha = \cos^{-1}\left(\frac{6371}{200}\right) = 0.9$$

$$T_{ecl} = \frac{\pi - 2\alpha}{2\pi} \times T \quad (4.11)$$

$$T_{ecl} = \frac{\pi - 2(0.9)}{2\pi} \times 5300 = 1131 \text{ seconds}$$

The total angle of orbit spent in eclipse:

$$\theta_{ecl} = \frac{\pi - 2\alpha}{2\pi} \quad (4.12)$$

$$\theta_{ecl} = \frac{\pi - 2 \times 0.9}{2\pi} \times 360 = 77 \text{ degrees}$$

The angular rotation rate of solar panels in the eclipse phase:

$$\omega_{ecl} = \frac{180}{1131} = 0.159 \frac{\text{deg}}{s} = 2.77 \times 10^{-3} \frac{\text{rad}}{s} = 9.54 \frac{\text{deg}}{\text{min}} \quad (4.13)$$

Angular rotation rate in target tracking:

The maximum angular rotation rate required was found to be occurring during the target pointing mode, As shown in Figure (4.4), the solar panels had to be rotated by 180 degrees through the time of traversal over the arc indicated in red. And the solar panel's velocity profile (speed versus time graph) during this period would be a sinusoidal curve with the peak angular speed occurring right over the ground station.

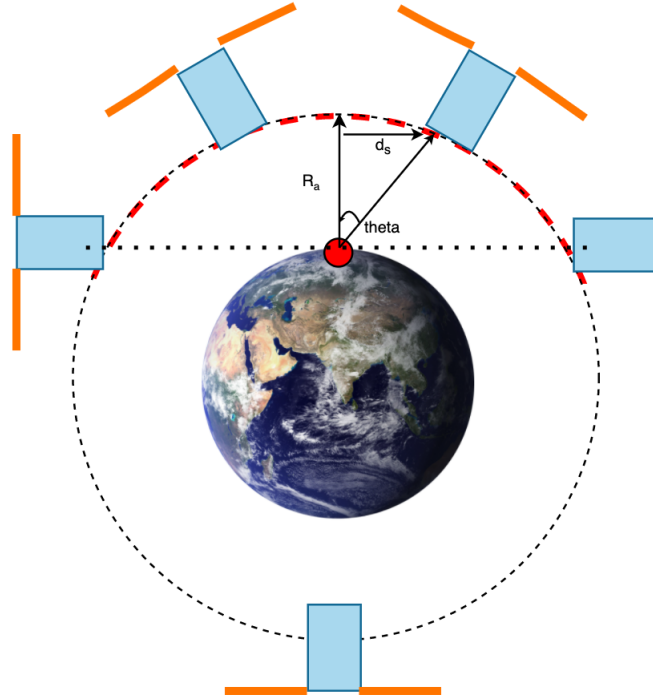


Figure 4.4: Angular rotation rate of target tracking satellite

For a unit second where the satellite is just over the ground station, the angular rotational speed is expressed as change in the angle over the time interval expressed as shown below:

$$\omega_{tt} = \frac{d\theta}{dt} \quad (4.14)$$

The momentary angle subtended between the satellite positions after one second and the satellite position when over the ground station is expressed as:

$$\theta = \tan^{-1} \frac{d_s}{R_{sat}} \quad (4.15)$$

The distance traversed by the satellite in unit second is found by:

$$d_s = V_c \times t_s = \sqrt{\frac{\mu_e}{(R_{sat} + R_E)}} \times 1 \quad (4.16)$$

For a satellite altitude (R_a) of 200 km:

$$d_s = \sqrt{\frac{3.986 \times 10^{14}}{((200 + 6371) \times 10^3)}} \times 1 = 7.788 \text{ km} \quad (4.17)$$

$$\theta = \tan^{-1} \frac{7.788}{200} = 2.23 \text{ degrees} \quad (4.18)$$

$$\omega_{tt} = \frac{d\theta}{dt} = \frac{2.23}{1} = 2.23 \text{ degrees/sec} \quad (4.19)$$

The units will be converted to rad/s so that they can be used in calculations of the later sections.

$$\omega_{tt} = 0.0389 \text{ rad/s} \sim 0.04 \text{ rad/s} \quad (4.20)$$

The maximum angular rotational speed of the satellite in target tracking mode is:

$$\omega_{\max} = 0.04 \text{ rad/s} \quad (4.21)$$

The angular rotational speeds for the different mission scenarios calculated in this sub-section have been summarised in the table (4.1) below.

Phase	Angular rotational speed (rad/s)	Angular rotational speed (RPM)
Sunlight	1.6×10^{-3}	1.52×10^{-2}
Eclipse	2.77×10^{-3}	2.6×10^{-2}
Target tracking	0.04	0.381

Table 4.1: Summary of angular rotational speed calculations

Torque calculation

The next step in calculating the mechanical power is calculating the torque required to rotate the solar panels. Torque is also composed of 2 factors which are the inertia of the panels and the angular acceleration rate of the panels, as shown in the equation below:

$$\tau = I_{sa} \alpha_{sa} \quad (4.22)$$

The above equation represents the primary effect of the torque that the actuator has to provide. The actuator also has to provide enough torque to overcome secondary effects like the inertia of connected parts like shaft and gears, friction between moving parts, etc. The complete equation to estimate the minimum torque required to be provided by the actuator is given by European Cooperation For Space Standardization (ECSS) Mechanisms design guideline [179] as:

$$\tau_{min} = 2(1.1\tau_I + 1.2\tau_S + 1.5H_m + 3F_R + 3H_Y + 3H_A + 3H_D) + 1.25\tau_D + \tau_L \quad (4.23)$$

Inspecting the above equation, various safety factors can be eliminated for the current application. Adhesion torque (H_D), Hysteresis torque (H_Y), Harness torque (H_A) & Spring torque (τ_S) are not pertinent to the current design and are usually very low in magnitude compared to friction resistive torque. Therefore they can be eliminated. The motor magnetic losses (H_m) are also usually negligible compared to the torque provided by the motor. The system would not be operational when the satellite is accelerating, so the Inertial resistance torque can also be eliminated from the equation. This leaves a simplified equation (4.24) pertinent for this application as shown below:

$$\tau_{min} = 2(3F_R) + 1.25\tau_D + \tau_L \quad (4.24)$$

The worst-case friction torque (F_R) is contributed by the friction from the bearings, gearbox, motor bearings, etc. These are not known at the beginning of the design. Therefore, the above equation shall be used in later sections to verify the feasibility of the design. To calculate the torque to be provided by the actuator considering the primary effects as shown in equation (4.22), the inertia of the solar panels will be calculated, followed by the angular acceleration.

Solar array inertia calculations

The mass and dimensions of the solar array are necessary to calculate the inertia of the solar array. A typical solar panel consists of components like - a substrate material (like FR-4, Honeycomb or Aluminum), substrate insulation layers in the front & back (usually Kapton, Kevlar or Fiber-glass), Photo-Voltaic (PV) cells, cover glass, wires, inter-connectors, sensors like (temperature sensors, sun-sensor, magnetometer), hinges, cutouts for hold down points & adhesive. The axes notation, panel, array, length and breadth of a typical 12U solar array are shown in Figure (4.5) and the cut-section of a typical solar panel is shown in Figure (4.6).

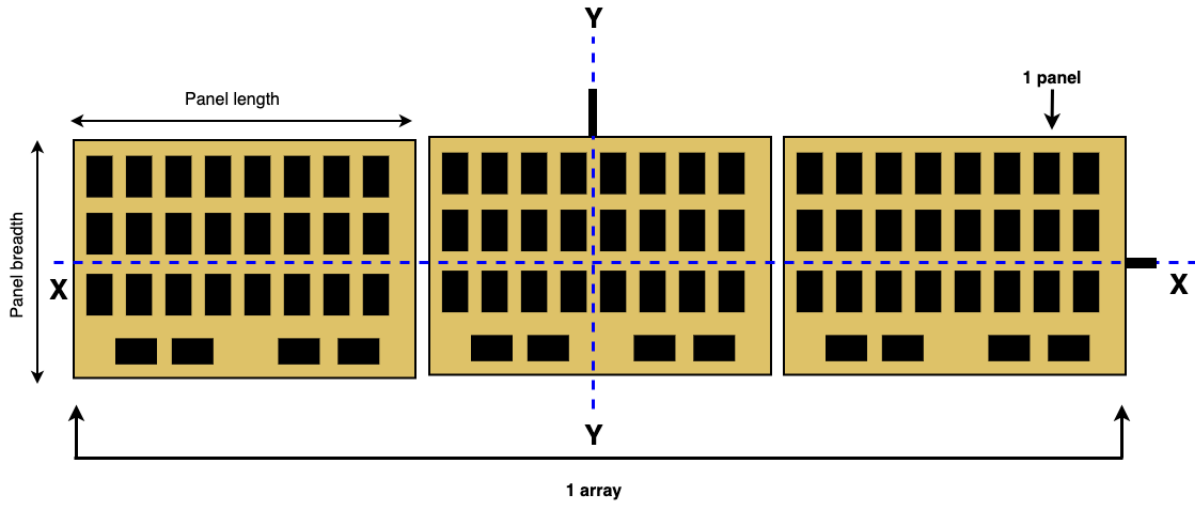


Figure 4.5: A typical 12U solar array & its axes

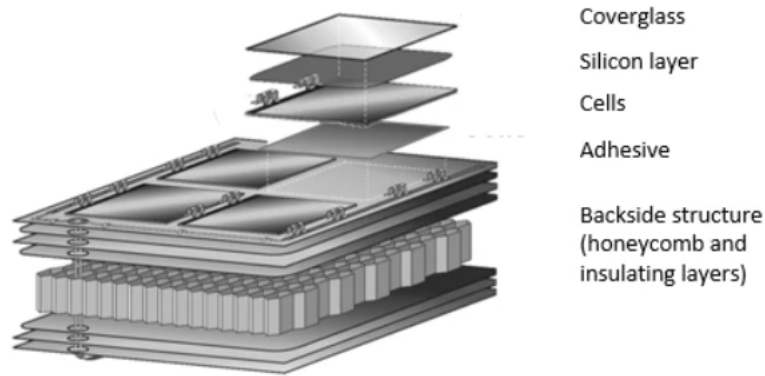


Figure 4.6: Cut-section of a typical solar panel [68]

A few assumptions have been made to calculate the inertia of the solar array:

- The entire solar array is assumed to be a continuous, rigid & flat rectangular plate.
- The thickness of the cover glass and solar cell are assumed to be negligible compared to the thickness of the substrate.
- The mass of the cover-glass, substrate insulation, inter-connectors & adhesives are considered negligible compared to the mass of the solar cells and the substrate because of their thickness being in the order of micro-meters. (Thickness values referred from Table 1 of [117]).
- The mass of the inter-connectors, wires, sensors & hinges are highly variable & design dependent, and there is no credible way to predict them at this stage. Thus they will be considered under the safety factor of the mass calculations.

Based on the above assumptions, the inertia of the solar arrays along the x and y axis are as given below:

$$I_{xx} = \frac{M_{array} (w_{panel}^2 + t h_{panel}^2)}{12} \quad (4.25)$$

$$I_{yy} = \frac{M_{array} (l_{array}^2 + t h_{panel}^2)}{12} \quad (4.26)$$

The mass of the solar array is dependent on the number of panels and mass of each solar panel, as shown in the equation (4.27) below. The total number of panels were already defined to be three according to SADM-FUN-001.

$$M_{array} = N_{panels} \times M_{panel} \quad (4.27)$$

The mass of one solar panel further is dependent on the mass of the Photo-Voltaic cells and other constituents, as shown in the equation below:

$$M_{panel} = M_{PVcell_{panel}} + M_{sub_{panel}} + M_{ins_{panel}} + M_{cov_{panel}} \quad (4.28)$$

The mass of the PV cells per panel is further dependent on the number of PV cells per panel, which is shown in the equation below:

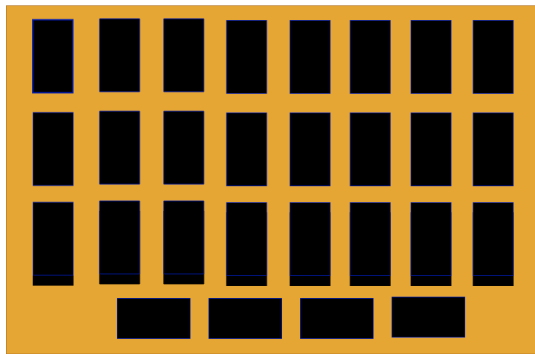
$$M_{PVcell_{panel}} = N_{cell_{panel}} \times M_{cell} \quad (4.29)$$

The number of Photo-Voltaic cells that can be fit in a panel of fixed size is highly dependent on the layout of the cells. In most cases, the number of PV cells in a panel is packed to fit in as many cells as possible so that maximum solar energy can be generated per unit area of the panel. The mathematical model for optimised PV cell configuration layout is detailed in the subsequent sub-section.

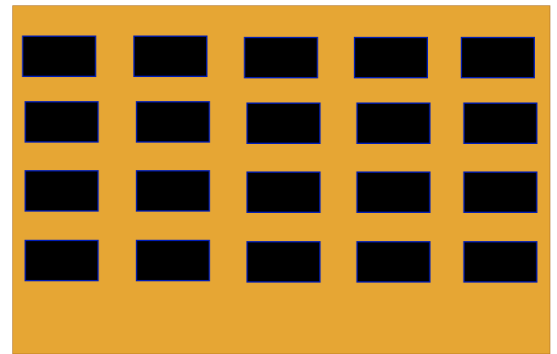
Mathematical modelling & selection of optimal PV cell layout

A mathematical model was developed to find the maximum number of PV cells that could fit on a standard 12 U size panel (340 x 190 mm) [19, 24]. This was done by arranging the PV cells in 2 configurations:

- The length of the PV cell aligned to the length of the solar panel as shown in Figure (4.7a).
- The breadth of the PV cell aligned to the length of the solar panel as shown in Figure (4.7b).



(a) PV cells aligned along length



(b) PV cells aligned along breadth

Figure 4.7: PV cells alignment configurations

The gap between the PV cells was also calculated to ensure a sufficient positive margin was present. The total number of cells that could fit on a panel in each case was found, and the configuration where the maximum number of cells could fit was chosen to calculate the mass and other electrical parameters in later sections.

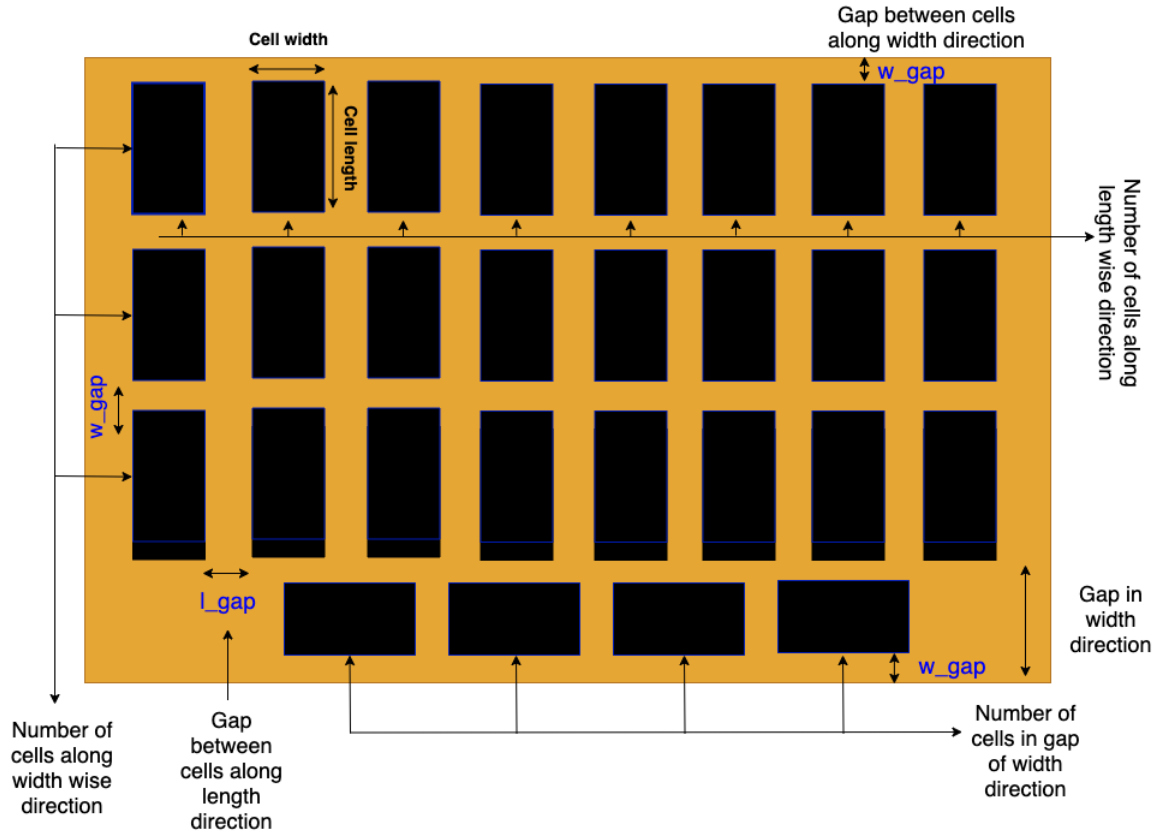


Figure 4.8: PV cell layout

The total number of PV cells in a panel include the sum of cells in each row and the cells in the gap, this is shown in the equation below:

$$N_{cell_{panel}} = (N_{cell_{len-wise}} \times N_{cell_{wid-wise}}) + (N_{cell-rows_{wid-wise-gap}} \times N_{cell_{wid-wise-gap}}) \quad (4.30)$$

Each of the above terms is further related to other geometrical parameters of the panel and the PV cell, as shown in the equations below. The 2 equations (4.31 & 4.32) below calculate the number of PV cells that can be fit along the length & width of the panel.

$$N_{cell_{len-wise}} = \frac{w_{cell}}{l_{panel}} \quad (4.31)$$

$$N_{cell_{wid-wise}} = \frac{l_{cell}}{w_{panel}} \quad (4.32)$$

The equations (4.33 & 4.34) below gives the number of PV cell rows that can be fit in the gap that exists along the width direction of the panel after the previously calculated PV cells are arranged in the panel.

$$N_{cell-rows_{wid-wise-gap}} = \frac{w_{panel} - (N_{cell_{wid-wise}} * l_{cell})}{w_{cell}} \quad (4.33)$$

$$N_{cell_{wid-wise-gap}} = \frac{l_{panel}}{l_{cell}} \quad (4.34)$$

In order to carry out the above calculations, some of the most commonly used commercially available PV cells for satellites were considered - Spectrolab XTE-SF[50], Spectrolab - XTJ[51], Azurspace 4G32C[16], Azurspace 3G30C [15] & CESI CTJ 30[17]. The number of PV cells that could fit within a panel in each of the 2 configurations using the above 5 commercially available PV cells are summarised in Table (4.2). As found by

calculations and as shown in Table (4.2), the maximum number of cells that can be fit within a panel was achieved when the width of the PV cell was aligned with the length of the panel, as shown in Figure (4.7a).

	Spectrolab XTE-SF [50]	Spectrolab – XTJ[51]	Azurspace 4G – 32C[16]	Azurspace 3G – 30C[15]	CESI CTJ 30[17]
PV cell dimensions (<i>mm</i>)	6.91×3.97	6.91×3.97	8×4	6.9×3.9	8×4
Efficiency (%)	32.2	29.5	31.8	29.8	29
PV cells per panel if cell's width aligned with panel's length	20	20	16	20	16
PV cells per panel if cell's length aligned with panel's length	16	16	16	16	16

Table 4.2: Number of PV cells that can fit in a panel

Now, as the maximum number of cells that can be fit within a solar panel has been calculated, the mass of one solar panel can be found. As stated earlier and as shown in Figure (4.6). A typical solar panel comprises a substrate, PV cells, cover-glass and adhesive. Therefore, the total solar panel mass would include the mass of all these components as expressed in equation (4.28). Each of these individual mass contributors would further be split, and relations with their geometrical parameters would be expressed in the upcoming equations.

$$M_{panel} = M_{PVcell_{panel}} + M_{sub_{panel}} + M_{ins_{panel}} + M_{cov_{panel}}$$

The substrate is the biggest contributor to the solar panel's total mass. Three possible commonly used substrate materials (Aluminium, FR-4 and Honeycomb composite structure). Aluminium with a thickness of 1.6 mm would be chosen for calculations in this application. This is because Aluminium (2710 kgm^3) has the highest density compared to FR-4 (1850 kgm^3) and honeycomb composite structure (1540 kgm^3), by using the densest material, an estimate of the maximum mass of the panels can be made. The thickness value has been referred from AAC Hyperion's solar panel and other competitors. The mass of the substrate can be calculated by multiplying the volume of the substrate by its density, as shown in equation (4.35) below:

$$M_{sub_{panel}} = l_{panel} \times w_{panel} \times t_{h_{sub}} \times \rho_{sub} \quad (4.35)$$

Cover-glass is used to reduce the degradation of the PV cells due to radiation [146]. The most common cover-glass material used in satellites are cerium di-oxide doped glass and have 3 commonly available commercial variants - CMX (2600 kg/m^3), CMG (2540 kg/m^3) & CMO (2540 kg/m^3) [45]. Among the three variants, CMX cover glass material has the highest density so it will be used in the calculations to get the maximum mass possible due to the cover-glass. The mass of the cover-glass can be calculated by multiplying the volume of the cover-glass by its density, as shown in equation (4.35) below.

$$M_{cov_{panel}} = l_{panel} \times w_{panel} \times t_{h_{cov}} \times \rho_{cov} \quad (4.36)$$

Insulation layers on the solar panel are used to thermally & electrically insulate the solar panels. They keep the temperature of the solar panels under the desired range by not allowing them to get overheated on long exposure to sunlight. There are 3 most commonly used insulation layers in the space industry which include Kapton [35], Kevlar [36] & fiber-glass [27]. The mass of the insulation can be calculated by multiplying the volume of the cover-glass by its density, as shown in equation (4.35) below.

$$M_{ins_{panel}} = l_{panel} \times w_{panel} \times t_{h_{ins}} \times \rho_{ins} \quad (4.37)$$

4.3. Design calculations

The total thickness of the panel would include the thickness of the substrate, cover-glass, PV cells and adhesive layer. The thickness of the cover glass is usually in the order of micro-meters and is negligible compared to the thickness of the solar panels, which are usually in the order of millimetres. There is no reliable way to predict the adhesive thickness and is manufacturer-dependent. Therefore, the panel thickness would be approximated by the sum of the thicknesses of the substrate and PV cells as shown in equation (4.38) below:

$$th_{panel} = th_{sub} + th_{pv-cells} \quad (4.38)$$

Using the equations derived above, the mass of a solar panel and eventually the mass of a solar array and its inertia for different PV cells were calculated and have been summarized in the table (4.3) below:

	Spectrolab XTE-SF	Spectrolab -XTJ	Azurspace- 4G32C	Azurspace- 3G30C	CESI-CTJ- 30
PV cell mass (g)	2.268	2.268	1.78	2.35	2.683
Max PV cells per panel	20	20	16	20	16
Substrate mass (kg)	0.28				
Insulation layer mass (kg)	9.17×10^{-3}				
Thickness of panel (mm)	1.66				
Mass of one panel (kg)	3.35×10^{-1}	3.35×10^{-1}	3.18×10^{-1}	3.37×10^{-1}	3.33×10^{-1}
Mass of one wing (kg)	1.1	1.1	1	1.1	1
Inertia along x-axis (kgm^2)	3.33×10^{-3}	3.33×10^{-3}	3.03×10^{-3}	3.33×10^{-3}	3.03×10^{-3}
Inertia along y-axis (kgm^2)	9.54×10^{-2}	9.54×10^{-2}	8.67×10^{-2}	9.54×10^{-2}	8.67×10^{-2}

Table 4.3: Summary of inertia & mass calculations

The maximum values for each parameter among the different configurations have been highlighted in yellow, and these values will be used in later sections to size and select components. In summary, from this section, it was found that:

- The **maximum mass of a solar array** with three 12-U sized panels would be **1.1 kg**
- The **maximum inertia of the solar array along the x-axis** is **$3.33 \times 10^{-3} \text{ kgm}^2$**
- The **maximum inertia of the solar array along the y-axis** is **$9.54 \times 10^{-3} \text{ kgm}^2$** .

The next step in calculating the torque required to rotate the solar panels is to calculate the angular acceleration of the solar array. This will be calculated in the next sub-section.

Solar array angular acceleration calculations

The angular acceleration of a rotating body is given by the equation below:

$$\alpha_{SA} = \frac{\omega_f - \omega_0}{t} \quad (4.39)$$

The final angular accelerations of the solar panel are those calculated for the different mission scenarios as calculated in section (4.3.1) and summarized in table (4.1). The angular acceleration rate would be calculated from rest therefore the initial angular velocity will be zero. The time period for acceleration will be considered

as an unit second. Based on these values, the angular acceleration for the three different mission scenarios are summarized in Table (4.4) below. It can be observed that the angular acceleration rate of the solar arrays are maximum in the target tracking scenario as highlighted in the table.

Phase	Angular acceleration (rad/s^2)
Sunlight	1.6×10^{-3}
Eclipse	2.77×10^{-3}
Target tracking	0.04

Table 4.4: Summary of angular acceleration calculations

Summary of torque calculations

Now, as the inertia and the angular acceleration of the solar arrays are known, the torque required to rotate the solar arrays can be calculated using equation (4.22). In order to calculate the torque values, the inertia values summarised in Table (4.3) & the angular acceleration values summarised in Table (4.4) will be used. The resultant torque values for the different mission scenarios and the array's rotational axis are summarized in the Table (4.5) below. As highlighted in the table, the maximum torque required to rotate the solar arrays were found to occur during the target tracking scenario when the arrays are rotated along the y-axis. The **maximum torque required from the actuator** rotating the solar arrays would therefore be **3.816 mNm**.

Phase	Torque to rotate along x-axis (mNm)	Torque to rotate along y-axis (mNm)
Sunlight	5.33×10^{-3}	0.153
Eclipse	9.22×10^{-3}	0.264
Target tracking	0.133	3.816

Table 4.5: Summary of torque calculations

Mechanical power calculations

The main motive of this section was to calculate the mechanical power required to rotate the solar arrays. As the torque and the rotational speeds are now known, the mechanical power required to rotate the solar arrays in different mission scenarios and different rotational axis can be calculated using equation (4.40) and are summarized in Table (4.6) below. As highlighted in the table below the **maximum power required** to rotate the solar arrays was found to be **0.153 mW** which is expected to occur in the target tracking phase. The calculated power is very low because of the low inertia of the solar arrays and the low RPM that the SADM operates at. The actuator would definitely have to provide more power than the calculated value as it has to overcome the friction dissipated in tribological elements.

$$P_{mech} = \tau \omega \quad (4.40)$$

Phase	Power to rotate along x-axis (mW)	Power to rotate along y-axis (mW)
Sunlight	8.528×10^{-6}	0.245×10^{-3}
Eclipse	25.54×10^{-6}	0.731×10^{-3}
Target tracking	5.32×10^{-2}	0.153

Table 4.6: Summary of mechanical power calculations

Summary of rotational speed, torque & power calculations

A brief summary of the maximum angular speed, torque required and the power required to rotate the solar arrays have been summarized in the Table (4.7) below. As highlighted in the table below, it was found that the maximum speed, torque and power required to rotate the solar arrays will be required when the solar arrays are rotated about the y-axis during the target tracking mission phase.

Phase	Maximum torque	Maximum rotational speed	Maximum power required
Units	mNm	rad/s	mW
Sunlight	0.153	1.6×10^{-3}	0.245×10^{-3}
Eclipse	0.264	2.77×10^{-3}	0.731×10^{-3}
Target tracking	3.816	4×10^{-2}	0.153

Table 4.7: Summary of maximum torque, speed & power required calculations

4.3.2. Electrical power calculations

One of the main functions of the SADM is to transfer the power generated by the PV cells to the satellite's power system whilst allowing relative rotational motion as stated in SADM-FUN-003. The maximum electrical power characteristics are also necessary to be known in order to answer research question 2b and to eventually design the power and data transfer mechanism of the SADM. The worst-case characteristics (current & voltage) of the electrical power transferred from the solar panels to the CubeSat must be known for sizing and designing the power transfer mechanism. The maximum current determines the conductor properties required to transport the current. The maximum voltage will determine the appropriate insulator properties for this application. This section will calculate the maximum voltage and current to be transferred by the SADM.

Electrical characteristics of PV cells

A typical PV cell is electrically equivalent to a p-n junction diode. Its electrical characteristics are shown in Figure (4.9). As shown in the figure, the main parameters influencing the design are the open circuit voltage (V_{OC}), saturation current (I_{SC}), voltage (V_{MP}) and current (I_{MP}) at the maximum power point. The open circuit voltage is the maximum voltage across the PV cell when no load is connected, i.e. when the circuit is open ($I=0$). When operated in a short circuit condition (leads connected to each other), the saturation current flows through the cells ($V=0$). But, as the product of voltage and current are zero in these cases, no power can be obtained from the solar cells in these states. The solar cells attain a maximum power point for a particular voltage and current value for which their product is the highest.

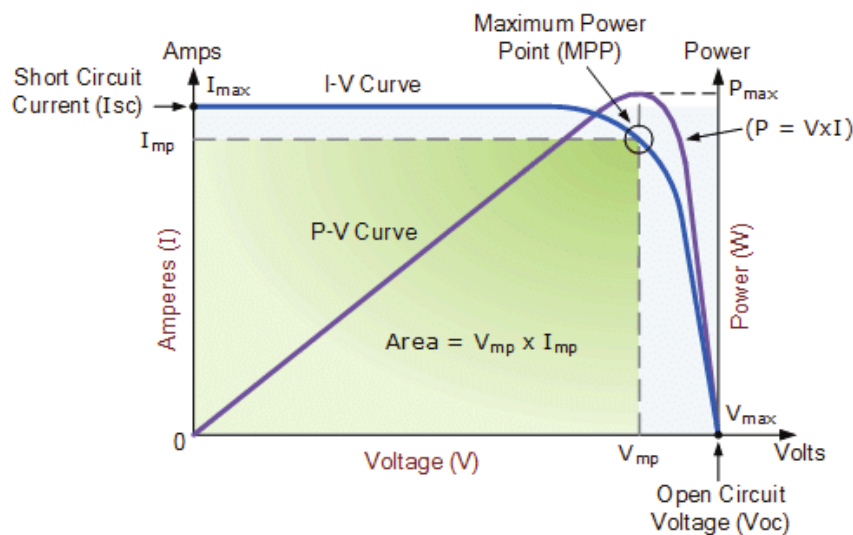


Figure 4.9: Typical I-V curve of a PV cell [42]

The electrical output characteristics of a solar array does not only depend on its I-V characteristics but also on other factors as listed below:

- **Connection configuration:** The electrical characteristics for a group of PV cells depend on how they are connected to each other. Two ways to connect them are in series, parallel, or combination. This effect will be explored in detail further in this sub-section.
- **Temperature:** The electrical characteristics of a PV cell vary a lot with their temperature because the

temperature influences the potential energy of the electrons in the depletion region of the PV cell. Depending on whether the temperature is high or low with respect to an ambient temperature, the electrons gain enough potential energy to overcome the band gap potential barrier or need more energy to overcome the band gap potential, respectively. This is shown in the ideal diode equation below. As this application is designed to be operational in space, the operating temperature of the solar panels has been defined as -40 to 80 degrees [43] Celsius by the stakeholder (AAC Hyperion). The lowest temperature of the solar panels occur just when exiting the eclipse condition and the hottest temperature occurs at the end of the sunlight phase.

$$I = I_{SC}(e^{\frac{qV}{k_B T}} - 1) \quad (4.41)$$

- **Incident irradiation intensity:** The intensity of incident irradiation is another important factor determining the electrical characteristics of the power generated by the PV cell. The saturation current is directly proportional to the incident light intensity, whereas the open circuit voltage increases logarithmically with an increase in light intensity as expressed in equation (4.42)[23]. The intensity of light from the Sun varies with the distance of the power generation source from the Sun, and it decreases with distance. In the current application, where the satellite is operational in the LEO, the intensity of irradiation would be assumed to be constant at a value of 1350 W/m^2 .

$$V_{OC} = \frac{nkT}{q} \ln\left(\frac{L_{Sun} I_{SC}}{I_0}\right) \quad (4.42)$$

- **Angle of incident irradiation:** The power produced by the solar panels also depend on the incidence angle of the irradiation from the Sun with respect to the solar panel's normal. The power produced and the angle of the incident irradiation are related by a cosine function as expressed in equation (4.43) and as shown in Figure (4.10).

$$P_f = P_0 \cos\theta_i \quad (4.43)$$

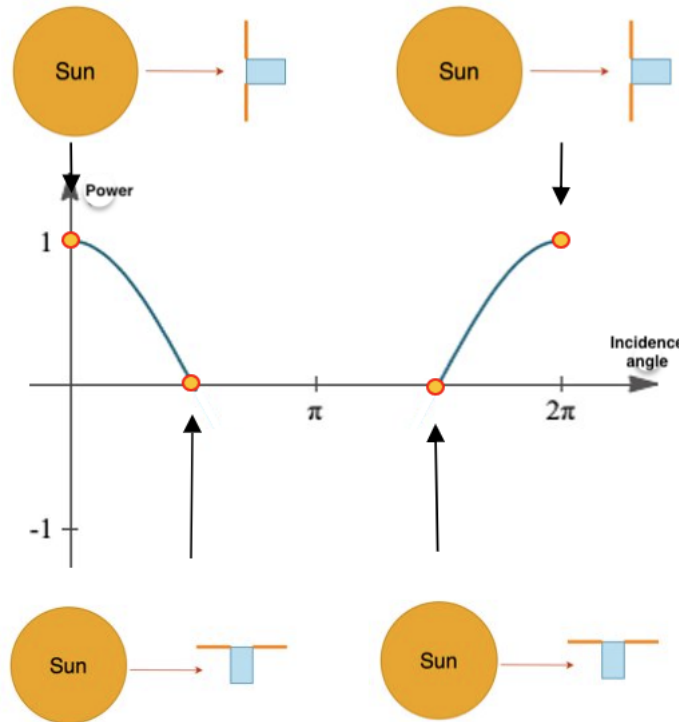


Figure 4.10: Cosine relation between power produced & incidence angle

- Degradation:** As the solar cells are operational in LEO for a period of 5 years as stated in SADM-ENV-001, they degrade due to radiation. Solar cells degrade due in radiation environment due to interaction of particles such as electrons, protons, neutrons or ions in the space environment with the solar cell. This interaction is usually in the form of collision that result in displacement damage or results in ionisation. As a result of these damage mechanisms, the PV cell's open-circuit voltage and saturation current decrease which in turn leads to reduced power generation ($P_{max} = V_{OC} \times I_{SC}$). Their power generation capabilities (efficiency) reduce with time and exposure to radiation. As the system should be designed to handle maximum power, the Begin Of Life conditions would be considered while neglecting the End Of Life conditions for this application. This is because the solar cells will generate maximum power at the beginning and will degrade to produce lower power over time. A simple relation for the lifetime degradation of the PV cells are provided in the equation (4.44) [201] below:

$$L_d = (1 - RD)^{life-time} \quad (4.44)$$

- Shadow:** As discussed earlier, the amount of power generated by the solar cell is directly dependent on the incident light intensity. Shadows could be cast on the satellite's solar panels due to deployable structures and the CubeSat structure. This self-shadow effect can cause a decrease in power generation. These effects are highly dependent on the satellite structure and its position with respect to the Sun, as these effects are difficult to model for a generic mission configuration, and as they vary with orbit type and position, they would be neglected for the current application design calculations.

Effect of connection configuration & temperature on PV array's electrical output

PV cells are commonly connected in series, parallel, or a combination of both. Series connection is when the cells are connected end-to-end and parallel connection is when the cells are connected to a common point across each other's leads. The series and parallel connections are shown in Figure (4.11) below:

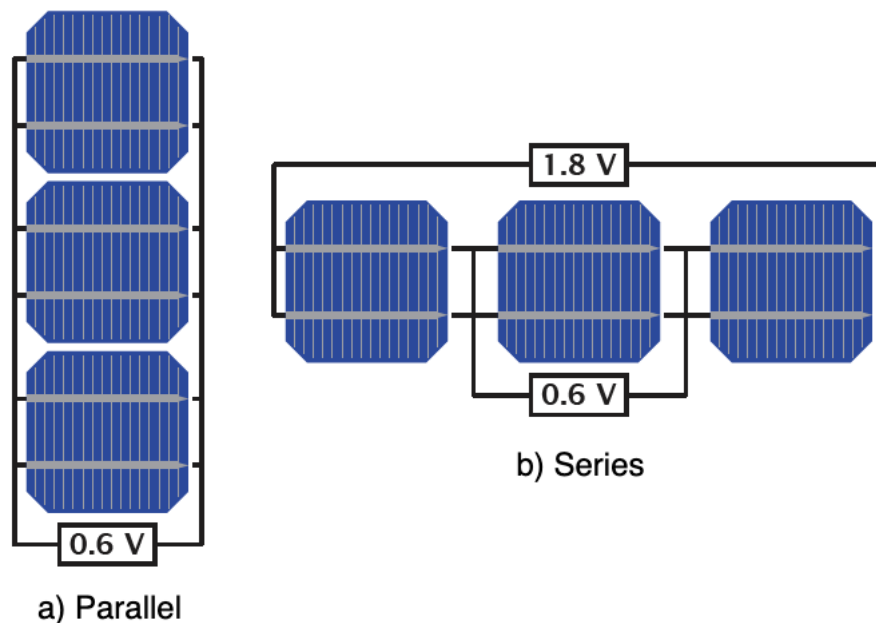


Figure 4.11: PV cell connection configurations a) parallel b) series

Electrically the main difference between series and parallel connection of the PV cells comes in the resulting voltage and current of the connections. When the PV cells are connected in series, the voltage of the cells is added while the amperage remains constant. When the PV cells are connected in parallel, the current of the cells is added while the voltage remains constant, as shown in Figure (4.12b).

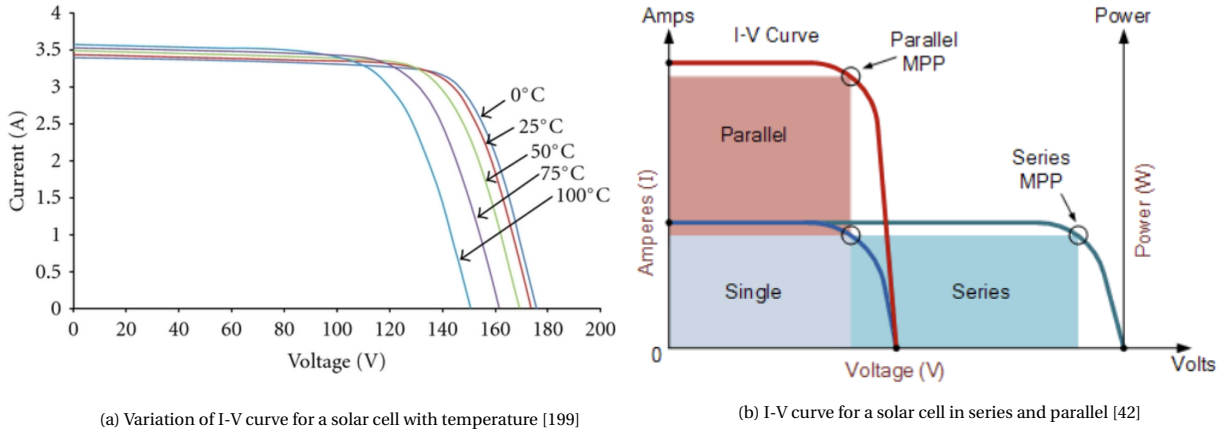


Figure 4.12: Variation of electrical characteristics of PV cell

The maximum voltage per array is obtained by the product of the number of PV cells connected in series and the PV cell's open circuit voltage as shown in equation (4.45).

$$V_{\max} = V_{OC@T} \times N_{\text{cells-per-string}} \quad (4.45)$$

The open-circuit voltage of the PV cell is further dependent on the temperature of the panel and the voltage at maximum power point as related in equation (4.46). The coefficient of change in voltage at maximum power per unit change in temperature is usually negative. It can then be inferred from the equation (4.46) that as the temperature of the panel increases, the voltage generated by the PV cell decreases and vice-versa as the panel temperature increases.

$$V_{OC@T} = V_{OC@28C} + \frac{\Delta V_{OC}}{\Delta T} \times (T_{SA} - T_{amb}) \quad (4.46)$$

The maximum current per array is obtained by the product of the number of strings connected in parallel and the PV cell's saturation current as shown in equation (4.47).

$$I_{\max} = I_{SC@T} \times N_{\text{strings}} \quad (4.47)$$

The saturation current of the PV cell is also temperature dependent along with being related to the saturation current density of the PV cell as shown in the equation (4.48) below. The coefficient of change in saturation current density per unit change in temperature is usually positive. It can then be inferred from the equation (4.48) that as the temperature of the panel increases, the current generated by the PV cell increases and the current generated decreases as the panel temperature decreases.

$$I_{SC@T} = I_{SC@28C} + \frac{\Delta J_{sc}}{\Delta T} \times A_{\text{cell}} \times (T_{SA} - T_{amb}) \quad (4.48)$$

The voltage and current at the maximum power point of the solar cell are given by the equations (4.49 4.50) respectively. The voltage and current at the maximum power point will be multiplied by the number of PV cells to get an estimate of the maximum power that can be generated by a string, wing or array. As the previous parameters, the current and voltage at the maximum power point are also temperature dependent as expressed in the equations below:

$$V_{mp@T} = V_{mp@28C} + \frac{\Delta V_{mp}}{\Delta T} \times (T_{SA} - T_{amb}) \quad (4.49)$$

$$I_{mp@T} = I_{mp@28C} + \frac{\Delta I_{mp}}{\Delta T} \times A_{\text{cell}} \times (T_{SA} - T_{amb}) \quad (4.50)$$

PV cell connection configurations

To calculate the worst-case conditions, the common connection configurations must be explored. Usually, the PV cells are combined in series and parallel to meet the customer's requirement for the current and voltage on the satellite bus or the EPS. The same five commercially available PV cells that were used in earlier sections to calculate the inertia of the panel will be used to calculate the maximum voltage and current. Some of the possible PV cell connection combinations are listed below, along with their electrical parameters calculated based on equations listed in the earlier sub-section.

1. **Configuration-1:** Length-wise PV cells across all panels are connected in series & strings are connected in parallel. This combination of connections is **not practical** because the number of PV cells in each row is not equal, as shown in the figure below. Only four PV cells can fit in the gap remaining in the panel's width direction after the other three PV cell rows are aligned. This difference in the number of PV cells would lead to different voltage lines being connected to each other. That would further lead to current flow from the higher potential line to the lower potential line to achieve a common voltage. This would lead to current flow in the four PV cells (comparatively a diode) in the reverse direction, which would cause heating of the solar cell and potential damage.

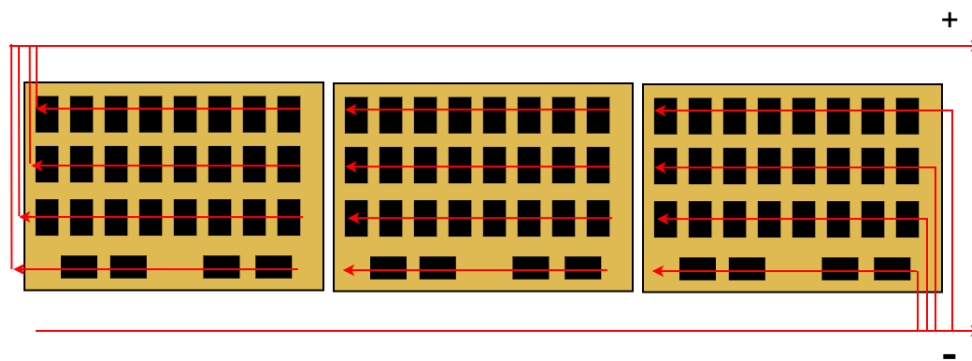


Figure 4.13: PV cell connection configuration-1

2. **Configuration-2:** All cells in the panel are connected in series, and the panels are connected in parallel. This configuration leads to only 2 wires coming through the shaft to the SADM. The electrical power transfer parameters calculated for this configuration based on equations (4.45-4.50) are summarized in Table (4.8).

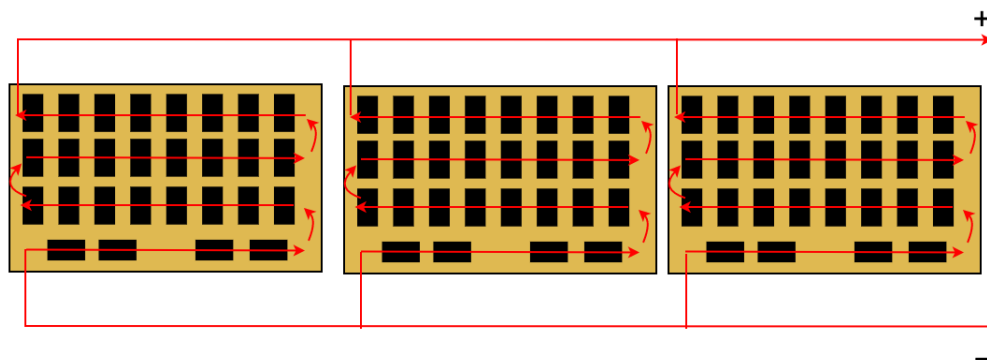


Figure 4.14: PV cell connection configuration-2

Parameter	Spectrolab XTE-SF		Spectrolab XTJ		Azurspace 4G32C		Azurspace 3G30C		CESI CTJ-30	
	-40 C	80 C	-40 C	80 C	-40 C	80 C	-40 C	80 C	-40 C	80 C
Configuration nomenclature	20S 3P		20S 3P		16S 3P		20S 3P		16S 3P	
Number of cells per panel	20		20		16		20		16	
Maximum voltage (V)	62.6	49.17	60.9	46.32	64.3	48.22	62.4	47.55	47.5	37.33
Maximum current (A)	1.44	1.55	1.35	1.46	1.37	1.37	1.30	1.42	1.52	1.68
Maximum power per array (W)	81.14	62.17	73.78	55.7	75.10	53.64	73.68	56.14	63.38	52.64

Table 4.8: Voltage, current and power calculations for PV cell connection configuration-2

3. **Configuration-3:** All PV cells in one panel are connected in series and individually connected to the EPS, thus no parallel connections. This is one of the most commonly used connection configurations because of the high voltage and low current, which is good for low power transmission losses through a conductor as it would result in minimal I^2R losses.

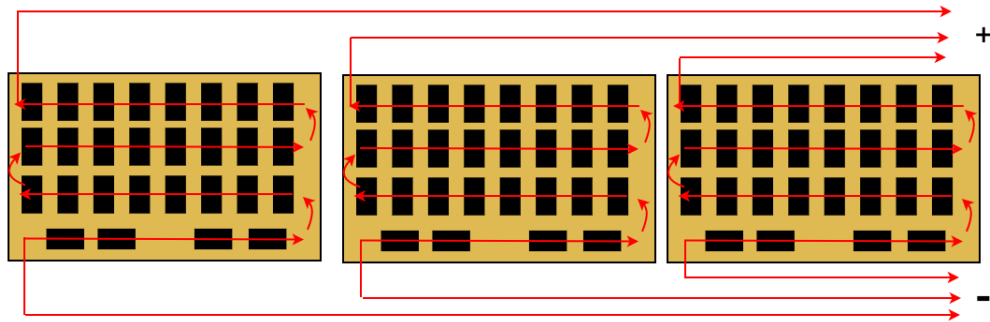


Figure 4.15: PV cell connection configuration-3

The electrical power transfer parameters calculated for this configuration based on equations (4.45-4.50) are summarized in Table (4.9).

Parameter	Spectrolab XTE-SF		Spectrolab XTJ		Azurspace 4G32C		Azurspace 3G30C		CESI CTJ-30	
	-40 C	80 C	-40 C	80 C	-40 C	80 C	-40 C	80 C	-40 C	80 C
Configuration nomenclature	3 x 20S 0P		3 x 20S 0P		3 x 16S 0P		3 x 20S 0P		3 x 16S 0P	
Number of cells per panel	20		20		16		20		16	
Maximum voltage (V)	62.62	49.18	60.96	46.32	64.35	48.22	62.43	47.55	47.55	37.33
Maximum current (A)	0.48	0.52	0.45	0.48	0.45	0.45	0.43	0.47	0.50	0.56
Maximum power per panel (W)	27.04	20.72	24.6	18.56	25.03	17.88	24.56	18.71	21.12	17.55

Table 4.9: Voltage, current and power calculations for PV cell connection configuration-3

4. **Configuration-4:** All PV cells in one panel are connected in series, and panels on opposite sides of the

CubeSat are connected in parallel. The electrical power transfer parameters for this configuration are summarized in Table (4.10).

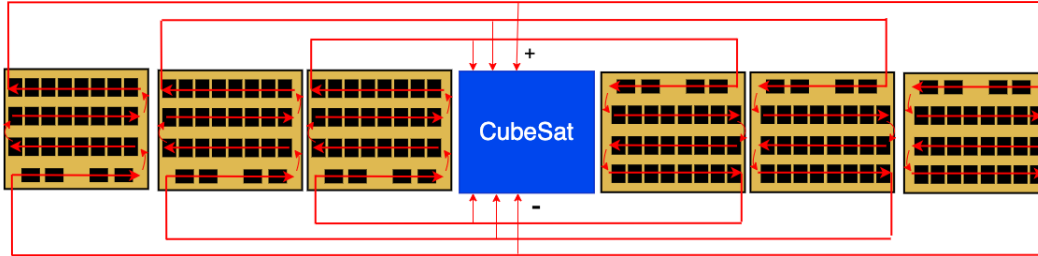


Figure 4.16: PV cell connection configuration-4

Parameter	Spectrolab XTE-SF		Spectrolab XTJ		Azurspace 4G32C		Azurspace 3G30C		CESI CTJ-30	
	-40 C	80 C	-40 C	80 C	-40 C	80 C	-40 C	80 C	-40 C	80 C
Configuration nomenclature	3 x 20S 2P		3 x 20S 2P		3 x 16S 2P		3 x 20S 2P		3 x 16S 2P	
Number of cells per panel	20		20		16		20		16	
Maximum voltage (V)	62.62	49.18	60.96	46.32	64.35	48.22	62.43	47.55	47.55	37.33
Maximum current (A)	0.96	1.03	0.90	0.97	0.91	0.91	0.87	0.95	1.01	1.12
Maximum power per line (W)	54.16	41.44	49.18	37.13	50.06	35.76	49.12	37.42	42.25	35.09

Table 4.10: Voltage, current and power calculations for PV cell connection configuration-4

5. **Configuration-5:** Length-wise PV cell strings are connected in series & directly connected to the EPS thus no parallel connections. This configuration would again have one line with a different voltage and current than the other two because of the difference in the number of cells. But the EPS can be modified to suit the requirements. The electrical power transfer parameters for this configuration are summarized in Table (4.11).

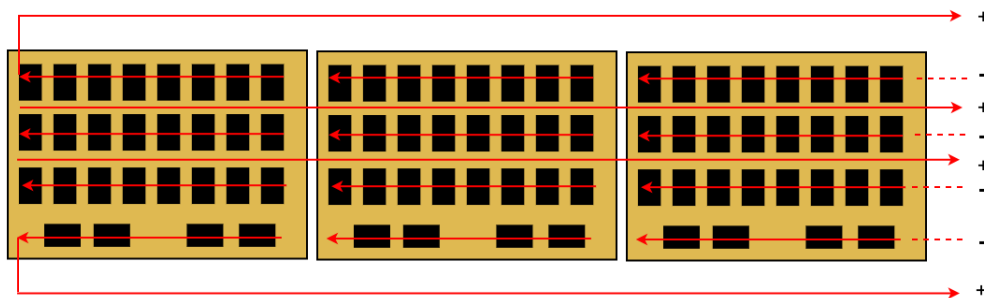


Figure 4.17: PV cell connection configuration-5

Parameter	Spectrolab XTE-SF		Spectrolab XTJ		Azurspace 4G32C		Azurspace 3G30C		CESI CTJ-30	
	-40 C	80 C	-40 C	80 C	-40 C	80 C	-40 C	80 C	-40 C	80 C
Configuration nomenclature	2 x 24S0P 1 x 12S0P		2 x 24S0P 1 x 12S0P		2 x 24S0P		2 x 24S0P 1 x 12S0P		2 x 24S0P	
Number of cells per panel	20		20		16		20		16	
Maximum voltage (V)	75.14	59	73.15	55.58	96.53	72.34	74.92	57.06	71.32	56
Maximum current (A)	0.48	0.52	0.45	0.49	0.46	0.46	0.43	0.47	0.51	0.56
Maximum power per line (W)	32.46	24.87	29.51	22.28	37.55	26.82	29.48	22.46	31.69	26.32

Table 4.11: Voltage, current and power calculations for PV cell connection configuration-5

Summary of electrical power calculations

Based on the current, voltage and power calculations performed in the previous sub-section, the maximum current, voltage, power transferred per line, and the maximum number of wires required for power transfer among all the different configurations have been summarized in Table (4.12) below. These values will be used as the design parameters for the power and data transfer mechanism design in the detailed design section.

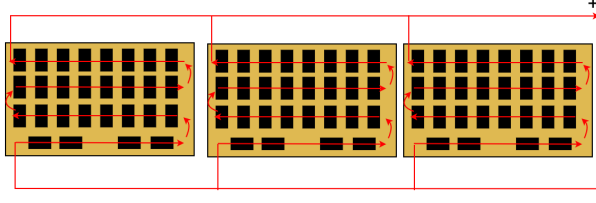
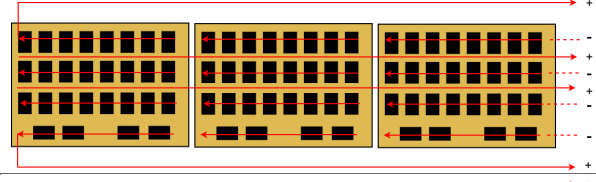
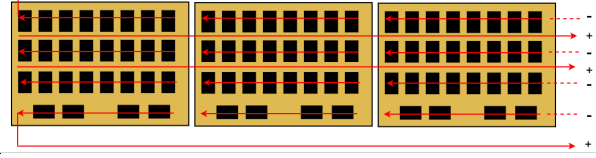
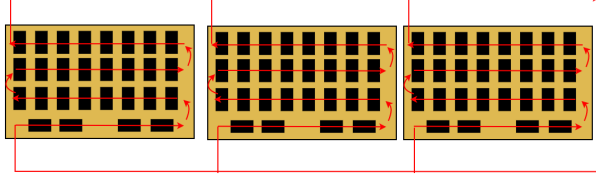
Parameter	Value	Configuration
Maximum current	1.7 A	
Maximum voltage	97 V	
Maximum number of power lines	6	
Maximum power per line	82 W	

Table 4.12: Maximum current, voltage, wires & power

It is important to note that the maximum power produced per panel or array does not change with the difference in connection because the power generated per PV cell is constant, assuming constant irradiation intensity and temperature. The power transferred remains constant irrespective of change in connection configuration, but the voltage and current per line change.

The maximum current of 1.68 A was found to occur in connection configuration-2 and has been rounded up

to 1.7 A. This configuration gives maximum current because of the large number of PV cells being connected in parallel. This configuration also transfers the maximum power per line compared to the other configurations because it connects all the PV cells in the array in 2 power lines, thus requiring the least number of power lines compared to other configurations. The maximum voltage of 96.53 V was found to occur in connection configuration-5 and has been rounded up to 97 V. This configuration gives maximum voltage because of the large number of PV cells connected in series. Configuration-5 also requires the most number of wires to transmit power from the PV cells because of three individual lines for series connection.

4.3.3. Launch loads

The SADM is exposed to various environments based on the loads they impose which are - Assembly, Integration and Testing (AIT), handling, transport, launch and operational. The SADM should be designed to withstand these loads so that it can perform its functions throughout its lifetime, as stated in SADM-ENV-001. Among the various loads that the SADM experiences during its lifetime, the launch load is the most critical load the system has to survive because of the comparatively larger magnitude of loads that the launcher imposes on the system. The launcher imposes various loads on its payloads due to factors like aerodynamic disturbances, stage separation, engine ignition, unsteady combustion and inertial acceleration. These loads get translated to the satellite as launch forces and act on all its components.

In this section, the launch loads will be explored and listed, and then the maximum launch loads for which the system has to be structurally designed to withstand will be identified. Then launch loads will then be adapted to the current application to calculate the maximum launch force acting on the SADM system.

Common launch loads

The different types of launch loads (adapted from Chapter 6 of [203]) imposed by the launcher on the satellite are summarized in the Figure 4.18 below:

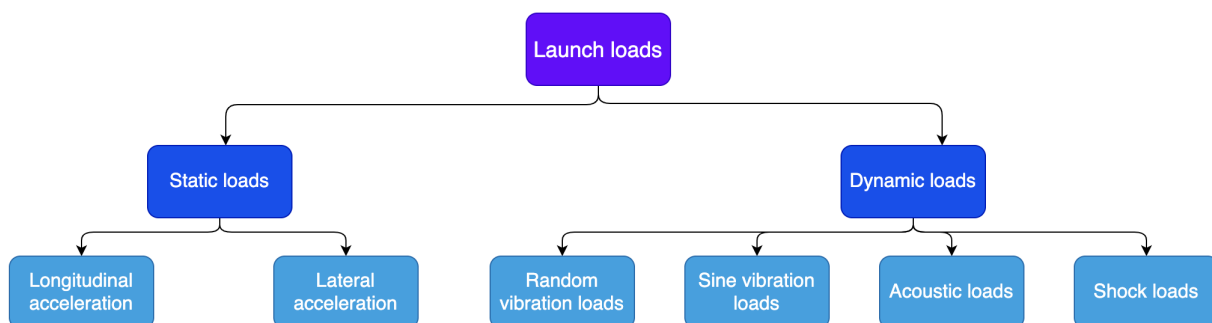


Figure 4.18: Launch loads classification

The nature and source of these launcher loads are explained in brief below:

- **Static loads:** Static loads do not change in magnitude with time. These are caused by inertial force due to the acceleration of the launch vehicle.
- **Dynamic loads:** Dynamic loads act at a random time during the launch period and are variable in magnitude. They are caused by various sources that generate random disturbances like unstable engine combustion, vibrations generated by the turbulent flow on the launcher's surface, separation of stages and other aerodynamic disturbances like wind gusts.
- **Random vibration loads:** Random vibration loads are dynamic loads with a higher frequency range (usually 20-2000 Hz). These are usually caused by boundary layer interactions and acoustic loads that are transformed into mechanical vibrations acting at the base of the satellite.
- **Sine vibration loads:** These are dynamic loads with a lower frequency (usually 5-100 Hz). They are caused by the interaction of the launcher's structure with the engine's combustion instabilities and the shock loads caused by thrust build-up.

- **Acoustic loads:** These are changes in sound pressure that are caused due to exhaust noises and aero-acoustic disturbances caused by turbulent boundary layer flow around the launcher.
- **Shock loads:** These are sudden loads with high intensity, high frequency and short duration. They are caused during a couple of events - the release of hold-down during lift-off, the separation of the rocket stages, fairing deployment, the separation of the satellite from the launcher and the start and stop of the engines.
- **Pressure variations:** The static pressure within the payload volume of the launcher varies as the launcher ascends from atmospheric pressure to vacuum. Vents are used to equalise the pressure.

Static loads - longitudinal (g)	
Maximum	10
Minimum	4
Static loads - lateral (g)	
Maximum	0.6
Minimum	0.2
Sinusoidal vibration qualification levels - longitudinal [14]	
Frequency (Hz)	Amplitude (g)
2 – 5	12.4 mm
5 – 50	1.25 g
50 – 100	1 g
Sweep rate	2 oct /min
Sinusoidal vibration qualification levels - lateral [14]	
Frequency (Hz)	Amplitude (g)
2 – 5	9.9 mm
5 – 25	1 g
25 – 100	0.8 g
Sweep rate	2 oct/min
Generalized random vibration qualification levels for < 22.7 kg [108]	
Frequency (Hz)	ASD level (g^2/Hz)
20	0.026
20 – 50	+6 dB/ oct
50 – 800	0.16
800 – 2000	–6 dB/ oct
2000	0.026
Overall	14.1G _{RMS}
Shock response spectrum qualification levels [14]	
Frequency (Hz)	SRS acceleration (g)
100	10
100	400
500	500
1000	700
10000	132
Acoustic vibration test qualification levels [14]	
Frequency (Hz)	Qualification level (dB)
31.5	131
63	134
125	139
250	136
500	132
1000	126
2000	119
Overall level & duration	142.5 2 minutes

Table 4.13: Environmental loads [108] [14]

The above-listed launch loads vary with each launcher; general load values for the design, qualification and acceptance of the satellite and its components are provided by [108] and are summarized in the table below. Some of the launch loads not specified in the NASA-GEVS [108] are adopted from the Ariane-5's user manual [14]. Among the launch loads summarised in the table (4.13) above, the qualification random vibration load is the highest load that would act on the satellite in all three axes. This was also higher than the loads specified by various launcher user manuals as compared in [166]. Therefore, this load would be used as a design load to size the SADM so that it can survive all the other launch loads.

Launch force calculations

The launch loads mentioned in the table above act on the satellite in all three directions. To be able to size and design the SADM to withstand these loads, the maximum design load that is now in the form of an acceleration load must be converted to a force. The following sub-sections will calculate the maximum force that will act on the SADM. The first step would be to convert the dynamic loads into a static force. Secondly, the static force acting on the solar panel would have to be translated to the shaft and depending on the different configurations and number of hold-down points, the reaction force acting on the shaft of the SADM will be calculated, and the maximum force among the calculated values will be used to design and size the components in later sections.

Conversion of dynamic loads to quasi-static loads:

In the previous subsection, the launcher's random vibration load was found to be the highest load that will act on the satellite. This load will act on the solar panels hinged to the SADM's shaft, as shown in Figure (4.19). This force on the solar panels gets translated to the SADM through its shaft. The maximum force translated from the solar arrays to the shaft will be the design load for the SADM. The random vibration load magnitude of $14.1 G_{RMS}$ has a $1-\sigma$ probability of occurrence according to [108]. The random vibration load will be multiplied by 3 to get the $3-\sigma$ or worst-case load.

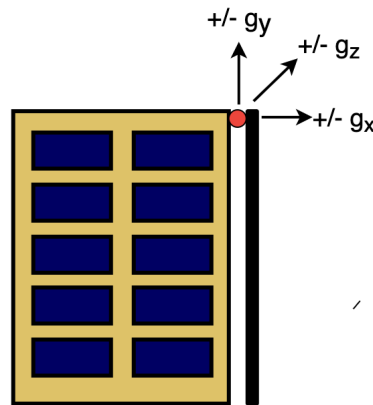


Figure 4.19: Launch loads acting on satellite shaft

$$F_{\max} = G_{RMS} \times g \times m_{SA} \times \sigma = 14.1 \times 9.81 \times 1.1 \times 3 \quad (4.51)$$

$$F_{\max} = 456.46 N \sim 460 N \quad (4.52)$$

This maximum force acts in all 3 directions on the solar array. For ease of calculation, this force will be considered to be a distributed load $W(x)$ throughout the length of the panel (0.34 m) and acting in the negative x-direction.

$$W(x) = \frac{460}{0.34} = 1353 N/m \quad (4.53)$$

Structure simplification & assumptions:

The solar array is attached to the CubeSat structure at the top endpoint (Point-1 in Figure (4.20)) using a shaft that is also a hinge which allows the solar panels to be bent around the z-axis. This shaft with a hinge would

be modelled as a pin-joint support because it provides a vertical and horizontal reaction force but cannot provide a reaction moment.

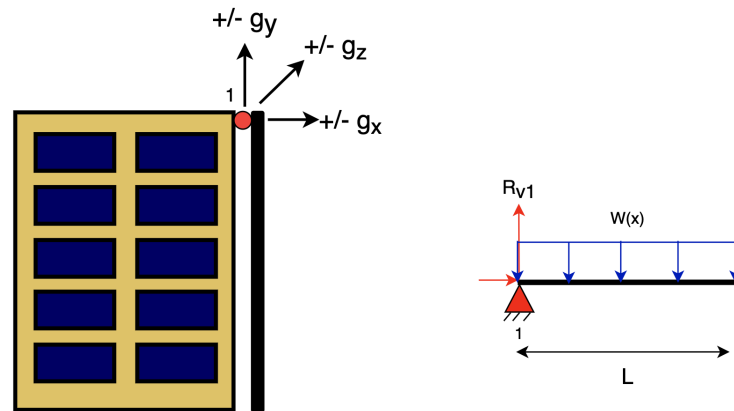


Figure 4.20: Structural simplification of the satellite with a hinge

The shaft with hinge alone is insufficient to constrain the solar wings along 3-DOF during launch. Thus hold-down & release mechanisms are used. The number of hold down points and their position along the panel is dependent on the customer's requirement and design. Their main function is to constrain the motion of the solar arrays in all 3 directions. Thus they would be modelled as fixed support. Four common hold-down point configurations are possible, and that has been considered in this design calculation:

- **Case-1:** One hold down point at the end of the panel
- **Case-2:** One hold down point in the middle
- **Case-3:** Two hold down points at one-third distance from either end
- **Case-4:** Two hold down points at half the distance from either end

The solar array is assumed to be a beam even though it is a flat plate in reality. This is because the classical plate theory is just an extension of the beam theory to an additional dimension which would improve the accuracy of the calculations, which is not necessary at this design stage [107]. Moreover, solving those equilibrium equations would require finite element modelling as they are in differential form. The plates also undergo bending and torsion moments, which complicate analysis. To avoid this added complexity and to get an initial estimate for design, the plate is assumed to be a beam in this calculation.

Case-1: Hold-down point at end of the panel

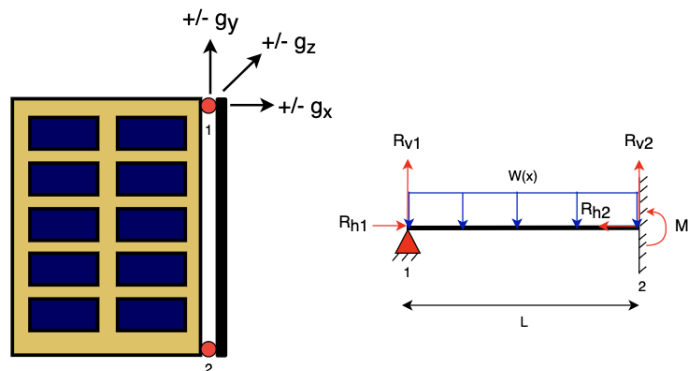


Figure 4.21: Free body diagram of solar panel under launch loads with hold down point at the end of panel

Equilibrium equations:

$$R_{v1} + R_{v2} = WL \quad (4.54)$$

$$M_2 = \frac{WL^2}{2} - R_{v1}L \quad (4.55)$$

$$R_{h1} = R_{h2} = 0 \quad (4.56)$$

The above case is statically indeterminate, because the number of unknowns (R_{v1} , R_{v2} & M_2) are more than the number of equilibrium equations (4.55 & 4.54).

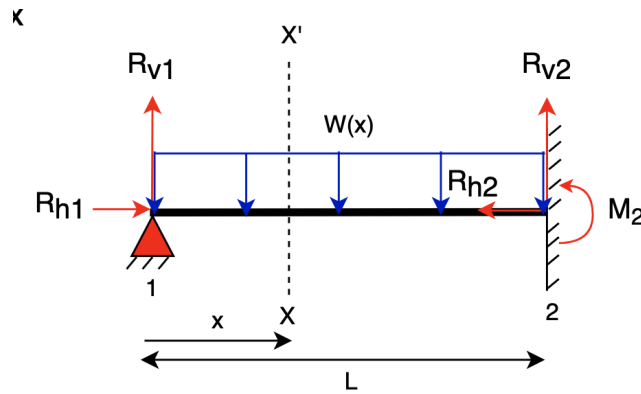


Figure 4.22: Beam splitting for case-1

Bending moment at section X-X':

$$M(x) = R_{v1}x - \frac{Wx^2}{2} + R_{v2}x - M_2 \quad (4.57)$$

$$EI \frac{d^2y}{dx^2} = R_{v1}x - \frac{Wx^2}{2} + R_{v2}x - \frac{WL^2}{2} + R_{v1}L \quad (4.58)$$

Slope at section X-X':

$$EI \frac{dy}{dx} = R_{v1} \frac{x^2}{2} - \frac{Wx^3}{6} + R_{v2} \frac{x^2}{2} - \frac{WL^2x}{2} + R_{v1}Lx + C_1 \quad (4.59)$$

Deflection at section X-X':

$$EIy = R_{v1} \frac{x^3}{6} - \frac{Wx^4}{24} + R_{v2} \frac{x^3}{6} - \frac{WL^2x^2}{4} + R_{v1}L \frac{x^2}{2} + C_1x + C_2 \quad (4.60)$$

Boundary conditions:

1. $y(0) = 0$ Deflection at fixed end is zero
2. $y(L) = 0$ Deflection at pinned/hinged end is zero
3. $y'(L) = 0$ Slope at fixed support is zero
4. $y''(0) = 0$ Moment at hinged support is zero

Using Boundary condition (1) & (2) in deflection equation:

$$C_2 = 0 \quad (4.61)$$

Using Boundary conditions (4) in moment equation:

$$0 = -\frac{WL^2}{2} + R_{v1}L \quad (4.62)$$

$$R_{v1} = \frac{WL}{2} \quad (4.63)$$

Using the above result in the equilibrium equation:

$$R_{v1} + R_{v2} = WL \rightarrow \frac{WL}{2} + R_{v2} = WL \quad (4.64)$$

$$R_{v2} = \frac{WL}{2} \quad (4.65)$$

Case-2: One hold down point in the middle

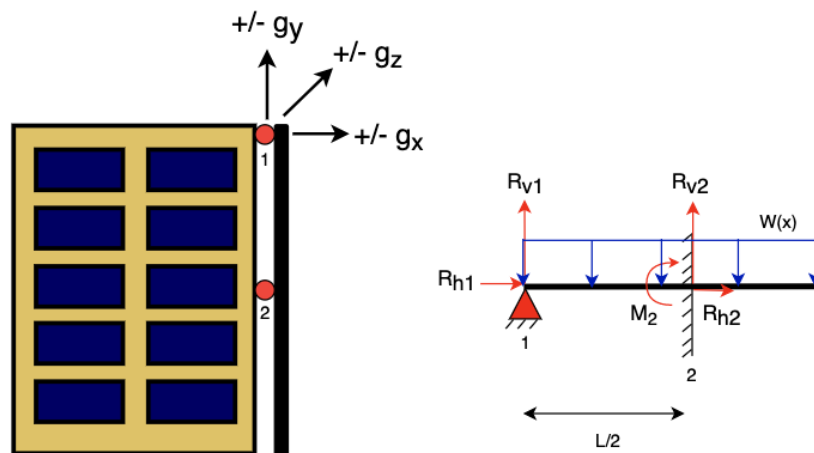


Figure 4.23: Free body diagram of solar panel under launch loads with hold down at midpoint

Equilibrium equations:

$$R_{v1} + R_{v2} = WL \quad (4.66)$$

$$R_{h1} + R_{h2} = 0 \quad (4.67)$$

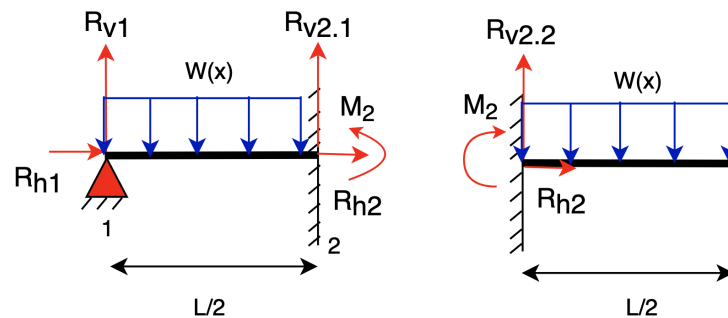


Figure 4.24: Beam splitting for case-2

Equilibrium equations:

$$R_{v1} + R_{v2} = WL \quad (4.68)$$

$$R_{v2} = R_{v2.1} + R_{v2.2} \quad (4.69)$$

$$R_{v1} + R_{v2.1} = W \left(\frac{L}{2} \right) \quad (4.70)$$

$$R_{v2.2} = W \left(\frac{L}{2} \right) \quad (4.71)$$

As the case on the left is similar to case-1, the results can be applied to this case as well:

$$R_{v2.1} = \frac{WL}{4} \quad (4.72)$$

$$R_{v1} + R_{v2.1} = W \left(\frac{L}{2} \right) \rightarrow R_{v1} + \frac{WL}{4} = W \left(\frac{L}{2} \right) \quad (4.73)$$

$$R_{v1} = \frac{3WL}{4} \quad (4.74)$$

$$R_{v2} = R_{v2.1} + R_{v2.2} \rightarrow R_{v2} = \frac{WL}{4} + \frac{WL}{2} \quad (4.75)$$

$$R_{v2} = \frac{3WL}{4} \quad (4.76)$$

Case-3: Two hold down points at one-third distance from either end

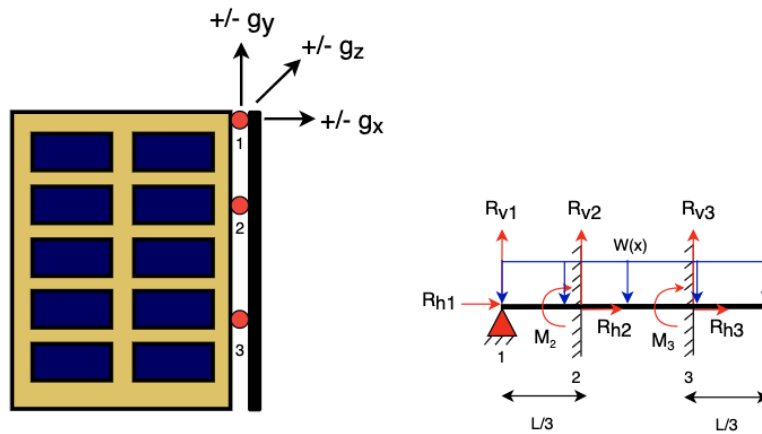


Figure 4.25: Free body diagram of solar panel under launch loads with 2 hold down points

Equilibrium equations:

$$R_{v1} + R_{v2} + R_{v3} = WL \quad (4.77)$$

$$R_{h1} + R_{h2} + R_{h3} = 0 \quad (4.78)$$

The above equations are also indeterminate therefore, the beam-splitting method will be used to make the system statically determinate.

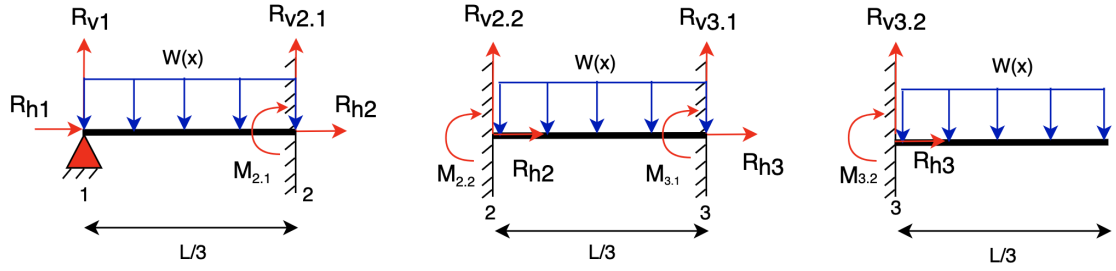


Figure 4.26: Beam splitting for case-3

Equilibrium equations:

$$R_{v1} + R_{v2.1} = \frac{WL}{3} \quad (4.79)$$

$$R_{v2.2} + R_{v3.1} = \frac{WL}{3} \quad (4.80)$$

$$R_{v3.2} = \frac{WL}{3} \quad (4.81)$$

$$R_{v2.1} + R_{v2.2} = R_{v2} \quad (4.82)$$

$$R_{v3.1} + R_{v3.2} = R_{v3} \quad (4.83)$$

Again, left-most part of beam is same as solved for case-1, therefore:

$$R_{v2.1} = \frac{W(L/3)}{2} \rightarrow R_{v2.1} = \frac{WL}{6} \quad (4.84)$$

$$R_{v1} + \frac{WL}{6} = \frac{WL}{3} \rightarrow R_{v1} = \frac{WL}{6} \quad (4.85)$$

$$R_{v2} = R_{v2.1} + R_{v2.2} \rightarrow \frac{WL}{6} + \frac{WL}{6} \quad (4.86)$$

$$R_{v2} = \frac{WL}{3} \quad (4.87)$$

$$R_{v3} = R_{v3.1} + R_{v3.2} \rightarrow \frac{WL}{6} + \frac{WL}{3} \quad (4.88)$$

$$R_{v2} = \frac{WL}{2} \quad (4.89)$$

Summary of launch force calculations

From the above calculations, the parameter important for design is the reaction load on the shaft of the SADM. The reaction force on the shaft was calculated by substituting the load calculated in equation 4.53 which was 1353 N/m for a panel length of 0.36m. The maximum reaction load experienced by the shaft among all these cases was found to occur in case-1, when there was no hold-down point. But this case is not practically viable because then the solar arrays would have rotational freedom about one axis and can get damaged due to launch loads. This is why at least one hold-down point is utilised on the solar array compulsorily. The case with the next highest magnitude of the force acting on the shaft is the case where the hold down point is placed at the other end-point of the solar panel (case-2). Therefore, this reaction force of **243.5 N** would be considered the **maximum design load** for sizing the SADM. This calculation was preliminary and does not consider dynamic effects such as eigenmode shapes of the solar panel in response to the vibration loads. This was not feasible within the timeline of the thesis. But the worst case launch force has been calculated using the worst case load which is 3σ value of the maximum random vibration load. This way the structural reliability of the SADM has been ensured in the initial stage of the design, the author would recommend carrying out a dynamic analysis in the future scope of this project to verify the calculated launch force.

Case #	Reaction load at shaft	Calculated reaction force value	Load diagram
1	WL	487 N	
2	$\frac{WL}{2}$	243.5 N	
3	$\frac{WL}{4}$	121.7 N	
4	$\frac{WL}{6}$	81.2 N	

Table 4.14: Launch force on shaft for different hold-down point placement

4.4. Chapter summary

In this chapter, the mechanical power required to rotate the solar arrays, electrical power to be transferred by the SADM and the launch forces acting on it were calculated. The SADM's operation was defined firstly by exploring the mission scenarios it will encounter during its lifetime and by detailing its operating modes. It was calculated that the target tracking phase of the mission required the maximum rotational speed of the solar arrays, maximum torque and maximum mechanical power as summarized in the Table 4.15 below. The maximum current was found to be 1.7A and the maximum voltage was calculated as 97V for different PV cell connection configurations as stated in Table 4.12. The maximum launch force of 243.5 N was found to act in all three directions of the shaft when there was only one hold-down point positioned in the middle of the solar panel.

	Maximum	Value	Reference
Mechanical parameters	Rotational speed	0.04 rad/s	Target tracking (4.3.1)
	Torque	3.816 mNm	Target tracking (4.3.1)
	Power	0.153 mW	Target tracking (4.3.1)
Electrical parameters	Current	1.7 A	Cells in panel connected in series & panels connected in parallel (2)
	Voltage	97 V	All PV cells across length in all panels are connected in series (5)
	Power	82 W	Cells in panel connected in series & panels connected in parallel (2)
Launch load	Force	243.5 N	One hold-down point in the middle (4.3.3)

Table 4.15: Summary of preliminary design calculations

5

Detailed system design

In this chapter, the main elements of the SADM will be designed, selected or sized. This chapter is split into 9 sections that will detail each element. Each section will start by defining the research question for the section which will be adapted from the initially set research questions followed by setting requirements for the element that flow from the requirements set for the SADM sub-system. The element design, sizing and selection are then performed based on these requirements. The first section 5.1 will describe about the housing design as it encloses rest of the elements. The mechanical power required to rotate the solar arrays was calculated in the earlier chapter, the next section 5.2 will select the rotary actuator that will provide this mechanical power. Mechanical power is composed of rotational speed and torque, the SADM has to rotate the solar arrays at particular speeds and torque, the torque and rotational speed provided by the actuator must be matched with the required torque and speed of the solar arrays. This is resolved by using a mechanical power transfer mechanism that transforms the input torque and speed to required value of torque and speed. The next section 5.3 will discuss the mechanical power transfer mechanism design. One of the most important functions of the SADM is to transfer the generated electrical power to the relatively stationary satellite systems. This is followed by a section 5.4 describing the selection process and rationale behind the electrical and data interfaces of the SADM that will allow it to interact with other elements and satellite systems. The next section 5.5 will design and size the power and data transfer mechanism to transfer the electrical power based on the parameters calculated in section 4.3.2. The next section (5.6) will discuss about the most common failure causing elements of mechanisms - bearings. The chapter culminates in section 5.8, which gives a brief overview of the results achieved in this chapter.

5.1. Housing design

In this section, the housing design would be elaborated. The housing is designed first among the other components of the SADM because it has to house the other components and by knowing the dimensions and volume available within the housing, other components can be designed and sized. The housing design would be carried out by firstly understanding its purpose in sub-section 5.1.1 and followed by defining its requirements in sub-section 5.1.2. The housing design concepts are then explored and one is selected in sub-section 5.1.3 and the housing is sized for radiation shielding in sub-section 5.1.4. The section ends with a summary of the housing design in sub section 5.1.6.

5.1.1. Purpose

The main purpose of the housing is to encapsulate all the components and elements of the SADM and hold them in place throughout the SADM's lifetime whilst withstanding launch loads and protecting the internal components from the space environment. The space environment imposes radiation, thermal variations, vacuum and atomic oxygen. The launch environment imposes loads on the structure. The housing must stand in the way of these detrimental environmental effects to protect the elements that it encloses. The housing is especially crucial in protecting the electronic components from degradation and malfunction due to radiation. The housing holds the components by serving as a mechanical interface for all the components and functions as a load path from the components to the CubeSat structure. As the satellite revolves around

the Earth, its temperature increases and decreases due to heating of the Sun caused by its relative position change in orbit.

5.1.2. Requirements

The SADM requirements were defined in chapter 3, some of these requirements apply to the housing and they would have to be translated to the element under discussion in this section - the housing. The requirements that are pertinent to the housing's design characteristics are SADM-DES-002, SADM-DES-003, SADM-INT-001, SADM-INT-002, SADM-INT-003 and all the environmental requirements (SADM-ENV-001 to SADM-ENV-011). These requirements are translated to the housing as shown in Table 5.1. The requirements SADM-HSG-001 & SADM-HSG-002 have already been considered in section 3.2 as it has considered the dimensional constraints and has defined the dimensional limits within which the housing must fit within.

Identifier	Requirement	Parent requirement
SADM-HSG-001	The housing shall be compatible to fit on the external surface of a 12U CubeSat	SADM-INT-001 & SADM-INT-002
SADM-HSG-002	The housing shall be scalable to CubeSats of size 3-16U	SADM-DES-002
SADM-HSG-003	The housing shall be designed such that it can be applied for more than one panel mounting configuration	SADM-DES-003
SADM-HSG-004	The housing shall not extend beyond one plane	SADM-DES-004
SADM-HSG-005	The housing shall be compatible with the environmental conditions.	SADM-ENV-001 to SADM-ENV-011

Table 5.1: Housing requirements

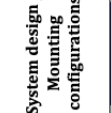
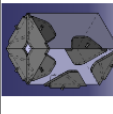
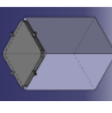
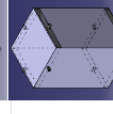
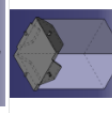
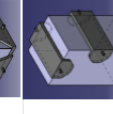
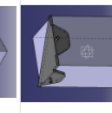




Considering these requirements and the housing's purpose a question can be framed to be addressed in this section, as stated below. The remaining sub-sections will aim to answer this question.

"How to design housing that fits externally on a 12U CubeSat and is modular, scalable and survives the environmental conditions?"

5.1.3. Housing design concepts trade-off

Initially, to arrive at a design concept of the housing, the SADM-HSG-003 requirement will be considered. To design a SADM system that applies to multiple panel mounting configurations, the most commonly used panel mounting configurations in various CubeSat missions were found, and different SADM housing concepts were designed. The different housing design concepts have been traded-off against the different panel mounting configurations based on their applicability to the mounting configuration, as shown in Figure (5.1). If the housing design can be applied in a particular panel mounting configuration, then the cell is coloured in green, and a score of one is given to the panel mounting configuration. If the housing design concept cannot be applied to a particular panel mounting configuration, then the corresponding cell is coloured in red, and a score of zero is given to the panel mounting configuration. If a housing design concept requires two such SADM systems to apply to a particular panel mounting configuration, then the corresponding cell is coloured in orange, and a score of 0.5 is given to the panel mounting configuration. The scores are then summed for each housing design concept, and the total score is summarized in the extreme right hand of the table.

It can be inferred from the trade-off that, clearly, **housing design concept-1** is the most widely applicable design across multiple solar panel mounting configurations, thus making it the **most modular design** among the other housing design options considered. The housing design concept-1 does not apply only to the one panel mounting configuration, as shown in the Figure 5.1. This is the panel mounting configuration used in the MARCO mission [177], which is an inter-planetary CubeSat mission to Mars, and the panels have been placed in such a way so that the spacecraft experiences minimal disturbance torque due to drag due to solar radiation pressure. As this system is designed predominantly for LEO missions, it can be inferred from the trade-off that the housing design concept-1 is optimal for application in all the commonly used panel mounting configurations in LEO. By selecting design concept-1, the requirement SADM-HSG-003 has been fulfilled.

Design number	System design / Mounting configurations	Other mounting configurations	Total number of configurations possible
1			5/6
2			3.5/6
3			4/6
4			3.5/6
5			4/6
6			2/6

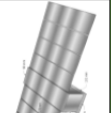





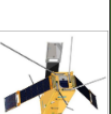


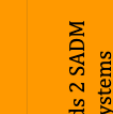


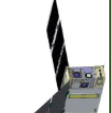











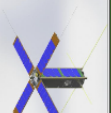





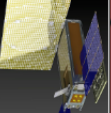





					
					
					
					
					
					

Figure 5.1: Housing design concepts trade-off

5.1.4. Sizing for radiation shielding

Another important function of the SADM's housing is safeguarding the internal components from the space and launch environment as defined in SADM-HSG-005. The most critical component of the environment that

affects the system performance after the launch loads is radiation. The housing merely transmits the launch loads acting on the solar panel to the CubeSat structure via the shaft. Therefore the shaft is the main load-bearing element as discussed and calculated in the earlier section 4.3.3. The housing is also mounted on the external surface of the spacecraft; this means that the SADM will experience a higher dose of radiation than if it were to be mounted on the inside of the CubeSat, where it could be shielded by the CubeSat's structure. Therefore, the housing will primarily protect the internal components from radiation. To design the system to withstand radiation, the radiation environment in LEO will be explored and understood in the forthcoming sub-section.

Radiation environment in LEO

Radiation in space originates from the charged particles originating from the Sun or outside the solar system. The radiation from Sun is caused due to multiple mechanisms, but the prominent source is the fusion reaction happening in its core and its magnetic field interactions with the surface causing the ejection of large masses of charged particles (Coronal Mass Ejections). The radiation coming from outside the solar system originates from high-energy events like a supernova. Radiation can be classified into two groups based on its energy, ionizing and non-ionizing radiation. Ionizing radiation has enough energy to remove the electrons from the valence shell of the incident material, thus leaving the target material charged or ionized. Non-ionizing radiation does not have enough energy to cause the same effects.

Based on these radiation causes, there are three radiation sources in the Low Earth Orbit environment:

- Trapped particle belts around Earth:** The charged particles coming from the Sun and outside the Solar system are trapped by the magnetic field of the Earth, this forms a belt of trapped electrons and protons around the Earth called the "Van Allen radiation belt" as shown in Figure (5.2). It has two belts that are toroidal in shape, the inner and the outer belt. The inner belt mainly consists of protons and extends from 0.2-2 times the Earth's radius distance from the surface of the Earth. The outer belt mainly comprises electrons, extending from 3-10 times the Earth's radius. The electrons are trapped in two belts with different energies and distributions. The most notable feature of the trapped radiation belts is the South Atlantic Anomaly (SAA) that is a high radiation area at 200km above sea level close to the coast of Brazil. This region is formed at the intersection of the Van Allen belt's inner ring with the Earth's magnetic field. As this region contains a concentrated density of high-energy protons, it causes a lot of trouble for the satellites in LEO. This is the worst-case environment in terms of radiation dosage on spacecraft.

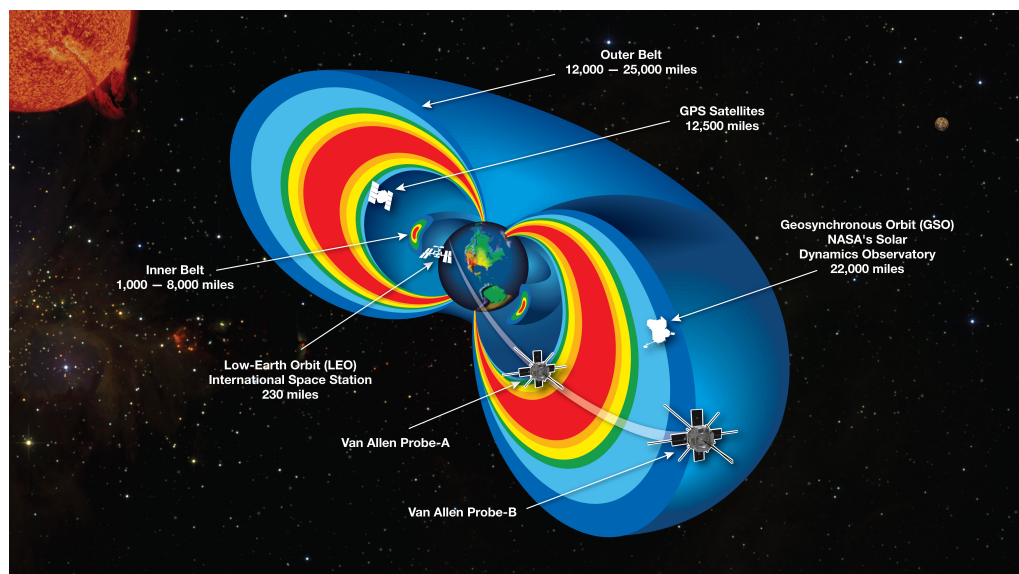


Figure 5.2: Trapped radiation belt around Earth [54]

- Galactic cosmic rays (GCR):** GCR originate outside the solar system and are generated by astronomical mass ejection events like a supernova explosion, black holes, neutron stars and active galactic nuclei. They enter the solar system isotropically. They are composed of ionised particles of all the elements

in the periodic table, from Hydrogen to Uranium. It is roughly composed of Hydrogen (85%), Helium (14%) and other heavy ions(1%) [94]. The energy of this radiation ranges from 100 to 10^8 MeV [99] and their flux increases during the solar minimum up to 4 particles/ cm^2 [129]. This is because the incoming GCR is influenced by the plasma ejected by the Sun that deflects it. The Earth's magnetic field stops most of the GCR particles with a magnetic rigidity lower than the geomagnetic potential. Even though heavy ions contribute the least to the total flux of the GCR, they are highly penetrative and cause secondary radiation. The main mechanism by which the GCR radiation affects the target material is by secondary radiation, where the primary radiation further results in electromagnetic and nuclear reactions to form ions and neutrons. The resultant neutrons are hard to shield using any kind of material. This kind of radiation is also not prevalent in the LEO environment and is most significant for interplanetary and other missions outside the influence of Earth's geomagnetic field.

- **Solar Particle Events (SPE):** SPE is a transient event that occurs randomly but peaks during solar maximum activity. One of the major SPE is the Coronal Mass Ejection that releases a large mass of material ($10^{14} - 10^{15}$ g) in the form of a bow shock that travels at up to 3000 km/s [99]. They are composed of protons, electrons, alpha particles and heavy ions. With protons contributing to the majority of the radiation flux. The energy of the proton flux ranges up to 100 MeV [170]. A handful of major SPEs have been recorded so far that occurred in February 1956, August 1972, October 1989, and July 2012 [143] and serve as the worst case design condition included in radiation software analysis tools. The SPEs are a major concern for interplanetary missions because the incoming radiation is blocked by the magnetic field of the Earth.

Effects of radiation environment

The main takeaway from the previous sub-section is that the main radiation sources in space are electrons, protons and heavy ions. These particles have two kinds of interactions: nuclear and ionic. Nuclear reactions are the reactions where the radiation particle interacts with the nucleus of the target material's atom and displaces the atom; this is also called the displacement effect. Ionic reactions are when the radiation particle interacts with the charge field of the atom. The charge field is mainly composed of electrons, so when the incident radiation transfers enough energy to the electrons in the atom's valence shell, the electrons surpass the threshold energy and are free to move around in the lattice of the crystalline material (Silicon Dioxide). This is why it is called ionising radiation.

The effects of radiation on materials can be classified based on the time taken for the effect to manifest as cumulative and single event effects. The three main kinds of radiation effects on electronics are listed and detailed below:

- **Total Ionizing Dose (TID):** This is the total energy deposited on the electronics due to ionisation caused by the radiation particles. This ionization energy increases the energy of the electrons in the lattice and creates electron-hole pairs in the semi-conductor. The newly created electron-hole pairs can recombine, can act as current carriers or can form trapped charges at the interfaces. This further leads to measurable effects on the electronics like change in threshold voltage, leakage currents, decreased mobility of current carriers and increased gate charge. Shielding is one of the most effective measures to mitigate the effects of TID because the shielding material reduces the energy of the radiation particles and therefore the energy deposited is also lower. Another measure to mitigate effects of TID is to test the COTS electronics as their reliability and response to radiation can be very different even though they are mass produced.
- **Displacement Damage:** As the name suggests, this is a cumulative effect caused due to collisions between radiation particles and the electronics which lead to displacement of the atom from its position in the lattice structure of the semi-conductor. By knocking the atom in the semi-conductor to an interstitial site, new conduction paths are generated or designed conduction paths in the semi-conductor have lower conduction. This further leads to observable effects on the electronics such as leakage currents, decreased carrier mobility and heat generation due to recombination.

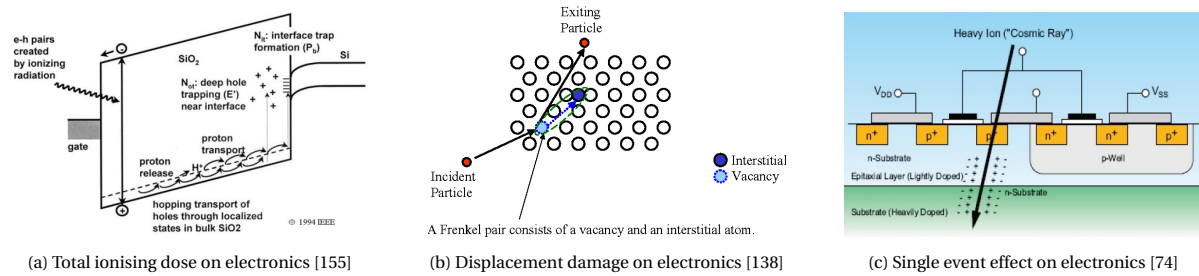


Figure 5.3: Different effects of radiation on electronics

- **Single Event Effects (SEE):** These are a group of effects caused due to a single particle interacting with the electronics. Proton is the main cause of this effect which originates from SPEs, GCR & trapped radiation belt. The proton leaves behind an ionization column (electron-hole pairs) in the material. Based on the nature of the damage the effect leaves on the material, single-event effects can be classified as destructive and non-destructive. Destructive effects cause permanent and non-reversible damage. Non-destructive effects cause reversible damage.

Acronym	Effect	Description
SEU	Upset	Digital circuit changes logic state (bitflip)
SEL	Latchup	High current withdrawal state
SEGR	Gate Rupture	Failure of power transistor
SEB	Burnout	Permanent failure of the device
SEFI	Functional Interrupt	Device no longer performs designed function
SEMBE	Multiple Bit Error	Multiple logic state changes
SET	Transient	Transient current in circuit
SEIDC	Induce Dark Current	Increased dark current in Charge Coupled Device (CCD) arrays
SES	Snap Back	Drain to source break-down leading to high current

Table 5.2: List of SEE and their description

Radiation mitigation strategies

The undesirable effects of radiation can be mitigated using multiple strategies applied at different hardware and software development design stages. Some of these mitigation techniques are classified in the Figure (5.4). As the current project is at the initial system hardware design stage, only system-level radiation mitigation strategies will be considered here. The system-level mitigation strategies can be further subdivided into hardware and software techniques. Redundancy is utilizing redundant components for critical parts to avoid system failure. It can be implemented based on hardware, software, information or time. Error detection and correction is also performed on software. Re-initialization recovery is a method where a watchdog timer is used to restart the system if the system does not send a pulse within a given time interval or frequency of a time period. This method is also implemented via software design. Scrubbing is a method where the hardware and software are inspected in the background for errors and corrected. This method is also pertinent to electronics and software design, so it will not be considered in this project. The last option for system-level radiation mitigation is shielding. Shielding is a method that uses materials to physically reduce the intensity of radiation incident on the enclosed electronics. This is a very effective hardware-based method to lower the effects of radiation on electronics, which is why this method will be considered further in this project. The shielding material and its thickness can be chosen based on the radiation environment and lifetime requirements.

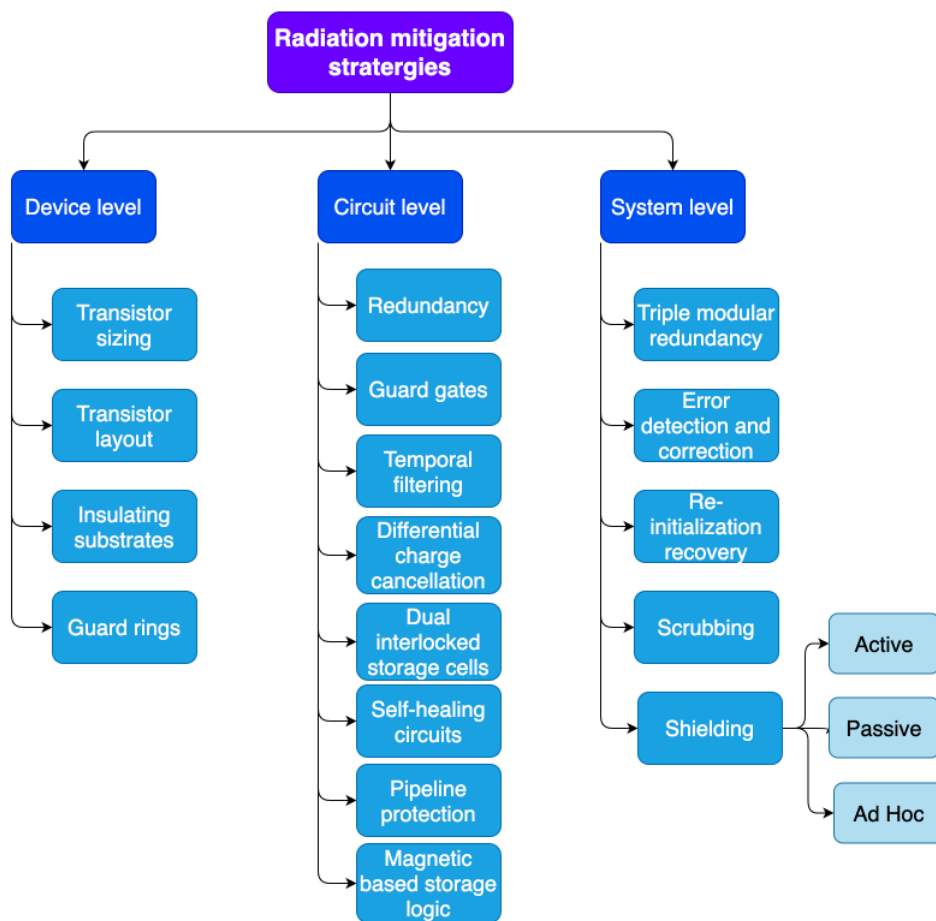


Figure 5.4: Radiation mitigation strategies at different levels of design

Shielding design

Shielding can be of three types - Active, passive and Ad-Hoc shielding. Active shielding is a shielding method that mimics Earth's magnetic field to repel the charged particles. The electromagnetic field prevents the radiation from interacting with the enclosed electronics. The drawback of this method is that it requires a lot of power, and the E-M field will also interact with the spacecraft's systems. Passive shielding is a method that utilizes extra material mass to absorb energy from the incident radiation; it covers the whole system. Ad-Hoc shielding is when a part of the system is shielded. It is an effective method when lower mass is a critical design factor. The components with higher susceptibility to failure by radiation are shielded using this method. Ad-Hoc shielding uses multiple layers to shield against different kinds of particles. As a basic design principle, lower atomic number materials are used to shield against protons and ions. The secondary radiation from heavy ions does not receive many contributions from a low atomic number material because of the low mass of the nucleus. High atomic number materials are good at shielding against electrons and photons. To implement Ad-Hoc shielding, the critical parts of electronics must be identified which is not possible at this design stage. Therefore, the suitable radiation shielding method for this application at this stage is passive shielding which uses a single material's inherent mass and thickness to absorb the radiation.

The main design factor of a passive shield is the thickness of the shield and the material. To decide on a material and its thickness, the total mission dose over the lifetime must be known, and the radiation dose limit of the electronics must be known. Other constraints like weight considerations and volume available also influence the material choice and the thickness of the shielding. Therefore there are two approaches to designing the shielding. If the volume and mass constraints are not strict, a shielding thickness adequate enough to allow a lower radiation dose than the radiation dose limit of the electronics will be used. If there are strict volume and mass constraints, the material with the lowest density is chosen, and the maximum thickness within the volume constraint is provided. If this thickness of shielding allows more total radiation dose than the specified radiation tolerance limit of the electronics, then there are two design options that

can be followed - radiation-hardened electronics (electronics that have a radiation tolerance of 100 krad to 1 Mrad [186]) can be used, or circuit or design level based mitigation strategies as mentioned in Figure (5.4) can be utilised.

For designing the passive shield for this application, firstly, the radiation tolerance limit of electronics will be found, followed by finding the total radiation dose in LEO for the lifetime of five years SADM-ENV-001. It was found from multiple sources that COTS electronics have a radiation limit of 10 krad [158, 186]. But, this was a rough value for the initial design, and this could be different for different electronics components and could show signs of faulty behaviour at lower doses. Testing is the best way to be sure of the limit and functioning. The electronic components that will be used are not known at this stage of the design. Therefore a limit of 10 krad will be considered as the limit for which the shielding will be designed.

The next step is to find the radiation dose in LEO. The "Ionizing dose for simple geometries" mode of SPENVIS software was used to find the total radiation dose for these different orbit types. To find the radiation energy expected in LEO, three different orbit types common in LEO have been considered - Polar orbit, Heliosynchronous and an orbit with SAA Passover. It was stated previously in subsection (5.1.4) that the SAA has the worst case radiation environment in LEO, which is why this orbit has been considered for simulation. Polar orbits are the most common orbits in LEO for Earth observation CubeSats because of the advantage that the orbit offers for taking pictures at the same time of the day during each orbit and a view of the entire Earth through the passage of one orbit. Sun Synchronous Orbit (SSO) or Heliosynchronous is the other orbit type used by LEO CubeSats for imaging, reconnaissance and weather monitoring. It has the advantage of even illumination for imaging. These orbits were simulated for a period of five years with different shielding materials like Aluminium, Titanium, Iron and Tantalum for different material thicknesses from 10^{-4} to 6mm in steps of 0.2mm. These were the only options of metals that were offered by SPENVIS software. This model considers the metal as a sphere of uniform thickness around Silicon and calculates the maximum radiation dose absorbed by the enclosed Silicon wafer over the lifetime of the orbital conditions fed as input. Much complex analysis could have been performed by using the MULASIS (Multi-Layer Analysis) mode of the software, but that mode is preferable to design a shielding incorporating multiple layers of different materials. Such a design is required for shielding sensitive electronics and for radiation environments that have a pronounced effect of heavy ions, photons, etc which is the case in GEO and interplanetary missions. As the electronics specification is unknown at this stage, the author would suggest using this mode for future shielding optimisations in case the current shielding and other mitigation strategies are insufficient. Moreover, the current application operates in LEO, whose radiation environment is dominated by electrons, protons and ions for which, a single metal layer is sufficient to shield. The orbital parameters, environmental parameters and the equivalent shielding thickness of the different materials compared to Aluminium are detailed in section (A.3). The thickness of the different materials required to achieve a total mission dose of less than 10krad was found from the data generated for each orbital case for each metal, and the results are summarized in Table (5.3).

Material Density (g/cm^3)	Vacuum 0	Aluminium 2.71	Titanium 4.5	Iron 7.78	Tantalum 16.6
Polar orbit (A.3.3)					
Material thickness	1.00E-04	3.50E+00	2.10E+00	1.20E+00	5.66E-01
TID at given thickness (rad)	1.32E+08	8.89E+03	8.11E+03	7.81E+03	9.05E+03
Orbit through SAA (A.3.1)					
Material thickness	1.00E-04	3.50E+00	2.10E+00	1.03E+00	4.85E-01
TID at given thickness (rad)	1.20E+08	8.42E+03	7.70E+03	9.72E+03	1.00E+04
Heliosynchronous orbit (A.3.2)					
Material thickness	1.00E-04	2.00E+00	1.08E+00	6.71E-01	2.91E-01
TID at given thickness (rad)	4.35E+07	8.71E+03	9.76E+03	9.60E+03	9.58E+03

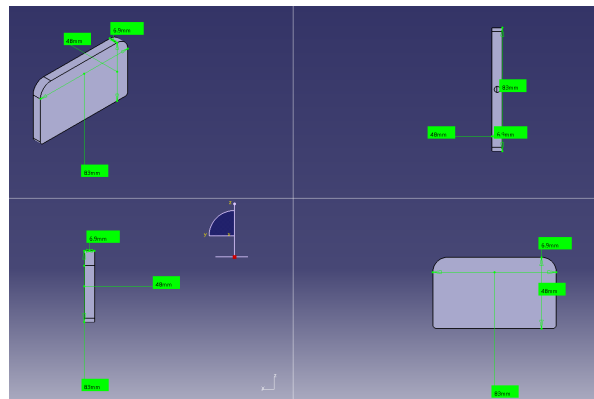
Table 5.3: Summary of material thicknesses required for TID less than 10krad in different orbits

As shown in the data above, maximum radiation in LEO was found to occur in the polar orbit and the orbit with SAA passover which is in the order of 10^5 krad. The difference in TID at vacuum is due to the minimum material thickness permitted by the software. Aluminium with a thickness of 3.5 mm was found to be sufficient to achieve a TID of 10 krad in the worst-case orbital conditions. As the maximum height of the

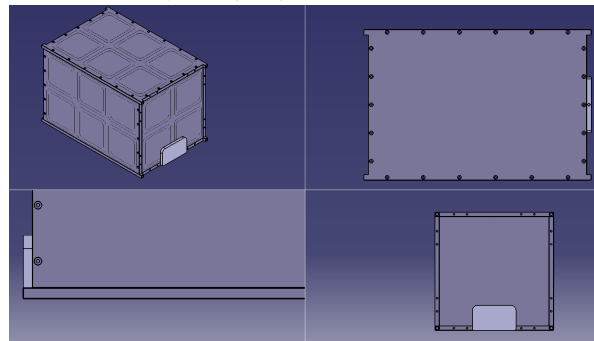
housing is 6.9 mm this still allows around a 3.4mm height limit for the electronics, which is sufficient. Moreover, the material with the least density will be preferred for the housing to have the least weight. Comparing the densities of the metals considered, aluminium has the least density and requires a shielding thickness achievable with the imposed dimensional constraints. Therefore, **aluminium will be the material of choice for the housing with a shielding thickness of 3.5 mm**. The shielding thickness would have to be applied only over electronic components as they are prone to radiation damage. The housing material can be designed to have a lower thickness at other parts where there are only structural elements. Aluminium has many grades and alloys ranging from 1000 to 8000 series with varying compositions that lead to different strength and corrosion resistance properties. Most of the satellite structures are usually made of Aluminium 6061-T6 grade alloy [91, 187]. This grade of aluminium alloy is composed of silicon (0.40 - 0.80 %), magnesium (0.80 - 1.2 %), copper (0.15-0.4 %), iron (%), manganese (0.15 %), chromium (0.04 - 0.35 %), zinc (< 0.25 %) and titanium (< 0.15 %). This grade of aluminium is desirable because of various advantages like low density, high strength, workability, resistance to corrosion and acceptance of surface coatings. Elements like copper, magnesium and manganese make the alloy heat treatable and improve its strength and hardness properties. It is desirable to have the housing made of the same material as the CubeSat structure to avoid differential thermal expansions and galvanic corrosion. Therefore, the SADM's housing will be made of **Al-6061-T6** grade aluminium alloy. Now that the material is selected, the thermal expansion of this material along direction of thickness for a temperature change of 95 C (120-25 C) considering room temperature and maximum operational temperature was calculated as $0.15 \mu\text{m}$ ($\Delta L = \alpha L \Delta T$, where $\alpha = 23.6 \mu\text{m/mC}$). This is much lower than the clearance value assumed earlier. Therefore, a clearance of 0.1 mm would suffice to avoid contact with deployer structure.

Thermal variations can cause expansion and contraction of the material leading to induction of thermal stress within the material. In such an operational condition it is favourable to have the housing to be black in color as it would make it a good absorber and emitter of radiation heat. Moreover having a shiny metal surface will lead to stray light interference for optical instruments of the CubeSat which is not desirable. Considering the atomic oxygen in space and contaminants like oxygen and moisture on Earth, aluminium could undergo oxidation and form Aluminium oxide. Corrosion of aluminium is not as detrimental as corrosion of Iron but it would reduce the strength of the material and stress corrosion cracking which is not desirable. There are three ways to mitigate corrosion of aluminium which include painting, powder coating and anodizing. Unlike painting and powder coating, that are applied to the surface and can chip or peel anodization is an electrochemical process that creates an oxide layer on the metal surface. In other words, anodization is controlled oxidation. This oxide layer cannot be peeled or chipped as it is ingrained in the material. And as it is porous, smooth surface finishes and paints can be easily attained and applied. Therefore, the author would recommend anodization of the housing to prevent corrosion and to apply black color to attain high absorptivity and emissivity of radiation. By implementing these measures, the requirement SADM-HSG-005 has been accounted for in the design of the SADM.

5.1.5. Preliminary housing CAD model



(a) Preliminary housing design with dimensions (83x48x6.9 mm)



(b) Preliminary housing fitted to a 12U CubeSat

Figure 5.5: Preliminary housing design

Based on these initial design decisions carried out in the previous sub-sections, the initial size and dimensions of the housing can be fixed. All requirements set for the housing have been considered and implemented until now except for SADM-HSG-004. This requirement has also been considered now and the initial design of the housing is as shown in the Figure 5.5. The final dimensions will depend on the dimensions of the elements the housing will enclose, therefore these dimensions are subject to change in the later sections.

5.1.6. Summary of housing design

In this section, the housing has been designed considering applicability to multiple panel mounting configurations, scalability to different sizes of CubeSats and environmental considerations. Modularity and scalability have been implemented by design as shown in Figure 5.5. The housing will be fabricated out of Al-6061-T6 with a thickness of 3.5mm in places where electronics are housed. The housing will also be anodized and have a black color surface finish.

5.2. Rotary actuator selection and sizing

In this section, the rotary actuator that is responsible for providing the mechanical power to rotate the solar arrays will be chosen. This section is aimed at addressing the research question 2a. In order to choose or design the right rotary actuator, firstly the requirements for the rotary actuator would be defined and a trade-off would be performed to choose the right technology suitable for the application based on its requirement.

5.2.1. Purpose

A rotary actuator is required in this application in order to rotate the solar panels and position them normal to the Sun as their relative position changes during the course of the satellite's orbit. This is one of the key functions of the SADM system as stated in requirement SADM_FUN_001.

5.2.2. Rotary actuator requirements

In order for the actuator to rotate the three rigid 12U sized solar panels, the actuator must be capable of providing enough power during all the mission scenarios. This maximum output power required from the actuator was calculated in section (4.3.1) as 0.153 mW and the maximum torque required was 3.816 mNm as summarized in Table (4.7). Thus, the output power of the rotary actuator would be the primary selection criteria to choose a suitable rotary actuator for the current application.

5.2.3. Rotary actuator design options & trade-off

Design options

Rotary actuators can be classified in to 3 categories based on how they utilize power for actuation as shown in Figure (5.6).

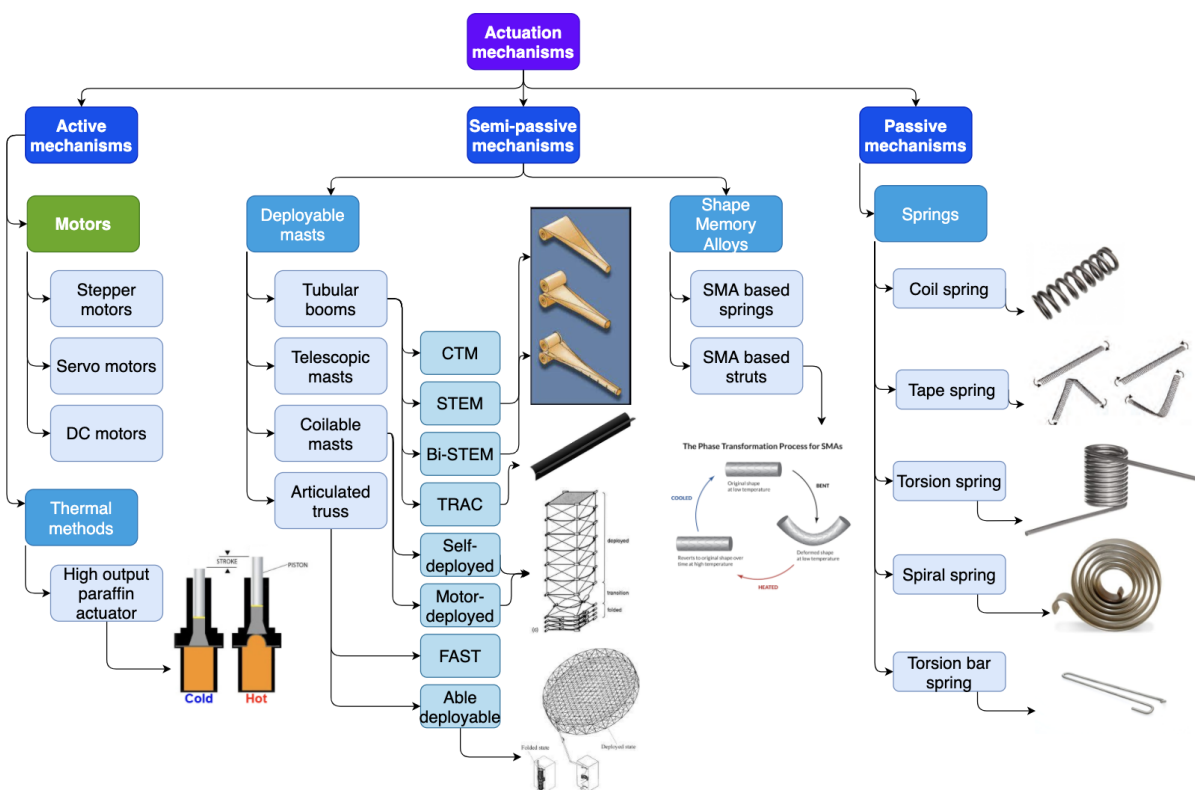


Figure 5.6: Actuator design options

- **Active mechanisms:** The actively controlled mechanisms are the type of actuators that are controlled and positioned continuously over their operation period, they need constant power supply for their

operation. Motors fall under this category because they use electrical energy to perform linear or rotary actuation. Some motors also consume power to maintain a fixed position.

- **Semi-passive mechanisms:** The semi-passive actuators are the kind of actuators that require power initially or at limited phases of the operation (like re-orientation) but not during the entire operation lifetime. Shape Memory Alloy and deployable masts fall under this category of actuators.
- **Passive mechanisms:** Passive mechanisms on the other hand need no external energy supply for their actuation, these mostly include springs as they rely on the stored strain energy for deploying the stowed structures. Springs usually fall under this category of mechanisms. These category of mechanisms cannot change their position once they are deployed.

Broad trade-off

In the figure (5.6) above, the rotary actuator design option marked in green is the selected design option for further consideration, whereas the rest of the design options have been eliminated because of the reasons stated below:

- **Passive rotary actuator mechanisms** cannot be used in this application because this application requires continuous tracking of the Sun and orienting the panels normal to the Sun as stated in SADM-PER-001. Whereas, passive mechanisms once deployed cannot undergo position change.
- **Semi-passive actuator mechanisms** are not suitable for the current application. It would seem desirable for an actuation application because they require power only while actuation and not for maintaining the position but they have disadvantages that make them undesirable for the current application. Rotary actuators based on shape memory alloys have been designed [207] based on pulleys and cables but they have to be designed for specific applications and are not commercially available. This also means that rotary actuators based on shape memory alloys require multiple parts to perform the rotary motion and multiple individual parts leads to higher chances of failure. This application has a requirement that it shall use COTS components as and when required as per SADM-DES-001. Therefore, SMA based actuators cannot be considered for this application because they are mostly used for linear actuation, the rotary SMA-based actuators are not commercially available and designing one especially for this project is not feasible within the given timeline and also has its associated risks. Deployable masts make use of tape-spring like elements that deploy linearly. This means that they are usually used in combination with flexible solar panels or solar sails that can be rolled or the deployed tape spring itself used as a deployable antenna. But the current product is being designed for rigid solar panels as stated in SADM-FUN-001 thus, this mechanism cannot be used for this application.
- Among the active rotary actuator mechanisms **thermal methods** are eliminated from further design consideration because they use thermal expansion of fluids or semi-solids to actuate. Storage of fluids are in general avoided according to CubeSat design standards [139] due to their requirement for special enclosures and probability of contamination.

That just leaves the motors for further consideration in the trade-off process. Motors have various advantages that make them suitable for the current application like ease of control, positioning accuracy and commercial availability. Motors also have multiple options based on their working principle. The motor technology trade-off & selection will be performed in detail in the next section.

Motor technology design options & trade-off

The Figure (5.7) below shows the motor technology design options. As observed from the requirements and the actuator requirement calculations (section 4) performed in the earlier sections, this application requires an actuator that can provide high torque, low rotational speed, considerable positional accuracy and operation with DC voltage. The selected technology option is in green and the rejected technology options are indicated by red.

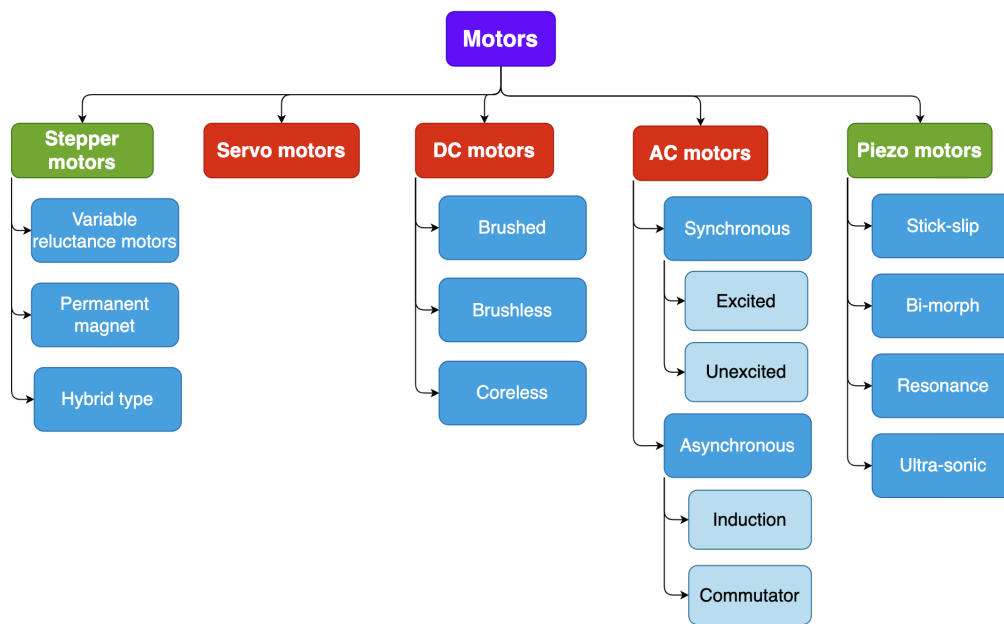


Figure 5.7: Motor technology design option

The reasoning for the selection is detailed below:

- AC Motors:** Alternating Current (AC) motors cannot be considered for use in this application because they are usually used in high torque and high RPM applications. These kind of motors have cogging at low RPM. This application does not need high RPM. This application is slow-moving and requires positional accuracy. Additionally, they are not available in miniature versions.
- DC-motors:** DC-motors cannot be used in this application because of disadvantages like brush wear, power-loss through the brushes, debris generation due to brush wear & arcing. This results in limited lifetime and performance risks. Brush-less DC motors overcome most of the disadvantages faced with Brushed DC motors. But they are typically used in high RPM and low torque applications. Positional accuracy can be achieved with closed-loop control. This application again requires low rotational speed (RPM) & high torque and DC motors are typically used in high RPM applications. In fact, DC motors are not desirable for low speed applications because of cogging at low RPM.
- Servo motors:** Servo motors are constructed by coupling a DC or AC motor with transmission gear and a negative feedback control loop. Thus, they have the same disadvantages as the AC & DC motors. These commercially available servo motors come with compatible gears, but for the current application these COTS servo motors cannot be used because they are dimensionally incompatible and are not space grade (because they come with plastic gears & out-gassing lubricant).

The piezo-motor and the stepper motor are the only remaining two options for this application. Piezo and stepper motors are typically used in precise positioning applications which is also a prerequisite for this application. But each of these motor types also have their advantages & disadvantages as described in the Table (5.4) below.

Piezo-electric motors		Stepper motors	
Advantages	Disadvantages	Advantages	Disadvantages
Capable of resolutions less than a degree usually in the order of micro-radians.	Susceptible to failure due to vibrations	Variable step resolution usually greater than one degree.	Lowered torque with higher position resolution
High torque	High & uneven wear due to contact-based actuation	High torque at low speeds	Torque decreases with increased speed
Integrated position feedback sensors	Hysteresis losses	Open-loop control achieved by principle of working	Closed loop control required to make sure steps are not missed due to resonance or inertia imbalance
Unpowered holding	Drift problem	Can also provide un-powered holding torque	Holding torque has to be overcome for rotation which reduces torque while running and this effect is more pronounced at high speeds
Magnetic & electrical field disturbances are minimal because of contact based actuation due to piezo-electric working phenomena	Need additional components to produce circular motion, thus more moving parts in contact	Variable speed & direction control	Steps can be missed due to resonance or uneven load conditions

Table 5.4: Stepper versus piezo motor technology trade-off

The above table shows that both stepper and piezo-motors have their equal share of advantages and disadvantages when compared against each other. Therefore, commercially available stepper and piezo-electric motors were searched for and traded off based on the extent to which the motor specification meets the requirements calculated for this application like dimensions, torque, power output, operational temperature and vacuum-compatible lubrication. The motor's parameter that meets or exceeds the corresponding requirement is shaded in green; if the parameter does not meet the requirement, it is shaded in red. The motor that meets most of the application requirements will be selected for use in this application. This trade-off is presented in the Table (A.14).

In the trade-off carried for the COTS stepper and piezo-motors, it can be seen that the piezo-motors do not fit the tight dimensional requirements imposed by the system. Another important observation from the trade-off above is that even though most of the stepper motors seem to provide more than enough power required by the application, none of them offer enough torque compared to that required by the application. This leads to the need of a mechanical power transmission system (gearbox) that increases the torque for a given power output of the motor. This mechanical power transmission system will be discussed in detail in the next section. The two remaining COTS stepper motors (Faulhaber DM0620 [75] and Micromotion's MaalonDrive HighAcc 6mm - Type 3 motor [76]) seem to satisfy an equal number of requirements by the application. Therefore the trade-off is advanced by going one more level in detail to find the best-suited motor among the two motors. This is done by considering factors like cost, gearbox availability, space suitability and lead times. This trade-off is presented in the Table (5.5) below. The advantage of a motor corresponding to trade-off criteria is highlighted in green, and the disadvantage is highlighted in yellow. Each motor's total number of advantages is summed and displayed at the bottom of the table.

Parameter	Faulhaber DM0620-0130 [75]	Micro-motion GmbH MaalonDrive HighAcc 6mm - Type 3 [76]
Cost	Cheaper (285 euros – includes motor, gearbox & motion controller circuit)	Expensive (2230 euros)
Gearbox	Compatible gearbox with high gear ratios (256 to 4096) this would lead to smaller external gear ratio requirement	Compatible gearbox with low GR (120) this would lead to bigger external gear ratio requirement
Space suitable	Does not have space-grade lubrication or vacuum compatible (re-lubrication maybe possible)	Can be customised to have space-grade lubrication
Lead time	Motor & gear-box have a short lead time but motion control electronics not in stock. Electronics can be custom designed as well	Motor & gear-box have a long lead time (15-18 weeks)
Total advantages	3	1

Table 5.5: Faulhaber v/s Micro-motion trade-off

It is very evident from the above table that the Faulhaber DM0620 [75] is better suited for this application than the Micromotion's stepper motor. Therefore, this motor will be considered for the design of the SADM.

5.2.4. Summary

The stepper motor is the right rotary actuator technology for this application because of its positional accuracy and good low RPM performance (absence of cogging torque). The **Faulhaber DM0620 stepper motor** was the **best-suited** one considering power, cost, shorter lead times and gearbox availability. With this, the research question 2a has been answered. It was also found that a mechanical power transmission system (gearbox) was required to alter the torque produced by the motor to achieve a higher torque value which the current application needs.

5.3. Mechanical power transmission element design

In the previous section, it was found that the rotary actuator provides enough power required to rotate the solar arrays but not enough torque and to resolve this, using gear as a mechanical power transmission mechanism was considered. Gears can be combined with the motor to produce the desired output torque and rotational speed for particular motor input power. The gears can be included as a part of the motor (as a gearbox) or external or can be combined together to achieve a particular gear ratio. The main parameter to select and size the gear is the gear ratio. This section will describe the calculation of the gear ratio required for this application, followed by the selection of the type of gear and its design process.

5.3.1. Purpose

The transmission gear is required for 2 main purposes:

1. **To match the actuator's torque & speed characteristics with the load's (solar panel) torque & speed requirements.** The graph (5.8) below compares the torque-speed profile for the actuator (A.10) and the solar panels (4.7). As it is visible that the two of them do not coincide, the function of the transmission gear would be to bridge the gap and make sure the actuator's torque and speed output is matched to the solar panel's torque & speed requirement. It can be seen from the Figure (5.9), that the motor actually provides lower torque for a range of higher rotational speeds in the magnitude of 1000 RPMs whereas the solar arrays need a higher torque at a range of very low rotational speeds almost close to 0 RPM.

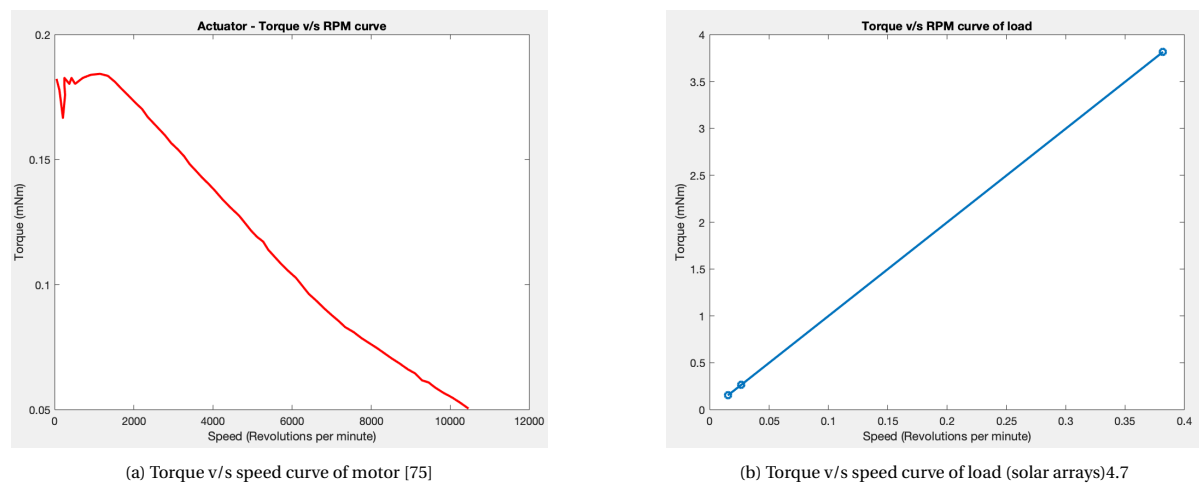


Figure 5.8: Difference between torque v/s speed of motor and load (solar arrays)

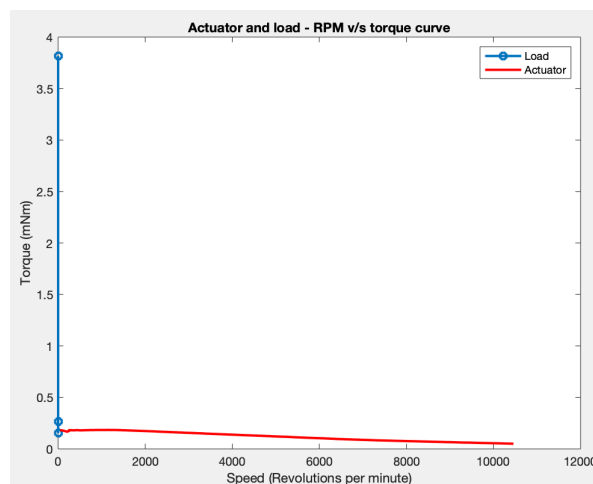


Figure 5.9: Comparison of the torque and speed curves of the motor and the solar arrays

2. **Prevent direct transmission of design loads on motor shaft:** As discussed in section (4.3.3), the solar panels act as a load source during launch and transmit the force on the shaft that it is connected directly to. The bearings are the main load-bearing elements, but the transmission gears would be secondary, which would prevent the launch loads imposed on the solar array to be transmitted to the fragile motor shaft.

5.3.2. Requirement

Some system requirements also translate to the gears and influence their design. The gears must fit within the dimensional constraints of the system, which was defined in section (3.2) as less than 6.9 mm. All the environmental requirements applicable to the system as defined in Table (3.4) are also applicable to the gears.

5.3.3. Theory of gears

This sub-section aims to educate a new reader to the concept of gears by exploring their working principle, nomenclature used and the process used to size and select them. This is necessary to understand the design process detailed in the rest of this section.

A mechanical power transmission element

Gears belong to a category of machine elements called power transmission elements. These class of elements transfer the power from an actuator to the load. As mechanical power is composed of torque and speed, these elements can transform the input power by altering the torque and speed to suit the requirements of the output. Ideally, such an element would not cause transmission power losses but in real world this is not possible due to friction. This class of machine elements include gears, power screws, pulleys, chains, brakes, clutches and belts [134] [188]. In this project, only gears would be dealt with because of their advantages over other power transmission devices like miniaturisation, allow easy combination to achieve required power output parameters (torque & speed) and higher efficiency of power transmission which is important for this application. They can be classified in to categories based on the position of the shaft axes, peripheral velocity, type of gear and the teeth position [101].

Using gears of different diameters causes a change in rotational speed among the two. The change in speed can also be achieved by using gears with different number of teeth. As the speed changes while ideally maintaining the transmitted mechanical power, the torque changes in inverse relation to the change in rotational speed. This relation is expressed in equation (5.1) below.

$$GR = \frac{\omega_1}{\omega_2} = \frac{N_1}{N_2} = \frac{T_2}{T_1} = \frac{d_2}{d_1} = \frac{z_2}{z_1} \quad (5.1)$$

This system is analogous to electrical power transformer where the voltage and current get stepped up or down depending on the number turns in the primary and secondary coils as expressed in equation (5.2).

$$\frac{V_p}{V_s} = \frac{I_s}{I_p} = \frac{N_p}{N_s} \quad (5.2)$$

Working principle

Gears in general are cylindrical wheels that transfer mechanical power from one rotating shaft to the other by inter-meshing teeth. The gears work by the principle of conjugate action. This means that the teeth must have complementary shape or profile with respect to each other such that they mesh together to produce constant angular velocity when meshing. There can be many possible shapes for this, but gears commonly make use of an involute profile. This is because of with such a curve, the point of contact always occurs at the tangent to the two surfaces and the instantaneous forces are directed along the normal as shown in Figure (5.10c). Another reason why involute curves are the most prevalently used profile in gears is because they can tolerate change in center to center distance without causing an effect on the constant angular velocity motion desired. The constant angular motion is required from the gears to maintain a constant torque profile.

Common terminologies

- **Pitch circle:** The theoretical circle upon which all calculations are usually based; its diameter is the pitch diameter. The pitch circles of a pair of mating gears are tangent to each other.

- **Module:** The ratio of the pitch diameter to the number of teeth.
- **Addendum:** The radial distance between the top land and the pitch circle. The circle with a radius of the of the addendum is called as the addendum circle.
- **Dedendum:** The radial distance from the bottom land to the pitch circle. The circle with a radius of the of the dedendum is called as the dedendum circle.
- **Pinion:** The smaller of two mating gears, it usually the driver.
- **Circular pitch:** The distance measured on the pitch circle, from a point on one tooth to a corresponding point on an adjacent tooth.
- **Clearance:** The amount by which the dedendum in a given gear exceeds the addendum of its mating gear.
- **Backlash:** The amount by which the width of a tooth space exceeds the thickness of the engaging tooth measured on the pitch circles.
- **Line of contact:** When a pair of involute gears is meshed, the contact occurs on the line of contact and the contact point moves along the line of contact.
- **Pressure angle:** The angle formed by the radial line and the line tangent to the profile at the pitch point.

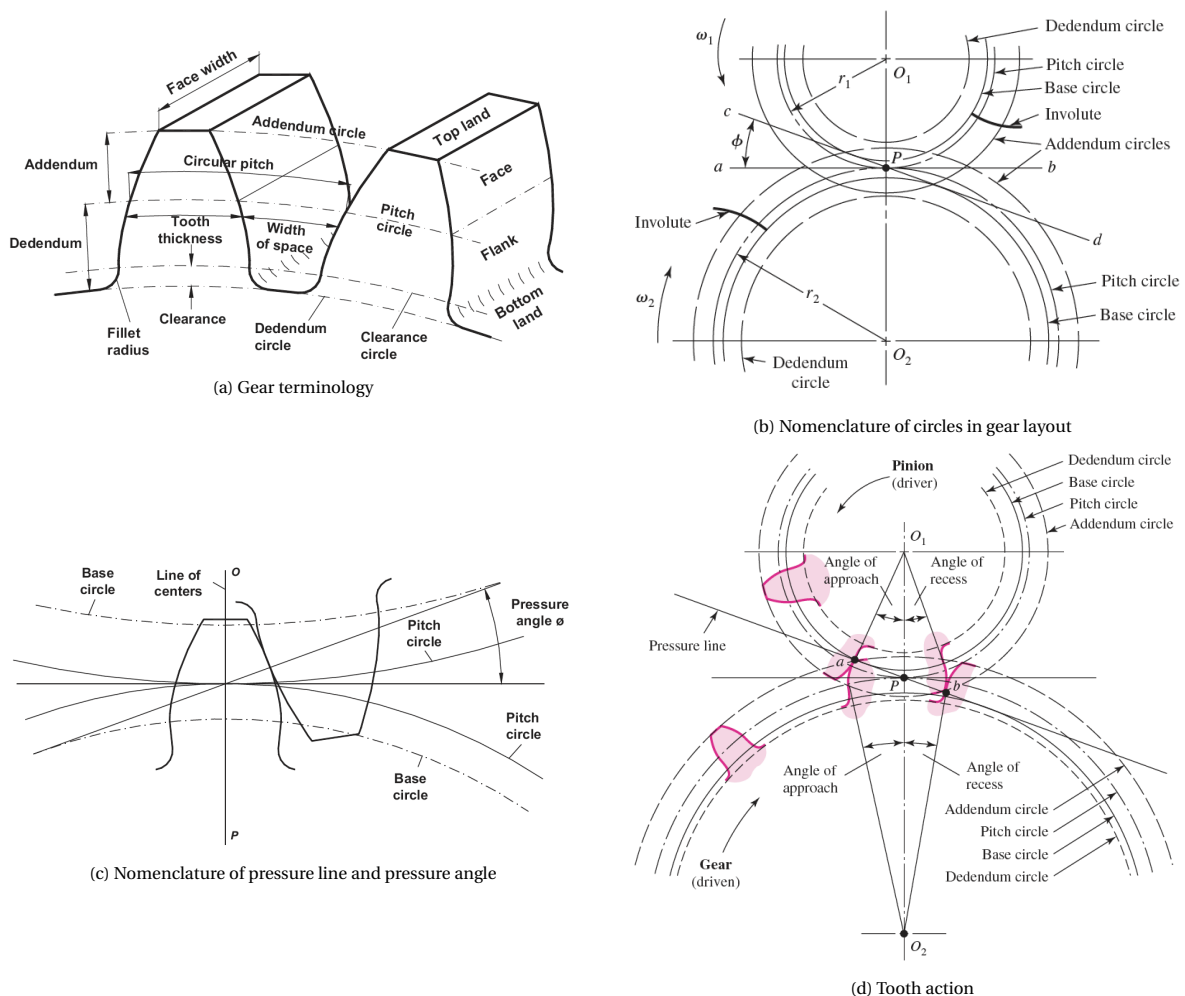


Figure 5.10: Common gear nomenclature [104] [111]

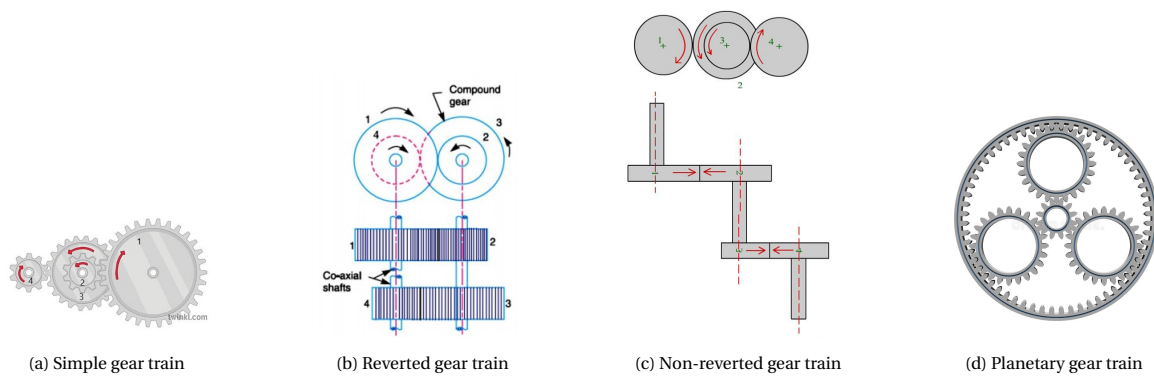


Figure 5.11: Types of gear trains

General selection & sizing process

The first step in choosing the right gear for an application is by calculating the gear ratio that the application requires. This is then followed by selecting the number of teeth on pinion and gear. The module of the mating gears are then matched by considering the dimensional constraints. This is then followed by material selection, calculation of pitch line velocity and force on the gear such that it does not exceed the strength limits [111]. The force on the gear face is given Lewis's equation. Some sources like the American Gear Manufacturers Association (AGMA) also suggest designing the gear to withstand failure due to surface pitting [114]. Based on the gear ratio required and the application's design constraints, multiple gears can be combined together in different configurations to achieve the required gear ratio. Gears as a single component are not much useful, they are usually combined with each other to form a compound gear train or planetary gear train that multiplies the torque or speed ratios based on how they are combined together. Compound gear trains can be classified in to simple, reverted and non-reverted [111]. Reverted gear trains have co-axial input and output shafts rotating in opposite directions. Non-reverted compound gear trains have non co-axial shafts that rotate in the same direction. The different gear trains are shown in Figure (5.11).

5.3.4. Gear ratio calculation

As learned from the previous sub-section detailing the theory of gears, it was learned that finding the gear ratio required for the application is the first step in choosing the right gear and its configuration for an application. This section will calculate the gear ratio required for this application by considering different optimisation cases.

There are three main ways to optimise the right gear ratio for this application by considering different factors. These optimisation cases are listed below:

1. **Inertia matching:** The inertia of the load as seen by the motor would be unity by increasing the gear ratio until the inertia ratio (inertia of load/inertia of motor) is close to unity.
2. **Torque matching:** As the torque provided by the motor is lower than that required by the solar arrays, the gear ratio can be increased until the torque provided by the actuator and the gearbox is higher than the required torque.
3. **Maximum power point matching:** The gear ratio could be optimised such that the maximum power produced by the motor corresponds to the maximum power required by the load. This ensures optimal power transfer between the two systems with the least losses.

Each of these cases will be explored in detail, and the optimum gear ratio considering each case will be calculated in the subsequent sub-sections.

Inertia matching

Matching an actuator's inertia to the solar panel's inertia is desirable to improve the loading's positioning accuracy and smooth motion. The inertia is matched using a gearbox [118][147]. In case the inertia of the load is greater than the actuator's rotor, when the load is accelerated, due to the load's high inertia, it will tend to be in motion according to Newton's second law and will overshoot the desired position and will try to return to

the equilibrium position (position with least magnetic reluctance) after a couple of damped oscillations [95]. This is why it is desirable to match the inertia of the load and the actuator's rotor. Inertia matching for the current application will be performed below. Also, the motor's starting and stopping rates can be achieved with a lower inertia mismatch. This means the motor can be accelerated from rest to high step rates or quickly decelerated to rest without a phase lag between the rotor speed and the stator switching speed. An expression for finding the optimum gear ratio for the motor's inertia and load to be close to unity is derived below. The motor torque as a function of the motor's inertia, gear ratio, angular displacement, damping co-efficient and angular acceleration is expressed in the equation below:

$$T_m = \left[J_m + \left(\frac{N_m}{N_l} \right)^2 J_l \right] \ddot{\theta}_m + \left[B_m + \left(\frac{N_m}{N_l} \right)^2 B_l \right] \dot{\theta}_m \quad (5.3)$$

Equivalent inertia of the system is given by , where gear ratio = $r = \frac{N_m}{N_l}$:

$$J_e = J_m + \frac{J_l}{r^2} \quad (5.4)$$

Acceleration of the motor is expressed as:

$$\alpha_m = \frac{T_m}{J_e} \quad (5.5)$$

Acceleration of load:

$$\alpha_l = \frac{T_m}{J_e r} = \frac{T_m}{r J_m + \frac{J_l}{r}} \quad (5.6)$$

For maximum acceleration of load:

$$\frac{d}{dr} \left(r J_m + \frac{J_l}{r} \right) = 0 \quad (5.7)$$

$$J_m - \frac{J_l}{r^2} = 0 \quad (5.8)$$

$$r_{opt} = \sqrt{\frac{J_l}{J_m}} \quad (5.9)$$

The motor's inertia is known from its datasheet. But the load inertia (J_l) as seen by the motor includes the inertia of other components that it drives like the gears (J_D), couplings (J_C), external (J_E) load (solar arrays) and gearbox (J_G). In general, the load gear ratio is expressed in the equation below [193]:

$$J_l = \frac{J_D + J_E + J_C}{GR_i^2} + J_G \quad (5.10)$$

In the expression above, the inertia of the drive system (J_D) and the inertia of the coupling (J_C) can be eliminated because the inertia of the drive system (gear in this case) is not known and even if it will be known it can be considered negligible compared to the load and the system does not use a coupling. This results in the load inertia expression being reduced to:

$$J_l = \frac{J_E}{GR_i^2} + J_G \quad (5.11)$$

The inertia of the gearbox (J_G) can be assumed to be negligible compared to the inertia of the solar panels because the inertia of the motor's rotor is of the order $0.5 \times 10^{-9} \text{ kgm}^2$ and the minimum inertia of the solar panels is $3.33 \times 10^{-3} \text{ kgm}^2$. The inertia of the gearbox is not mentioned in the datasheet but with the given size it is comparable or less than the motor's rotor inertia.

$$J_G \sim J_m \quad (5.12)$$

The inertia of the gearbox can be neglected as it is 10^6 times lower in magnitude compared to the load's (solar array's) inertia.

$$J_L \gg J_m, J_G \Rightarrow 3.33 \times 10^{-3} \text{ kgm}^2 \gg 0.5 \times 10^{-9} \text{ kgm}^2 \quad (5.13)$$

The load inertia now reduces to:

$$J_l = \frac{J_E}{GR_i^2} \quad (5.14)$$

Substituting the above load inertia equation (5.14) in the optimum gear ratio equation (5.9), we get:

$$GR_{opt} = \sqrt{\frac{J_E}{GR_i^2 \times J_m}} \quad (5.15)$$

For the current application, the solar arrays can be rotated along two axes as discussed and calculated in Table (4.3). The optimum gear ratio equation for the two axes (x and y) of rotation is as shown below:

$$GR_{opt-x} = \sqrt{\frac{I_{xx}}{GR_i^2 J_m}} \quad (5.16)$$

$$GR_{opt-y} = \sqrt{\frac{I_{yy}}{GR_i^2 J_m}} \quad (5.17)$$

The optimum external gear ratio required for each case of the gearbox ratios available with the motor (A.12) was calculated for the x and y-axis of rotation. The final optimum gear ratio for each internal gearbox option was calculated as the average of the gear ratios required in the x and y rotation axis cases. This result is summarised in the table (5.6) below:

S No	Internal gearbox ratio options	Optimum external gear ratio required to reach unit Inertia ratio in x-axis & y-axis	Optimum external gear ratio
1	4	3453 and 645	1899
2	16	863 and 161	512
3	64	215 and 40	127
4	256	53 and 10	31
5	1024	13 and 2	7.5
6	4096	3.3 and 0.6	1.95

Table 5.6: Optimum external gear ratio for different internal gearbox ratios and axis of rotation

Rotational speed matching

To match the rotary actuator's output to the gear, the maximum required rotational rate of the solar panels is matched to the mid-point of the operation range of the stepper motor. The mid-point of operation limit was chosen because, at the maximum RPM point of the stepper motor, the torque diminishes to zero, but the current application requires maximum torque during the maximum RPM operation. Whereas, at the beginning of the stepper motor's torque-speed curve, the torque is maximum. But a low RPM point on the motor's torque-speed curve was not chosen because as shown in the graph (5.8a), the initial phase has a lot of torque irregularities. This may be due to the static friction of the motor's bearings. It would not be ideal to operate the motor in such a regime, considering the smoothness of operation desired. The low RPM point was also not chosen because it gives a very small envelope over the curve to map the motor's output to match the solar panel's torque-speed requirement. Furthermore, if a point on the actuator's torque-speed curve corresponding to a lower RPM was chosen to size the gear, then all the different operating speeds of the solar panel have to be matched to the actuator's torque-speed profile starting from 0 RPM to that low RPM point. The mid-point on the motor's torque-speed curve roughly corresponds to a RPM of 5250 and a torque of 0.1172 mNm. The maximum speed required by the solar arrays was calculated to be 0.04 rad/s as summarised in Table (4.7). These rotational speeds will be matched to each other using the gear ratio formula below:

$$GR = \frac{\omega_1}{\omega_2} = \frac{N_1}{N_2} = \frac{T_2}{T_1} = \frac{d_2}{d_1} = \frac{z_2}{z_1} \quad (5.18)$$

On calculating the gear ratio for the rotational speeds of the motor and the solar arrays:

$$\frac{\omega_1}{\omega_2} = \frac{5250 \times \frac{2\pi}{60}}{0.04 \times 2} = 13745 \quad (5.19)$$

$$GR_{opt-2} = 13745 \quad (5.20)$$

The above value of gear ratio is large, therefore multiple gears have to be combined to achieve this gear ratio. The motor already has compatible gearboxes with different gear ratios ranging from 4 to 4096 (A.12). The value of gear ratio required for an external gear for different options of motor's gearbox to attain the calculated gear ratio of 13745 was calculated and the results are presented in Table (5.7).

S No	Internal gearbox ratio options	Total external gear ratio required	Optimum gear ratio of additional external gear
1	4	13745	3436
2	16	13745	859
3	64	13745	215
4	256	13745	54
5	1024	13745	14
6	4096	13745	3

Table 5.7: Optimum external gear ratios required for different internal gearbox ratios for rotational speed matching

The amplification in torque for the calculated total gear ratio can be calculated as:

$$Gr = \frac{T_2}{T_1} = \frac{T_2}{0.1172} = 13745 \Rightarrow T_2 = 1.61 Nm \quad (5.21)$$

The calculated torque is very well over the maximum torque requirement calculated for the solar arrays which was 3.816 mNm.

Maximum power point matching

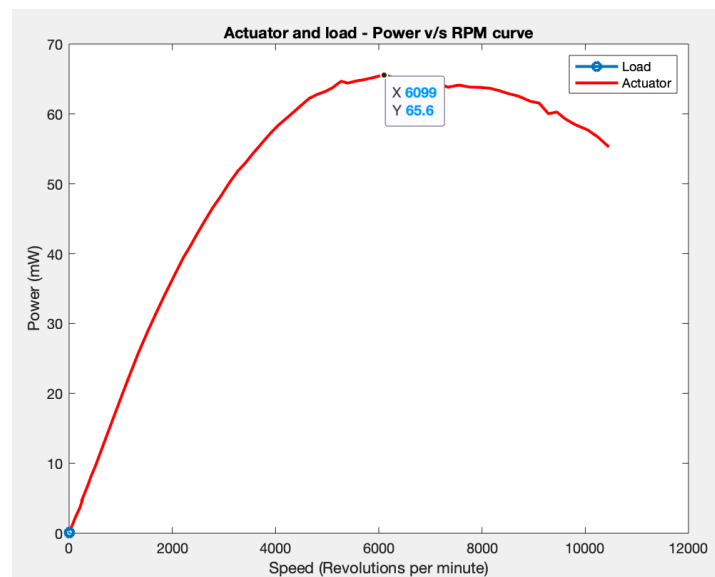


Figure 5.12: Power versus RPM curve of the actuator

As shown in the figure (5.12) above, the actuator delivers maximum power at a point close to the mid-point of the curve. This point corresponds to a RPM of 6100 and a power output of 65.6 mW. The solar array's

maximum power demand point, as summarized in table (4.7) can be matched to this point so that the power transfer is efficient. The maximum power point of the actuator also corresponds to the maximum efficiency point of the motor. The solar array's maximum power demand point corresponds to a RPM of 0.04 and the power demand at this point corresponds to 0.153 mW. If the gear ratio were to be calculated for this case, to step down the speed of the motor to that required by the solar panel during its maximum power point demand, we get the gear ratio as calculated below:

$$\frac{\omega_1}{\omega_2} = \frac{6100 \times \frac{2\pi}{60}}{0.04} = 15970 \quad (5.22)$$

Similar to the previous cases, the above gear ratio value is large. Therefore, multiple gears have to be combined to achieve this gear ratio. The value of gear ratio required for an external gear for different options of the motor's gearbox to attain the calculated gear ratio of 15970 was calculated and the results are presented in Table (5.7).

S No	Motor gearbox ratio options	Total external gear ratio required	Optimum gear ratio of additional external gear
1	4	15970	3992
2	16	15970	998
3	64	15970	250
4	256	15970	62
5	1024	15970	16
6	4096	15970	4

Table 5.8: Optimum external gear ratios required for different internal gearbox ratios for maximum power point matching

Considering the low mechanical power requirement of 0.153 mW, it is not crucial to optimise for efficient power transfer but the optimum gear ratio calculated for rotational matching is very similar in magnitude to optimum gear ratio calculated for maximum power transfer. Both of these gear ratios are very high in the order of 10^4 . The optimum gear ratio calculated for inertia matching is also in the same order of magnitude. With such high gear ratios, the mechanical power transfer efficiency drops as the power transfer efficiency is indirectly proportional to gear ratio. This behaviour is caused due to the friction involved in achieving such high gear ratios. In such a case, where the efficiency drops, it is desirable to consider optimising for maximum power transfer.

Summary of gear ratio calculation

The optimum gear ratios considering inertia matching, maximum rotational speed matching, maximum power transfer and efficiency matching were carried out. Each of these cases had an optimum gear ratio which was almost comparable in value. In order to have a gear ratio value optimal for this application, an average of the three gear ratio values will be taken and considered for the next step in gear selection. The average gear ratio value of the three cases is taken to attain a gear ratio close to the optimal value for all three cases. This can be considered as the global optimum gear ratio for the application. This averaged value of the gear ratio is presented in the table (5.9).

Motor gearbox ratio options (GR_i)	Optimum gear ratio for inertia matching	Optimum gear ratio for rotational speed matching	Optimum gear ratio for maximum power point matching	Average optimal gear ratio ($GR_{opt-avg}$)	Total optimal gear ratio ($= GR_i \times GR_{opt-avg}$)
4	1899	3436	3992	3109	12436
16	512	859	998	790	12640
64	127	215	250	197	12608
256	31	54	62	49	12544
1024	7.5	7.5	16	12.5	12800
4096	2	2	4	3	12288

Table 5.9: Optimal gear ratio

It is important to note that the total gear ratio required is almost constant, which is approximately around 12522 (with a maximum deviation from central of ± 278) for all the cases, it is only the motor's gearbox ratio,

and the external gear ratio required that changes to meet this total gear ratio. For the minimum optimal gear ratio of 12288 and mid-point operation of the rotary actuator (RPM = 5250, Torque = 0.1172 mNm), the amplification in torque can be calculated as:

$$Gr = \frac{T_2}{T_1} = \frac{T_2}{0.1172} = 12288 \implies T_2 = 1.44 Nm \quad (5.23)$$

The calculated torque is well over the maximum torque requirement calculated for the solar arrays, which was 3.816 mNm. This shows that the motor with a gearbox combination is capable of providing more than adequate torque than what the application requires as opposed to just using the motor.

5.3.5. External gear design

Now that the optimal gear ratio required for the application is known, the next step would be to find the right gear type that matches this gear ratio and the system's design requirements and constraints. To achieve this goal, the gear types would be explored and then traded off based on their applicability to the requirements.

External gear design options

Gears can be classified based on the arrangement of their axes as parallel, intersecting, non-intersecting and other gears. Parallel, intersecting, and non-intersecting axes gears are suggestive of their names and relates to their arrangement of axes. The category of other gears is used for special purposes like timing and profile generation. The classification of the gears is shown in the figure (5.13) below:

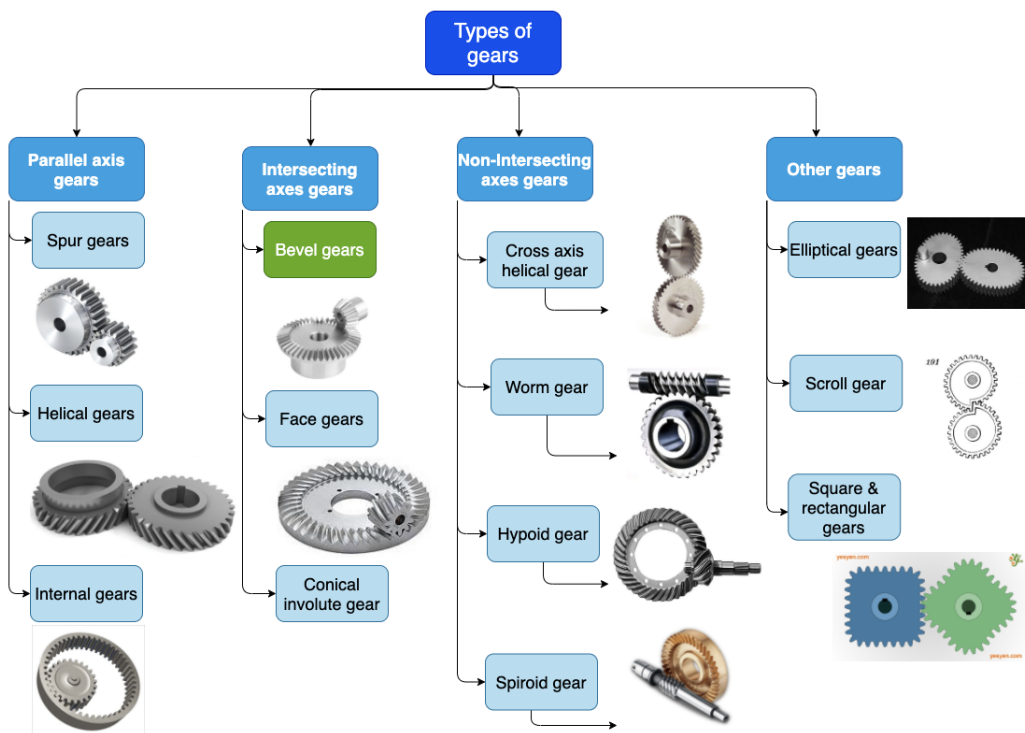


Figure 5.13: Gear design options

A brief description of each gear type is given below:

- **Spur gears:** They have teeth parallel to the axis of rotation.
- **Helical gears:** They have teeth inclined to the axis of rotation. The inclined teeth make them less noisy because of the gradual engagement and disengagement of the teeth.
- **Internal gears:** They are spur gears or helical gears with teeth on the inside rather than the external surface.

- **Bevel gears:** They have teeth formed on conical surfaces and are used for transmitting motion between intersecting shafts. they also have a variation where the teeth form a circular arc and are called as spiral bevel gears
- **Face gears:** face gears are also used to transmit motion between intersecting shafts, but unlike bevel gears, their teeth are formed on cylindrical surfaces.
- **Cross-axis helical gears:** They have inclined teeth & transfer motion between non-intersecting shafts.
- **Worm gear:** Worm gears use a screw-like element called the worm, which engages with a circular gear with mating teeth called the worm wheel. They are made so that one gear's teeth partially wrap around the other. Based on the direction of the thread, they are further classified as right-handed or left-handed. They can achieve higher gear ratios in a compact space than other gears and have self-locking properties. This means the gear cannot drive the pinion due to high resistance torque caused by friction of the teeth in the reverse direction.
- **Hypoid gear:** These gears are similar to spiral bevel gears in terms of the teeth profile, except that their axes are non-intersecting and offset with respect to each other.
- **Spiroid gear:** Spiroid gear combines worm as a pinion and hypoid gear as the driven gear.

External gear type trade-off & selection

In this sub-section, the gear types among those that were described in the previous sub-section will be traded-off and the most suitable one will be selected. There are three main criteria for selecting the gear type suitable for an application:

1. **Gear ratio:** Six options of gear ratios based on the gear ratios of the motor's gearbox and the optimum conditions of maximum power transfer, rotational speed matching and inertia matching were arrived upon in the previous sub-section (5.3.4) and summarized in Table (5.15).
2. **Dimensional constraints:** The dimensional constraints required for this application were defined in section (3.2), where the housing had a height limit of 6.9 mm including the shielding.
3. **Axes arrangement suitable for design:** As gears are classified based on their relative position, the arrangement axes preferable for the design is very crucial in selecting the right type of gear for the application.

Each of the gear types described in the earlier section (5.3.5) have a useful gear ratio range within which they are applicable, this is summarized in table (5.10).

Gear type	Ratio range	Efficiency (%)
Spur	1 to 6	98-99
Helical	1 to 10	98-99
Bevel	1.5 to 5	93-97
Worm	5 to 75	98-99
Crossed helical	1 to 6	-
Hypoid	10 to 200	80-95
Spiroid	10 to 400	-

Table 5.10: Gear types and their useful gear ratio range[111, 192]

The motor's gearbox gear ratio options and the corresponding external gear ratio required was calculated in Table (5.9). The table (5.11) below lists these options and graphically depicts the trade-off performed. The options that have been eliminated are in red and the selected option is highlighted in green. Each option's suitability for the requirements will be detailed in this sub-section.

S No	Motor gearbox ratio options	Average optimal gear ratio	Applicable gear type	Total optimal gear ratio
1	4	3109	None	12436
2	16	790	None	12640
3	64	197	Spiroid, Hypoid, Worm	12608
4	256	49	Spiroid, Hypoid, Worm	12544
5	1024	12.5	Spiroid, Hypoid, Worm	12800
6	4096	3	All parallel and intersecting axes gears	12288

Table 5.11: Optimal gear ratio

- **Gear ratios greater than 400:** Based on the useful range of the gears listed in table (5.10), it can be said that a gear ratio of more than 400 cannot be attained with a single gear. Therefore, the options of using a motor gearbox with ratios 4 and 16 corresponding to a single-stage external gear with a gear ratio of 3109 and 790, respectively are not feasible. This leaves gear ratio combination options 3, 4, 5 and 6 with external gear ratios of 197, 49, 12.5 and 3, respectively, for the trade-off.
- **Non-intersecting axes gears:** Four types of gears fall under the category of non-intersecting gears - Worm, spiroid, hypoid and cross-axis helical gears. These gears have an advantage over the other gear families as they can provide a high gear ratio with just one gear. These gears are suitable for gear ratio combination options 3 and 4 that require a gear ratio of 197 and 49, respectively. But, this gear family is unsuitable for this application for the reasons stated below.

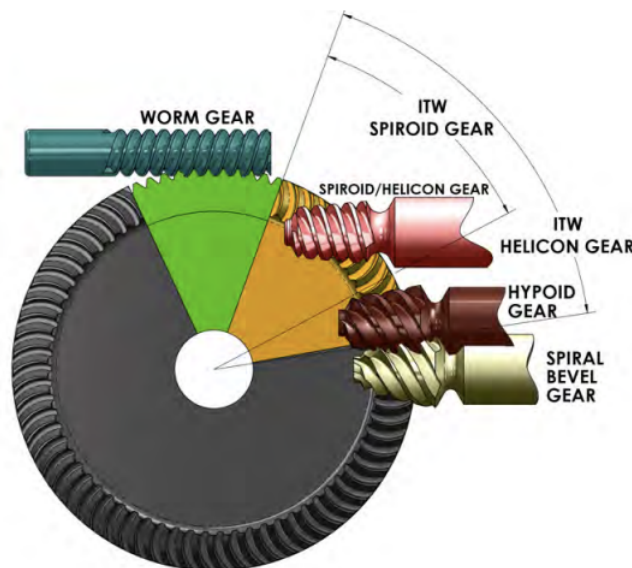


Figure 5.14: Non-intersecting axis gear configurations[89]

- **Spiroid and hypoid gears:** The spiroid and hypoid gears have the advantage of applying to a wide range of gear ratios from 10 up to 200 as shown in table (5.10). This makes these type of gears a good match for option 3 in Table (5.11), where a gear ratio of close to 200 is required from the external gear. As a rule of thumb, the gear ratio is directly proportional to the ratio of the number of teeth on the pinion and the gear. This means that around 200 teeth would have to be fit on gear to achieve a gear ratio of 200, this would be dimensionally incompatible. Moreover, commercially available spiroid and hypoid gears have a beginning diameter of 38 mm [73]. As these gears are non-intersecting, they would have to be placed in a non-intersecting manner, which means that they would be non-planar and would thereby violate requirement SADM-DES-004.
- **Worm gear:** Worm gears are applicable for the gear combination options 4 and 5, which requires an external gear with ratio 49 and 12.5 respectively. The worm gears are applicable for a gear ratio range of 5 to 75 as shown in Table (5.10). But they are non-intersecting axes gears, meaning

they have to be placed perpendicular to each other. There are multiple ways in which this can be achieved, as shown in Figure (5.15) below. By keeping the gears in two orthogonal planes of the CubeSat, the SADM housing becomes L-shaped to house the gears. This would result in the housing taking up the volume available for the solar panels on the sides. This was restricted by AAC Hyperion's design requirement according to design requirement SADM-DES-004. Therefore, the worm gears are eliminated from consideration in this application.

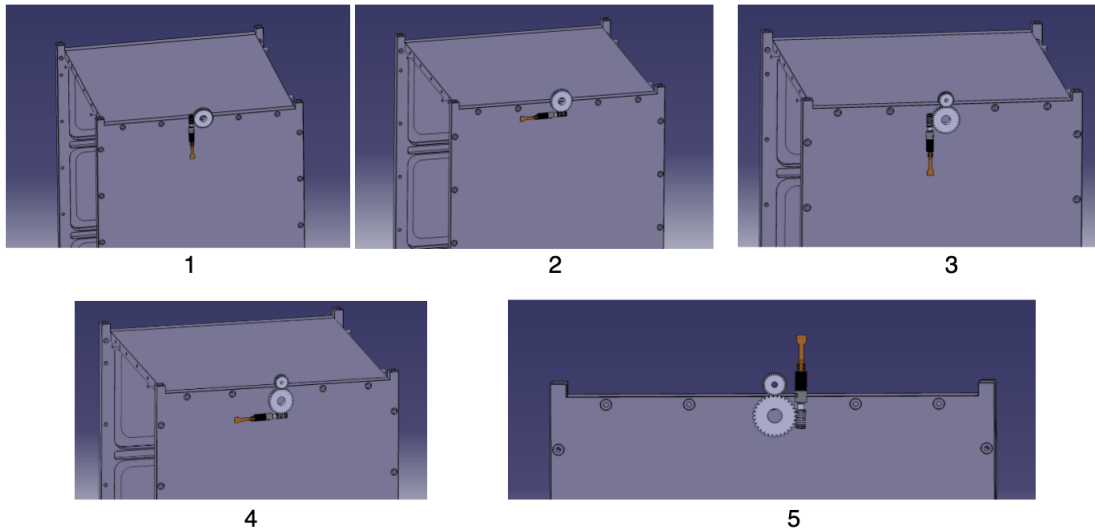


Figure 5.15: Worm gear configurations

- **Cross-axis helical gear:** Cross gears also belonging to the family of non-intersecting gears have to be placed orthogonally to function as intended, which would lead to the same drawback and will hinder the same design requirements as discussed for worm gears. Therefore, this gear will also be excluded from consideration. This leaves only gear combination option 6, which requires an external gear ratio of 3.
- **Other gears:** These gears are used for special purposes like timing and profile generation or path following. This application does not require any such special requirements. Therefore, this family of gears are not suitable for this application.
- **Parallel axis gears:** The only gear combination option that remains now is option 6, which requires an external gear ratio of 3. The family of parallel axes gears is unsuitable for this application because it elongates the housing along one dimension, as shown in Figure (5.16). This makes the housing extend the design dimension limit of 83 x 83 x 6.9 mm as defined in section (3.2). It is important to note that parallel axis gears can be combined together in the form of epicyclic or other compound gear trains to reach any external gear ratio. But this is being implemented within the gearbox of the motor. Implementing a compound gear to reach a gear ratio is not attractive for this application as it will increase the number of components that are hard to assemble and unnecessary. The other main use of the external gear in this case, apart from reaching the optimal gear ratio, is to prevent the launch loads from directly acting on the motor shaft.

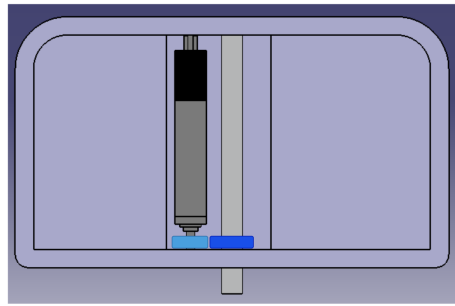


Figure 5.16: Motor with parallel axis gear

Therefore, the only remaining option now is the intersecting axes gear and especially the bevel gear. This gear will be used to design the external gear for a gear ratio of 3 as computed in Table 5.9.

External gear sizing

The bevel gear has to be sized for a gear ratio of three. The first step to sizing the gears is to fixate on the pitch circle diameters corresponding to the gear ratio as expressed in the equation 5.24 below. Where, d_1 denotes the pitch circle diameter of the driver or pinion gear and d_2 denotes the pitch circle diameter of the driven gear.

$$GR = \frac{d_2}{d_1} \quad (5.24)$$

A pitch diameter of 1mm would be too small to fabricate, a pitch diameter of the pinion is taken as 2mm which would lead to driven gear pitch diameter of 6mm for a gear ratio of 3 as per equation 5.24 which is below the housing height limit of 6.5mm. A pitch circle diameter increment of 0.5 mm in the pinion gear would lead to driven gear pitch diameter (7.5mm) to exceed the height limit. So, the pitch circle diameters of the driver and the driven gear are fixed to 2 mm and 6 mm respectively. The next step is to fix the number of teeth and match the modules of the gear. The relation between the gear ratio and the number of teeth are expressed using equation below:

$$GR = \frac{T_2}{T_1} \quad (5.25)$$

A minimum of six pinion teeth is required to ensure a circular profile and even inter-meshing of the gears. For a gear ratio of 3, this would lead to 18 teeth on the driven gear. The module for both these gears is given by the equation below. The module is 0.3 for both the gears, thereby matching them to inter mesh.

$$m = \frac{d}{T} \quad (5.26)$$

The gear geometrical parameters are calculated using the equations in Table A.15, the values calculated using the formulas are stated in the Table 5.12 below. This gives the geometric parameters of the gear for the required gear ratio of 3 and pitch circle diameters.

Gear parameter	Value for pinion	Value for driven gear
Shaft angle		90 degrees
Pressure angle		20 degrees
Number of teeth	6	18
Cone distance		2.85 mm
Tooth width		0.95 mm
Addendum		0.3 mm
Dedendum		0.375 mm
Tooth height		0.675 mm
Tip diameter	2.37 mm	5.59 mm

Table 5.12: Gear parameters for pinion and driven gears

Material selection

Gears can be made of two types of materials - metals or plastics. The most commonly used metals for gears are bronze because of their high surface hardness properties and corrosion resistance. Both metals and plastics have their advantages and disadvantages. The SADM has some special requirements. The SADM has to survive launch environment where there are vibrations as defined in SADM-ENV-007 that are transmitted from the stowed solar arrays to the shaft and eventually to the gears. Metal gears undergo plastic deformation under vibration loads but plastics are good at absorbing such vibration loads and therefore their lifetime is longer. Plastics are much durable to wear as compared to metals. Moreover, plastics have much lower elastic modulus as compared with metals this means that they will undergo lower deformation than metals. This again means that plastics will have a longer life due to reduced deformation. Metals require lubricants applied on their surface to ensure smooth rotation, whereas plastics can rotate without lubricants. Lubricants applied to rotating plastic surfaces can definitely reduce friction and decrease wear, but considering the high surface smoothness of plastics, this is not absolutely necessary. Considering the requirements of the current application to survive launch vibration loads and to prevent usage of lubricants, plastics will be considered for the gear material and metals will not be considered further.

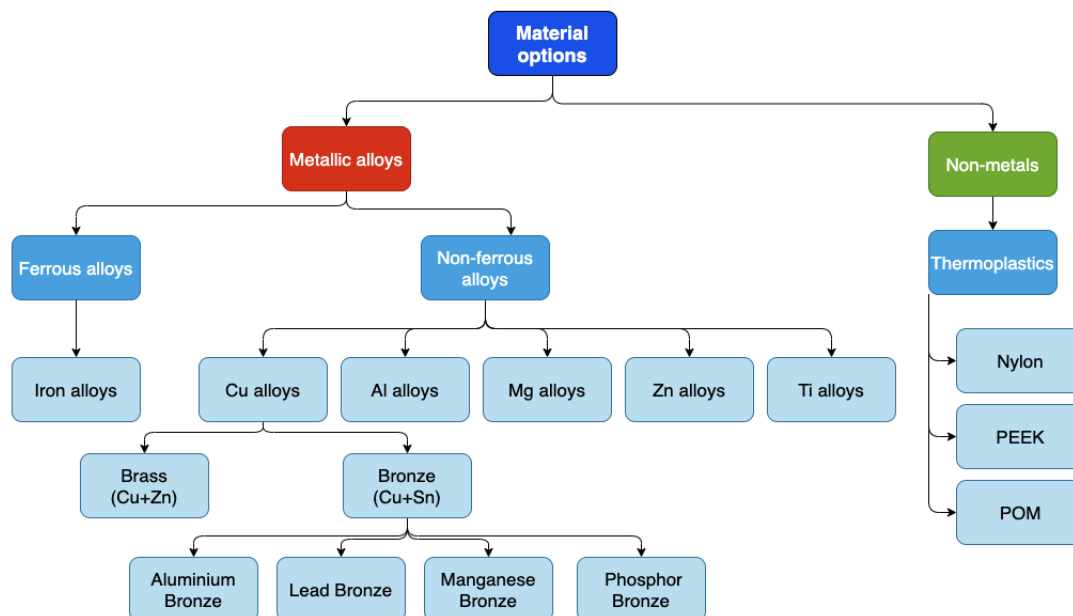


Figure 5.17: Gear material options

Among plastics, common materials used for gear fabrication include Nylon, Poly Ethyl Ether Ketone (PEEK) & Polyoxymethylene (POM). The most suitable material among these three options are selected by considering tensile strength, melting point, co-efficient of thermal expansion and surface hardness as measured by Rockwell Hardness-D testing standard. It is desirable to have the gear material with high surface hardness so that the shock and vibration loads do not create dents on the surface. Low co-efficient of thermal expansion is desirable because the thermal loads will cause warping of the material and would lead to unwanted behaviour such as change in clearance between the teeth. The melting point of 125 degrees was chosen considering the maximum operation temperature as defined in SADM-ENV-003. All the three plastic materials seemed to adequately meet this requirement of melting point. Maximum tensile strength is required from the gear material because it must withstand the stress caused by bending at the root of the teeth. Considering these trade-off criteria, the parameter meeting the requirement is highlighted in green.

Material	Tensile strength ultimate (N/mm ²)	Melting point (C)	Avg Co-efficient of thermal expansion ($\mu\text{m/mC}$)	Rockwell Hardness Shore-D
Requirement	Max	>125 C	Min	Max
Cast Nylon [88]	75.3	220	82.2	81.1
Unreinforced PEEK [84]	99.5	340	115	85.6
Unreinforced POM [85]	56.6	167	108	81

Table 5.13: Material selection for gears

As highlighted in the trade-off table above, **unreinforced PEEK** met most of the trade-off criteria and has been selected as the material of choice for the gears.

5.3.6. Summary

A motor gear box with a gear ratio of 4096 and an external bevel gear with a gear ratio of 3 was designed to optimise the gear for inertia matching, torque amplification and maximum power transfer. The bevel gear will be placed at 90 degrees with respect to each other and will be fabricated out of PEEK material considering shock absorption, elimination of lubricants and low wear compared to metals.

5.4. Interface selection & sizing

Interfaces form an important aspect of any system as they allow it to interact by exchanging data, transferring mechanical load or electrical power with other systems. In this section, the interfaces pertaining to the SADM will be designed and selected. For this purpose, firstly, the different types of interfaces required by the SADM are discovered in sub-section 5.4.1. The specifications for these interfaces are translated from the system requirements in section 5.4.2. The interface sizing and selection are carried out based on these requirements. Three kinds of interfaces were found to be required by the SADM - mechanical, electrical and data. The mechanical interface for the SADM is sized and selected in section 5.4.3 followed by the selection of data and electrical interface for the SADM in section 5.4.4. The chapter culminates with a brief summary of the highlights in section 5.4.5.

5.4.1. Purpose

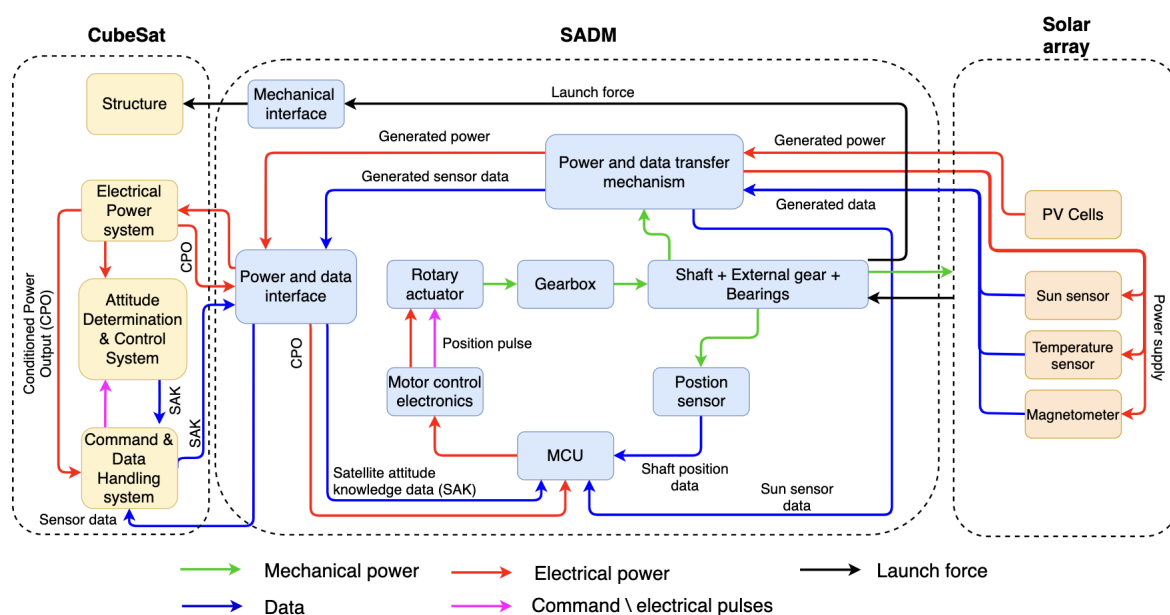


Figure 5.18: System interface diagram

The SADM is a sub-system made of multiple elements. The SADM can work only if the elements are in place and can communicate with each other. Similarly, the CubeSat can work properly only if its systems can communicate. The SADM is also connected to other systems of the CubeSat and is dependent on them for its functioning. The SADM transfers the power generated by the solar panels to the EPS of the CubeSat, which distributes the power to the satellite's systems; without the electrical power, none of the other systems of the satellite can work. The SADM is also connected to the Command and Data Handling (CDH) of the CubeSat and is dependent on it for commands and data like the satellite's orientation, for example. Interfaces are those components that allow these elements to transfer power and data between each other and also ensure they are held together in place throughout the satellite's lifetime.

Based on their function, interfaces can be classified into three types - mechanical, electrical and data. Mechanical interfaces ensure the components are mechanically constrained and fixed to be held in place during launch and operation. Electrical interfaces allow the electrical power to be transferred from one component or sub-system to another. Data interfaces allow data transfer between components.

Mechanical interfaces are required to fasten and mechanically constrain the SADM to the CubeSat structure. The mechanical interfaces are also required to maintain the position of the elements of the SADM within its housing. These are usually fasteners.

The SADM needs electrical interfaces to transfer the power generated by the solar panels to the EPS. It also needs electrical interfaces to receive input power to operate its motor and circuits from the EPS. The SADM also needs data interfaces to transfer the data generated by the panel-mounted sensors, position sensor and control circuits from the SADM to the satellite's CDH. The SADM also receives data like the satellite's position

data from other CubeSat systems like the ADCS. The electrical and data interfaces are not two separate types of components but rather part of a single component. This is because data is also transferred in electrical pulses where an electrical pulse corresponds to a digital one, and an absence of an electrical pulse is a digital zero. The electrical and data interface component are usually a COTS connector.

It was found in section (2.3.2) that interfaces were one of the main causes of anomalies in space missions after tribological sources. As stated below, a research question 2d was formulated pertinent to interfaces.

" How to design (size & select) interfaces that can survive the environmental loads and be reliable throughout its lifetime? "

This section will answer this research question systematically by translating the system requirements to the interface components, followed by selecting and sizing the interfaces that meet these requirements.

5.4.2. Requirements

The SADM needs two power and data interfaces, one to connect itself with the goose-wrap's FPC and the other to transfer this power to the EPS this is stated in SADM-IF-002 & SADM-IF-001 respectively. And both of these interfaces must comply with the current and voltage values calculated in section (4.3.2) and defined for the PDTM. This has been translated to the power interface as stated in the requirements SADM-IF-004 to SADM-IF-006. The interfaces were required to be attachable and detachable as stated in SADM-IF-003 to make assembly and troubleshooting easy. As discussed in the previous sub-section, the SADM needs mechanical interfaces to fix itself to the CubeSat structure as defined in SADM-IF-008.

Identifier	Requirement	Parent requirement
SADM-IF-001	The system shall have a power and data transfer interface to connect with the CubeSat mounted systems.	SADM-INT-004 & SADM-INT-005
SADM-IF-002	The system shall have a power and data transfer interface to connect with the goose-wrap FPC.	SADM-INT-004
SADM-IF-003	The system shall have interfaces that are detachable and re-attachable.	-
SADM-IF-004	The power transfer interface shall be capable of handling 2 lines of the maximum current of 1.7 A	SADM-PDTM-001 & SADM-INT-004
SADM-IF-005	The power transfer interface shall be capable of handling 4 lines of current of 1.2 A	SADM-PDTM-002 & SADM-INT-004
SADM-IF-006	The power transfer interface shall be capable of handling 6 lines of the maximum voltage of 97 V	SADM-PDTM-003 & SADM-INT-004
SADM-IF-007	The data transfer interface shall allow 15 lines that can handle 0.1A of the panel mounted sensors.	SADM-PDTM-004 & SADM-INT-005
SADM-IF-008	The system shall have a mechanical interface fixing the SADM to the CubeSat.	SADM-INT-003
SADM-IF-009	The interfaces shall be compatible with the environmental conditions.	SADM-ENV-001 to SADM-ENV-011

Table 5.14: Power and data transfer mechanism requirements

The next step is to size the mechanical interfaces and select the COTS electrical and data interfaces capable of meeting these requirements; this will be discussed in the forthcoming sub-sections.

5.4.3. Mechanical interface sizing

Mechanical interfaces are required to mount and fix the SADM to the CubeSat structure. There are multiple mechanical fastener options like rivets, screws, adhesives, pins, keys, welding, etc. The bolts are chosen as the fastener for this application as they are easily attachable and detachable as required by this application and stated in SADM-IF-003. Bolts work by engaging a spiral tooth form with a mating spiral cavity in the part required to be fixed. The bolt is driven into a nut with the mating spiral cavity to fix and tighten the bolt on the other end.

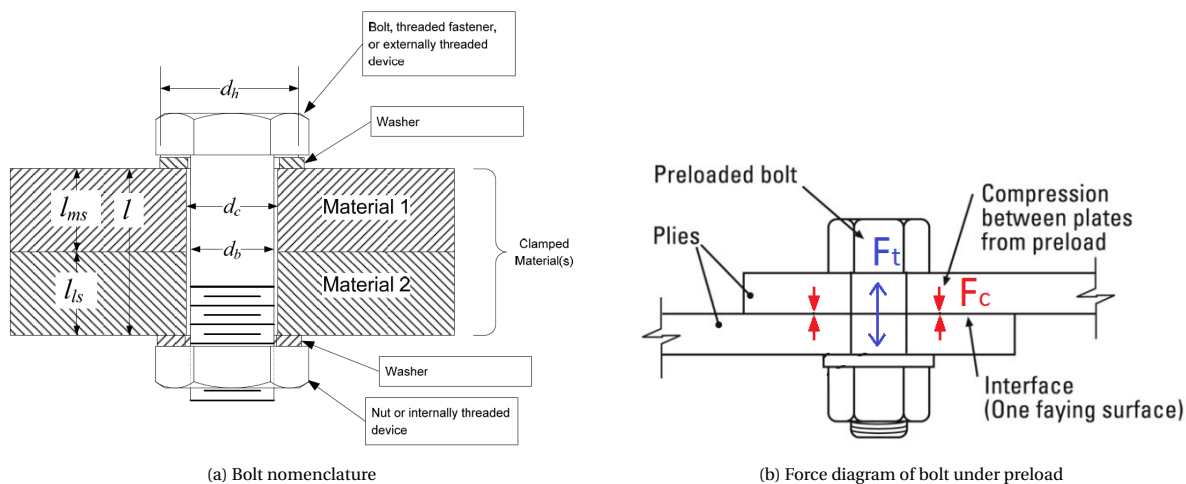


Figure 5.19: Nomenclature & forces of a bolt joint

The effective working of a bolt is defined based on three criteria as defined by NASA [110]:

1. Bolt and joint must have adequate strength.
2. Joint must not experience separation under loading.
3. Bolt must have adequate fracture and fatigue life.

There are four steps involved in sizing the bolts for an application as defined by ECSS standards [72]:

1. **Define loads:** To meet the effective working criteria, the first step to sizing bolts is to define the loads acting on them, both mechanical and thermal.
2. **Compute preload by considering safety margins & failure modes:** The next step is to define the size and preload of the bolt. Bolts are usually pre-loaded such that they are in tension, and the materials under union are under compression force, as shown in Figure (5.19b). The bolt is said to be failed when the materials under union can move relatively, as stated by the second criterion. This would violate the bolt's purpose, which occurs when the bolt's preload is lost. The bolt under preload takes up the external force applied; if the launch-induced forces exceed the bolt's preload, it fails. Therefore, the main criteria to size the bolt is to define the preload in such a way that it is less than the launch-induced force acting on the bolt and also to make sure that the stress induced in the bolt due to preload is lower than the material's tensile strength. The bolt can also expand or contract and change internal stress with strain caused by the change in temperature. It is important to also consider this effect will sizing the bolt. This way, the first and second working criteria are met by the bolt. The third criterion for sizing the bolt is considering the fracture and fatigue life caused by dynamic (magnitude varying with time) and cyclic loads. The spacecraft experiences dynamic loads only during launch, usually for a few minutes. The dynamic load acting for such a short period cannot cause significant fatigue loads on the bolts; therefore, this criterion can be neglected for the current application. Moreover, the dynamic launch load has been converted to static load and has been used to calculate the maximum launch force expected for this system in section 4.3.3.
3. **Take precaution against corrosion & define preload method:** The next step is to consider environmental factors like corrosion and take necessary precautions to mitigate them. This is followed by specifying the lubricant, if required and the preloading method.
4. **Quality control & testing:** Once the bolted joint has been sized and designed, the acceptable variations must be specified. The variations include process variations (surface finish, preload ,etc), material variations (strength, friction and corrosion) and dimensional tolerances. As a final step, based on the criticality of the joint, it can be tested for strength, fatigue or corrosion.

It was found that the maximum force on the system occurred during launch in all three directions on the shaft with a magnitude of 250N. The SADM being rectangular in shape requires a minimum of 3 fixation

points to constrain its motion in all six degrees of freedom. This would mean that the bolts are arranged in a triangular position relative to each other. This would result in one bolt overloaded than the other two in the front. This is because the load from the solar arrays is transferred to the shaft, which transmits the force to the bearings, which in turn will transmit the force to the SADM's housing; the housing has four edges on which it rests on the CubeSat structure and thereby transmits the launch force to the CubeSat structure via its bolts. If four edges were to transmit this force through three bolts, one of the bolts would transmit the load from three edges. If four bolts were utilised, each bolt would be in the load path of two edges. Thus, all of them will experience the same load distribution. Therefore, the author will consider four fixation points so that all the bolts are equally loaded by the four edges. The launch force of 250N will be split equally among these four bolts as calculated below. The bolt material preferred by AAC Hyperion was Stainless steel grade 304 [71], whose properties will be used in the calculations.

$$F_{bolt} = \frac{F_{launch}}{N_{bolts}} = \frac{250}{4} = 62.5N \quad (5.27)$$

The design condition for the bolt is that it should be capable of handling more preload force than the launch force, and the stress induced in the bolt due to preload should be lower than the tensile stress of the bolt material so that failure is avoided. This is expressed as shown below:

$$F_{preload} > F_{bolt} \quad \& \quad \sigma_{bolt} < \sigma_{tensile} \quad (5.28)$$

The stress induced in the bolt due to the preload force is expressed in the equation (5.29) below:

$$\sigma_{bolt} = \frac{F_{preload}}{\pi d^2 / 4} \quad (5.29)$$

The bolt manufacturer usually specifies the tightening torque, the preload force induced in the bolt of diameter (d) due to this torque on the bolt is expressed in the equation (5.30) below. k, is the nut factor that considers the part of the applied torque that goes into overcoming the friction in the threads and tensioning the bolt. The nut factor depends on the lubricant used and the bolt material, various such nut factors for different cases are mentioned in Figure (A.25). For the current application, an unlubricated steel fastener is considered; therefore, the nut factor used will be 0.2, as mentioned in the Figure (A.25).

$$\tau = kdF_{preload} \quad (5.30)$$

If the nut factor were to be expanded, the tightening torque consists of 3 components which include i) torque needed to stretch the bolt ii) the torque needed to overcome the friction of bolt threads & iii) torque needed to overcome the friction between nut & bearing surface. These terms correspond to the terms in the order they appear within the parentheses of the equation (5.31). A typical distribution of torque between these components is 10% for stretching the bolt; 30% of the torque is absorbed by the friction in threads, 50% of the friction is absorbed by friction under the head of the bolt or nut and 10% by the self-locking thread if such a nut is used.

$$\tau = F_{preload} \left(\frac{p}{2\pi} + \frac{\mu_t r_t}{\cos\beta} + \mu_n r_n \right) \quad (5.31)$$

The preload force and the stress induced in the bolt due to this preload force for different bolt sizes were calculated using equation (5.30) & (5.29) respectively and have been summarized in Table (5.15). The tightening torques were taken from the manufacturer's data sheet as mentioned in Figure (A.26).

Metric bolt specification	Launch load on each bolt (N)	Specified tightening torque (Nm)	Calculated preload for specified torque (N)	Stress due to preload (N/mm ²)	Tensile strength (N/mm ²)
M2	62.5	0.16	400	127.32	200
M3	62.5	0.6	1000	141.47	350
M4	62.5	1.1	1375	109.42	350
M5	62.5	5	5000	254.65	350

Table 5.15: Bolt preload for different sizes

As shown in the table (5.15) above, all the bolt sizes seem to meet the required design criteria of having more preload force than the launch force and having lower stress due to preload than the tensile stress. In

this case, the next factor considered was the tensile strength; the manufacturer had specified a lower tensile strength for the M2 bolt than the other bolt sizes. The reason is unknown, but a lower tensile strength is not favourable. Therefore, the next best option will be chosen, which is the M3 bolt. M3 bolts were found to be adequate to survive the launch loads. Therefore, **four M3 bolts will be used to fasten the SADM to the CubeSat structure.**

The next steps mentioned in the ESA standards [72] was to consider the corrosive environment and preloading method. Any space-compatible grease lubricants mentioned in [72] can be used if required to prevent corrosion and reduce friction in threads. The most commonly used preloading method is by using a torque wrench, but this method induces torsional stress within the bolt. The alternative is to use a hydraulic preloading method that does not induce torsional stress. The author leaves these choices up to AAC Hyperion based on their AIT requirements and tool availability.

5.4.4. Electrical & data interface selection

As shown in Figure (5.18), the SADM needs a power and data transfer interface that can transfer the power generated by the solar cells and the data measured by the sensors to the CubeSat mounted systems. The system also needed this power and data transfer interface to receive data from the CubeSat CDH and regulated power supply for the SADM from the EPS. Considering the tight dimensional constraints and weight saving desired, it is preferable to use one single connector that can serve as the power and data interface. But, it can be observed from the requirements for the interfaces (3.3) that the power and data interfaces have a profound distinction in terms of current, voltage and the number of lines required. The power interface requires two lines with a capability to handle 1.7 A, four lines that can handle 1.2 A and all six lines capable of handling a voltage of 97V. Whereas, on the other hand, the data interface requires 15 lines that can handle 0.1A current and voltage in the order of milli-volts. Apart from the power characteristics, the interfaces also had to comply with dimensional and environmental requirements. This meant a dimensional limit for the interface of less than 6.9 mm and environmental restrictions like no outgassing, capable of multiple mating and demating cycles, and operation over a temperature range of -65 to 125C. A market survey was conducted to find a single connector that can satisfy this broad range of power characteristics and data transfer requirements. Unfortunately, no such connector was found. Thus, two different interfaces were considered, one for transferring and receiving power with fewer pins and high voltage and current handling capability. A separate interface for transferring and receiving data with more pins but lower power handling capability. After a market survey of exploring various companies like TE Connectivity, Amphenol, Souriau-Sunbank and Omnetics, a brief specification of the two different interfaces that were selected for this application are summarized in Table (5.16) below:

Power interface	
Company & product	Omnetics - Micro-D Single row socket A92000-009 (A.27)
Number of pins	9
Current rating	3 A
Voltage rating	600 V
Temperature range	-55 to 125 C
Shock strength	50 G
Dimensions (l x b x h)	18.67 x 8.64 x 3.18 mm
Cost	304 €
Mating & de-mating cycles	2000
Data interface	
Company & product	Omnetics - Dual row Nano-D socket A29100-025 (A.28)
Number of pins	25
Current rating	1 A
Dimensions (l x b x h)	11.94 x 5.72 x 3.56 mm
Cost	190 €

Table 5.16: Selected power and data interface [67] [57]

The above two interfaces were most appropriate for this application's requirement as they met the dimensional, environmental, voltage and current requirements. Thereby satisfying requirements SADM-IF-001 to SADM-IF-009.

5.4.5. Summary

In this chapter, the mechanical, electrical and data interfaces required by the SADM was sized and selected so that the SADM can be fixed to the CubeSat structure, transfer, receive power and data from CubeSat mounted systems. Four stainless steel M3 bolts were chosen as the mechanical interface by sizing them considering preload and strength to withstand launch forces. A 25-pin nano-D connector [57] was chosen as the data interface between the SADM and the CubeSat mounted systems. A 9-pin micro-D connector [67] was chosen as the power interface. These interfaces were integrated with the CAD model of the SADM.

5.5. Power and data transfer mechanism design

In this section, the Power and Data Transfer Mechanism (PDTM) will be explored, selected and designed. Transferring power and data is one of the main functions of the SADM as described in earlier sections. In order to design this mechanism, firstly the purpose of the element and the flow of system level requirements to this element will be set down and the different design options will be explored. The best design option will be selected based on the option's suitability to the requirements. The selected technology will be sized and designed according to the current application's design requirements and constraints.

From the literature review it was found that the sliprings were the most conventional power and data transfer mechanism used in satellites. It was also found that this system had a lot of issues that caused them to malfunction and cause mission failures in many cases, as summarized in Table 2.3. The main cause of the slipring failures was due to their working mechanism that made use of brushes which wore down with operation and formed debris that caused sparking and short circuit [149]. Therefore, one research objective for this project was to find and design an alternative power and data transfer mechanism that can overcome the shortcomings of the conventional slip-ring. To achieve this objective, a research question 2c was formulated as stated below. Finding an answer to this question would be the main goal of this section.

"How to design a power & data transfer arrangement capable of transferring the maximum power and data with least degradation over its lifetime in such a way that it overcomes the shortcomings of conventional sliprings?"

5.5.1. Purpose

The power and data transfer mechanism is supposed to perform three main functions:

1. Allow relative rotational motion between the CubeSat and the solar panels.
2. Transfer the power generated by the solar panels to the CubeSat mounted Electrical Power System (EPS) with the least losses.
3. Transfer the data generated by the panel-mounted sensors to the CubeSat-mounted systems.

5.5.2. Requirements

The SADM requirements defined in Chapter 2 translate to this element as shown in Table 5.17. The maximum current and voltage to be transferred were calculated in section 4.3.2 and have been summarized in table 4.12. It was found that the solar panel connection configuration-2 had the maximum current transferred per line which was calculated to be 1.7 A and had two lines. The configuration that had the second most current per line was configuration-4 which was calculated to be 1.2A and had six individual lines. The other connection configurations had around 0.6 A current in two or six lines. Six power lines are required to make the SADM capable of applying to all the configurations. Where two lines are capable of carrying 1.7A and 4 of them are capable of handling 1.2A current. This is the rationale behind the requirement SADM-PDTM-001 and SADM-PDTM-002. It was also observed that the configuration-5 had the maximum voltage per line as 97 V and had six lines, this is the rationale behind the requirement SADM-PDTM-003. The system will be designed to transfer the data generated by three panel mounted sensors as stated in SADM-PDTM-004, because this is the usual number of sensors mounted on the solar panels as inferred from similar products [19]. The three common panel mounted sensors include temperature sensor [80, 86, 87], sun sensor [82, 90] and magnetometer [77]. Each of these sensors can contain a different number of lines (for example, thermocouples [87]) have only 2 lines, and some temperature sensors can require up to 10 pins [86] and a customer may not use all three sensors. Thus, to design the system to be compatible with all these different possible configurations, the five common lines for most sensors have been considered as the baseline requirement for each sensor. These five lines include the supply voltage, reference voltage, ground and two communication lines (Serial Clock Line & Serial Data Line or RS-485 +ve & RS-485 -ve) based on the communication protocol required by the customer. It was referred from the data sheets of these sensors that they require a maximum of 5V and a current in the order of a few micro-amperes. Thus a conductor capable of handling 0.1 A will be used so that it can handle the maximum current from these sensors and will not be too oversized.

Identifier	Requirement	Parent requirement
SADM-PDTM-001	The power & data transfer mechanism shall be capable of handling 2 lines of the maximum current of 1.7 A	SADM-FUN-003
SADM-PDTM-002	The power & data transfer mechanism shall be capable of handling 4 lines of current of 1.2 A	SADM-FUN-003
SADM-PDTM-003	The power & data transfer mechanism shall be capable of handling 6 lines of the maximum voltage of 97 V	SADM-FUN-003
SADM-PDTM-004	The power & data transfer mechanism shall allow 15 lines that can handle 0.1A of the panel mounted sensors.	SADM-FUN-004
SADM-PDTM-005	The power & data transfer mechanism shall allow relative motion between the satellite body and the solar panels in 1-DOF throughout 360 degrees.	SADM-FUN-001
SADM-PDTM-006	The power & data transfer mechanism shall be compatible with the environmental conditions.	SADM-ENV-001 to SADM-ENV-011
SADM-PDTM-007	The power & data transfer mechanism shall have a compatible interface with solar panels and the SADM's power distribution circuit.	SADM-INT-004
SADM-PDTM-008	The power & data transfer mechanism shall fit within the housing.	SADM-INT-005
SADM-PDTM-009	The power & data transfer mechanism shall have 29200 in-orbit duty cycles.	SADM-PER-003

Table 5.17: Power and data transfer mechanism requirements

5.5.3. Power & data transfer mechanism design options and trade-off

Now that the requirements and the research objectives for this mechanism have been set, the design options for power and data transfer will be explored in this sub-section and their suitability for this application based on the set requirements will be evaluated. There are six different kinds of power and data transfer design options as shown in Figure 5.20. Each of their working principle will be briefly detailed after the picture.

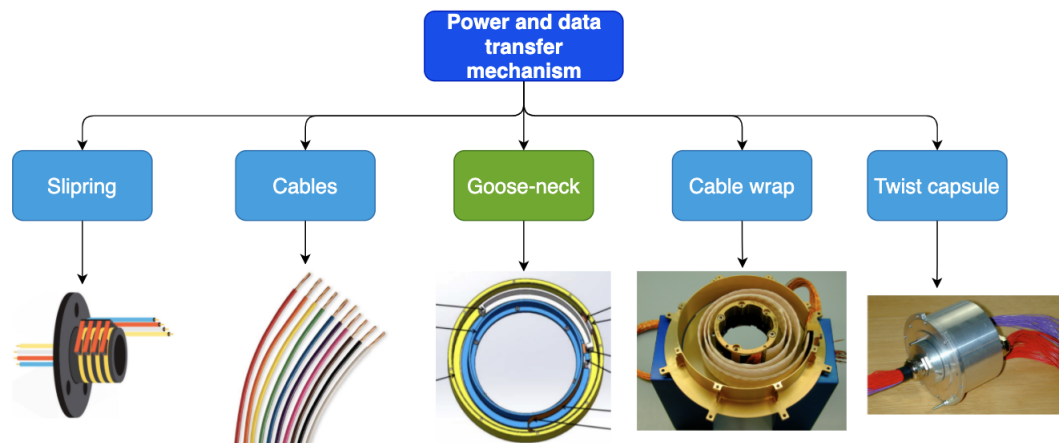


Figure 5.20: Power and data transfer mechanism design options

- Slip-rings:** Slip rings are the most conventionally used solution for transferring data and power between a rotating platform and a stationary platform in satellites. The system works based on a simple principle of electrical conduction, where the power and data from a rotating shaft is conducted to a stationary ring utilizing conducting brushes or sliding contacts. A stator assembly with conducting brush is made to be in contact with the rings. The power or data that was conducted to the ring by the rotor assembly is conducted to the stator assembly via the contacting brushes. They are commercially available in multiple types and sizes, making them a preferred design option for power transfer in rotating applications.
- Cables:** Cables, in general, are the most commonly used mode of power and data transfer. They have a simple construction of a cylindrical conductor core covered with an electrically insulating material. But, cables are used in stationary applications, where once they are connected, they remain fixed. If these cables were to be flexed continuously the insulator undergoes damage and exposes the conductor underneath which can lead to accidental short-circuit if these wires touch each other.
- Goose-neck:** This mechanism makes use of a Flexible Printed Circuit (FPC) instead of brushes to trans-

fer power and data between the stationary and rotating rings. The FPC is composed of thin layers of copper sandwiched between insulating layers using adhesives. The FPC is bent into an U-shape profile and fixed between the stator and the rotor, and as the rotor moves, the U-part also elastically deforms and moves along with it to allow relative rotational motion with respect to the stator. Meanwhile, the copper layer conducts electrical power and transmit data from the rotating to the non-rotating platform. They can be further subdivided into horizontal and vertical goose-neck configurations based on the orientation of the flexible circuit. This mechanism is designed to allow rotation of the rings only up to a limited rotation angle which is bound by the minimum bending radius of the FPC. The advantage of this mechanism is that it does not generate debris and it is very compact.

- **Cable wrap:** Cable wraps are an arrangement where ribbon-like or sheet-like flat cables are wound in a spiral manner (like a clock-spring) connecting a rotor and a stator. Due to the limited cable length and bending radius, the cable wraps only allow a limited rotation angle. Cable wraps are not only used in satellite power transfer applications but also in the steering wheels of millions of automobiles.
- **Twist capsule:** Twist capsules use flexible and pre-shaped wire bundles connected to the rotor and wound around the stator or shaft. The relative rotation causes the twisting of the cable and thus allows for the limited rotation of the rotor with respect to the shaft. As the rotation is facilitated by twisting the cables, the rotation capability of the twist capsule is limited.

Broad trade-off

The broad elimination of the design options is carried out by first reviewing the application requirements and comparing them with the functionality and purpose of the design option. The design option whose functionality does not meet the application's requirement is eliminated. This process is described below:

- **Cables:** They cannot be considered in this application because they are designed for use in stationary applications and the SADM requires relative motion as its basic function as stated in (SADM-PDTM-004). Moreover, if cables are repeatedly bent or twisted, they would undergo fatigue failure.
- **Slip-rings:** This option will not be considered in this application because they have considerable disadvantages like brush wear, debris generation, tribological interactions [116], arc generation, maintenance of optimal brush pressure, short-circuiting [164], heating, brush softening at high current densities [112] and gas breakdown at high voltages [97]. All these failure mechanisms lead to noise in the data transmitted and increased friction for rotation. Due to these disadvantages, many earlier missions such as the SeaSat [153] have failed. In spite of these disadvantages the slipring is a common solution because they are commercially available in various sizes and specifications. Utilising a ready-made power and data transfer mechanism reduces the design time and thereby makes them attractive for many terrestrial applications. The current SADM has strict volume requirements as defined in SADM-PDTM-008 (height < 6.9 mm) and a very special power transfer requirement than many usual applications in the sense that it needs two lines for transferring high current of 1.7 A and Considering the mechanism's reliability throughout its lifetime, slip-rings will not be considered for use in the current application.

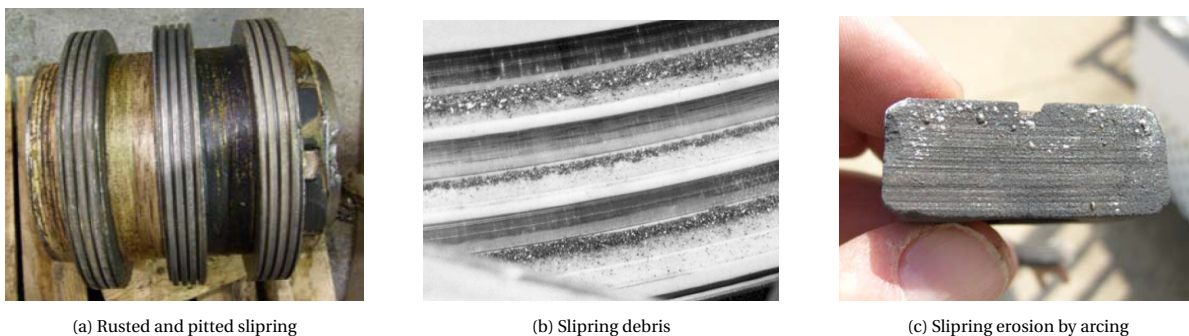


Figure 5.21: Failure mechanisms of sliprings [133]

- **Twist capsules:** This option is not suitable for this application because of multiple reasons.

- **Constraint of limited rotation:** Firstly, they only allow limited rotation constrained by the twisting capability of the wire. A simple first order calculation is carried out to find the torque requires and the resultant torsional stress in the wire when it is twisted by 180 degrees. To allow complete 360-degree accessibility, the conductor should be capable of rotating up to at least 180 degrees in either direction. The least current that the SADMM has to conduct is 0.1 A. A standard AWG 30 size wire is required to conduct a current of 0.1 A which corresponds to a conductor diameter of 0.255 mm [78]. The 0.1 A wire diameter is chosen for this calculation because of the least diameter this corresponds to. Wires are usually constructed by bundling smaller diameter wires to form a bigger one, therefore a wire that has to conduct 1.7 A will have a diameter of around 0.723 mm corresponding to a AWG 21 size wire composed of a bundle of smaller diameter wires. The diameter of these smaller wires are manufacturer dependent and not mentioned in data-sheets therefore the conductor diameter corresponding to carry 0.1 A is chosen to get an estimate for all the cases and the relation between wire diameter and stress. The first step is to calculate the polar moment of inertia of the wire:

$$J = \frac{\pi R^4}{2} = 4.15 \times 10^{-16} \text{ Nm}^4 \quad (5.32)$$

Nextly, the torque required to twist a wire of unit length (1m) by 180 degrees (π radians) is calculated:

$$T = \frac{\alpha L}{JG} = \frac{3.1416 \times 1}{4.15 \times 10^{-16} \times 4 \times 10^{10}} = 1.9 \times 10^5 \text{ Nm} \quad (5.33)$$

The torsional stress induced in the wire resulting from the 180 degree rotation is calculated as:

$$\tau = \frac{TR}{J} = \frac{1.9 \times 10^5 \times 0.1275 \times 10^{-3}}{4.15 \times 10^{-16}} = 5.8 \times 10^{16} \text{ N/m}^2 \quad (5.34)$$

As shown below, the torsional stress induced in the copper wire is more than the yield stress of copper ($3.33 \times 10^7 \text{ N/m}^2$). This would result in the inelastic deformation of the material and fatigue failure.

$$\tau > \sigma_y \longrightarrow 5.8 \times 10^{16} \text{ N/m}^2 > 3.33 \times 10^7 \text{ N/m}^2$$

Substituting the polar moment of inertia (5.32) and the torque equation 5.33 in to the torsional stress equation, we get a relation as shown below which shows that the torsional stress is inversely proportional to the 8th power of the wire's radius.

$$\tau = \frac{4\alpha L}{G\pi R^8} \quad (5.35)$$

It is possible that the individual strands of conductor used to build the individual wires are even smaller than 0.255 mm in diameter. In this case according to equation 5.35 the stress in wires will still be larger than the yield stress of Copper. It is possible to get a customised wire with higher flexibility but this will make procurement expensive, long and will hinder with the requirement to use COTS components as much as possible.

- **High resistive torque:** Also, the torque required to rotate the system would be very high as it would have to twist the cable resulting in storage of potential energy in the cable and releasing them during unfurling. This is also the cause non-linear behaviour of the wire with twist angle.
- **Applicable for higher diameter ratios:** This design option is also suitable for applications that have a diameter (outer to inner) ratio greater than unity [160]. This application requires a compact design that can fit within 6.9mm height.

Therefore, twist wires are not suitable for usage in this application.

The only remaining design options after the broad trade-off are the goose-neck and cable wrap that have a more or less similar working principle. These two design options would be compared and traded-off in the next sub-section.

5.5.4. Current carrier design options & trade-off

The cable wrap and the goose-neck are similar in terms of construction because they use a flat current carrier which coils and uncoils to allow rotation. The main difference between the two design options comes from the current carrier, a cable wrap uses a Flat Flexible Cable (FFC) whereas the goose-neck uses a FPC. The advantages & disadvantages of the two options are summarised in the table below. A FFC is multiple lines of wires with rectangular or circular cross-section in the form of a flat ribbon as shown in Figure (5.22a) and the FPC is a type of a flexible PCB where the copper is etched on to a flexible substrate that allows it to bend as shown in Figure (5.23b).

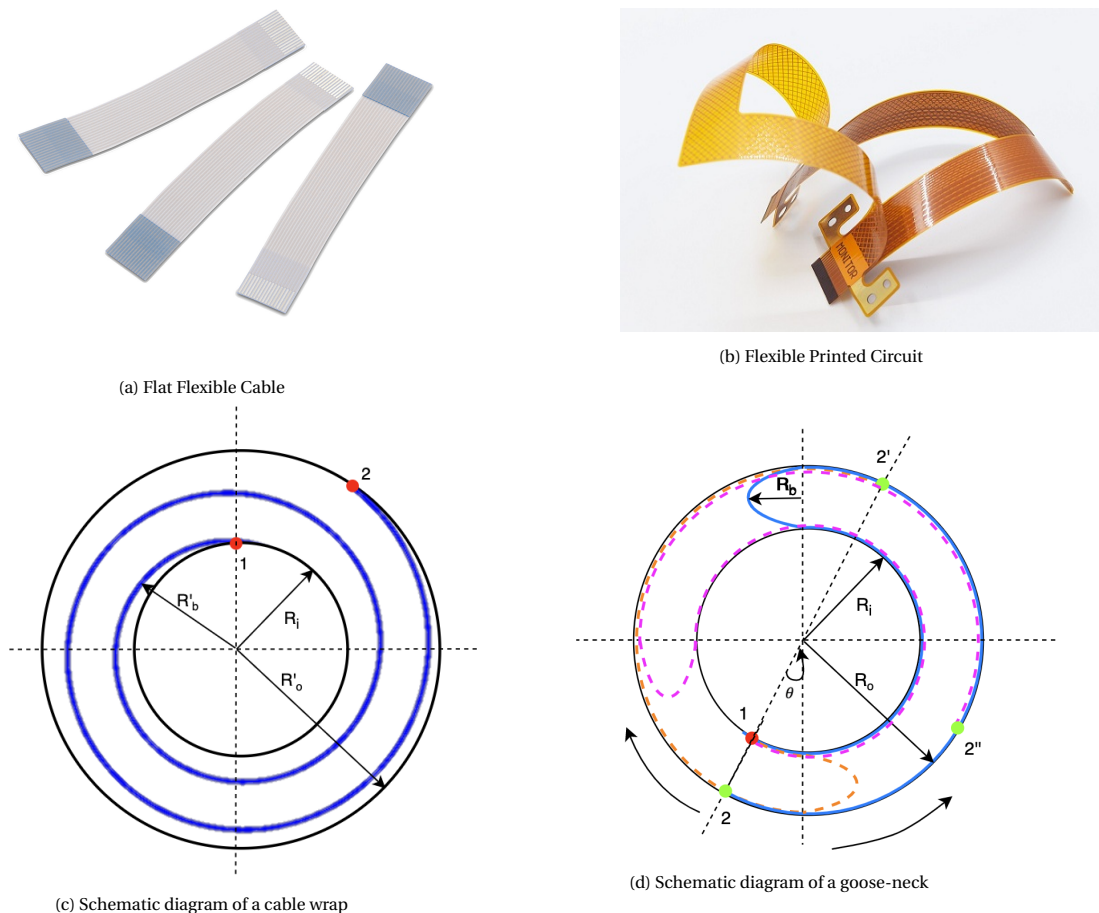


Figure 5.22: Conductor carrier options & the mechanisms they are used in

The cable wrap schematic is shown in the Figure (5.22c), the spiral in blue is the FFC and the points marked 1 and 2 are the attachment points. R_i is the radius of the shaft, R_o is the outer radius of the shaft and R_b is the bending radius of the cable. The goose-neck schematic is shown in the Figure (5.22d), where R_o is the outer radius of the shaft and R_b is the bending radius of the FPC. The blue line with a U-bend represents the FPC in the initial state and the points 1 and 2 represent the attachment points to the stationary shaft and the rotating housing respectively. The pink dashed line corresponds to the new state of the FPC when the housing is rotated in the anti-clockwise direction and the point 2'' shows the new position of point 2. The orange dashed line corresponds to the new state of the FPC when the housing is rotated in the clockwise direction and the point 2' shows the new position of point 2. Note the difference in the bending radius of the cable wrap and the goose-neck, for similar inner and outer diameters, the cable wrap has a higher bending radius of the conductor than the goose-neck. This means that the conducting medium is under lower mechanical stress in the cable wrap when compared to the goose-neck.

The cable wrap and the goose-neck design options will be compared based on the merits and demerits of their construction and its suitability to the application's design requirement. This is shown in Table (5.18). If a design option's characteristic does not meet the application's requirement, it is shaded in red and awarded

a score of 0; if the requirement is satisfied or over-satisfied, then the cell is coloured in green, and a score of 1 is awarded to the design option and if the design option is partially fulfilled the cell is shaded in orange, then a score of 0.5 is awarded. The scores are added and displayed at the bottom of the table. It can be observed from the trade-off that the cable wrap has a slightly higher advantage overall than the goose-neck because of its spiral winding of the cable, which allows a higher rotation angle limit and lower bending radius.

Power transfer design option	Cable wrap	Goose-neck	Application requirement
Diameter ratio	Preferable when high outer/inner diameter ratio is available	Preferrable when the diameter ratio tends to unity	As low as possible because of dimensional constraint
Angular rotation range	Cable wraps allow more than 720 degrees rotation [160]	Goose-necks allow larger than 360 degrees rotation (up to 400) [160]	360 degrees
Bending radius of wire	Lower bend radius due to spiral shape	High bending radius due to U-shape bend	Lower the better to avoid stress and to increase flex life
Total advantages	2	1.5	Highest

Table 5.18: Gooseneck and cable-wrap trade-off

The FFC and the FPC are the two current carrier design options used in the cable wrap and the goose-neck respectively. The advantages and disadvantages of these conductor options are traded-off based on their suitability to the application's requirement as shown in Table (5.19). Lower resistive torque is preferable because the power produced by the actuator can be transferred more optimally for solar panel rotation rather than dissipative sources such as overcoming PDTM resistance torque. It can be inferred from this trade-off that the FPC is very suitable for this application compared to the FFC because of its low thickness, which allows for lower bending radius and higher flex cycles.

Power transfer medium	Flat cables	Flexible Printed Circuit	Application requirement
Resistive torque	Higher torque required & non-linear with angular position because of thicker wires	Lower parasitic torque & constant with angular position because of thin trace-width and conductor thickness	Lower the better
Bending radius of wire possible	Lower bend radius not possible due to thicker conductor cross-section	Low bending radius possible due to thin cross-section	Least possible
Flex life	Upto 10^5 flex cycles at 10 mm bending radius for a wire rated for 1.4 A. (A.15)	Up to 10^6 flexes because of thinner cross-section. [83]	29200 in-orbit flex cycles SADM-PDTM-009
Wire thickness	Thicker wires	Thinner conductor width	Thinner the better
Total advantages	0	4	Highest

Table 5.19: Conductor carrier options trade-off

The trade-off has revealed interesting results because the cable wrap construction is desirable for this application, but the cables as a conducting medium is not so desirable. Meanwhile, the FPC used in the goose-neck design is favourable for this application, but the goose-neck construction is not so favourable. Therefore, a combination of the desirable elements from both worlds would be taken to form a new design suited to this application. The FPC would be wound as a spiral around the shaft in this new design. This new design would be termed the "**Flex-wrap**". The schematic of this design option is same as the one shown in Figure (5.22c), but instead of the cable the FPC will be coiled in the form of a spiral. The first step in designing the Flex-wrap will be to arrange and size the conductors connecting the solar panels to FPC and followed by sizing the FPC to carry the current and voltage levels defined for the PDTM. This will be further followed by designing the shape of the FPC. The design of the Flex-wrap will be carried out step by step in the upcoming sections.

5.5.5. Flex-wrap configuration selection

The conductors from the solar panel to the Flex-wrap can be mounted on the inside or outside of the shaft as shown in Figure (5.23). The orange circles are the conductors coming from the solar panels. The blue spiral is the FPC coiled around the shaft in the form of a spiral. Each configuration have their own advantages and disadvantages.

If the conductors were to pass through inside the shaft, the advantages include - more volume for the flex-PCB leading to higher bending radius. To realise this configuration, a hollow shaft with a slot will be required so that the wires can pass through the shaft and come out of it to interface with the FPC on the outside. This would firstly lead to a shaft with reduced strength considering and secondly passing the wires through a small slot on a 4 mm shaft will be extremely hard.

In the second configuration where the wires are placed outside the shaft and around it, the strength of the shaft will not be compromised as it does not have to be hollow in this case. The assembly will be challenging owing to the fact that the dimensions are small but it is feasible as it does not have to fit through a slot. The disadvantage for this configuration will be the fact that the wires will now have a dimensional constraint imposed by the remaining space in the housing after the volume taken by the shaft.

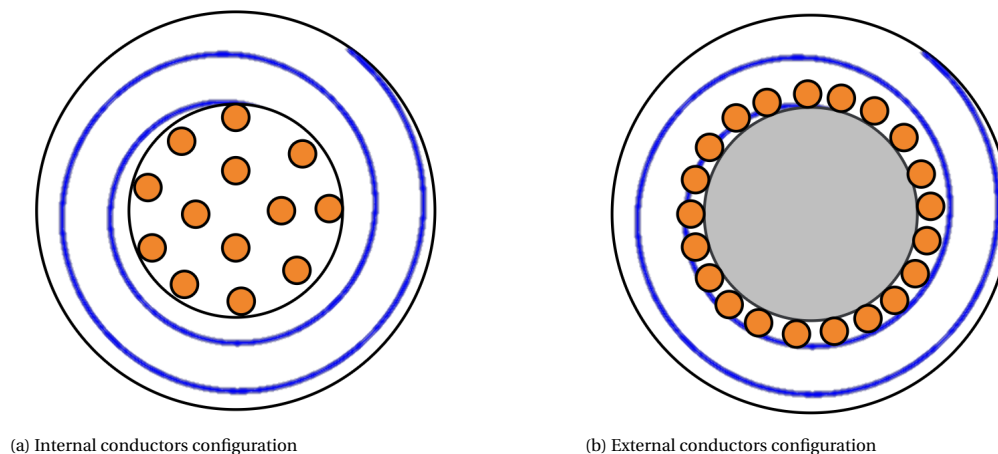


Figure 5.23: Flex-wrap conductor arrangement configurations

Comparatively, the **second configuration** with the conductors on the external surface of the shaft is practical from an assembly perspective and does not hamper the strength of the shaft therefore this configuration will be **selected** for use in this application. The next step is to select, size and arrange these wires in an optimal fashion around the shaft.

5.5.6. Wire sizing & arrangement

As specified by SADM-PDTM-006, the SADM and its components must be capable of surviving the environmental conditions throughout the operational lifetime. One main environmental factor affecting the cables is the radiation and vacuum. The vacuum causes the material to outgas, and radiation in high doses alters the cable response through multiple mechanisms caused by the build-up of electric fields in the dielectric material [204]. Therefore, this application requires radiation tolerant wires as the wires connecting the solar panels to the SADM is exposed directly to space.

Space-grade cable options

The most commonly used space-grade wires designed for radiation tolerance and no out-gassing are made by Raychem. The company provides two grades of such cables - SPEC 44 and SPEC 55. The main difference between the two grades roots from their construction. The SPEC-44 cable has dual wall construction using a cross-linked Polyvinylidene Fluoride (PVDF) insulator, which allows a -65 to 150 degree Celsius operating temperature range. The SPEC-55 cable has a single wall insulator construction made of radiation cross-linked Ethylene tetrafluoroethylene (ETFE) which allows an operating temperature range of -65 to 200 degrees Celsius.

The current application requires 2 conductors to carry 1.7 A, 4 conductors to carry 1.2 A and 15 wires to carry 0.1 A for the sensors as mentioned in SADM-PDTM-001 & SADM-PDTM-002. The corresponding wire specifications for SPEC-44 and SPEC-55 grade cables are as shown in Table (5.20). The wire size for a particular current value have been chosen considering the American Wire Gauge (AWG) ratings [78], which is an industry standard for wire sizing.

Power cable selection

As highlighted in the table, SPEC-55 cable has been chosen because of its lower diameter than the SPEC-44 for power transfer. To make this choice, firstly, the diameter of the shaft was fixed considering the clearance available after the wires were fixed on the surface of the shaft. Considering the strength, it is desirable to have a shaft with the maximum diameter possible and less than 6.9 mm for this application. But such a large diameter shaft is not desirable because the wires from the solar panel that passes over the shaft's surface would then interfere with the housing material. To solve this optimization problem, an initial shaft diameter of 3 mm was assumed, and the maximum conductor diameter was added to this, which is 1.40mm in this case, as shown in Table (5.20). This would lead to a combined diameter of 5.8 mm, a sufficient clearance margin from the required dimensional limit. So a higher diameter of 4 mm was considered, giving a combined diameter of 6.8 mm, just 0.05 mm clearance from the dimensional limit. Therefore, the shaft cannot be made any larger than this diameter of 4mm. It is also important to note that the housing would have a dimension of 6.9 mm, and the volume envelope inside the housing will be even less because of the thickness of the housing material. It was calculated in section (5.1) that the minimum material thickness required to allow a radiation tolerance limit of 10krad was around 3.5 mm of Aluminium. But then, shielding is required only to protect the electronic components from the effects of radiation as this is an electrical component. The housing can be made less thick than the calculated thickness value to get more height for the wires. As a 0.05 mm clearance will require the housing to be 0.05 mm thick at the space near the Flex-wrap shaft, it would make the housing weak at this spot, which is not desirable. Therefore, the shaft diameter is kept constant at 4 mm and the SPEC-55 cable is used, which has a lower wire diameter due to single-wall construction. The wire has a diameter of 1.27 mm, which gives a resultant diameter along with the shaft as 6.54 mm. This leaves at least 0.15 mm thickness of the housing at the spot above the shaft, which is a considerable thickness value than 0.05 mm considering the strength. Therefore, the SPEC-55 cable was selected as the preferred conductor for transferring the maximum current of 1.7 A. Multiple arrangement configurations of wire with the options mentioned above were carried out. The best configuration was selected based on the number of wires that could fit on the shaft and the ability to reduce the effects of EMI. As the SPEC-44 cables had a larger diameter than the SPEC-55, a lower number of wires could be fit on the shaft. Therefore, the SPEC-55 cables were selected for the 4 lines that conducted 1.2 A.

Data cable selection

Variations of the wire construction have been considered for data transfer like twisted, shielded and jacketed versions. This is to reduce noise induced in the cable from external disturbances and from Electro Magnetic Induction (EMI) disturbances from adjacent conductors. As these non-desirable effects are more pronounced in sensor data lines because of the low magnitude signal amplitude, adopting noise mitigation strategies in these cables is desirable. The main purpose of the shield is to protect the conductor from EMI. It acts in both ways to prevent the current carrying conductor as an EMI source that acts like an antenna or to prevent external interference from affecting the signal within the conductor. The shield is usually the same as the conductor material and is grounded to transmit the induced EMI to the ground. Thus, the noise is reduced. There are 2 types of shields – braid & foil. Foil is thin and offers 100% coverage but is hard to work with because it is thin and can tear easily, so it is not good for dynamic flexing and bending applications. A Braid shield is thin wires wound around the primary wire. It offers 95% coverage but also allows flexibility to an extent. The jacket protects the conductor from external contaminants like fluids, flame, etc. Twisting wires is also done to reduce the effects of EMI which is achieved by turning the conductors' electromagnetic fields in such a way that they oppose each other, thus reducing induced noise. As shown in the table, the twisted and shielded cables have a larger diameter than the single wire; this means that all the 15 sensor lines made of the twisted wire cannot fit on the shaft. Only four lines will use this because only the data lines of the sensor are sensitive to noise and need this EMI mitigation measures. Four lines were the maximum that could be fitted on the shaft after considering the power lines and the total number of lines required.

Current (A)	Number of lines	AWG Rating	Wire specification	Conductor diameter (mm)	Wire outer diameter (mm)
1.7	2	20	SPEC 44 - Single wire (Dual wall)	0.812	1.40
			SPEC 55 (Single wall)	0.812	1.27
1.2	4	24	SPEC 44 - Single wire	0.573	1.02
			SPEC 55	0.573	0.94
0.1	15	30	SPEC 44 - Single wire	0.255	0.69
			SPEC 44 - Twisted pair	2 × 0.255	1.37
			SPEC 55 - Primary wire	0.255	0.61
			SPEC 55 - Single wire shielded and jacketed	0.255	1.51
			SPEC 55 - Twisted wire unshielded	2 × 0.255	1.27

Table 5.20: Wire sizes for current rating

Optimal cable arrangement

Different arrangements of the wire around the shaft are possible. The main factor considered for the wire arrangement was to minimize EMI. As these wires are placed close to each other to pack as many wires as possible, the moving current produces a magnetic field around the cable, which can magnetically couple the wires inducing noise in the data lines. The electrical field in the two wires causes capacitive coupling and induces capacitive charge to be stored in the dielectric. The EMI is minimised by placing the wires carrying the current or signal right next to the return or ground line. The opposing direction of the current induces a magnetic field around the conductors so that they cancel each other's effects. Another measure taken to mitigate EMI is to use twisted cables, which are also used in this arrangement. The best arrangement considering the volume occupied and the required number of lines to be fit around the shaft is shown in Figure (5.24).

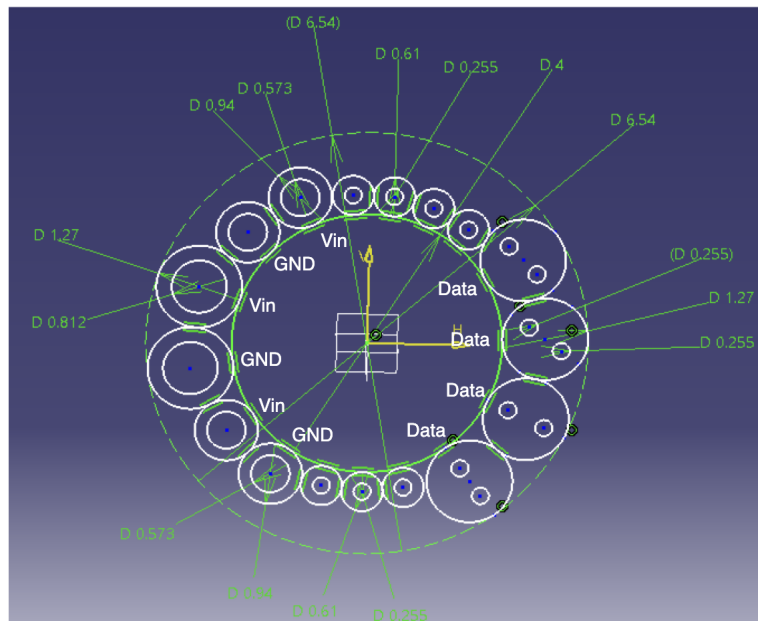


Figure 5.24: Optimal cable arrangement around shaft

5.5.7. Flex-wrap sizing & design

Now that the conductors from the solar arrays are sized, selected and arranged, the next step is to design the flex-PCB that will be connected to the wires and be coiled around the shaft to allow relative rotation of the solar arrays and the housing. The Flex-wrap schematic is as shown in Figure (5.23), and the blue spiral is the flex-PCB as seen from the front of the shaft. The cross-section of the flex-PCB is shown in Figure (5.25).

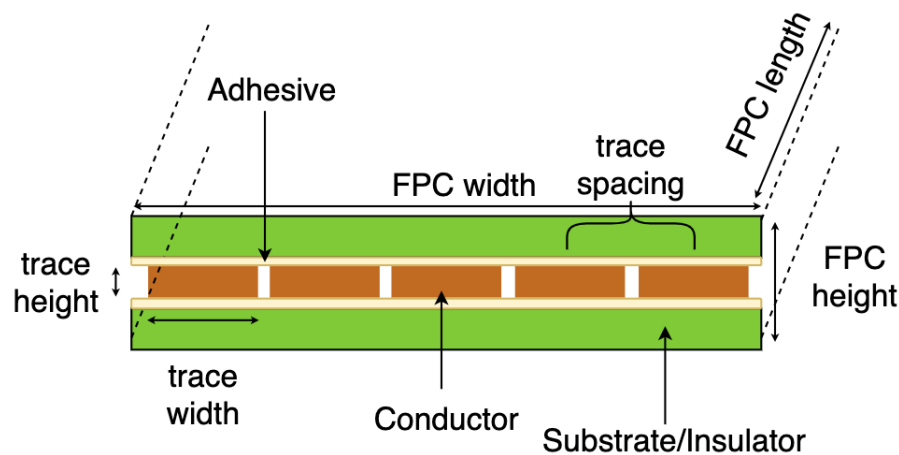


Figure 5.25: Cross-section of the FPC

The FPC of the Flex-wrap has two categories of design parameters as observed from the Figures 5.25 & 5.23b - intrinsic and extrinsic design parameters. Intrinsic design parameters refer to the conductor and insulator specifications of the FPC like the trace width of the conductor, trace height, spacing between the traces, adhesive layer thickness and insulator thickness. These intrinsic parameters further affect the extrinsic design parameters like the FPC height, FPC width, FPC length and shape. The FPC height is the combined height of the trace, insulator and adhesive layers. The FPC width is the combined length of the trace width and inter-trace spaces. Therefore, for designing the FPC, an inside to outside approach will be followed by first designing for the intrinsic parameters and then followed by extrinsic parameters. These parameters are heavily defined by the materials used for conduction, insulation and adhesion. Firstly the material choices have to be made.

Choice of materials

The FPC is composed of three materials, the conductor, adhesive and the insulator, as shown in Figure 5.25. The conductor layer is sandwiched between two insulator layers by using adhesive layers. The conductor chosen for this application is Copper, which has the highest electrical conductivity after silver and is cheap and commercially mass-produced, making it easy to procure. The insulator, in this case, requires that it be flexible and have a high dielectric constant and high operating temperature ranges. Usual substrate materials used by the industry for manufacturing PCBs include FR-4, CEM, Polytetrafluoroethylene (PTFE) and Polyimide or Kapton. Kapton [35] will be the substrate of choice in this application because of its wide operating temperature range (-269 to 400 degree Celsius) and flexibility compared to the laminates like FR-4 and CEM and plastics like PTFE which make a good choice for rigid PCBs. The adhesive material is usually epoxy, as specified by manufacturers.

Trace specifications

The current will be carried through the FPC in its conductors, in a PCB or FPC these conductors are called traces. The trace dimensions and their spacing is necessary to calculate the FPC width and height. The conductor cross-sectional area is usually constant for a given current rating as specified by FPC and PCB design standards - IPC-2221 [140], IPC-2152 [141], IPC-2223 [142] and ECSS-Q-ST-70-12C [123]. The trace calculation is initiated by firstly calculating the cross-section area required to carry the different currents as specified in SADM-PDTM-001, SADM-PDTM-002 & SADM-PDTM-004. This area is calculated using equation 5.36 below. The basic formula has been referred from IPC-2221 [140] and has been adapted to Kapton in vacuum environment using data provided in IPC-2152 [141]. The 2 is a safety factor and 1550 is the conversion factor to get the cross-sectional area in mm^2 . The maximum temperature of 80 degree Celsius has been considered with a temperature change of 10 degree Celsius to calculate the cross-sectional area of the trace. The maximum operational temperature was defined in SADM-PDTM-006. The maximum operating temperature has its impact on the resistance and power loss but not on the cross-sectional area. The maximum change in temperature of 10 degree Celsius was the initial value defined in the IPC conductor sizing graphs, this was chosen in order to compare the computed values with the graph for verification.

$$A_c = \frac{2}{1550} \left(\frac{I}{k_0 \Delta T^{k_1}} \right)^{\frac{1}{m_0 \Delta T^{m_1}}} \quad (5.36)$$

Where,

$$k_0 = 0.0756$$

$$k_1 = 0.4375$$

$$m_0 = 0.5000$$

$$m_1 = 0.0301$$

Traces are usually rectangular in cross-section and the trace specifications are adapted to the calculated cross-sectional area. The trace specifications, calculation expressions and dependent factors are described below:

1. **Trace thickness:** Trace thickness is the height of the trace as shown in Figure 5.25. Trace thickness affects the FPC thickness. Manufacturers usually define trace thickness as a standard in multiples of 35 μm (1 Oz). Moreover, manufacturers specify adhesive layer thickness and substrate layer thickness based on the trace thickness as described in subsection A.7.2. The FPC thickness is the sum of thickness of its constituent layers of adhesive and insulator. Therefore, the total conductor thickness is found using the expression 5.37 below:

$$Th_{FPC} = 2th_{Cu} + 2th_{Adh} + 2th_{Ins} \quad (5.37)$$

As this application has a limited volume of just 6.9 mm height, the bending radius of the FPC is a crucial design parameter. The bending radius of the FPC is primarily dependent on the thickness of the FPC and related by direct proportion as expressed in the equation below.

$$R_{bend} \propto Th_{FPC} \quad (5.38)$$

The shaft radius was set to 4mm considering cable layout and strength in sub-section 5.5.6. The housing has a height of 6.9 mm and needs to have some minimum material thickness for structural integrity. A minimum thickness of 0.4 mm is considered in the location over the Flex-wrap considering the volume required for the wires as described in sub-section 5.5.6. This is a minimum thickness assumed and the structural strength would have to be verified later using proper simulation of loads using a finite element model. This material thickness of housing would leave only 1.25 mm of space around the shaft for the flex-wrap to fit in. This is extremely stringent in terms of dimensions which is another reason why the FPC is favourable over other power transfer mediums such as FFC due to its low thickness (in range of micrometers). As the FPC has to fit within this volume of 1.25 mm, high trace thickness will not be favourable for this application. If the FPC is thick it will have a higher bending radius limit and will occupy more space from the available 1.2mm space within the housing. The bending radius of the FPC is expressed in equation 5.39 [142]. The IPC-2223 standard recommends using a 0.3% allowable deformation (E_B) of Copper or a bending radius to total conductor thickness ratio of 31.

$$R_{bend} = \frac{th_{Cu}}{2} \left[\frac{100 - E_B}{E_B} \right] - th_D \quad (5.39)$$

2. **Trace width:** Trace width is the breadth of the trace selected based on the cross-sectional area of the conductor recommended to carry a specific value of current. As the conductor cross-section is constant for a given current value and as the traces are rectangular in cross-section, the trace width will be calculated by dividing the calculated cross-sectional area by the trace thickness. This means that for a constant conductor cross-section area, the trace width is indirectly proportional to the trace thickness as expressed in equation below.

$$w_{tr} \propto \frac{1}{th_{Cu}}; w_{tr} = \frac{A_c}{th_{Cu} + tolerance} \quad (5.40)$$

The trace width influences the total width of the FPC. If the traces are too wide, the FPC becomes wide and occupies more volume inside the housing and will increase the housing dimensions, which is not preferable. If the traces are less wide, the conductor thickness would have to increase in proportion to maintain constant conductor cross-section. If the conductor thickness increases, the FPC will not be as flexible and will have a higher bending radius requirement. A tolerance is also added to the trace width based on the thickness of the trace. This is defined by the manufacturer as defined in [83] and has been considered in the trace width calculations in Table 5.21.

3. **Inter-trace spacing:** It is the distance between center of two adjacent traces. The spacing between the traces affects the total width of the FPC. It's dependent on the voltage between the lines and the distance of insulator required to prevent a dielectric break-down due to the potential between the two conductors as expressed in equation below.

$$w_{gap} \propto V_{peak} \quad (5.41)$$

The inter-trace spacing is defined according to IPC-2221 [140]. This standard states that for a voltage of 31-100 V the minimum recommended gap between traces must be 0.1 mm, for a voltage of 101-150 V, the gap between traces must be 0.2 mm and for voltages less than 30V, the gap was defined as 0.05 mm. The current SADM has six lines carrying 97 V as defined in SADM-PDTM-003, which is the maximum for this design. As defined in IPC-2221, a space of 0.1 mm will be used between these six traces. For other lines a gap of 0.1 will be used. In this case, the space is between the edge of the adjacent traces and not between the center of the traces. The total width of the FPC considering the trace widths and the gaps between them has been expressed in the equation 5.42 below.

$$W_{FPC} = w_{edge} + N_{tr} (w_{tr} + w_{gap}) + (w_{edge} - w_{gap}) \quad (5.42)$$

The number of lines required for power and data transfer had already been defined in requirements SADM-PDTM-001 to SADM-PDTM-004 as 21 along with their current and voltage limits. The trace specifications for these current and voltage values have been computed and are summarized in the Table 5.21. Three different trace thicknesses have been considered - 18, 35 and 70 μm . The cross-sectional area corresponding to the current value was computed using equation 5.36. The trace-width was obtained by dividing the cross-sectional area with the trace thickness. The bending radius was calculated using two approaches, one by using equation 5.39 that is defined by IPC standards and the other by using the FPC design guidelines of Minco [83], a PCB & FPC manufacturer. The design guide by Minco specifies that the minimum bending radius of the FPC is obtained by multiplying the circuit thickness by a factor of six as shown in Figure A.17.

Current (A)	Cross sectional area (mm^2)	Trace thickness (μm)	Trace width (mm)	Total FPC thickness (mm)	Bending radius (mm)		Number of lines
					Minco's design guide [83]	IPC-2223 [142]	
1.7	6.53×10^{-2}	70	1.01	0.157	0.42	11.58	2
		35	1.92	0.130	0.21	5.76	
		18	3.67	0.106	0.108	2.935	
1.2	3.43×10^{-2}	70	0.564	0.157	0.42	11.58	4
		35	1.03	0.130	0.21	5.76	
		18	1.928	0.106	0.108	2.935	
0.1	3.3×10^{-2}	70	0.0797	0.157	0.42	11.58	15
		35	0.0595	0.130	0.21	5.76	
		18	0.0434	0.106	0.108	2.935	

Table 5.21: Trace and FPC specifications for different current and voltage values

As stated earlier, low conductor thickness would result in low bending radius limit which is preferable, but would lead to long total FPC width which is preferable as it would increase housing dimension. A high

conductor thickness would lead to high minimum bending radius which is not preferable for the low dimensional limit allowable. As shown in the Table 5.21, the 35 μm is the best option considering this trade-off between the FPC width and the bending radius. The current SADM requires a bending radius of 2mm considering the case where the FPC is completely wound around the shaft that has a diameter of 4mm. Looking at this requirement, the bending radius calculated using Minco's guidelines seems to be adequate for all three conductor thickness values. But the bending radius value calculated using IPC-2223 does not seem to be adequate for any value of trace thickness. If a spacing of 0.2 mm is considering on either edges of the FPC and a gap of 0.1 mm between the traces are considered, then the FPC using 70 μm thick traces will have a total width of 7.87 mm, if the trace thickness was 35 μm then the **total width would be 11.25 mm** and considering a trace thickness of 18 μm then the total FPC width would be 18.1 mm. All the FPC widths are lower than the housing length of 48mm, but the housing would also have to include other elements like the bearings along its shaft, therefore least width of conductor is preferable. Taking into account the need for high bending radius limitation and the low FPC width, the **trace thickness of 35 μm is selected** because it is a compromise between the two requirements. The bending radius limitation calculated for this thickness is still over the requirement of 2 mm according to IPC-2223, this mismatch can lead to early failure but this is an empirical relation and the assumptions behind these expressions are unknown. On the other hand, the bending radius calculated using the manufacturer's design guide seems to meet the bending radius requirement with a large margin. This inconsistency can be explained by the fact that these relations are empirical in nature and the assumptions and conditions involved in calculating them are unknown. Therefore, it is wise to use these expressions as guidelines and not the final qualification factor of the design. The author would recommend testing the designed FPC for the defined flex cycles at the determined bending radius to understand the actual response of the FPC as this is a novel design that has not been implemented in any similar power and data transfer application.

FPC length calculation

Now, that cross-sectional or intrinsic parameters of the FPC are known, the overall FPC parameters like the length and shape of the FPC can be found out. The Flex-wrap has the FPC coiled in the form of a spiral. The length of the spiral has to be adequate to allow ± 180 degrees rotation to achieve 360 degrees rotation capability of the solar arrays as defined in SADM-PDTM-005. The spiral must also fit within the defined volume limit of 1.25 mm between the shaft and the housing, this means that the spirals must have adequate gap between the spiral layers otherwise they rub against each other and undergo surface wear. To calculate the length of the FPC required to allow this angle of rotation, the spiral was modeled as an Archimedean spiral which can be mathematically expressed in polar and Cartesian format as shown in the equation 5.43 below. In the polar equation, 'a' controls the origin of the spiral and 'b' controls the gap between the layers.

$$r = a + b\theta ; \quad y = x \tan \sqrt{x^2 + y^2} \quad (5.43)$$

To calculate the gap between the layers, the thickness of the FPC had to be considered and cannot be modeled as a single line. The total thickness of the FPC including all the layers for a trace thickness of 35 μm was found to be 0.13 mm as shown in Table 5.21. This was accounted for in the modelling and as depicted in Figure A.18 the FPC was made to have a neutral axis which was the central core of the FPC and the inner and outer layers which are represented by blue and red dotted lines respectively. The black circles enclosing the spiral are the shaft with a diameter of 4 mm and the outer envelope with a diameter of 6.5 mm. The length of the spiral was calculated by considering the spirals as circles and is given by equation 5.44 below:

$$L_{\text{spiral}} = \pi N_{\text{turn}} \frac{D_i + D_o}{2}; \quad (5.44)$$

The gap between the layers were computed by dividing the distance between the outer envelope and shaft with the thickness of the FPC spirals, as shown in equation 5.45 below:

$$\text{Gap} = \frac{(D_o - D_i/2) - (N_{\text{turn}} + 1)Th_{\text{FPC}}}{N_{\text{turn}}} \quad (5.45)$$

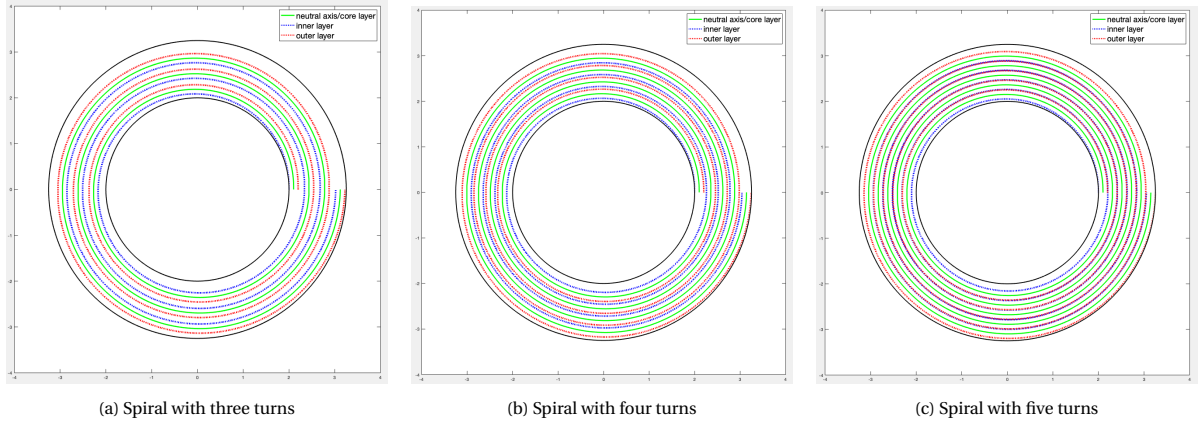


Figure 5.26: Plotting spiral shape of the Flex-wrap for different turns

As the spiral is composed of Copper and Kapton layers, when they are bent in to the shape of a spiral, part of the energy spent in bending the FPC is stored as potential energy in the material due its elasticity. The spirally coiled FPC is analogous to a clock spring in working. As it stores potential mechanical energy in coiled state, it is constantly trying to regain its equilibrium position which is the flattened out configuration. A moment has to be applied to overcome this potential energy and to rotate the spiral FPC by 180 degrees. This means a reaction torque would be applied by the FPC at its fixation point on the shaft. The torque is necessary to know because this induces stress in the FPC and the reaction torque must be considered to know reaction force that the interface of the FPC must resist. To know this torque, the coiled FPC can be modelled as a clock spring made of copper and Kapton layers. Adhesive layer can be ignored as it is not elastic in nature and cannot be modelled as an isotropic material. As there is one layer of copper trace sandwiched between two layers of Kapton, the coiled FPC can be modelled as three separate clock-springs, one made of copper and two made of Kapton, which are connected in parallel because all three layers are connected to the same fixation points on both ends. For the simplification of calculation, the copper traces would be assumed as one continuous layer or sheet having the same width as the FPC. Moreover the gap between the traces are 0.1 mm which is much less compared to the overall FPC width of 11.25 mm. The Kapton layers would also be assumed as one single sheet having the same width as the FPC. If the springs are connected in parallel, then the resultant moment and force will be sum of the individual spring forces.

Firstly to calculate the moments and forces, the moment of inertia of the cross-sections of the copper and Kapton layers are calculated using the expression 5.46 below. For the calculated copper layer thickness of 35 μm and width of 11.25 mm, the inertia is $4.02 \times 10^{-5} \text{ mm}^4$. For the copper layer thickness considered, the manufacturer specified substrate thickness is 25 μm as shown in Figure A.7.2. The inertia for this thickness of Kapton is $1.5 \times 10^{-5} \text{ mm}^4$.

$$I_{Cu} = \frac{W_{FPC} t_{Cu}^3}{12} ; I_{ins} = \frac{W_{FPC} t_{ins}^3}{12} \quad (5.46)$$

The moment or torque required to rotate the spiral FPC by an angle ' θ_{rot} ' is given by the equation 5.47 below [114]. The active length of the spring 'L' is as calculated using equation 5.44. An elastic modulus of $1.2 \times 10^5 \text{ MPa}$ was used for copper and an elastic modulus of $2.5 \times 10^3 \text{ MPa}$ was used for Kapton [35]. It can be observed that the moments are low in magnitude due to the low moment of inertia of copper and Kapton layer cross-sections.

$$\theta_{rot} = \frac{ML}{EI} \Rightarrow M = \frac{EI\theta_{rot}}{L} \quad (5.47)$$

As stated earlier, the FPC is assumed to be composed of three layers excluding the adhesive. The moment due to the constituent copper and Kapton layer are different due to their different cross-sections and material properties like elastic modulus. The total moment required to rotate the FPC by 180 degrees is equal to the sum of the moments required to rotate the individual layers as expressed in equation 5.48 below. The total moment required to rotate the FPC by 180 degrees was found and have been stated in the fourth column of

Table 5.22. This moment maybe slightly different than the actual moment required to rotate the FPC because the adhesive layers have been neglected and the copper traces are assumed to be continuous. But the current values give a good approximation. It can be observed that the moment decreases as the number of spiral layers increases, this is because for the same angle of rotation, the force is distributed over a larger length leading to lower moment required to rotate the FPC.

$$M_{tot} = M_{Cu} + 2M_{ins} = \frac{E_{Cu}I_{Cu}\theta_{rot}}{L} + 2\frac{E_{Kp}I_{Kp}\theta_{rot}}{L} \quad (5.48)$$

By applying a moment to rotate the spiral FPC, a counter moment is applied by the FPC on the shaft at the point of fixture. This is also equal to the force applied by the shaft to rotate the FPC by 180 degrees. The force can be calculated from the moment equation by dividing it with the distance between the center of the shaft and position of application of force. In this case, the distance is the surface of the shaft which is the radius of the shaft. The force acting on the attachment point due to the moment is expressed in equation 5.49 below. This force is only for one layer of the material.

$$M = \frac{FD_i}{2} = \frac{EI\theta_{rot}}{L} \Rightarrow F = \frac{2EI\theta_{rot}}{LD_i} \quad (5.49)$$

As the three layers act like parallel springs, the force due to each layer will be summed to obtain the total force. The total force for the moment calculated using equation 5.47 for different spiral turns are calculated and stated in fifth column of Table 5.22. As there are two layers of Kapton, the force due to a single insulator layer will be multiplied by two. The same trend of decreasing force with increase in number of loops can be observed from the values in Table 5.22. The reason for the trend is due to the direct proportional relation that the force has with the moment. As the moment decreased due to distribution of force over the length of the spiral, the force also decreases.

$$F_{tot} = F_{Cu} + 2F_{ins} = \frac{2E_{Cu}I_{Cu}\theta_{rot}}{LD_i} + \frac{4E_{Kp}I_{Kp}\theta_{rot}}{LD_i} \quad (5.50)$$

As a moment is applied to the FPC spiral at one end, it undergoes rotational displacement, this would mean that the layers of the FPC would undergo stress. This stress is dependent on the angle of rotation, inertia of cross-section and material properties. The maximum stress occurs at the inner and outer edges of the FPC which are under compression and tension respectively. The distance of the layer from the neutral axis in which the stress is computed is represented by 'c' in equation 5.51. As the maximum stress occurs at the edges, this distance is taken as $t/2$ in this case. This stress is important to know because, if the stress in the cross-section exceeds the yield strength of the material for a given cross-section, then the material fails by plastic deformation. Considering the dynamic bending requirement of this application, it is desirable to have the stress in the layers lower than the yield strength of the materials. The stress due to applied moment is given by equation 5.51 below [114].

$$\sigma_{max} = \frac{6Mc}{I} = \frac{6M}{W_{FPC}t^2} \quad (5.51)$$

The stress in the copper and Kapton layers are found using the equations stated below. The stress values for these layers are computed using the moment values from equation 5.48, for a FPC width of 11.25 mm, copper thickness of 35 μm and Kapton thickness of 25 μm . The computed values are listed in columns six and seven of Table 5.22. The same trend of decreasing stress values with increase in number of spirals or spiral length is observed because of the decrease in moment values. The stress in the layers is directly proportional to the moment applied. As the moment decreases with increase in spiral length due to distribution of force over a larger length of the FPC, the stress per layer also decreases in proportion. The unusually low stress of Kapton is due to its relatively lower elastic modulus and 2.5 times lower cross-sectional inertia as compared to copper's elastic modulus and inertia. As stress is directly proportional to the elastic modulus and the inertia, a decrease in these two parameters results in a decrease in stress per layer of the insulation layer. Considering the low value of reaction forces induced by the rotational moment, the adhesive strength calculations will be neglected because the common space-compatible adhesive

$$\sigma_{Cu} = \frac{6M_{Cu}}{W_{FPC}th_{Cu}^2} ; \sigma_{ins} = \frac{6M_{ins}}{W_{FPC}th_{ins}^2} \quad (5.52)$$

Number of spirals	Length of spiral (mm)	Gap between adjacent layers (mm)	Moment for 180 degree rotation (Nmm)	Force at root of spiral (N)	Stress in Copper layer (N/mm^2)	Stress in Kapton layer (N/mm^2)
2	33	0.43	0.466	0.233	200	3
3	49.5	0.243	0.3	0.155	133.33	2
4	66	0.15	0.233	0.117	100	1.5
5	82.5	0.094	0.187	0.093	80	1.2
6	99	0.0566	0.155	0.077	66	0.99

Table 5.22: Length and forces of FPC spiral

The spiral of the Flex-wrap works by increasing one loop when rotated clock-wise and decreases a loop when rotated anti-clockwise. This is why one spiral loop has not been considered as it would not allow anti-clockwise rotation. Among the various number of spirals and their resultant implication on the FPC as shown in the Table above, one particular configuration has to be chosen.

The main trade-off criteria considered firstly is the gap between the adjacent layers. It is desirable to have more gap between the layers to prevent wear caused by rubbing of the adjacent layers. It was found that the gap between layers reduced to less than 0.1 mm in cases of 5 and 6 spiral loops. This can lead to even more decreased gap between the layers when the FPC rotates. Therefore, these two configurations are not suitable for this application. The next criteria considered in selecting the right configuration is the stress in the layers. It can be observed that the stress increases with the decrease in number of loops. The ultimate tensile strength of copper is 210 MPa [12] and the ultimate tensile strength of Kapton is 207 MPa [35]. In the case of two spiral loops, the stress in the copper layer is close to the ultimate strength, this is not desirable for operation, therefore, this configuration will not be considered further in this application. The two remaining options are the spirals with three and four loops. Both of these configurations have the stress in each layer lower than the ultimate tensile strength. The selection then comes down to the gap between the layers. As the gap increases with lower number of spiral loops, the spiral configuration with 3 loops is selected as there is more gap between the layers as compared to the configuration with four loops. Moreover, the increase in stress in the layers is not significant compared to the configuration with four loops. Therefore, the **flex-wrap will have three loops** in the home position (zero degrees) with a **spiral length of 50 mm**.

The FPC would have to be fixed over the shaft using adhesive because it is circular in shape and suitable annular connectors could not be found for this application. The simplest way to bound the FPC around the shaft is to use adhesive. The adhesive would have to withstand the reaction force applied by the FPC when rotated by a certain angle. Considering the low reaction forces induced due to the rotational moment, the adhesive strength considerations will be neglected. This is because the common space compatible adhesive (used in AAC Hyperion) Scotch-weld-2216 epoxy [58] was found to have more than adequate peel strength and tear strength to resist forces greater than 1N.

Shape of the FPC

The FPC of the Flex-wrap is connected to the solar panel on one end and the external power and data interfaces on the other end as shown in Figure 5.27. In order to comply for such a connection the FPC had to be designed in the shape of an L. The base of the 'L' is connected to the wires coming from the solar array to the SADM. They must be soldered to the FPC. The width of 12.5 mm in the solar panel end of the FPC was computed based on the perimeter of the shaft that has a diameter of 4mm. This is because, this part of the FPC would have to be completely wrapped around the shaft and fixed to it using adhesives. The blue-dotted line represents the line along which the wires will be soldered. The diagonal is chosen as it has the longest length possible and the conductor lines can be arranged along this line with adequate spacing. The computed spiral length of 50 mm is included in the body of the 'L'. This part will be twisted around the shaft to form a spiral with three loops. The 12 mm width of the body of the FPC was calculated based on the trace widths and inter-trace spacing as calculated in Table 5.21. The right hand side of the FPC would be connected to the interfaces. With this, the intrinsic and extrinsic parameters of the FPC have been calculated and the FPC has been designed for the main parameters. The detailed design would have to be carried out in a dedicated PCB design software where the trace widths and solder pads can be modelled along with connections and inter-trace spaces.

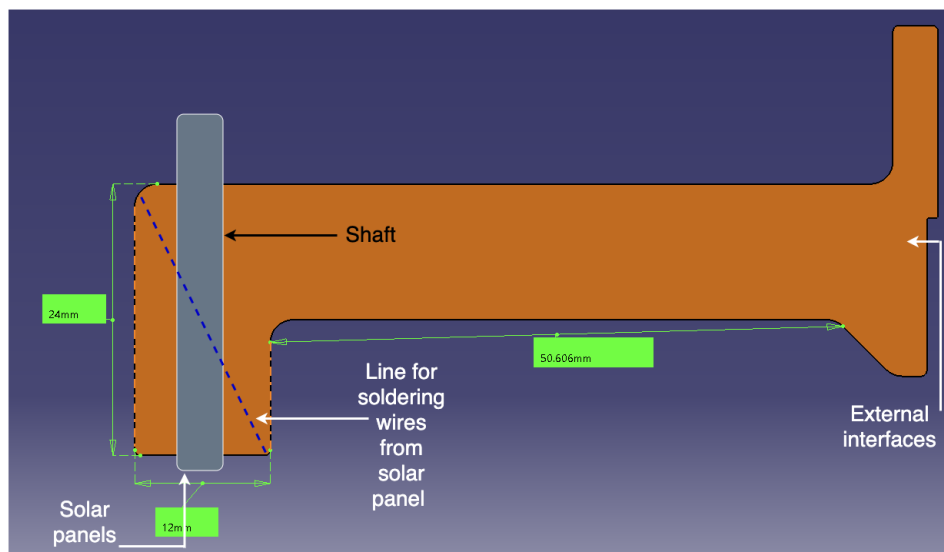


Figure 5.27: Shape of the FPC in uncoiled state

5.5.8. Failure modes of the Flex-wrap and mitigation

The Flex-wrap was invented and designed to overcome the drawbacks of the conventional power and data transfer mechanisms like the slipring, goose-neck and cable-wrap. The Flex-wrap definitely mitigates tribological failures like debris generation, arcing, corrosion and erosion by eliminating brushes. The Flex-wrap eliminates the low bending radius that was encountered in the goose-neck, thereby avoiding high stresses and premature fatigue failure. The Flex-wrap also overcomes the need for high diameter ratio and volume required by the cable-wrap. This does not necessarily mean that the Flex-wrap is the most ideal PDTM solution. The Flex-wrap also has drawbacks like rubbing of adjacent layers, fatigue performance and thermal considerations. As the flex-wrap is rotated clock-wise and anti-clockwise, the gap between the layers decreases and increases. The constant gap of 0.24 mm as calculated in Table 5.22 will not hold. This means that the layers would rub against each other when rotated. But compared to the wear and debris created by brushes in sliprings, this would be much minimal. The wear of the rubbing surfaces can be accounted for by coating the surfaces with a thin protective material. Given the fact that this is a new technology that has not been implemented or designed earlier, the fatigue strength characteristics of this design can be known only by life-testing. The author would recommend to measure and monitor the signals transmitted through the FPC before, while and after dynamic bending for the required flex-cycles to characterise the robustness of the solution. The transferred signal quality and the mechanical response of the FPC must be measured to characterise the robustness. Given the fact that the SADM has to operate in space the only way of heat transfer is radiation and conduction because of the absence of air. Heat of a conductor is directly proportional to the product of square of current and resistance. Even though the operating temperature range of Kapton is very wide, it is desirable to know the combined effects of heat, dynamic bending and wear on the electrical and mechanical performance of the FPC. The requirement SADM-PDTM-009 can be verified only by life-testing the Flex-wrap mechanism which is not possible within the scope of this thesis.

5.5.9. Summary of power and data transfer mechanism design

This section started with the motive of finding an alternative power and data transfer mechanism to conventional sliprings. It was desirable of the PDTM to overcome tribological failures that were the main root cause of the failure of sliprings. The current SADM had stringent dimensional constraints. Firstly SPEC-55 cables were chosen and sized to carry the required current. An optimum arrangement of the cables was arrived upon considering EMI effects. The optimal cable arrangement and strength considerations led to the optimal shaft diameter of 4mm. Among the various PDTM design options, the cable wrap provided the advantage of higher bending radius of cable due to its construction. On the other hand the goose-neck had the disadvantage of low bending radius but the FPC used in the goose-neck mechanism was found to have the advantages of higher flexibility and low thickness. A new mechanism has been designed and termed as the **Flex-wrap** that combines the best features of both the mechanisms. The Flex-wrap uses a spirally coiled Flexible Printed

Circuit to transfer power and data while allowing rotation by coiling and uncoiling. The FPC was designed to have a conductor thickness of $35\text{ }\mu\text{m}$ by making a trade-off between bending radius and total width of FPC. The FPC length was calculated by modelling it as a spiral and a length of 50 mm was chosen considering a trade-off between the gap between the adjacent layers and the stress induced in the FPC layers for rotating by an angle of 180 degrees. Finally, the shape of the FPC was designed as an 'L' considering its interface with solar panels and external connectors. With the new Flex-wrap PDTM design solution, the research question set for this section has been answered along with consideration for all the requirements pertaining to the PDTM (SADM-PDTM-001 to SADM-PDTM-009).

5.6. Bearing selection

This section will select a bearing technology based on its requirements derived from the application's requirements. This section will also focus on finding a solution to overcome the root causes of failure of conventional tribological systems with a history of causing mechanism failure. This will be done by systematically exploring the failure mechanisms of conventionally used roller bearings and their root causes, and after understanding this, a solution will be arrived at to mitigate this failure mechanism. The section then describes the selection process of a commercial bearing that fits the demands of this application.

5.6.1. Purpose

The main purpose of the bearing is to allow smooth motion of the shaft relative to the housing throughout its lifetime in ground & space.

It was found in the lessons learned section 2.3.2, that the roller bearings were one of the most crucial components of any mechanism because they were the root cause for multiple mission failures (Refer sub-section 2.3.1). Roller bearings caused failure mainly because of wear & debris generation, which were caused due to multiple mechanisms like non-optimal preloading, lubricant depletion, surface reaction and vibrations. The wear and debris generation leads to high friction or, in the worst case, complete immobilization of the bearings, which cannot be overcome by the actuator, thus leading to complete mechanism failure. Research questions were formulated to find a solution to this problem in the context of this application. The research question that is pertinent to bearings and tribological elements is 2c. The research question 2c has been adapted for bearings. This section will aim to answer this research question.

"How to select and size a bearing that overcomes the failure mechanisms of a conventional (roller) bearing used in space mechanisms?"

5.6.2. Requirements

Some of the system requirements defined for the SADM translate to the bearings, and this has been stated in the Table (5.23) below. One of the preliminary selection criteria for choosing the bearing is the dimensions. The bearing has to fit within the height limit of the housing, which is the rationale behind the requirement SADM-BG-001. The next criteria for selecting and sizing the bearing is its capacity to withstand the maximum load it will experience during its lifetime. The maximum load on the shaft was calculated in section 4.3.3 and was found to be 250 N. The bearing will have to be sized to withstand this maximum force which forms the rationale behind the requirement SADM-BG-002. Most of the bearings use lubricants which are solid, liquid or gel-based. As the environmental requirements apply to all sub-systems, they shall also apply to this sub-system. This includes operating temperature ranges, launch loads and vacuum conditions. This forms the rationale behind requirement SADM-BG-003. The liquid and gel-type lubricants have a hydrocarbon oil base which can lead to out-gassing in vacuum and deposition on other components of the SADM resulting in failure or malfunctions. To avoid this, requirement SADM-BG-004 was formulated for this application. The verification method applicable to the parent requirement shall also apply to the child requirements.

Identifier	Requirement	Parent requirement
SADM-BG-001	The bearing shall fit within the housing	SADM-INT-002
SADM-BG-002	The bearing shall withstand a maximum load of 250 N	SADM-ENV-007
SADM-BG-003	The bearing shall be compatible with the environmental conditions.	SADM-ENV-001 to SADM-ENV-011
SADM-BG-004	The bearing shall not use volatile lubricants.	SADM-RAMS-002

Table 5.23: Bearing requirements

5.6.3. Bearing design options

Bearings can be classified into two major categories based on their working principle. Sliding and rolling element bearings as shown in Figure (5.28). These types, their working principle and sub-categories will be explored below.

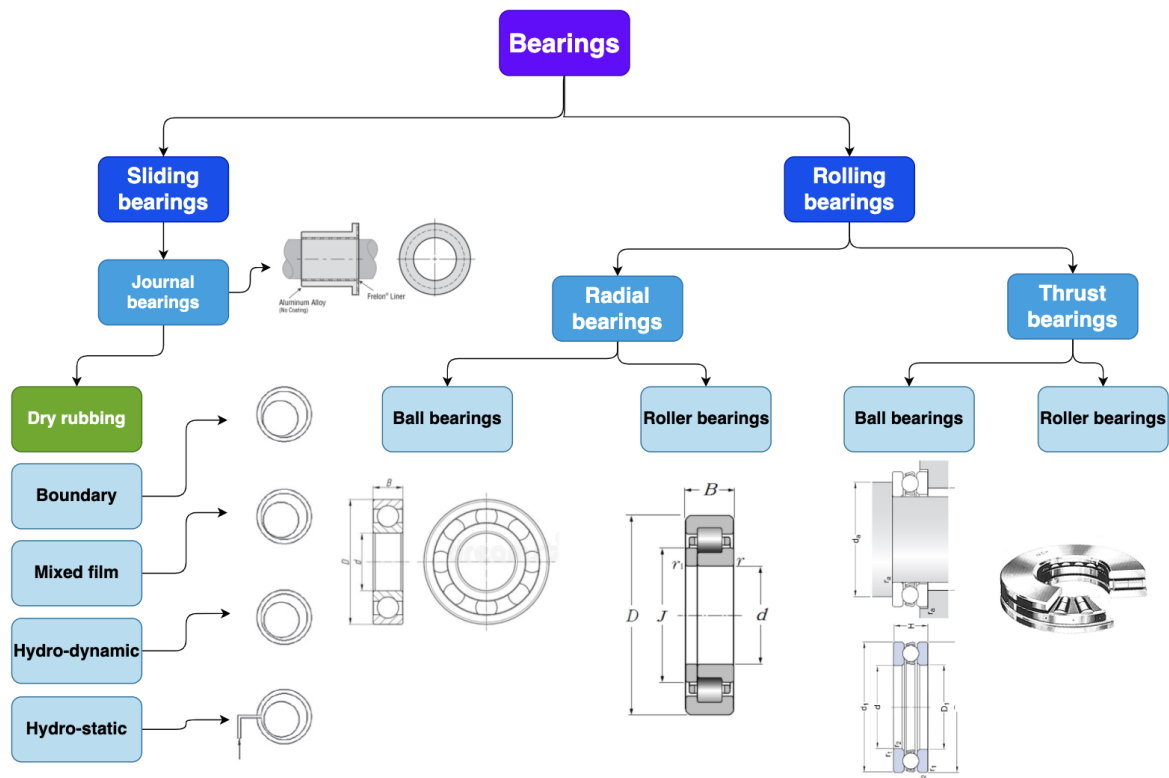


Figure 5.28: Classification of bearings

- **Sliding bearings:**

Sliding bearings do not have rolling elements; they simply work by having the shaft slide over low friction, co-efficient surface. They are also called journal or sleeve bearings. They can be classified based on the material used as metallic and non-metallic, the loading direction as axial and radial, and the lubrication regimes. In this application, the sleeve bearings will be explored based on their lubrication regimes because it is defined based on the relative speed. The solar array speed has been calculated in section (4.3.1), which is an important factor in the bearing selection.

Conventionally, journal bearings use a film of lubricant between the sliding surfaces to reduce the friction between them, as shown in Figure (5.29a). The surfaces rest over each other at zero velocity, and when the shaft starts rotating, it lifts up due to the lubricant seeping between the surfaces [148]. Based on the lubrication regime that the bearing operates in, they can be classified into five types - Hydrodynamic, hydrostatic, elastohydrodynamic, boundary and dry-rubbing [111]. The Stribeck curve shows these lubrication regimes, as shown in Figure (5.29c). Boundary lubrication occurs at low speeds where the shaft surface almost touches the bearing surface, and a very thin layer of lubricant separates the two surfaces, as shown in the first images of Figure (5.29b & 5.29d). In this regime, the velocity is not enough to generate enough pressure in the lubricant to lift the surface of the shaft. Mixed film lubrication is the regime where the relative velocity is just enough to lift the surface, as shown in the second image of Figure (5.29b & 5.29d). Hydrodynamic lubrication is the regime where the relative velocity is high enough to generate pressures to lift the surfaces so that the shaft floats or rides on the layer of lubricant between the surfaces, as shown in the third image of Figure (5.29b & 5.29d). Hydro-static lubrication is when a lubricant is pumped at a pressure to cause the lift-off between the surfaces. This method does not need relative motion. Elastohydrodynamic lubrication applies to rolling element bearings where the lubricant is induced between the rolling elements of the bearing. Dry-rubbing bearings suggestive of the name do not use any lubricants and are usually made of a non-reactive noble metal (gold, silver, etc.) or thermoplastics and are manufactured to have a high surface smoothness. They are temperature and speed limited because they do not use any lubricants. Therefore they are favourable for low-speed applications. The shaft, in this case, is usually made of metal. Self-lubricating bearings use a porous material impregnated with lubricant released at a slow pace to maintain boundary layer lubrication between the shaft and the bearing.

5.6. Bearing selection

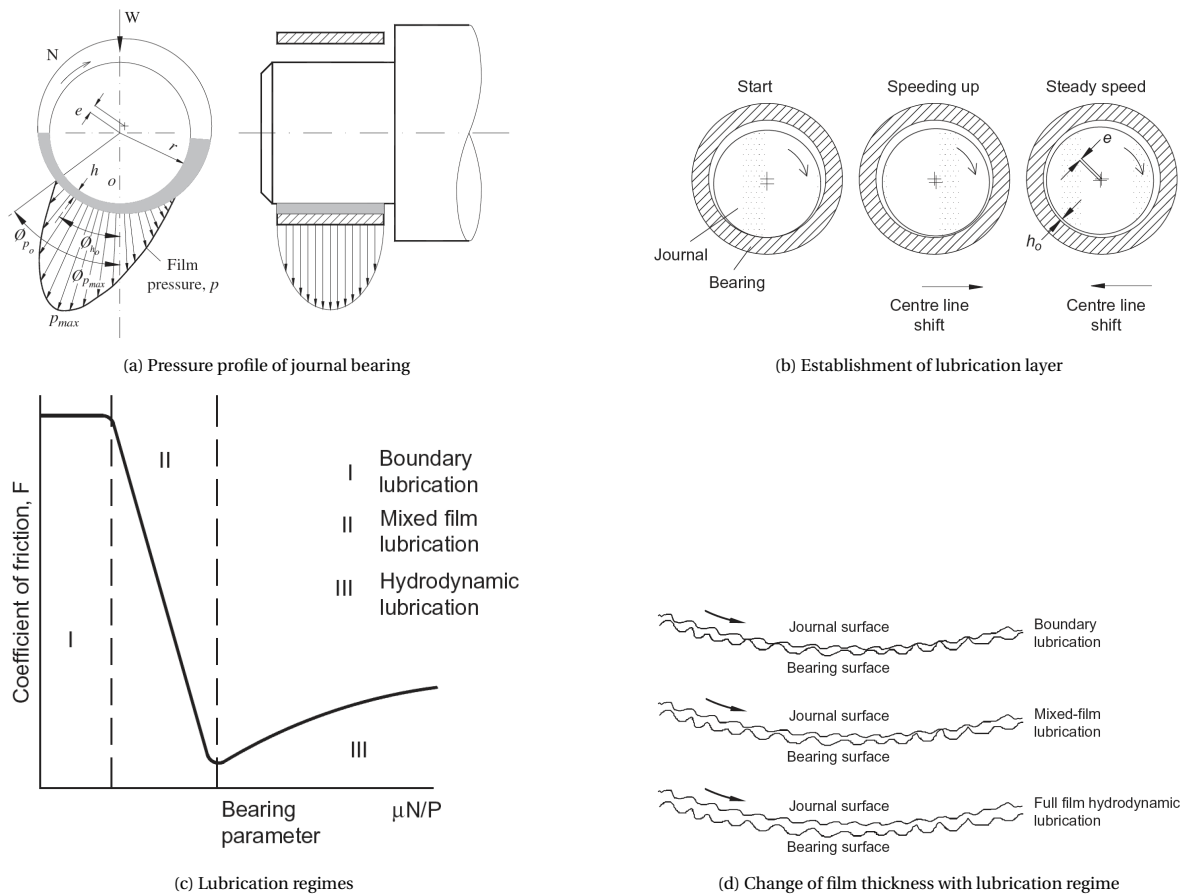


Figure 5.29: Working and lubrication regimes of Journal bearing [111]

• Rolling bearings:

On the other hand, rolling element bearings utilize circular or cylindrical elements to allow relative rotation between the two surfaces. The rolling element bearings can be further classified into radial and thrust bearings based on the direction they can take loads in. Radial bearings are designed to take loads in the radial direction of the bearings, and thrust bearings are designed to take loads along the axial direction of the bearing. Each type of bearing can be further classified based on the shape of its rolling element as the ball and roller bearings. Each of these bearing types is applicable for a specific purpose based on the application's requirement on speed, the direction of load, accuracy, friction torque, acceptable misalignment and rigidity [40].

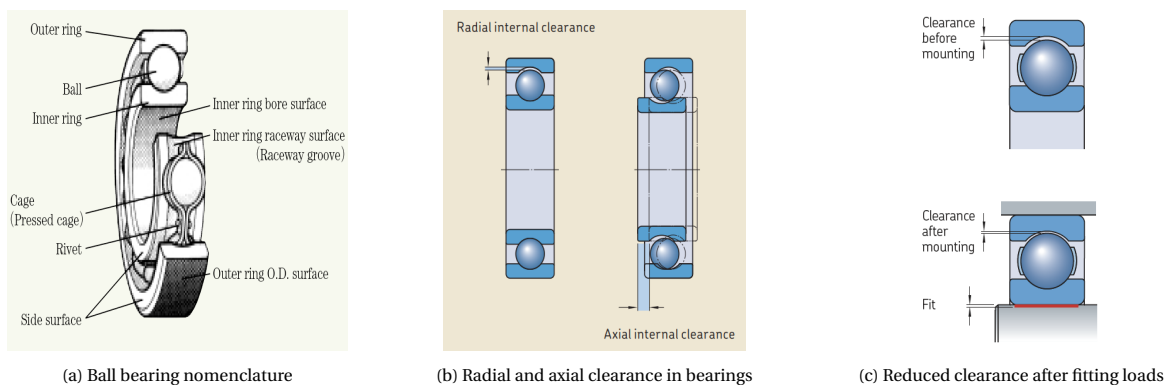


Figure 5.30: Bearing nomenclature and clearance

Ball and roller bearings have a simple working principle: the rolling element is held between two rings, where one ring rotates and the other remains stationary with respect to the ball. The inner ring is usually moving and tight-fitted with a shaft. The outer ring is usually stationary and is press fitted to housing as shown in Figure (5.30a). The rolling element rotates about its own axis. The rolling element sits on a mating surface in the shape of a circular depression called as the raceway. There is initially a clearance or play between the rolling element and the rings in the axial and radial directions, as shown in Figure (5.30b). The clearance or play is reduced to a required value to ensure the ball is in full contact with the raceways. If the clearance is to be maintained at a constant value throughout its lifetime a load corresponding to reduce the distance is applied. This method is called as hard preload as shown in Figure (5.31b). The clearance distance also changes with temperature as the materials expand or contract with increase or decrease in temperature as shown in Figure (5.31a). If an application has a high range of operational temperature ranges and load conditions that constantly change this clearance distance, it is preferable to use a compliant element like a spring that can deform itself causing a change in force that it applies to the bearings thereby adjusting the clearance value between the bearings and the rings according to the change in temperature or load conditions. This method is called as the soft preload as shown in Figure (5.31c).

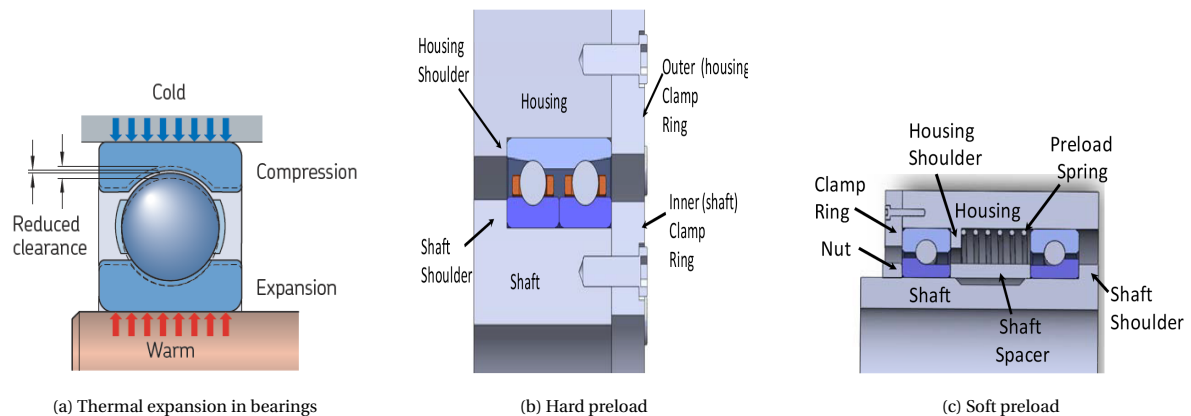


Figure 5.31: Bearing preload methods [48, 197]

5.6.4. Failure mechanisms of roller bearings & their causes

There are multiple failure mechanisms in roller bearings as mentioned in ISO-15243 [34]. Below is a brief explanation of each failure mechanism phenomenon and its sub-types, cause and effect.

1. **Fatigue:** Fatigue in bearings is caused due to cyclic loads. The cyclic loads occur at the contact surfaces of the rings and the balls. A bearing in axial, radial or combined load conditions has a particular region under a higher load than the rest. Due to the cyclic change in this region's stress, there are two possible effects: sub-surface and surface-initiated fatigue. In sub-surface initiated fatigue, the material micro-structure in the highly stressed region changes, and micro-cracks are initiated below the surface, propagating with time and forming cracks. This leads to spalling. In surface-initiated fatigue, the micro-asperities of the contact surfaces increase, leading to crack formation and material removal from the surface. This effect is usually triggered by under-lubrication or material defects when manufacturing. This material removal from the surface is called flaking.
2. **Wear:** Wear is the gradual removal of material. Wear, in general, can result from many effects like fatigue, corrosion, adhesion, abrasion, vibration and erosion [196]. Other mechanisms are discussed as their own, while adhesion and abrasion are the main contributors to wear in bearings. Adhesive wear is a mechanism triggered by under-lubrication. When there is low lubrication, the surfaces start to slide over each other and at high velocities, there is enough heat generation to cause micro-welding of asperities on the surface. But due to the high speeds, the material tends to stick to one surface and gets transported with the moving surface. This causes one material to be deposited on the other, which is called smearing and causes wear. Abrasive wear is a mechanism that is also caused by under-lubrication or contaminants. The micro-particles come in between the contact surfaces as they roll over each other and cause material removal due to friction.

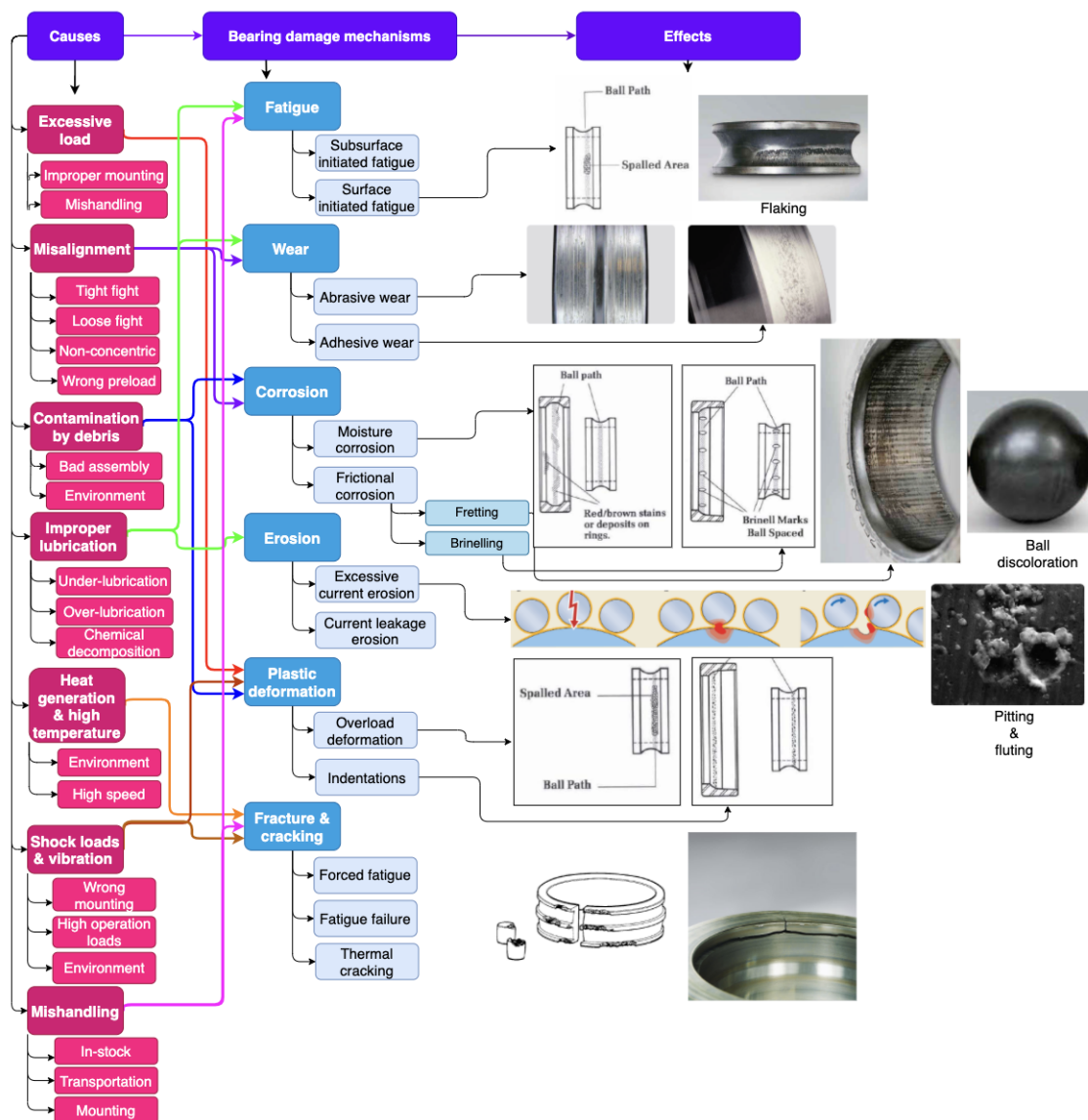


Figure 5.32: Roller-bearing failure mechanisms causes and effects [34, 37, 39, 48]

3. **Corrosion:** Corrosion is a chemical reaction caused due to contaminants like water & other oxidants or due to friction caused by loose-fitting. Most bearing elements are made of metals like steel which can oxidise under the influence of oxidants like humidity in the environment and other oxidants. This process can be accelerated at high temperatures. This causes rust formation, which is black or red in colour. These particles cause surface roughness which leads to increased friction and bearing damage. The other corrosion mechanism is the friction caused by the loose-fitting of the shaft and the bearing or housing. This causes small particles to be generated, accumulating in the ring's troughs and oxidising faster. These oxidised particles hinder the bearing operation by increasing friction and leading to further material removal from the rings and balls.
4. **Erosion:** Erosion is an electro-mechanical wear process that is caused by current flow. As the bearing elements are made of metal, there is a possibility for the current from the environment or the components in contact or electrostatic charges caused by triboelectric (friction between conductively dissimilar materials) charge generation mechanisms. This current, when passing through the metallic moving surface of the bearing, causes welding at the surface, which causes part of the surface to stick onto the moving surface, leaving a pit or micro-crater on the other surface. Based on the current magnitude, the effects are classified as excessive current erosion and current leakage erosion. Erosion leads to the

micro-crater formation on the surface, leading to bearings' friction.

5. **Plastic deformation:** Plastic deformation is the irreversible damage caused to the materials. They are usually caused by high shock loads during operation or mounting. This overloading leads to depressions in the material. Plastic deformation is also caused by debris from the environment or generated by wear within the bearing. This causes dent formation, leading to high bearing friction and noise.
6. **Fracture & cracking:** Fracture is a material failure when the applied load causes stress more than the tensile load of the material. There are three ways in which fracture of bearing material can occur. The first mechanism is due to sudden shock or impact loads that may occur during the operation, mounting, or assembly. The next cause is due to micro-crack propagation. The micro-cracks generated under or on the surface due to fatigue loads can cause the crack to propagate over time and cause material failure. The third mechanism is due to thermal stresses in the material that are caused due to differential thermal expansion of the metal components of the bearing and their surroundings. This induces stress in the material, which can cause failure if it exceeds the material's tensile strength.

Main causes of failure:

After the detailed analysis carried out above about the different mechanisms of rolling bearing failures and exploring their causes and effects on the bearing, some major observations can be made regarding these failure mechanisms. All the failure mechanisms cause material wear and particle debris generation, which leads to high friction or material failure like cracking. Both are detrimental to bearing operation as it reduces the smoothness of rotation and, in worst cases, can cause complete stopping of the bearing. This is the final effect observed in many failed mechanisms that stop functioning before their end of life. It can be observed that a few causes contribute to most of the failure mechanisms. These major causes can be listed as:

1. **Internal causes:** These are caused by the construction and working principle of rolling bearings.
 - (a) **Lubricant:** Lubricant is the root cause of failure mechanisms like fatigue and erosion. Choosing the right lubricant that does not degrade in space and does not react with surrounding materials itself is a challenging step. Maintaining adequate lubrication throughout the lifetime of bearing is again challenging because storage of fluids is not permissible in CubeSat systems. Over-lubrication causes high friction torque. Under-lubrication leads to wear and fatigue failure.
 - (b) **Metals:** Using metal as bearing components is the cause of multiple failure modes. This is because metals can corrode, erode & undergo micro-structure transformation at high loads.
 - (c) **Alignment maintenance:** Maintaining the balls in optimal contact with the raceways requires proper mounting and pre-load. In a dynamic environment where the space mechanisms have to operate, the system has to endure a short period of high loads and then has to operate in a demanding environment like wide temperature fluctuations and vacuum; it is hard to design the preload system to handle such varied loading conditions. This leads to the ball overloading or not being in contact, which leads to wear, friction and noise. [197]
2. **External causes:** These are caused by external factors like humans and the environment.
 - (a) **Assembly:** Very careful and accurate assembly is required to ensure proper concentricity of shaft and bearing. Proper load measuring equipment is necessary to ensure the right load is applied to fit the bearing.
 - (b) **Uncontrolled environment:** Need for a controlled environment in terms of temperature and contaminants (like debris & oxidants).

Most of the above failure causes stem from the working principle of the rolling bearing itself that requires preloading, uses metals, needs accurate fitting and has an elliptical point of contact. Next, the failure mechanisms of the sliding bearing will be explored.

5.6.5. Sliding bearing failure mechanisms

Sliding has its own advantages and disadvantages over conventional rolling element bearings. Because of the difference in construction and working principle, they overcome some disadvantages of rolling element bearings. Some of the common sliding bearing failure mechanisms are stated and explored below:

- **Wear:** Wear, being the most common form of failure in all tribological elements, is also present in this kind of bearings because of the moving parts. Wear as a failure mechanism is inevitable in tribological elements, but its effects can be slowed down if the right amount of lubricant is supplied and maintained throughout its lifetime. The main causes of damage due to wear is caused by under-lubrication and lubricant contamination.
- **Oil whirl:** This is an instability observed in hydrodynamic sliding bearings that uses oil as a lubricant where the shaft rides on the lubricant film at the highest point of the pressure gradient [200]. If the shaft received a sudden shock, more oil would be withdrawn from the supply due to the low pressure. The entry of more oil creates additional pressure on the shaft and causes it to drive forward the oil's motion. In a normal state, the shaft drives the oil film around. This creates a whirling motion of the shaft and causes it to rub and hit on the surrounding housing as shown in Figure (5.33a). In some cases, it may dampen, but this usually leads to vibration, friction and wear of the materials. Oil whirl can be caused by multiple factors like changes in oil properties, excessive bearing clearance and improper bearing design.
- **Oil whip:** Oil whip is similar to oil whirl as it is also caused by the liquid lubricant in hydrodynamic bearings where the shaft is driven around by the oil's erratic motion [200]. This occurs when the oil whirl frequency matches the system's natural frequency. This effect follows as a result of the oil whirl motion. In this mode, the oil moves in lateral and forward motion, moving the shaft along with it. Compared to the whirl motion, the whip motion causes the shaft to hit and rub the housing multiple times in one rotation and leads to non-circular trajectories of the shaft, as shown in Figure (5.33b). This effect leads to quick damage to the shaft and is usually encountered at high shaft speeds.
- **Touch rubbing:** Rubbing is a damaging mechanism that occurs in new bearing or in starting stages of the bearing operation where the shaft rubs against the bearing surface, as shown in Figure (5.33c), until the clearances are corrected. This is also a kind of wear mechanism.
- **Sintering:** Sauntering is the wear of the shaft and the bearing surface caused due to long-term lubricant starvation. It leads to wear, high friction and vibration of the shaft.

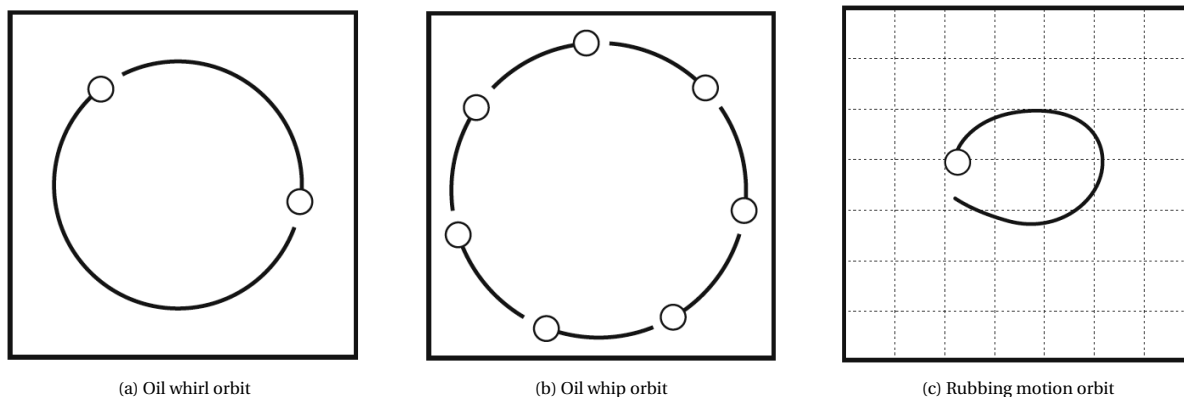


Figure 5.33: Shaft trajectory of sleeve bearing in different failure mechanisms [200]

After understanding the failure modes in sliding bearings, it can be observed that some causes are similar to the rolling bearings. But many causes that arise due to the difference in the construction of the bearings types are not the same, like precise alignment maintenance, strict assembly requirements and sensitivity to debris. Moreover, journal bearings also have the option of utilising plastics instead of metals which can overcome the drawbacks caused by metals. Apart from the above, some common causes of the failure modes in sliding bearings are stated below:

1. **Lubricant:** Lubricants are one of the major contributing causes of bearing failure in both types of bearings. In this case, the liquid lubricants cause damage due to their dynamics, which influence the shaft motion.

2. **High-temperature :** High temperature is both a cause and effect of failure mechanisms. High temperature in sliding bearings is caused by friction or high shaft speeds. The high temperature further changes lubricant properties, causing it to deteriorate. This forms a cycle that leads to damage to the bearings eventually.
3. **High speeds:** High speeds lead to an increase in the temperature of the lubricant. And as described above, it will lead to a cycle that will eventually lead to friction, vibration and wear of the shaft.

Now that the failure mechanisms of the roller and sliding bearings have been explored and their causes are known, the advantages and disadvantages of these bearing types are known. Based on this knowledge and the application's requirement, the most suitable bearing type will be chosen in the next sub-section.

5.6.6. Bearing type selection

Before selecting the bearing type for this application, it is necessary to review the bearing requirements of this application. Unlike other applications, the SADM is a very slow-moving mechanism. As calculated in Table (4.1), the maximum speed of the solar arrays is 0.04 rad/s which is close to 0.4 RPM. As the application is expected to be operational in space, the lubricants cannot outgas, and as the CubeSat standards specify, lubricants cannot be stored in enclosures. The maximum load expected in the application acts on the shaft, which is transmitted to the bearings. This maximum load was expected to occur during launch and was calculated as 250 N in section (4.3.3) as stated in SADM-BG-002. The bearing type will be selected based on these requirements as the main reasoning principle.

Rolling bearings:

Rolling bearings were one of the most commonly used bearing types in many applications. Ironically they were also one of the most commonly failing types of bearing in space mechanisms. The main research question for this section was to select a bearing that overcomes the drawbacks and failures caused by roller bearings. To answer this, the failure mechanisms and their root cause were found in the earlier section (5.6.4). It was found that the main causes of the roller bearing failure were lubricants, metals, alignment maintenance of balls, assembly and an uncontrolled environment. The external factors (assembly and uncontrolled environment) cannot be mitigated in the design phase. The internal factors can be accounted for in the design phase and selected for a design lifetime, but the main disadvantage with rolling element bearings is the need for proper contact of the ball with the raceways, which requires proper preloading throughout its lifetime across a wide range of temperature and loading conditions. It is very hard to practically realise and verify a spring system capable of meeting such a wide operation load range. Moreover, this bearing type is best suited for high and moderate RPM applications that require low friction at high RPMs. This application operates at low RPM and requires low friction at low speeds. Therefore, rolling bearings are not suitable for this application.

Sliding bearings:

Sliding bearings seem to overcome most of the failure root causes experienced with roller bearings. First and foremost, sliding bearings do not make use of rolling elements. Therefore, they do not require strict preload limits, which is crucial for the operation of roller bearings. Secondly, all kinds of sliding bearings do not require liquid lubricants to function. As shown in Figure (5.28), dry rubbing bearings use polymer materials with a low friction co-efficient surface. Moreover, the other sleeves bearing types are not applicable for this application as they require a liquid lubricant to be stored and pumped in certain cases. The dry rubbing sliding bearing overcomes multiple failure causes by eliminating the use of metals and lubricants. Contamination, decomposition and optimal level maintenance of lubricants were common causes of sliding and roller bearings failure. Failure mechanisms like corrosion and fatigue failure due to micro-structure change can be eliminated by avoiding the usage of metals. An entire plethora of failure mechanisms (refer 5.32 & subsection (5.6.5)) can be eradicated by avoiding the use of lubricants. But eliminating lubricants also leads to one big problem, which is increased friction. Fortunately, this application operates at extremely low speeds (0.4 RPM maximum) and has a lower lifetime of just 30000 revolutions in orbit compared to applications like reaction wheels that have a lifetime in the order of billions of revolutions in 5 years. Due to the low speed, the friction and wear experienced with dry rubbing sleeve bearings will be extremely low, thus making them a lucrative solution for this application. Therefore, **dry rubbing sleeve bearings** will be considered for use in this application. But precautions must be taken to ensure that these bearings do not cause more friction than what can be provided by the rotary actuator.

Now that a bearing type has been selected, the next step will be to find a COTS bearing of the same type that meets the application's requirements. This will be addressed in the next subsection.

5.6.7. COTS bearing selection

A company called Iglidur was found to make a wide range of dry rubbing polymer-based sliding bearings for various applications. The company offers various grades of materials suited for specific purposes as- G (general purpose), A (food-grade), H (media resistance), J (long-life applications), Q (high loads), F (electrically conductive & Electro Static Discharge (ESD) compatible), X and Z (high-temperature, chemical resistance & low moisture absorption) and R and D (low-cost & silicone-based). Among the various grades of materials offered by the company, the inappropriate materials for the application were eliminated first; this included material categories - G, A, F, R, Q and D. These categories of materials have been eliminated because they are designed for terrestrial applications (not vacuum compatible & radiation tolerant), have higher percentages of moisture absorption, not capable of handling high shock loads, and grade-F material is electrically conductive which is not desirable as it can cause micro-welding as discussed earlier.

Trade-off process, criteria and rationale

The remaining materials options are - H, J, X and Z. The properties of these materials will be compared and traded off in Table (5.24) with the application's requirements. If the material's specification meets or exceeds the requirement, the cell is coloured in green, and the corresponding material is awarded a score of 1. If the material's specification does not meet the requirement, the cell is coloured in red, and the corresponding material is awarded a score of 0. The material with the maximum final score is selected as it meets most requirements. The trade-off criteria used for this process were the bearing dimensions, coefficient of friction, surface pressure, vacuum operation, radiation tolerance, operating temperature range and service life. The trade-off criteria and their rationale are stated below:

1. **Bearing dimensions:** The bearing dimensions were chosen as a trade-off criterion because the bearing has to fit within the housing as defined in SADM-BG-001. It was found in section (5.5.7) that the optimal shaft diameter for arranging all the wires around the shaft and considering strength was 4mm. Therefore the bore diameter of the bearing shall be 4mm. This can be made lower by step-turning the shaft but it is not desirable as it will reduce the strength of the shaft. The outer diameter limit is kept as 6.9 mm, the maximum height of the housing, but the bearing's outer diameter will have to be lower than this dimension as it has to fit within the housing.
2. **Coefficient of friction:** The coefficient of friction was chosen as a trade-off criterion because the lower the friction, the lower the dissipative effects like wear, noise and heat.
3. **Surface pressure:** The surface pressure (P_{SP}) was chosen as a criterion because the bearing has to withstand the launch load of 250 N as specified in SADM-BG-002. The approximate maximum surface pressure expected to act on a sleeve bearing with a dimension of 4mm inner diameter and 5.5 mm is calculated below and was found as 21 N/mm^2 . The bearing length was chosen as 3mm for this calculation because, 3 to 12 mm was found to be the range of bearing length dimensions corresponding to 4mm inner diameter of sleeve bearings from Iglidur datasheets [60] [61], and as the surface pressure is inversely proportional to the length, the minimum length was chosen to get the maximum surface pressure.

$$P_{SP} = \frac{F_{\max}}{LD} \quad (5.53)$$

$$P_{SP} = \frac{250}{4 \times 3} = 20.833 \text{ N/mm}^2 \sim 21 \text{ N/mm}^2 \quad (5.54)$$

4. **Operation in vacuum & radiation tolerance:** As the system should be operational in the space environment as specified in SADM-BG-003, it is necessary that it must not outgas in vacuum conditions and should not deteriorate under the influence of radiation; the criterion of vacuum operation and radiation limit were chosen as the trade-off criteria. The materials tested in vacuum have been highlighted in green, whereas the materials that have not been but require a customised version to be applicable

are highlighted in orange. The limit of 10 krad on radiation was set because it was found by simulations in section (5.1.4) that a 3mm thick aluminium allows 10 krad of TID over a period of 5 years which is the design lifetime of the SADM system.

5. **Operational temperature:** The operational temperature was chosen as a trade-off criterion as the bearing must not change its properties within the operational temperature range of the system as stated in SADM-ENV-003.
6. **Service life:** The service life was included as a trade-off criterion because it determines the feasibility of the solution over its design lifetime. The service life required for this application was calculated to be 43000 hours considering five years of continuous operation (5 years × 365 days × 24 hours). The service life was obtained from the service life calculator of the Iglide bearings [59] for load conditions:
 - Bore diameter: The bore diameter was chosen as 4mm, corresponding to the shaft diameter.
 - Maximum dynamic load: 250 N was calculated as the maximum force due to launch loads.
 - Radial static load at rest: 10 N is the weight of the solar array on Earth.
 - Maximum temperature: 125 C was defined as the maximum operating temperature of the system.
 - Minimum temperature: -65 C was defined as the minimum operating temperature of the system.
 - Nominal RPM: 0.02 RPM is the average rotational speed of solar arrays in sunlit and eclipse regions (refer to Table 4.7).
 - Shaft material: Stainless steel - The shaft material is made of stainless steel, considering its strength.
 - Housing material: Aluminium - The bearing housing will be made of aluminium to match the thermal expansion of the SADM housing.
 - Maximum radial clearance: 0.025mm - This was the minimum permissible wear allowed by the software. The minimum value was chosen because minimal wear is desirable for any application to increase its lifetime.

Based on these environmental and load conditions, the software calculated the service life of the different bearing material types, as shown in Figure (A.19); this is used in the trade-off table.

Bearing material type	Bore & outer diameter (mm)	Co-efficient of static friction	Surface pressure limit (MPa)	Vacuum operation	Radiation limit (krad)	Operating temperature range	Service life (h)	Total
Requirement	4 & < 6.9 mm	Least possible	21	Necessary	10 krad	-65 to 125	43800 hrs	Max
J350	4 & 5.5	0.1 - 0.2	60	Possible	20	-100 to 180	610000	5
L350	4 & 5.5	0.07 - 0.18	60	Possible	20	-100 to 180	1993	4
L500	4 & 5.5	0.08 - 0.15	70	Possible	30	-100 to 250	2400	4
H1	4 & 5.5	0.06 - 0.2	80	Possible	20	-40 to 200	1400	3
Z	4 & 5.5	0.06 - 0.14	150	Tested	10 ⁴	-100 to 250	92072	7
X	4 & 5.5	0.09 - 0.25	150	Tested	2 x 10 ⁴	-100 to 250	5075	5

Table 5.24: COTS-bearing-selection

As depicted in the trade-off table above, **Z-type material** was the most **suitable material** for this application among the many polymer options of plain bearings offered by Iglidur. This material meets almost all the bearing requirements of this application, like dimension limit, least coefficient of friction, surface pressure, vacuum compatibility, radiation tolerance and operating temperature range. Compared to the other materials, this material exceeds the required service life by a factor of two. The J350 material had the highest service life for the given environmental and load conditions but it was known from communications with the company that the X and Z family of materials were the only materials tested for operation in vacuum conditions. Moreover, the Z-type material has a maximum moisture absorption level of 1.1 % of weight as compared to 1.6 % for the J350 material. Thus, making the Z material as the best-suited choice for the J350. The complete data sheet of this bearing is attached in (A.8).

The appropriate COTS bearing and the material have been selected. It was discussed in the sub-section (5.6.5) that even though these dry rubbing polymer-based sliding bearings overcome most of the drawbacks of the rolling element bearings, they have the disadvantage of high friction. Even though the selected bearing has

a low coefficient of friction, it is important to find if the maximum friction generated by this bearing is lower than the torque produced by the motor and the gearbox combination. The next sub-section will be aimed at finding this.

5.6.8. Bearing friction & load calculation

The bearing friction can be divided into two types based on the velocity of the shaft. If the shaft is stationary, then static friction is applied by the bearing on the shaft. If the shaft moves relative to the bearing, then dynamic friction comes into effect. The motor has to overcome this resistive motion to drive the solar arrays. The friction characteristics of the selected bearing are given in A.22 and as shown in Figure (5.34). The static and dynamic friction of the selected bearing will be calculated in the consequent sub-sections.

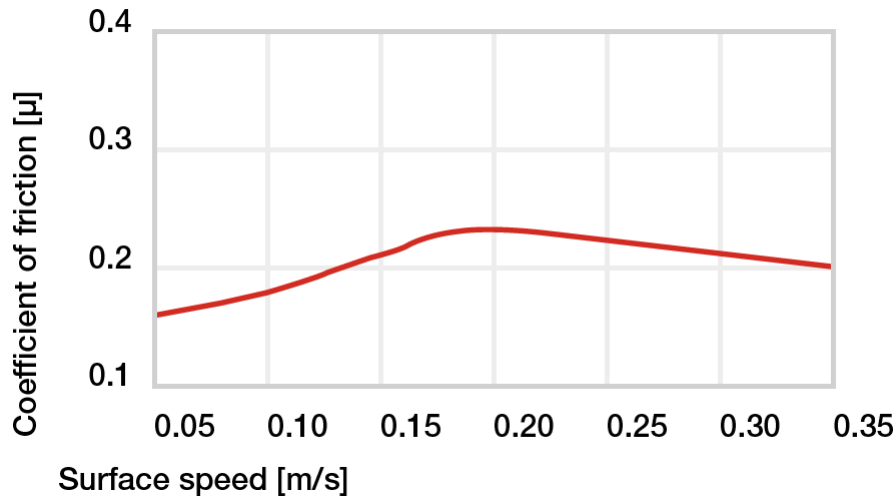


Figure 5.34: Friction co-efficient versus surface speed of Z-type plain bearing A.22

Static friction calculation

The friction coefficient corresponding to zero velocity in the graph (5.34) is close to 0.18 which is the static friction coefficient of the Z-type bearing. The static friction for this value is calculated as below:

$$f_s = \mu_s N \quad (5.55)$$

As static friction depends on the normal force, the normal force applied by the bearing surface on the shaft in ground conditions is just the weight of the solar arrays calculated below. The ground condition is considered to calculate the static friction because this is the maximum normal force that can occur during the operational period of the bearing as compared to when it is in space where the gravity is in the order of micro m/s^2 .

$$N = mg = 1.1 \times 9.81 = 10.791 N \quad (5.56)$$

The static friction corresponding to this normal force is calculated as below:

$$f_s = 0.18 \times 10.791 = 1.94 N \quad (5.57)$$

The static friction torque corresponding to the static friction is expressed in the equation below:

$$\tau_{fs} = f_s \times r \quad (5.58)$$

The friction torque corresponding to this static friction value is calculated as shown below, where the radius of the bearing is 2mm. The friction torque is calculated so that it is easy to compare with the actuation torque produced by the motor.

$$\tau_{fs} = 1.94 \times 2 = 3.88 Nmm = 0.00388 Nm = 3.88 mNm \quad (5.59)$$

Dynamic friction calculation

To calculate the maximum dynamic friction coefficient, the maximum speed of the shaft must be known. The maximum speed of the shaft was calculated as 0.04 rad/s as stated in Table (4.7). This is equal to 8×10^{-5} m/s. This corresponds to a very small increase in the friction coefficient value compared to the static friction value found in Figure (5.34) as this value is very close to zero. Calculating the friction value for this minute change in the dynamic friction coefficient does not render much significance. The dynamic friction coefficient can also vary with temperature and surface roughness caused by wear over the lifetime. This effect is hard to predict or model, therefore the maximum friction coefficient (0.25) plotted in the graph will be selected, and the dynamic friction will be calculated for this value to get a rough estimate of the worst-case friction that can be encountered in the application's lifetime considering unpredictable effects like temperature-induced effects and wear of the surface. The expression to calculate the dynamic friction force is as shown below:

$$f_d = \mu_d N \quad (5.60)$$

The worst-case dynamic friction force for the maximum dynamic friction coefficient value of 0.25 is as calculated below:

$$f_d = 0.25 \times 10.79 = 2.7 \text{ N} \quad (5.61)$$

The torque due to this dynamic frictional force as a function of the bearing radius & dynamic friction is shown in the expression below:

$$\tau_{fd} = f_d \times r \quad (5.62)$$

The worst-case dynamic friction torque for the application is as calculated below:

$$\tau_{fd} = 2.7 \times 2 = 5.4 \text{ Nmm or } 0.0054 \text{ Nm} \quad (5.63)$$

As every application requires two bearings to support the shaft, the static and dynamic frictions calculated will be twice the calculated values. In this case, the maximum dynamic torque for this application will be 0.0108 Nm. The dynamic friction value is 130 times lower than the torque provided by the combination of the motor, gearbox and the external gear, which was calculated as 1.44 Nm in section (5.3.4). This theoretically verifies that the chosen bearing is compatible with this application from a torque balance perspective.

Summary of bearing friction calculation

The static and dynamic friction values will be twice the calculated values as two bearings will be utilised; these values are summarised in Table (5.25) below. As highlighted in the table, the maximum friction and friction torque values occur in the dynamic case.

	Friction force (N)	Friction torque (Nm)
Static	3.88	7.6×10^{-3}
Dynamic	5.4	1.08×10^{-2}

Table 5.25: Summary of bearing friction calculation for two Z-type sliding bearings

The selected bearing will be integrated with the SADM as discussed in the next section.

5.6.9. Summary of bearing selection

At the beginning of this chapter, a research objective for this section was set, which was to select a bearing that overcomes the failure modes encountered with conventional roller bearings that caused most of the failures in space mechanisms and to size the bearing such that it meets the current application's requirements. To answer this question, the failure mechanisms of the roller bearings were explored in detail, and it was found that the root cause of most of these failure mechanisms were lubricants, inherent metal structure defects and the need for maintaining proper alignment of the rolling element and the difficulty in achieving it.

5.6. Bearing selection

Dry rubbing sliding bearings made of polymers seem to overcome most failure mechanisms by eliminating the causes -lubricants, metals, and rolling elements. But this type of bearing had the disadvantage of having higher friction than roller bearings. Due to the low speed and low application force encountered in this application, the resulting friction is also low, making it the most suitable choice. A COTS product, the Z-material type sliding bearing made by Iglidur A.20 was found to be the most appropriate bearing for this application's requirement and does not involve failure-causing elements that are a part of roller bearings.

5.7. Position sensing

In this section, the position sensor required to estimate the solar array position will be explored. This is done by firstly exploring the purpose of the position sensing element in sub-section 5.7.1. The SADMs requirements are then translated to the position sensing element in sub-section 5.7.2. Based on the requirements, the position sensor specifications are calculated in sub-section 5.7.3. The design options of the position sensors are explored in sub-section 5.7.4 followed by the trade-off and technology selection in the same section. The section ends with a summary 5.7.5 of the design decisions accomplished within this section.

5.7.1. Purpose

Even though the actuator selected for this application is a stepper motor that works on an open loop feedback where the number of steps made by the stepper motor can be kept account of by counting the number of control pulses, it is beneficial to have a position sensor for this application because of two reasons:

- The Flex-wrap has a rotation angle limit of ± 180 degrees & beyond the limit the flex PCB would get damaged. So the knowledge of a reference position of the shaft is necessary to prevent overshooting this defined range of rotation.
- The position knowledge of the shaft is also good to know when the ADCS is not powered or when the SADM has just rebooted. Then the shaft position can be used to compute the solar array position and rotated to the required position.

5.7.2. Requirements

The SADM requirements that are pertinent to the position sensor are SADM-PER-001 and SADM-PER-002. Apart from these requirements, the position sensor must also fit within the housing in order to be compatible with requirements SADM-INT-001 & SADM-INT-002. This would mean that the position sensor must fit within the 6.5mm height limit. As applicable for all other elements and components of the SADM, the position sensing element must also comply to the launch and space environment as stated in requirements SADM-ENV-001 to SADM-ENV-011.

5.7.3. Position sensor requirement calculation

To size and select the position sensor, two main parameters must be known, the resolution of the sensor and the update frequency at which the measurements must be made. There are also other performance parameters that quantify sensor performance like accuracy, precision and linearity. But these two parameters are sufficient for a preliminary selection and will be calculated in the following sub-sections.

Angular resolution

The pointing accuracy of the solar panels was defined to be ± 8 degrees as stated in SADM-PER-001. This would mean that the position sensor should have a minimum resolution of 8 degrees.

$$\theta_{res} = 8^\circ \quad (5.64)$$

Converting this to digital resolution:

$$\frac{360^\circ}{2^n} = 8^\circ \quad (5.65)$$

Solving for which:

$$n \sim 6 \quad (5.66)$$

Therefore, the sensor resolution should be greater than 6-bits for this application.

Update frequency

Update frequency states the number of measurements that have to be made by the sensor in unit time. This is mainly defined by the maximum speed of the shaft because the position sensing element would have to make the required measurement for the worst case of the application. If the position sensing element can make measurements in the worst case of the application in terms of speed, it can make the measurements at the required frequency also during other operation scenarios. The maximum speed of the solar arrays was

found to be 0.4 RPM as summarized in Table 4.6. The update frequency required for this speed is calculated as below:

$$\frac{0.4}{60} = 6.66 \times 10^{-3} \text{ Hz} \quad (5.67)$$

This is less than 1Hz, so any sensor with more than 1Hz update frequency would suffice for this application. The low update frequency required is due to the low RPM operation of the SADM.

5.7.4. Position sensor design options & trade-off

Position sensors can be classified based on continuity of position measurement and the working principle they use to measure position. Based on the continuity of position measurement, position sensors are classified as incremental and absolute encoders. Incremental encoder can only give the change in position which is useful to measure the speed & distance. Incremental encoders also lose track of reference position once powered on and off which would make them unsuitable for this application. Absolute encoder gives the exact position of the shaft at any given time which is useful to measure angular position. This application requires the shaft position knowledge at any given time. This is why the absolute encoder is the right choice for this application.

Based on the working principle used to measure position, position sensors are classified as stated below:

- **Potentiometric:** Potentiometers have a contact surface that moves along a resistive track and as the length changes, the voltage measured across the line changes which is used to compute the position. As they are contact based they can be easily damaged due to vibrations, they also use lubricants that may outgas in space. Therefore, they are not suitable for this application.
- **Optical:** Optical position sensors are usually termed as encoders. They have a light source that is made to pass through a slotted disc or reflected. The gratings have different slit widths or grey codes that correspond to the unique position location. This technology is not suitable for this application because optics darken in space due to radiation. Customization of optics used in encoders are difficult to achieve as they are mass produced.
- **Magnetic:** Magnetic position sensors are also called as encoders and have a similar working principle as the optical encoders but use magnetic poles instead of gratings to measure position. If the magnetic pulses are converted to voltage then it is a Hall-effect sensor that is the most common magnetic sensor.
- **Capacitive:** Capacitive encoders make use of the capacitive effect to measure position. The capacitance between two surface depends on the distance of separation between them, dielectric constant of material between them, percentage of overlap and area of the plates. A capacitive encoder can make measure the change in any of these parameters to measure distance.

A search was conducted for COTS magnetic and capacitive encoders, many of them met the resolution and update frequency requirement but none of them met the dimensional requirement of 6.5 mm. This means that the requirement SADM-IF-001 and SADM-IF-002 cannot be met using COTS encoders. An encoder has to be custom-designed which is not feasible within the scope of the thesis.

Alternatively, the reference position could be set by using a mechanical stop or a magnetic sensor switch. The search for the appropriate magnetic switch could not be conducted within this thesis, therefore a mechanical stop would be used and the author would recommend further investigation into position sensors and designing them if required.

5.7.5. Summary

In this section, the position sensor was found to be required to measure and keep track of the position of the shaft to prevent it from crossing the 180 degrees rotation angle limit and to control its position. A minimal resolution of 6 bits and an update frequency of 1Hz or more was found to be required. Magnetic and capacitive encoders were found to be suitable technology options but none of them were available in the dimensions required. Therefore, this aspect of the design will be left for future work.

5.8. Chapter summary

This chapter designed the main elements of the SADM by converting the design calculations made in chapter 4 and by considering the requirements and constraints defined in chapter 3. The chapter started by designing

a modular housing that drives only one solar array such that it is applicable to more than one panel mounting configuration. The housing will be fabricated out of Al-6061-T6 with a shielding thickness of 3.5 mm in parts covering the electronics. The stepper motor was found to be the right rotary actuator technology for this application because of its positional accuracy and good low RPM performance (absence of cogging torque). The Faulhaber DM0620 stepper motor was the best-suited one considering power, cost, shorter lead times and gearbox availability. It was also found that a mechanical power transmission system (gearbox) was required to alter the torque produced by the motor to achieve a higher torque value which the current application needs. A motor gear box with a gear ratio of 4096 and an external bevel gear with a gear ratio of 3 was designed to optimise the gear for inertia matching, torque amplification and maximum power transfer. The bevel gears will be made of PEEK considering shock absorption, low wear and lubrication-less functioning. Four stainless steel M3 bolts were chosen as the mechanical interface by sizing them considering preload and strength to withstand launch forces. A 25-pin nano-D connector [57] was chosen as the data interface between the SADM and the CubeSat mounted systems. A 9-pin micro-D connector [67] with 2A current limit was chosen as the power interface. A new power and data transfer mechanism has been designed and termed as the **Flex-wrap** that combines the best features of the cable wrap and goose-neck while overcoming drawbacks of the slipring (by eliminating brushes). The Flex-wrap uses a spirally coiled Flexible Printed Circuit to transfer power and data while allowing rotation by coiling and uncoiling. The Z-material type sliding bearing made by Iglidur A.20 was found to be the most appropriate bearing for this application's requirement and does not involve failure-causing elements that are a part of roller bearings like metals, need for preload maintenance, rolling elements and liquid lubricants. The next chapter will be aimed at integrating these elements in to one sub-system.

6

System integration

The previous chapter had described in detail about the design of each element of the SADM by exploring the design choices, trade-off and technology selection based on the requirements and finally the component design in the case of custom-made components like gears and the Flex-wrap's FPC. This chapter will bring together all these components by discussing how they will be integrated into the SADM, followed by evaluating the verification of the requirements. This chapter aims to answer the research question 3 by detailing the verification approach taken to verify the requirements. In order to achieve this, the chapter starts with a description of the resultant SADM design in section 6.1. The elements of the SADM have to be integrated mechanically and electrically, therefore the section describes the mechanical and electrical integration of the elements in sections 6.2 and 6.3 respectively. The key design features of the current SADM is the modularity and scalability, this dimension of the design is explored and verified in sections 6.4 and 6.5. The verification approach used to verify the requirements within this project and the verification plan for verifying requirements that could not be verified are discussed in section 6.6. The chapter ends with a summary in section 6.7.

6.1. Design description

The Figure (6.1) below shows the components of the SADM. The motor rotates the bevel gear attached to it and as a result the bevel gear attached to the shaft meshes with the motor's gear rotates thereby rotating the solar arrays attached to the shaft. The FPC of the Flex-wrap being spirally wound and attached to the shaft coils and uncoils as the shaft rotates clock-wise and anti-clockwise, thereby allowing rotation of the solar panels and also transferring electrical power from the solar arrays to the power interface mounted on the side of the SADM. The power and data interface attached on the right side of the housing distributes this power to data to the SADM system and other systems outside the CubeSat like the EPS & CDH. The shaft is supported by the two bearings placed towards the back of the housing and are held in place by their respective housings. The control circuits in the housing are responsible for the motor's operation. The design features of the system and each component will be described subsequently.

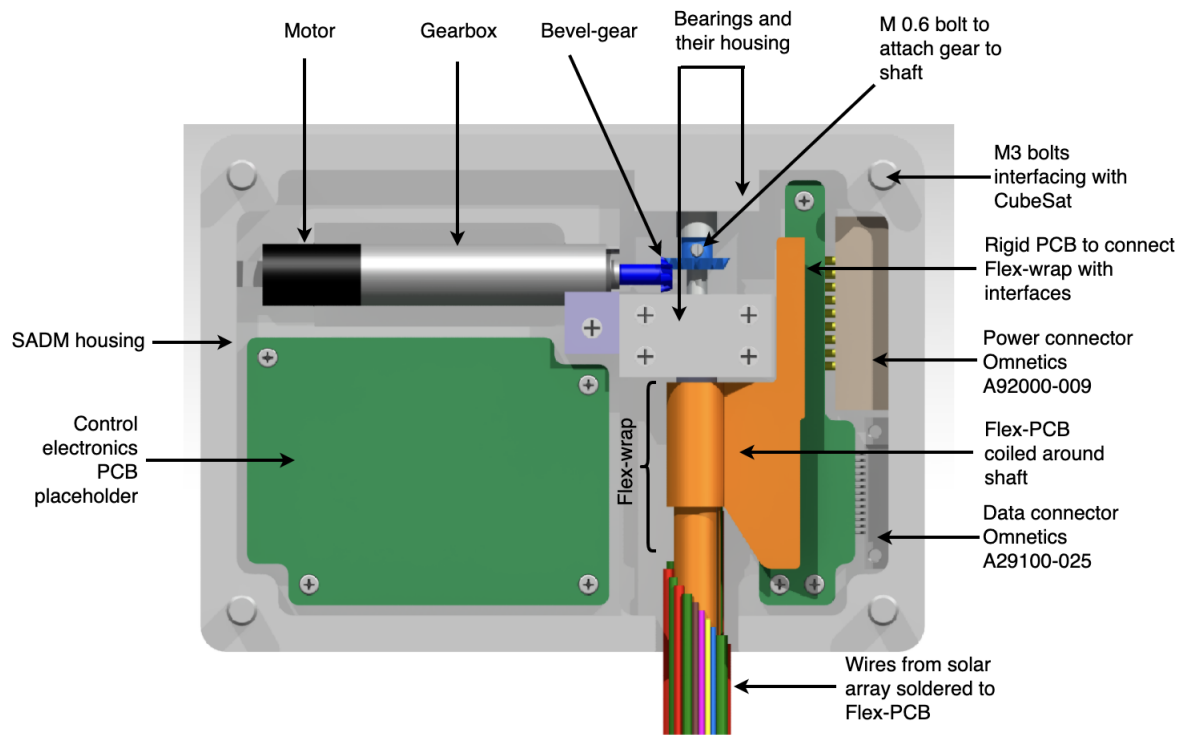


Figure 6.1: The SADM and its components labelled

Housing design

One of the first components of the SADM to be designed was the housing as it set an initial boundary on the dimensional constraints for the enclosed components. It was mentioned in section (3.2) that the housing shall be aimed to fit within $83 \times 83 \times 6.9$ mm in order to be compatible with the smallest CubeSat (3U). This was obtained from one of the design requirements SADM-DES-002. According to SADM-DES-003, the system shall also be modular in design such that it can drive more than one panel and it shall not extend beyond one plane as defined by SADM-DES-004. The housing was designed by considering all these design requirements and the resultant design is depicted in Figure (6.1). The housing drives one solar array to be applicable to multiple panel mounting configurations. The housing also has a shielding of 3.5mm as calculated in section (5.1.4) to allow a total absorbed radiation dose by internal electronics to less than 10 krad for the lifetime of five years. The shielding has been made variable so that the shielding material thickness of 3.5 mm is applicable only for the electronics. The thinnest part of the housing is 0.5 mm thick and is found in the region just below the shaft. Other components that are less susceptible to radiation like motor, shaft, FPC of the Flex-wrap, interfaces and bearings have a lower material thickness beneath them so that they can fit within the housing. It can be observed that the housing is not symmetric with respect to the placement of the shaft. The shaft has been placed at an offset from the center axis of the housing. This was done to save space. The gear had to be placed perpendicular to the shaft, the interfaces could be placed in the same orientation as the motor so that the housing is symmetric, but this would increase the dimensions of the housing exceeding the dimensional requirements. In result the housing was found to have a dimension of $70 \times 50 \times 6.9$ mm, which is very well below the defined dimensional requirement. The housing was made smaller than required dimensional limits by minimising the control electronics area. This was done on requirement of AAC Hyperion to keep the electronics area to the least minimum area possible. The housing has rounded edges externally and internally in the cut sections to avoid concentration of stresses in the corners. The motor sits on a mating cavity within the housing that is semi-cylindrical in shape. This cavity restrains the motor from moving forward or back. The cavity when machined could have tolerances resulting from the machining and there might also be differences induced due to the motor's dimensional tolerances which may cause error in fitting and alignment of motor axis with shaft axis. This has to be accounted for by calculating and considering the machining tolerances while manufacturing the housing. The excess tolerances and clearances can be accounted for by using glue to mount the motor to the cavity. The bearing mount has an extrusion towards its left side that clamps the motor on the top side, thus preventing the motor from counter-rotation. The

housing also has cut-outs on the side to allow the interfaces to fit within. The housing will be fabricated out of Aluminium 6061-T6 series grade because of the reasons stated in section 5.1.4. Therefore, housing would be machined using Computer Numerical Control (CNC) machine out of a single block of Aluminium.

Shaft design

The shaft is a solid piece of a cylindrical element that connects the motor to the solar arrays and is supported by the bearings. The shaft has a diameter of 4mm and will be made of stainless steel, considering its strength. The shaft will be made of two parts that will be joined to each other by screw-thread. This is shown in Figure (6.2). The shaft was made of two parts because the gear had to be fit into one of them, and the gear had a maximum diameter of 5.6 mm (Refer to Table 5.12) which meant the shaft of the gear was lower than 4mm and this had to be pushed into the shaft from one end. The final dimensions of the shaft have to be arrived upon by considering tolerances and fit with the bearings. The shaft must have slide fit with the bearings so that they can rotate. This would mean that the shaft must have a diameter few micrometers less than the inner diameter of the bearings. This would have to be determined based on differential thermal expansion of the shaft and bearing for the operating temperature range.



Figure 6.2: Two parts of the shaft

The next sub-sections will describe the assembly steps, mechanical and electrical connections of the SADM.

6.2. Mechanical integration

All the components have to be fixed on the housing mechanically to hold them in place. The components must be firstly mechanically assembled to allow electrical connections. The order of assembly of the components and the method of mechanical integration for each component are described below:

1. **Motor to housing:** The motor has to be first joined with the gearbox. Then this combination has to fit into the housing. As mentioned earlier, this will be achieved by mounting the motor to the semi-circular cavity in the housing. As the motor is constrained by removable attachments, it can be disassembled easily. The motor can also be fixed using adhesive to achieve a permanent joint before launch.
2. **Bevel gear to motor:** The bevel gear will be mounted to the motor utilizing a key that tight fits into the keyhole between the motor shaft and the gear.
3. **Bearing to housing:** The bearing has to be first inspected with a pin gauge to determine if it matches the dimensions and tolerances. Using an arbour press, the bearing is then press-fitted into the custom-made bearing housing. The bearing is also inspected for dimensions after fitting using a pin gauge. A pin gauge is a tool with a particular diameter, which is dropped into the bearing. If the pin slides without stopping the bearing has been fit perfectly and if it does not, the bearing was wrongly fit. The bearing housing is then attached to the SADM housing using M 1.7 screws as they were dimensionally compatible to fit four of them within the housing. The bearing housing will also be aluminium to avoid differential thermal expansions.
4. **Bevel gear to the first part of shaft:** The driven bevel gear will be attached to the first part of the shaft using a micro-screw that passes through the bearing and the shaft. It has to be ensured that the gear mates and inter-meshes with the driver gear attached to the motor. This can be adjusted manually by rotating the driven gear.
5. **Wires soldered to FPC:** The FPC must be firstly inspected for errors and adherence to design. The wires coming from the solar arrays must then be soldered to the FPC as shown in Figure 6.3c by keeping them on a flat surface. The next step must be carried out after the solder has dried.

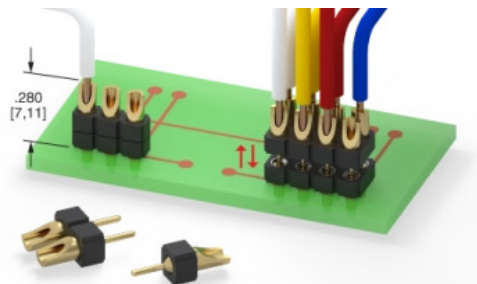
6. **FPC to shaft:** The most challenging part of the assembly is attaching the FPC to the shaft. The FPC has to be bonded to the shaft using adhesive. Length equal to the circumference of the shaft has to be applied with glue on the FPC and then wound around the shaft. The FPC can uncurl itself due to its spring-like nature. The coiled FPC must be kept in position using a jig that clamps and holds the coiled FPC in position. The adhesive of choice is 3M Scotch-Weld 2216 epoxy adhesive. After curing the adhesive for at least 24 hours, the next step must be carried out.
7. **Second part of the shaft to first part of shaft:** The second part of the shaft to which the FPC is now bonded can be simply attached to the second part by screwing it in. The inner part of the thread can be impregnated with industrial-grade thin adhesive to achieve a permanent connection before launch and to prevent loosening when rotating in the anti-clockwise direction.
8. **FPC to connector:** The other end of the FPC has to be connected to the electrical and data interfaces. The second PCB on the right-hand comes in handy for this purpose. The FPC is connected to these interfaces by soldering wires from the connector or by using connectors mounted on the PCB like Zero-Insertion Force connectors for FPC. Connectors would be much preferable as they allow disassembly but the choice depends on the electronics designer and the space available.
9. **Control circuits to housing:** The control circuits are connected to the housing by M1.4 stainless steel screws as there would be not much force acting on the PCB. A rubber or silicone-based o-ring can be used between the housing and the PCB to avoid direct contact of PCB with the housing and dampen vibrations.
10. **SADM to CubeSat:** The SADM is connected to the CubeSat structure by means of the four stainless steel M3 bolts as described in section (5.4.3). This step is carried out after the mechanical and electrical integration. Measuring the torque applied to tighten the bolt to achieve the required preload is important. This must be done using a torque wrench or a hydraulic preload.

6.3. Electrical integration

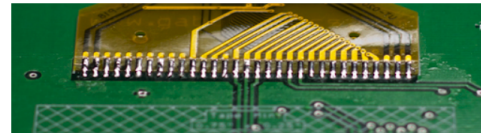
This section will describe about the electrical connections between the components.

1. **Solar panel wires to FPC:** The wires from the solar panels are arranged around the shaft in a circular layout. The wires have increasing lengths in such way that they form the diagonal of the FPC. This was a design choice to accommodate as many wires as possible as the rectangle's diagonal hypotenuse is the longest side. The wires will be connected to the Flex-wrap's FPC by soldering as shown in Figure 6.3c.
2. **FPC to interface connection:** The other end of the FPC will interface with the electrical and data interface of the SADM through the second rigid PCB on the right-hand side. The FPC will be connected to the rigid PCB ideally using a connector as shown in Figure 6.3d, and the wires from the power and data connector will also be soldered to the corresponding pads of the rigid PCB. Thereby serving as a connection board between the two. If the interfaces do not fit within the rigid PCB or if the mating interfaces meeting the dimensional requirements are not found, the FPC can be soldered to the rigid PCB as shown in Figure 6.3c and the wires from the data and power connector can be connected to the rigid PCB using connectors shown in Figure 6.3a.
3. **Inter-connection between the two rigid PCBs:** As the electrical and data interface bring regulated power from the EPS and satellite attitude knowledge data and commands from the CDH and as they interface with the rigid PCB on the right-side, the two rigid PCBs must be connected to each other. This connection will be achieved by Hirose DF-13 connectors.
4. **PCB connection with motor:** The motor also has a FPC connector that has to be connected to the control circuit PCB. This is achieved by a ZIF connector mounted on the PCB. This connection allows the control circuit to send pulses and control the stepper motor.
5. **SADM to CubeSat systems** The SADM has the two connectors on the left side of the housing, there would be mating connectors connecting the SADM to the CubeSat systems like the EPS. A hole would have to be made on the CubeSat structure for these wires to pass through. As the current SADM design

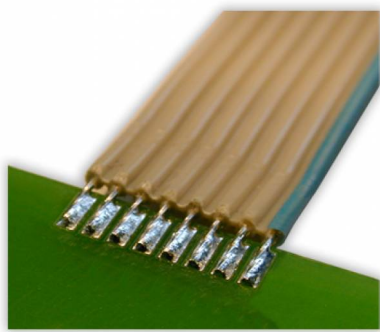
does not occupy all the area of a face compared to other SADMs, making a hole on this face for passing the wires would not be hard.



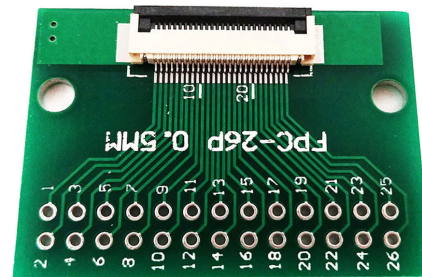
(a) Power interface to PCB



(b) FPC soldered to rigid PCB



(c) Wire soldered to PCB or FPC



(d) Zero-insertion force connector

Figure 6.3: Electrical connection methods

6.4. Modularity

One of the key consideration in designing the SADM was to design it modular for multiple panel mounting configurations as stated in SADM-DES-003. This requirement was considered while designing the housing and the housing shape was designed to be compatible with 5 or more panel mounting configurations as shown in Figure 5.1. Modularity in the design is achieved by driving a single solar array by one SADM system so that they can be combined in various combinations to attain different panel mounting configurations as required by the customer. Four SADMs mounted on the top face of the 12U CubeSat as shown in Figure 6.4, demonstrate this fact that the designed system is modular and fits within the dimensional constraints of the 12U CubeSat. Thus, satisfying requirements SADM-INT-001, SADM-DES-003 & SADM-DES-004. Observing Figure 6.4, it can be seen that a lot of space is left on the top face, this provides advantages such as weight saving and allowing area for payloads to have a viewing cut-out on the face where the SADM is mounted. This is not possible with common SADMs [1, 18, 46] that take up the entire face area. The SADM can also be mounted on other faces of the CubeSat as shown in Figure 5.1 but an XL deployer would have to be used.

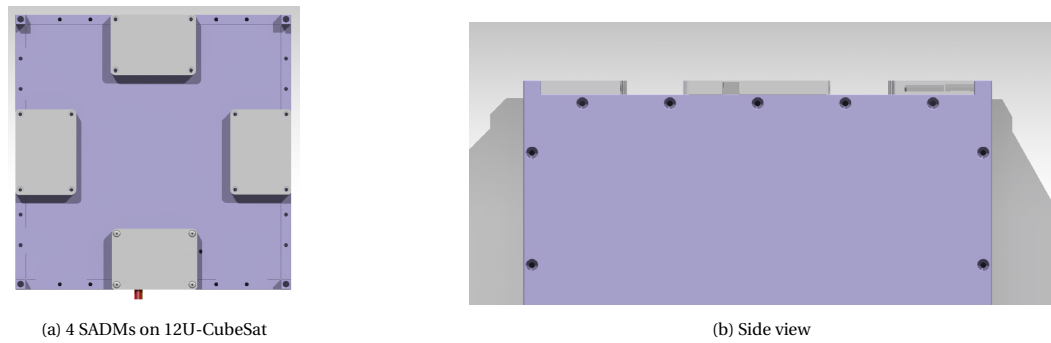


Figure 6.4: The SADM fitted to a 12U CubeSat

6.5. Scalability

Even though, the SADM was designed to be applicable specifically to a 12-U CubeSat, considering its low dimensional form factor the SADM can be applied to a wide range of CubeSat sizes. The SADM is also scalable to be applicable in 3U, 6U & 8U size CubeSats as shown in Figures 6.5 and 6.6. As they are applicable to smaller CubeSats, they are also dimensionally compatible with bigger CubeSats such as 16U, 24U and 36U. The mechanical and electrical requirements of these bigger CubeSats would exceed the current design specifications therefore, the current SADM shall not be considered to be applicable for these sizes of CubeSats. Scalability comes at a cost. As the current SADM has been optimised for a 12-U CubeSat in terms of electrical power transfer and mechanical power requirements, even though the SADM is scalable to different CubeSat sizes, it would not be optimised for performance. The current SADM has enough power lines with current and voltage handling capacity to meet the power requirements of smaller CubeSats (3U, 6U and 8U) but in this case it would be over-designed. For a 3U CubeSat that has a smaller solar panel compared to a 12U CubeSat results in lower solar cells per panel which would further result in lower currents and voltages. This would mean that the FPC of the Flex-wrap would not have to be 11.25 mm wide as in the current SADM. The FPC can be much lower in width which would lead to lower dimensions of the housing in its breadth direction. The mechanical power transfer system of gears and motors have been optimised to match the inertia, torque and power transfer efficiency of a 12U size solar panel. The same gear ratio is not optimum for other CubeSat sizes that would have a different solar panel size resulting in different mechanical power requirements. Therefore, the author would strongly recommend designing a different version of SADM optimised for smaller CubeSats like the 3U CubeSat. The current SADM as it is can be applied to two faces of the 6U CubeSat that have dimensions of 360 x 210 mm. The SADM designed for the 3U can be used on the other two faces of the 6U CubeSat. As the designed SADM fits to these different sizes of the CubeSats, it meets the requirement SADM-DES-002 as well by digital fit check or inspection.

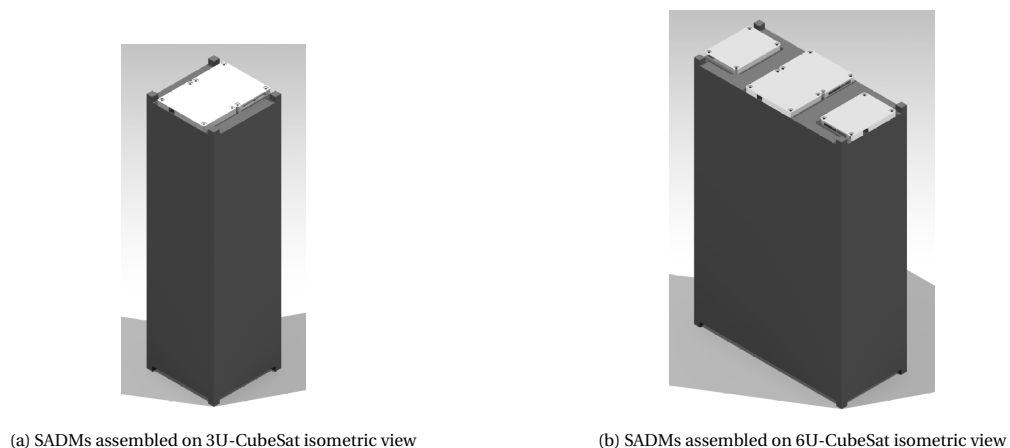
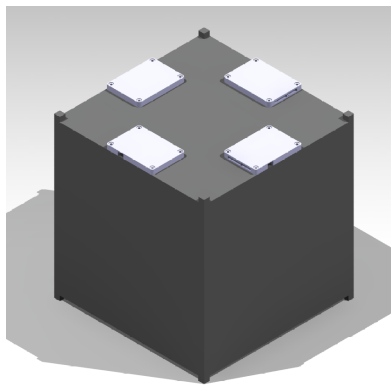
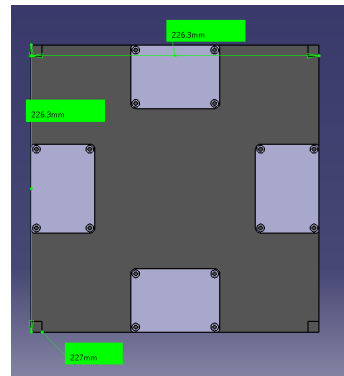


Figure 6.5: Scalability of the SADM to 3U and 6U CubeSats



(a) SADMs assembled on 8U-CubeSat isometric view



(b) SADMs assembled on 8U-CubeSat top view

Figure 6.6: Scalability of the SADM to 8U CubeSat

6.6. Verification

Considering the time constraint of the thesis, the prototype could not be fabricated. Therefore, requirements that had to be verified by demonstration and testing could not be verified. As the SADM was designed on CAD and verified for dimensional compatibility with different CubeSat structures, it fulfilled multiple interface and design requirements as shown by the Table below (6.1).

Identifier	Requirement	Verification rationale
SADM_INT_001	The system shall be compatible to fit on the external surface of a CubeSat of standard size 12 U.	Verified by fit check on CAD
SADM_INT_002	The system shall be stowed in the defined volume envelope specified for a standard 12U CubeSat deployer.	Verified by fit check on CAD
SADM-DES-002	The design of the system should be scalable to be usable in 3-16 U standard CubeSat sizes.	Verified by fit check on CAD
SADM-DES-003	The design of the system should be such that it can be applied for more than one panel mounting configuration.	Verified by CAD
SADM-DES-004	The system shall not extend beyond one plane.	Verified by design and inspection of design
SADM-RAMS-002	The system should not use volatile fluids.	Verified by review of design documentation
SADM-RAMS-003	The materials used in the system shall adhere to low out-gassing criterion such that they have a Total Mass Loss < 1 % and CVCMM < 0.1 %.	Partial verification by review of documentation

Table 6.1: Requirements verified by inspection and CAD

The remaining requirements require a working prototype to be verified by demonstration and testing. Most of the functional (Refer to Table 3.1) and performance requirements (Refer to Table 3.2) fall under this category. Once the prototype is ready, these requirements can be verified by the verification plan as summarized in Table 6.2 below:

Identifier	Requirement	Verification plan
SADM-FUN-001	The system shall be able to rotate an array consisting of 3 rigid solar panels of 12 U size (326*210 mm) each along one axis throughout 360 degrees in space & ground.	This can be verified by demonstration using a dummy mass for the solar panels with matching inertia and by rotating them for the required angle. The angle can be measured by an external marker. The space environment can be simulated by demonstrating in a vacuum chamber and weightlessness can be achieved by attaching the solar panels to a spring loaded rig that compensates gravitational acceleration.
SADM-FUN-002	The system shall deploy and stabilize the solar arrays after release from stowed position.	The spring loaded elbow was not designed within the scope of this thesis. This requirement can be verified by demonstration once the spring loaded extension of the shaft is designed and integrated with the SADM system.

SADM-FUN-003	The system shall allow the transfer of electrical power generated from three 12 U sized (326*210 mm) solar panels to the CubeSat bus.	82 W was found to be the maximum power to be transferred with a maximum current of 1.7 A and a maximum voltage of 97 V. These characteristics can be achieved using an external power source and the response of the system can be analysed in terms of temperature rise. This can also be carried out by simulations.
SADM-FUN-004	The system shall allow the transfer of data generated by the panel-mounted sensors to the CubeSat mounted systems.	This requirement can be verified by demonstration as the sensor data can be passed through the Flex-wrap FPC and tested if it is received at the other end. The system can also be tested for robustness by measuring the attenuation in signal for different environmental conditions and while dynamic bending of the FPC.
SADM-FUN-005	The system shall communicate the deployment status of the solar panels to the satellite OBC	This requirement can also be verified by demonstration. A simple micro-switch or pogo-pin connector at the position where the solar panels would come in contact once in deployed the position will be sufficient to transmit a pulse to notify the deployment. This has to be taken into account while designing the electronics of the system.
SADM-PER-001	The system shall point the solar panels with an accuracy of at least ± 8 degree + 3 sigma with respect to the solar incident angle (or beta angle).	A test setup would have to be made to measure the angle of the solar panels and the control electronics would have to be designed and integrated to test this. To simulate the Sun position a Sun simulator can be used or the system can be simply placed in sunlight and tested to track the position of the Sun. This can be achieved by using a simple shadow casting element in the middle of the solar panels, the control algorithm must automatically be able to rotate the panel such that least area of shadow is cast on the panels. Thereby positioning the solar panels perpendicular to the Sun.
SADM-PER-002	The system shall give the position of the solar panels at any point during operation with an accuracy of TBD degrees.	The shaft position sensor readout is sufficient to verify this requirement.
SADM-PER-003	The system shall have an in-orbit duty of at least 29200 cycles in LEO.	This requirement can be verified by testing the system's functionality in vacuum and temperature cycling. This will be a complete life test of the system. The performance of the system can be compared before and after the life-test to have a complete understanding. The analysis can be in the form of a micro-vibration measurement or functionality test or both.
SADM-PER-004	The system shall have 29200 on-ground working cycles.	The system can also be tested for part of the lifetime or the entire lifetime on ground and the change in performance can be evaluated.
SADM-INT-003	The system shall provide mechanical connection interface between solar panels and satellite.	This can be verified by assembling the SADM housing and its components together to the CubeSat structure. The mechanical integrity can be verified by random vibration testing of the system.

SADM-INT-004	The system shall provide electrical connection interface between solar panels and satellite power bus.	This can be verified by testing the electrical conductivity across the electrical interfaces and connections of the system.
SADM-INT-005	The system shall provide data interface between panel-mounted sensors and satellite data bus.	This can be demonstrated by monitoring sensor readout from the system.

Table 6.2: Verification approach for requirements needing demonstration and testing

As far as verification by testing is concerned, all environmental requirements (SADM-ENV-001 to SADM-ENV-011) fall under this category. The author would like to propose a verification plan to verify these environmental requirements. The testing can be split into two parts - mechanical and thermal environment. The mechanical environmental testing is carried out in a series of steps starting with functional testing and performance analysis, followed by resonance survey, sinusoidal vibration test, random vibration and again random vibration followed by performance test. This sequence is repeated for the three axes. Shock testing is carried out on all three axes followed by thermal testing. The mechanical loads are different for the acceptance and qualification stages as specified in [108]. The thermal testing involves cooling the system to the minimum operational temperature and after a set dwell time a functional test is conducted. The system is then heated incrementally upto the maximum operational temperature and allowed to dwell for a set period of time after which the functional testing is performed again. The number of cycles and the limits may vary with ECSS (ECSS-E-ST-10-03C) and NASA standards.

6.7. Summary

In this chapter, the integrated system design was described and its mechanical and electrical integration were specified. The modularity and scalability of the system were verified using CAD. It was found that the SADM is modular to be applicable to more than 5 different panel mounting configurations. The SADM was found to be scalable to smaller CubeSats (3U, 6U and 8U) but are recommended to adapt the design for a 3U CubeSat to avoid over-design. As the prototype could not be realised within the time-frame of the project interface and design requirements were verified by CAD and inspection of documentation. The environmental, functional and performance requirements can be verified only once the functional prototype has been realised. But a verification approach has been provided in this chapter.

7

Conclusions

The main goal of this thesis was to design a SADM for CubeSats in LEO, in particular a 12U CubeSat. The SADM was desirable to be modular, scalable and reliable. Initially, few research questions were formulated to reach this goal in sub-section 1.2. The thesis has designed a SADM that meets the requirements set by the stakeholders in chapter 3. This chapter will describe the resultant design and will answer the research questions that have been investigated over the time period of the thesis. As the timeline was restricted, a working prototype could not be achieved, therefore the chapter ends with a list of recommendations for continuing the project and to realize a functional and space-operational SADM.

7.1. Results and Discussion

In this section, the design of the SADM will be described followed by answers to the research questions and discussions.

7.1.1. Overview of the design

The popularity of CubeSats have grown increasingly over the years since its inception. It has grown from simple university-based research and technology demonstration missions to global-scale commercial applications like Earth observation, communications, hyper-spectral imaging, on-board Artificial Intelligence (AI)-based data processing and in-orbit manufacturing. Sufficient electrical power generation is a prime necessity to achieve this applicability of CubeSats to such a wide range of advanced missions because they demand a lot of power. The Solar Array Drive Mechanism is a solution to this demand that articulates the solar panels to optimally position (perpendicular) them with respect to the Sun such that maximum power can be generated by the solar panels. Market research was conducted, and a gap was found for a modular, scalable and failure-free SADM system. The existent commercial solutions were applicable to limited solar array mounting configurations on the CubeSat frame, making them less modular, and they had to be redesigned to be compatible with multiple CubeSat sizes or, in some cases, not scalable at all. Power system failure and mechanical failures combined were the most common cause of CubeSat mission failure after no-contact [119]. It was found that the solar array deployable mechanisms were most susceptible to failure compared to other deployable mechanisms based on insurance claims [172]. Tribological sources were the most prevalent cause of such failures. This project was aimed at filling this industrial and research gap by answering the question below:

" How to design a Solar Array Drive Mechanism for CubeSats that is modular, scalable and overcomes tribological failures experienced with space mechanisms? "

The main functional requirement of the SADM system was to rotate the solar arrays so they can be optimally positioned with respect to the Sun and to transfer the power generated by the PV cells to the CubeSat along with the data generated by the sensors mounted on the panels. Additionally, the system had to comply with space and launch environmental requirements which enforce vacuum operation, temperature cycling, vibration, shock loads and a lifetime of 5 years. Over the course of this thesis, a SADM system was designed to

meet these requirements while answering the research question. The designed SADM system is shown in the Figure (7.1) followed by a brief explanation of the design.

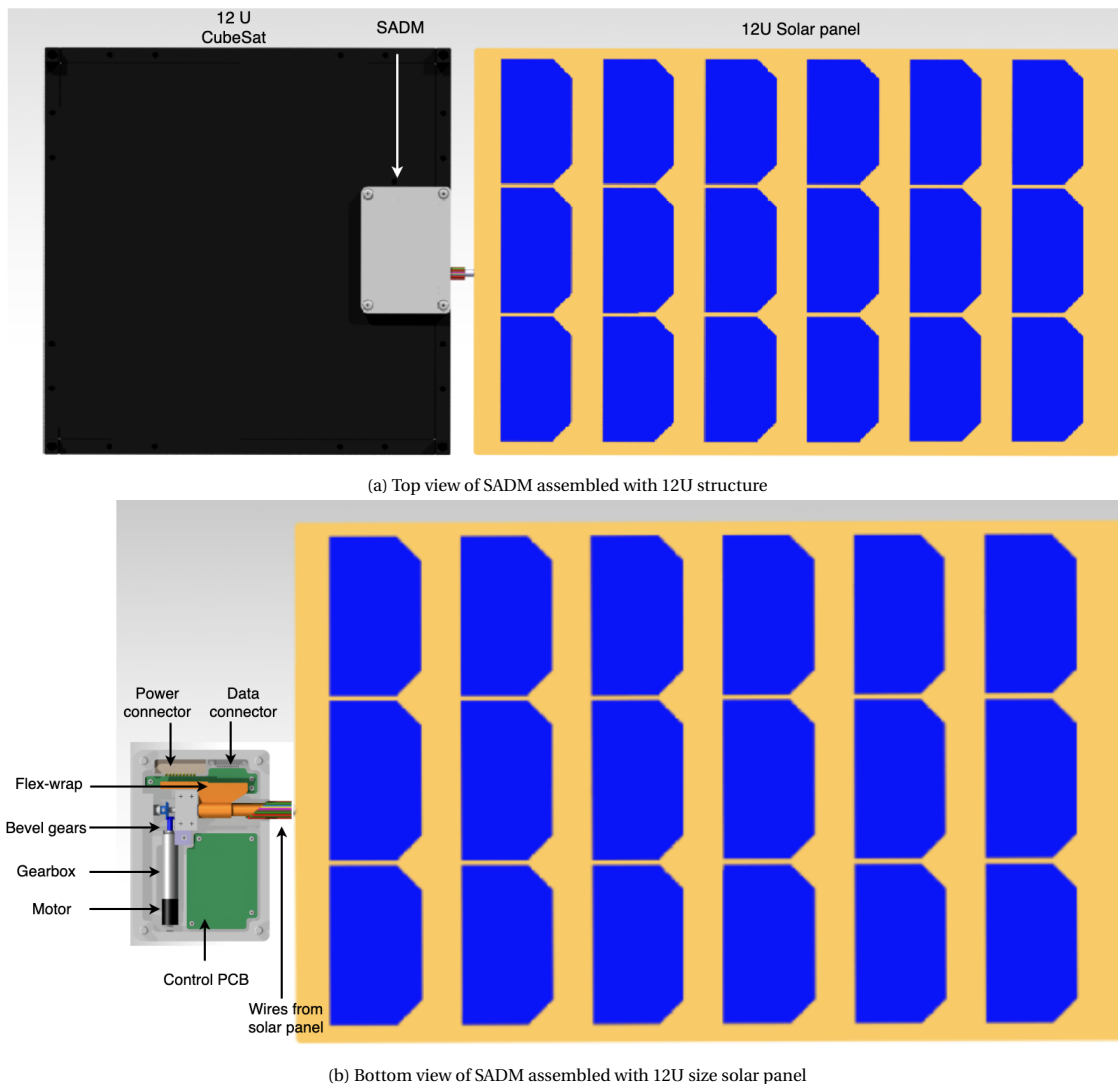


Figure 7.1: Final SADM design

As the system was desirable to be modular, the SADM drives only one solar array. So that multiple such SADMs can be combined together to achieve any panel mounting configuration. The SADM also fits within a dimension limit of $70 \times 50 \times 6.9$ mm such that two of such systems can fit on top of a 3U CubeSat, thereby also fitting on a 12U CubeSat, thus making it scalable. The stepper motor shown in the figure is responsible for rotating the solar panels. As the torque provided by the motor was insufficient, a gearbox and an external bevel gear were utilized to amplify the torque. Two polymer-based plain bearings were utilised to support the shaft, dissipate shaft loads and allow smooth rotation. Polymer-based plain bearings were chosen as they do not employ failure-causing elements like liquid or grease lubricants, metals that face corrosion or rolling elements that need accurate preloading for alignment maintenance. The **"Flex-wrap"** is the *novelty of the project*. It is a power and data transfer mechanism that uses a flex-PCB spirally wound around the shaft to allow shaft rotation. The Flex-wrap satisfies the second main requirement of transferring power and data while allowing rotation of the solar arrays. This mechanism overcomes the drawbacks posed by sliprings which make use of brushes that cause debris generation which led to friction and sparking. This design also overcomes the disadvantage of the goose-neck that imposed a high bending radius requirement of the FPC, which would lead to fatigue failure due to repetitive bending. It transfers the power and data from the solar arrays to the CubeSat mounted systems via the electrical and data interfaces mounted on the right

side of the housing. The electrical and data interfaces also bring data and regulated power from CubeSat mounted systems to the SADM. The control electronics contain all the electronic components required to drive the motors and ensure proper functioning. By eliminating the sources of tribological failure in the bearings and power and data transfer mechanism, the system aims to mitigate failure and achieve reliability over its lifetime. Thus answering the main research question for the thesis. The system is yet to be verified by testing but most of the requirements have been verified by inspection (report and design reviews).

7.1.2. Answers to research questions

1. Why design a SADM for CubeSats?

Three reasons were found to serve as the motivation for this work. The trend in increasing number of CubeSat launches per year, affinity for advanced missions (laser communication, in-orbit manufacturing, IoT, etc.) using CubeSats which require higher electrical power and limited products with similar design in the commercial market that do not adequately meet this need. SADMs solve the need for higher power by constantly positioning the solar arrays perpendicular to the Sun independent of payload pointing requirements.

(a) What causes space mechanism failure?

Many causes of space mechanism failure were found which include interfaces, shocks caused by explosives used in HDRM, thermal, electrical and software. The most prominent cause of space mechanism failure was found to be tribological in nature. Within the scope of the SADM's constituent elements, the bearings and the PDTM have tribological interactions.

(b) What is lacking in the existing state-of-the-art products?

From the market research, three of the six SADMs had the same external design. Desirable features like modularity (applicability to multiple solar array mounting configurations) and scalability (applicability to different CubeSat sizes) were found to be lacking in the currently existing SADMs.

2. How to design a SADM system for CubeSats that is reliable (less failure scenarios and probability of its occurrence)?

The design reliability of the SADM was ensured by identifying the failure scenarios and their root causes followed by eliminating these root causes in the design. These failure scenarios pertain to tribological elements and their root causes were identified as lubricants, metals, need for preloading and its maintenance. These root causes were eliminated in the context of the PDTM, gears and bearings used in this SADM.

(a) How to design or select an actuator that can rotate the solar arrays?

The actuator was selected based on the maximum mechanical power required to rotate the solar arrays, which is required at the maximum speed it would encounter during its lifetime. The maximum speed that the solar arrays would require to be rotated occurs during the target tracking mode of the mission which was calculated as 0.4 RPM. This mission phase also corresponds to the maximum torque and mechanical power requirement which were calculated as 3.816 mNm and 0.153 mW respectively. A stepper motor was selected as the rotary actuator due to its positional accuracy achieved by its working principle, absence of cogging torque at low RPMs, COTS availability and dimensional compatibility. Even though the power required was met sufficiently by the stepper motor, the torque required was not adequate. A gear transmission system had to be used to amplify the torque. The gear ratio required for the SADM was optimised for inertia matching (for smooth rotation), torque amplification and maximum power transfer which resulted in a total gear ratio requirement of 12522. This total optimal gear ratio could be achieved by combination of a gearbox with gear ratio 4096 and an external gear with a gear ratio of 3. An external gear ratio of 3 was achieved using a bevel gear made of PEEK. The material choice was made considering superior shock absorption, lack of need for lubricants and low wear compared to metals. The external bevel gear also performs the function of providing an alternate path for load transfer rather than transferring launch loads directly to the motor shaft.

(b) How to design a power & data transfer arrangement capable of transferring the maximum power with the least degradation over its lifetime as opposed to such shortcomings of conventional slings?

Firstly, to answer this question, the maximum power, current and voltage that the SADM had to handle were calculated to be 82W, 1.7A and 97V, respectively (refer to Table 4.12). The maximum power generated remains constant irrespective of the PV cell connection configuration. The maximum voltage was found to occur in a configuration where all the PV cells in a row of the solar array were connected in series. The maximum current was found to occur when the PV cells in one panel were connected in series and the panels in an array were connected in parallel. The main drawback of the sliprings was the conductive brushes that wear during operation and create debris that led to increased friction, sparking and arcing at high voltages. Among the various PDTM design options, the cable wrap provided the advantage of higher bending radius of cable due to its construction. On the other hand the goose-neck had the disadvantage of low bending radius which leads to high stress in the FPC but the FPC used in the goose-neck mechanism was found to have the advantages of higher flexibility and low thickness. A new mechanism has been designed and termed as the **Flex-wrap** that combines the best features of both the PDTMs. The Flex-wrap uses a spirally coiled Flexible Printed Circuit to transfer power and data while allowing rotation by coiling and uncoiling. The spiral construction imposes high bending radius thus low stress and the FPC occupies low volume which is favourable for the current application's stringent dimensional constraints. The FPC was designed to have a conductor thickness of 35 μm by making a trade-off between bending radius and total width of FPC. The FPC length was calculated by modelling it as a spiral. A length of 50 mm corresponding to three spiral loops was chosen considering a trade-off between the gap between the adjacent layers and the stress induced in the FPC layers for rotating it by an angle of 180 degrees.

(c) **What causes the failure-causing components in space mechanisms susceptible to failure and how can they be designed to have lower chances of failure through their lifetime?**

Tribological elements utilise surfaces in contact with each other in relative motion. These elements were susceptible to failure because of multiple causes, including wear, debris generation due to friction, lubricant interactions & corrosion. All these failure mechanisms eventually lead to increased friction and material damage which result in the space mechanism failure. These failure causes are pertinent to conventionally used tribological elements in SADM systems - the slipring, gears and roller bearings. The strategy adopted in the current project to reduce the chances of failure due to tribological elements was to eliminate the root cause of the failure. This was done by firstly researching the failure mechanisms, followed by investigation of their causes. By using a polymer-based sleeve bearing, various failure causes were eliminated, like the need for lubricants, need for strict alignment maintenance of rolling elements, corrosion due to metals and the impact of an uncontrolled environment. Using a Flex-wrap design for power and data transfer, debris generation due to the wear of brushes and lubricant interactions encountered in sliprings were eliminated. By fabricating the gears out of PEEK, shock applied on the gears are absorbed without dent formation, lubricant-less operation is possible and corrosion is mitigated.

(d) **How to design interfaces that can survive the environmental loads and be reliable through their lifetime?**

The interfaces were designed considering the launch and operation loads that were mechanical and thermal in nature. Reliability was achieved by considering sufficient margins on the environment-imposed requirements. Mechanical interfaces such as the bolt were sized to have a preload greater than the launch force but lower than the yield strength of the material. Electrical interfaces were selected to interface with components within the SADM and systems inside the CubeSat. They were selected to have multiple mating-demating cycles, the capability to withstand shock loads and operation in the space environment (temperature cycling and vacuum).

3. **How to verify the system's proper functioning and survival in a space environment for a given mission lifetime?**

This has been ensured by designing the system considering worst-case scenarios and by using sufficient margins. The requirements set at the beginning of the project were mostly verified by inspection due to the time constraints of the thesis. The system has to be tested, analysed and demonstrated to be completely verified which will be possible after the realisation of the prototype.

(a) **How to verify if the system is capable of surviving environmental conditions (ground, launch and space)?**

The mechanical elements have been designed considering worst-case launch loads with a margin for high reliability (3σ). It has been ensured by design that liquid lubricants or out-gassing substances are not utilised. The dimensional compatibility has been verified digitally by fit-checking on CAD. Therefore, part of the requirements have been verified by inspection of documentation. Most of the launch and space environmental conditions can only be verified by testing. This was not possible within the timeline of the thesis, but have to performed in order to qualify the SADM for application in space. The combined response of the SADM along with its interfaces, mechanical, electronic, electrical and software elements can only be verified by testing the functional prototype. Specifically, the Flex-wrap has to be tested for its response under combined conditions of lifetime flex-cycles and temperature in environmental conditions (vacuum & launch loads). This is because the Flex-wrap is a new design and its real-life behaviour has not been investigated.

(b) **How can the system be validated?**

The system can be validated by the customer once the SADM has been commercialized.

7.1.3. Comparison with state-of-the-art SADMs

The Table 7.1 below compares the specifications of the current SADM with other SADMs in the market. It can be observed from the table that clearly the current SADM has the least dimension among the others and is applicable to up to five different panel mounting configurations as depicted in Figure 5.1. This makes the current SADM, the smallest and the most modular SADM in the market. Of course, these statements can be accepted only when the SADM has been qualified for operation but the statement is considerable in the view of initial design stage. The PDTM and bearing technology used in these competitor products are not publicly known to compare the special features. But, the current SADM has taken measures to avoid failure by eliminating root causes of tribological element failure. By achieving these specifications, the thesis has achieved its design goals (Refer Table 3.6) defined by the stakeholders within the scope of this project.

Commercial SADM for CubeSats	IMT SRL μ -SADA [30]	HoneyBee nanoTrack	Tethers Unlimited Cobra HPX [9]	RevolvSpace SARA [46]	AAC Hyperion SADM
CubeSat sizes applicable	6U & 12U	3U	-	3U & 6U	3U, 6U, 8U & 12U
Dimensions	0.15 U (100x88x15 mm)	0.065U (100x100x6.5 mm)	0.37U (113x113x29.2 mm)	0.15 U (96x96x15 mm)	0.024 U (70x50x6.9 mm)
Possible panel mounting positions	3	3	1	3	5
Pointing accuracy	± 0.3 deg	-	± 0.077 deg	± 0.1 deg	-
Special features	Well suited for interplanetary missions	Smallest in market	3-DOF	Drag based attitude control	Flex-wrap

Table 7.1: Comparison of COTS CubeSat SADMs

7.2. Future recommendations

Given the limited time frame of the Master thesis, it was not possible to get to a stage where the working prototype of the SADM was realisable. As AAC Hyperion's goal is to achieve a working SADM system that can be sold commercially, the author recommends a series of steps as listed below that must be taken to achieve this goal.

1. Design bendable shaft interface with solar panels

One of the main mechanical elements missing from the current design is the SADM shaft's mechanical interface with the solar arrays. The design feature required from this interface is that it should allow the solar arrays to be stowed and must provide the restoration force for the panels to unfurl and become rigid once deployed. An important consideration in designing this component is to take in to account that the wires from the solar panels connected with the power and data transfer mechanism of the SADM must be accommodated.

2. Design of a incremental position sensor

As discussed in section 5.7, a COTS sensor meeting the dimensional requirement could not be found. The author recommends further investigation in this direction to design a custom solution to meet the resolution, update frequency and dimensional requirements defined for the current SADM.

3. Test the Flex-wrap dynamics

The Flex-wrap was the innovative invention of the entire SADM. It is a technology that has never been designed or tested before. Therefore, the author would suggest that this technology be explored in more detail to understand its behaviour over its lifetime. This can be done by testing the mechanism's resilience to bending over its lifetime requirements. The system's response to the combined effects of bending and thermal loads is yet to be tested and understood.

4. Load simulations & analysis

The current project has performed static load analysis with sufficient margins to design the SADM reliably. The dynamic load conditions in terms of loads and temperature can be simulated to verify the design and to detect abnormalities or undesirable elements early in the design. This could be stress concentrations in some parts of the structure, thermal stresses, bending modes, etc. Many undesirable structural responses stem from the flexible nature of solar panels. This effect can be modelled and simulated on structural analysis software.

5. Control electronics design & manufacture

Designing and manufacturing the electronics required to control the SADM will be the next step in achieving a prototype. The control electronics must be able to drive the motors based on the position required of the solar panels to generate maximum power. To achieve this position, the SADM must know the relative position of the Sun with respect to the solar panel. This requires using this position knowledge in a closed loop feedback control to optimally rotate and position the solar panels. To achieve this, it has to use the shaft position known from the position sensor and the attitude knowledge gained from the ADCS or the panel-mounted sun sensor. The shaft position is the solar panel's position, and the attitude knowledge will give the satellite's position with respect to the Sun.

6. Software development

The last step in achieving a working prototype is to develop the software that will control the SADM by allowing it to communicate and command with other electronic components (sensors & actuators) and elements of the CubeSat. The software gives commands to the hardware. The main function of the algorithm will be to track the Sun and optimally place the solar panels. The software must also be capable of performing fault diagnosis and correction when an error is encountered.

7. Testing & qualification with prototype

Once all the above steps are completed and after the hardware and software are integrated, the next step will be to test the prototype to verify if the SADM is working as required in all environmental conditions it may encounter during its lifetime. There are multiple tests that must be conducted to qualify the SADM to be operational in the space environment. This includes operation in vacuum, varying thermal conditions, sine vibration sweep testing, random vibration testing and functional testing after each type of testing. The prototype can still be redesigned or improved based on the learning from the test results.

8. Manufacture

The final step before commercialization will be manufacturing the design. This will include making drawings of the mechanical and electronic parts and manufacturing them, followed by assembly, integration and testing of the SADM.

9. Supply chain set up

This is where the process transitions from engineering to management and business administration. Various components and parts of the SADM are sourced from different companies and manufacturers across the continent. For example, the motor is sourced from Faulhaber, which is a German-based company, and the fasteners are sourced from a local distributor (Netherlands-based) of Misumi, which is a Japanese company, whereas some components will be manufactured by AAC Hyperion's partner manufacturers. The supply of all these components from various sources has to be set up to manufacture the SADM.

10. Detailed cost estimate and pricing

The next step before commercial selling the SADM is to arrive at a market value for the product. To arrive at this value, the first step is to make a bill of materials that gives a rough estimate of the cost of making the product by including all the constituent factors like component price, labour charges, transportation cost, engineering support charges, research and development expenditure, etc. The selling price is then fixed by using any of the pricing strategies. Initial pricing strategies are based on a positive profit margin on the product's cost or market comparison with similar products. Over time, if the product has a high demand, the product could be sold at a higher price based on the demand.

11. Commercialization of the SADM

The last and final step of commercialization of the SADM will be marketing and sales of the product. The author estimates this would take at least a year or one and a half from 2022 to achieve this stage, depending on the resources AAC Hyperion allocates to this project.

Bibliography

- [1] Solar array drive assemblies, . URL <https://www.honeybeerobotics.com/products/solar-array-drive-assemblies/#1562325851331-b2e4385b-5dd474f5-d928>.
- [2] Solar array drive assemblies, . URL <https://www.moog.com/products/space-mechanisms/solar-array-drive-assemblies.html>.
- [3] Solar array drive mechanisms, . URL <https://www.ruag.com/en/products-services/space/spacecraft/satellite-mechanisms/solar-array-drive-mechanisms>.
- [4] Sierra nevada corporation's space technologies product catalog, . URL <https://www.sncorp.com/media/3189/space-systems-product-catalog-2020.pdf>.
- [5] Solar array and drive mechanisms, . URL <https://www.thalesgroup.com/en/solar-array-and-drive-mechanisms>.
- [6] Explorer 6 - nasa - nssdc - spacecraft - details, . URL <https://nssdc.gsfc.nasa.gov/nmc/spacecraft/display.action?id=1959-004A>.
- [7] Vanguard 1 - nasa - nssdc - spacecraft - details, . URL <https://nssdc.gsfc.nasa.gov/nmc/spacecraft/display.action?id=1958-002B>.
- [8] Deployable solar panels for 3u and 6u satellites, . URL https://gomspace.com/UserFiles/Subsystems/datasheet/GS-DS-NanoPower_DSP_1018088_25.pdf.
- [9] Gimbals, . URL <https://www.tethers.com/robotic-gimbals/>.
- [10] Solar array drive assemblies, . URL <https://www.honeybeerobotics.com/products/solar-array-drive-assemblies/>.
- [11] Honeybee robotics delivers modular solar array drive system to mma design, . URL <http://spaceref.com/news/viewpr.html?pid=37108>.
- [12] Matweb-annealed-copper-data. URL <https://www.matweb.com/search/DataSheet.aspx?MatGUID=9aeb83845c04c1db5126fada6f76f7e>.
- [13] Arabsat 1a, 1b, 1c / insat 2dt mission overview. URL https://space.skyrocket.de/doc_sdat/arabsat-1a.htm.
- [14] Ariane-5 user manual. URL https://www.arianespace.com/wp-content/uploads/2011/07/Ariane5_Users-Manual_October2016.pdf.
- [15] Azurspace 3g30c datasheet, . URL http://www.azurspace.com/images/006050-01-00_DB_3G30C-Advanced.pdf.
- [16] Azurspace-4g32c datasheet, . URL http://www.azurspace.com/images/0005979-01-01_DB_4G32C-Advanced.pdf.
- [17] Cesi ctj 30 datasheet. URL <https://www.cesi.it/app/uploads/2020/03/Datasheet-CTJ30-1.pdf>.
- [18] Dhv micro-sada, . URL <https://dhvtechnology.com/products/microsada/>.
- [19] "solar panels for cubesats", . URL <https://dhvtechnology.com/products/solar-panels-cubesats/>.
- [20] Ecss-e-10-04a – space environment (21 january 2000), . URL <https://ecss.nl/standard/ecss-e-10-04a-space-environment-21-january-2000/>.

- [21] Ecss-s-st-00-01c, . URL <https://ecss.nl/standard/ecss-s-st-00-01c-glossary-of-terms-1-october-201>
- [22] Erbs (earth radiation budget satellite). URL <https://directory.eoportal.org/web/eoportal/satellite-missions/e/erbs>.
- [23] Effect of light intensity. URL <https://www.pveducation.org/pvcdrom/solar-cell-operation/effect-of-light-intensity>.
- [24] 6u deployable solar array. URL <https://www.endurosat.com/cubesat-store/cubesat-solar-panels/6u-deployable-solar-array/>.
- [25] Satellites to be built and launched by 2028. URL https://www.euroconsult-ec.com/research/WS319_free_extract_2019.pdf.
- [26] Thales alenia says eutelsat w5's solar array motor is malfunctioning. URL <https://spacenews.com/thales-alenia-says-eutelsat-w5s-solar-array-motor-malfunctioning/>.
- [27] Fiber-glass datasheet. URL <https://laminatedplastics.com/fiberglasslaminates.pdf>.
- [28] Goes mission status. URL <http://goes.gsfc.nasa.gov/text/goeskstatus.html>.
- [29] Aac clyde space im200 datasheet. URL <https://www.aac-clyde.space/wp-content/uploads/2021/11/IM200.pdf>.
- [30] Imt μsada. URL <https://www.imtsrl.it/products/imt-microsada>.
- [31] Isis antenna systems datasheet, . URL <https://www.isispace.nl/wp-content/uploads/2019/08/ISIS-Antenna-Systems-Brochure-V2R-web.pdf>.
- [32] Isis 12u cubesat structure, . URL <https://www.isispace.nl/product/12-unit-cubesat-structure/>.
- [33] Isis structures datasheet, . URL https://www.isispace.nl/wp-content/uploads/2015/12/ISIS.STS_.0.0.001-RevC-Sheet1-1-The-CubeSat-Family-A0.pdf.
- [34] Iso-15243 - rolling bearings damage and failure. URL <https://www.sis.se/api/document/preview/906198/>.
- [35] Kapton datasheet. URL <httphttps://www.dupont.com/content/dam/dupont/amer/us/en/products/ei-transformation/documents/DEC-Kapton-HN-datasheet.pdf>.
- [36] Kevlar datasheet. URL https://www.dupont.com/content/dam/dupont/amer/us/en/safety/public/documents/en/Kevlar_Technical_Guide_0319.pdf.
- [37] Koyo - ball & roller bearings: Failures, causes and countermeasures.
- [38] Historic landsat 5 mission ends. URL <https://landsat.gsfc.nasa.gov/article/historic-landsat-5-mission-ends/>.
- [39] Nsk - new bearing doctor maintenance of bearings, . URL <https://www.nsk-literature.com/en/new-bearing-doctor-maintenance/offline/download.pdf>.
- [40] Nsk - rolling bearings, . URL <https://www.nsk.com/common/data/ctrGpdf/bearings/e1102m.pdf>.
- [41] Stack-up for fpc - single layer fpc stackup. URL https://www.pcbway.com/pcb_prototype/Stack_up_for_FPC.html.
- [42] Temperature co-efficient of solar cell. URL <https://www.alternative-energy-tutorials.com/photovoltaics/temperature-coefficient.html>.
- [43] Photon cubesat solar arrays. URL https://www.aac-clyde.space/wp-content/uploads/2021/11/AAC_DataSheet_Photon_original.pdf.

- [44] Pioneer 11. URL <https://solarsystem.nasa.gov/missions/pioneer-11/in-depth/#:~:text=The%20vehicle%20then%20used%20Jupiter's,were%20interfering%20with%20other%20instruments.>
- [45] Qioptiq cover glass datasheet. URL <https://www.excelitas.com/product/space-qualified-cover-glass.>
- [46] Revolvspace rotary actuator. URL <https://www.revolvspace.com/product.>
- [47] Septa 33 solar array drive assembly manual. URL <http://hobbydocbox.com/Radio/121877392-Septa-33-solar-array-drive-assembly.html.>
- [48] Skf - bearing damage and failure analysis. URL https://www.skf.com/binaries/pub12/Images/0901d1968064c148-Bearing-failures---14219_2-EN_tcm_12-297619.pdf.
- [49] Sierra nevada corporation space products catalog. URL <https://www.sncorp.com/media/3189/space-systems-product-catalog-2020.pdf.>
- [50] Spectrolab-XTE-SF datasheet, . URL https://www.spectrolab.com/photovoltaics/XTE-SF_Data_Sheet.pdf.
- [51] Spectrolab - xtj datasheet, . URL https://www.spectrolab.com/photovoltaics/XTJ-Prime_Data_Sheet.pdf.
- [52] Swartout cubesat database. URL <https://sites.google.com/a/slu.edu/swartwout/home/cubesat-database.>
- [53] Thaicom 3 mission overview. URL https://space.skyrocket.de/doc_sdat/thaicom-3.htm.
- [54] Trapped radiation belt. URL https://svs.gsfc.nasa.gov/vis/a010000/a011200/a011212/Mona_2.jpeg.
- [55] Union of concerned scientists satellite database. URL <https://www.ucsusa.org/resources/satellite-database.>
- [56] Aac clyde space cubecat datasheet. URL <https://www.aac-clyde.space/wp-content/uploads/2021/10/CUBECAT.pdf.>
- [57] Dual row horizontal smt (type aa). URL https://www.omnetics.com/Portals/0/Files/Bi-Lobes/bdualrow_AA_contact.pdf.
- [58] Scotch-weld™ epoxy adhesive-2216 b/a-3m. URL <https://multimedia.3m.com/mws/media/1539550/3mtm-scotch-weldtm-epoxy-adhesive-2216-b-a.pdf.>
- [59] Iglidur configurator, . URL <https://www.igus.com/iglidurConf/Iglidur/Step1.>
- [60] Iglidur datasheet, . URL <https://www.acornbearings.co.uk/downloads/catalogues/aerospace/aerospace-fasteners/igus-plastic-bearings.pdf.>
- [61] Iglidur catalog of plain bearings, . URL <https://toolbox.igus.com/product-catalogs/iglide-bearings-2021-catalog.>
- [62] Failed telecommunications satellite drifts out of control. URL <https://www.space.com/6346-failed-telecommunications-satellite-drifts-control.html.>
- [63] Marco: Tiny cube satellites headed to mars. URL <https://earthsky.org/space/marco-satellite-cubes-mission-on-their-way-to-mars/.>
- [64] Ultra low-profile hex socket cap screw - m2 - m6. URL <https://us.misumi-ec.com/vona2/detail/110302280540/.>
- [65] Moog-3/5 solar array drive assembly datasheet. URL https://www.moog.com/content/dam/moog/literature/Space_Defense/spaceliterature/spacecraft-mechanisms/moog-type3-5-solar-array-drive-assembly-datasheet.pdf.

- [66] Nanosats database. URL <https://www.nanosats.eu/#figures>.
- [67] Single row micro-d solder cup (type ss). URL https://www.omnetics.com/Portals/0/Files/Single%20Row%20Micro-D/singlerow_microd_ss_full.pdf.
- [68] Solar sails for space activities. URL <https://www.ines-solaire.org/en/news/solar-sails-for-space-activities/>.
- [69] Spacecraft encyclopedia by claudelafleur, . URL <http://claudelafleur.qc.ca/Spacecrafts-index.html>.
- [70] Nano/microsatellite forecast, 10th edition (2020), . URL <https://www.spaceworks.aero/nano-microsatellite-forecast-10th-edition-2020/>.
- [71] Stainless steel 1.4301 -304 - datasheet. URL https://d2zo35mdb530wx.cloudfront.net/_legacy/UCPthyssenkruppBAMXUK/assets.files/material-data-sheets/stainless-steel/stainless-steel-1.4301-304.pdf.
- [72] Ecss-e-hb-32-23a, 2010. URL [http://escies.org/ftp/ecss.nl/Handbooks/ECSS-E-HB-32-23A\(16April2010\).pdf](http://escies.org/ftp/ecss.nl/Handbooks/ECSS-E-HB-32-23A(16April2010).pdf).
- [73] Theoretical performance ratings, 2016. URL <https://www.spiroidgearing.com/tools-references/theoretical-performance-ratings/>.
- [74] Radiation-driven 'single event effect', 2021. URL https://www.esa.int/ESA_Multimedia/Images/2012/12/Radiation-driven_Single_Event_Effect.
- [75] Series dm0620 two phase with disc magnet 20 steps per revolution, 2021. URL <https://www.faulhaber.com/en/products/series/dm0620/>.
- [76] Technical supply specifications:maalondrive® highacc 6mm - type 3, 2021. URL https://php.micromotion.de/produktdatenbank/pdfcontainer/product_id221_englisch.pdf.
- [77] Aac hyperion mm200 datasheet, 2022. URL <https://www.aac-clyde.space/wp-content/uploads/2021/11/MM200.pdf>.
- [78] Awg standards, 2022. URL https://en.wikipedia.org/wiki/American_wire_gauge.
- [79] Axon ffc datasheet, 2022. URL https://www.axon-cable.com/publications/axon-flat-flexible-cables_cg.pdf.
- [80] Intersil isl71590seh datasheet, 2022. URL <https://www.renesas.com/us/en/document/dst/isl71590seh-isl73590seh-datasheet?r=522286>.
- [81] Calculation of gear dimensions, 2022. URL https://khkgears.net/new/gear_knowledge/gear_technical_reference/calculation_gear_dimensions.html.
- [82] Bison64-et fm, 2022. URL <https://lens-rnd.com/sun-sensors/bison64-et/>.
- [83] Minco's flex circuits design guide, 2022. URL <https://www.minco.com/wp-content/uploads/Minco-Flex-Circuits-Design-Guide-2019.pdf>.
- [84] Matweb overview of materials for polyetheretherketone-unreinforced, 2022. URL <https://www.matweb.com/search/DataSheet.aspx?MatGUID=2164cacabcde4391a596640d553b2ebe&ckck=1>.
- [85] Matweb overview of materials for acetal copolymer-unreinforced, 2022. URL <https://www.matweb.com/search/datasheet.aspx?matguid=c3039ef87c9245448cdebe961b19a54c>.
- [86] Te tmp461-sp datasheet, 2022. URL https://www.ti.com/lit/ds/symlink/tmp461-sp.pdf?ts=1660998417039&ref_url=https%253A%252F%252Fwww.google.com%252F.
- [87] Te surface sensor for high rel & aerospace, 2022. URL https://www.te.com.cn/commerce/DocumentDelivery/DDEController?Action=showdoc&DocId=Data+Sheet%7FESCC_Surface_Sensors_Series%7FA%7Fpdf%7FEnglish%7FENG_DS_ESCC_Surface_Sensors_Series_A.pdf%7FCAT-NTC0049.

- [88] Matweb overview of materials for nylon 6-cast, 2022. URL <https://matweb.com/search/DataSheet.aspx?MatGUID=8d78f3cfc6b6f49d595896ce6ce6a2ef1&ckck=1>.
- [89] High torque skew axis gearing, 2022. URL <https://www.spiroidgearing.com/wp-content/uploads/2019/05/Spiroid-High-Torque-Gearing-Guide.pdf>.
- [90] Fss100 & css100 fine & coarse sun sensor, 2022. URL <https://tensortech.com.tw/wp-content/uploads/2022/01/Fine-Coarse-Sun-Sensor-Brochure-2022.pdf>.
- [91] Afaf M Abd El-Hameed and YA Abdel-Aziz. Aluminium alloys in space applications: A short report. *Journal of Advanced Research in Applied Sciences and Engineering Technology*, 22(1):1–7, 2021.
- [92] GF Abdelal, A Bakr Elhady, and M Kassab. Design of a deployment rotation mechanism for microsatellite. *International Journal for Simulation and Multidisciplinary Design Optimization*, 3(1):289–296, 2009.
- [93] Ian F Akyildiz and Ahan Kak. The internet of space things/cubesats: A ubiquitous cyber-physical system for the connected world. *Computer Networks*, 150:134–149, 2019.
- [94] Christopher S Allen, Martina Giraudo, Claudio Moratto, and Nobuyasu Yamaguchi. Spaceflight environment. pages 87–138, 2018.
- [95] Richard W Armstrong. Load to motor inertia mismatch: Unveiling the truth, 1998. URL <https://silo.tips/download/load-to-motor-inertia-mismatch-unveiling-the-truth>.
- [96] W Auer. A family of baptas for geo and leo applications. 1989.
- [97] Fabio Avino, P Martens, Alan Arthur Howling, D Bommottet, and I Furno. Gas breakdown mitigation in satellite slip rings. *Aerospace Science and Technology*, 85:229–233, 2019.
- [98] Vincent Barbet, Cyrille Le Quintrec, Xavier Jeandot, Alain Chaix, Eric Grain, and Jerome Roux. A compact sadm family. 591:41–45, 2005.
- [99] Joseph Barthel and Nesrin Sarigul-Klijn. A review of radiation shielding needs and concepts for space voyages beyond earth’s magnetic influence. *Progress in Aerospace Sciences*, 110:100553, 2019.
- [100] Gianluca Benedetti, Nicoletta Bloise, Davide Boi, Francesco Caruso, Andrea Civita, Sabrina Corpino, Erik Garofalo, Giuseppe Governale, Luigi Mascolo, Gianluca Mazzella, et al. Interplanetary cubesats for asteroid exploration: Mission analysis and design. *Acta Astronautica*, 154:238–255, 2019.
- [101] A. Bhatia. Basic fundamentals of gear drives. URL <https://www.cedengineering.com/userfiles/Basic%20Fundamentals%20of%20Gear%20Drives%20R1.pdf>.
- [102] Martin Blodt, Pierre Granjon, Bertrand Raison, and Gilles Rostaing. Models for bearing damage detection in induction motors using stator current monitoring. *IEEE transactions on industrial electronics*, 55(4):1813–1822, 2008.
- [103] Kevin H Brown, Charles W Morrow, Samuel Durbin, and Allen Baca. Guideline for bolted joint design and analysis: version 1.0. Technical report, Sandia National Laboratories (SNL), Albuquerque, NM, and Livermore, CA ..., 2008.
- [104] Richard Gordon Budynas, J Keith Nisbett, et al. *Shigley’s mechanical engineering design*, volume 9. McGraw-hill New York, 2011.
- [105] Michael Buttery. An evaluation of liquid, solid, and grease lubricants for space mechanisms using a spiral orbit tribometer. 2010.
- [106] Michael Buttery, Simon Lewis, Anthony Kent, Rachel Bingley, and Matthew Cropper. Long-term storage considerations for spacecraft lubricants. *Lubricants*, 8(3):32, 2020.
- [107] Erasmo Carrera, Fiorenzo A Fazzolari, and Maria Cinefra. *Chapter 4 - Fundamental of mechanics of beams, plates and shells*. Academic Press, 2017. ISBN 978-0-12-420066-1. doi: <https://doi.org/10.1016/B978-0-12-420066-1.00006-9>. URL <https://www.sciencedirect.com/science/article/pii/B9780124200661000069>.

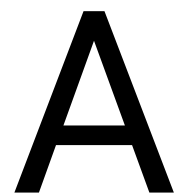
- [108] NASA Goddard Space Flight Center. Gsfc-std-7000a - general environmental verification standard. April 2005.
- [109] Rinu Chacko, MH Ravichandran, MK Sanoop, T Sabu, VT Sadasivan Achari, and CC Joseph. Magnetic slip ring—rotary transformer based novel non-contact signal transfer mechanism for spacecraft application. pages 1–5, 2014.
- [110] Jeffrey A Chambers. Preloaded joint analysis methodology for space flight systems. 1995. URL <https://ntrs.nasa.gov/api/citations/19960012183/downloads/19960012183.pdf>.
- [111] Peter RN Childs. *Mechanical design engineering handbook*. Butterworth-Heinemann, 2013.
- [112] Tommy WS Chow and HW Bishop. The effect of high current density and uneven current distribution on a current collection system. *IEEE transactions on components, hybrids, and manufacturing technology*, 14(3):650–656, 1991.
- [113] SR Cole and EW Glossbrenner. Long-duration life tests of slip ring capsule assemblies for inertial guidance platforms. 1974.
- [114] Jack A Collins, Henry R Busby, and George H Staab. *Mechanical design of machine elements and machines: a failure prevention perspective*. John Wiley & Sons, 2009.
- [115] AA Conte Jr and VS Agarwala. An investigation of gold alloy slip ring capsule wear failures. *Wear*, 133(2):355–371, 1989.
- [116] A Cunningham. Long life slip rings for vacuum operation. *IEEE Transactions on Parts, Materials and Packaging*, 7(1):48–61, 1971.
- [117] Antonio De Luca. Architectural design criteria for spacecraft solar arrays. 2011.
- [118] Clarence W De Silva. *Sensors and actuators: control system instrumentation*. CRC Press, 2007.
- [119] Zachary Scott Decker. *A systems-engineering assessment of multiple CubeSat build approaches*. PhD thesis, Massachusetts Institute of Technology, 2016.
- [120] R Devasahayam, VTS Achary, MH Ravichandran, S Simon, P Muralikrishna, CC Joseph, and PM Varghese. Performance enhancement of a 720-step stepper motor for solar array drive of indian remote sensing satellites to achieve low power micro-stepping. 1:264–268, 2003.
- [121] TA Dow and JW Kannel. Thermomechanical effects in high current density electrical slip rings. *Wear*, 79(1):93–105, 1982.
- [122] Jose Miguel EncinasPlaza, Jose Antonio VilanVilan, Fernando AquadoAgelet, Javier Brandiaran-Mancheno, Miguel LopezEstevez, Cesar MartinezFernandez, and Fany SarmientoAres. Xatcobeo: Small mechanisms for cubesat satellites-antenna and solar array deployment. 2010.
- [123] Requirements & Standards Division European Cooperation for Space Standardization. Design rules for printed circuit boards. 2014.
- [124] Katherine A Faist and Gloria J Wiens. Parametric study on the use of hoberman mechanisms for reconfigurable antenna and solar arrays. In *2010 IEEE Aerospace conference*, pages 1–8. IEEE, 2010.
- [125] Rodger Farley and Son Ngo. Development of the solar array deployment and drive system for the xte spacecraft. pages 268–282, 1995.
- [126] Robert L Fusaro. Lubrication of space systems (c). 1995.
- [127] Robert L Fusaro. Nasa space mechanisms handbook: lessons learned documented. 1999.
- [128] Giorgos Galatis, Jian Guo, and Jeroen Buursink. Development of a solar array drive mechanism for micro-satellite platforms. *Acta Astronautica*, 139:407–418, 2017.
- [129] LJ Gleeson and WI Axford. Solar modulation of galactic cosmic rays. *The Astrophysical Journal*, 154: 1011, 1968.

- [130] Martina Grandin and Urban Wiklund. Wear and electrical performance of a slip-ring system with silver-graphite in continuous sliding against pvd coated wires. *Wear*, 348:138–147, 2016.
- [131] Jian Guo, Liora Monas, and Eberhard Gill. Statistical analysis and modelling of small satellite reliability. *Acta Astronautica*, 98:97–110, 2014.
- [132] Allen T Guzik and Othmane Benafan. Design and development of cubesat solar array deployment mechanisms using shape memory alloys. 2018.
- [133] Richard D Hall and Roland P Roberge. Carbon brush performance on slip rings. pages 1–6, 2010.
- [134] A S. Hande. Power transmission devices. URL <https://www.kdkce.edu.in/upload//Machine%20elements,%20Power%20Transmission%20Devices.pdf>.
- [135] Hank Heidt, Jordi Puig-Suari, Augustus Moore, Shinichi Nakasuka, and Robert Twiggs. Cubesat: A new generation of picosatellite for education and industry low-cost space experimentation. 2000.
- [136] Richard E Hodges, Nacer Chahat, Daniel J Hoppe, and Joseph D Vacchione. A deployable high-gain antenna bound for mars: Developing a new folded-panel reflectarray for the first cubesat mission to mars. *IEEE Antennas and Propagation Magazine*, 59(2):39–49, 2017.
- [137] Patrick Hoehn. Design, construction and validation of an articulated solar panel for cubesats, 2010.
- [138] Keith E. Holbert. Radiation effects and damage 1. ionizing radiations. 2007.
- [139] Amy Hutputtanasin. Cubesat design specification rev -9, 2004. URL https://org.ntnu.no/studsat/docs/proposal_1/A8%20%20Cubesat%20Design%20Specification.pdf.
- [140] IPC International Inc. Generic standard on printed board design. 1998.
- [141] IPC International Inc. Standard for determining current-carrying capacity in printed board design. 2009.
- [142] IPC International Inc. Sectional design standard for flexible printed boards. 2016.
- [143] Piers Jiggins, Marc-Andre Chavy-Macdonald, Giovanni Santin, Alessandra Menicucci, Hugh Evans, and Alain Hilgers. The magnitude and effects of extreme solar particle events. *Journal of Space Weather and Space Climate*, 4:A20, 2014.
- [144] Alicia Johnstone. Cubesat design specification, revision 14. July, 2020.
- [145] Howard M Jones and Nell Roger. The design and development of a constant-speed solar array drive. *Mechani*, page 103, 1985.
- [146] C Kitchen, K Mullaney, M Price, A Dollery, K Fyles, H Eaves, R Crabb, and P Bula. Solar cell coverglasses for satellites in the intermediate earth orbit. In *Conference Record of the Twenty Sixth IEEE Photovoltaic Specialists Conference-1997*, pages 1011–1014. IEEE, 1997.
- [147] Bryan Knight. Understanding inertia ratio and its effect on machine performance. URL <https://us.mitsubishielectric.com/fa/en/support/technicalsupport/knowledge-base/getdocument/?docid=3E26SJWH3ZZR-41-13086#:~:text=As%20the%20figure%20shows%2C%20the,operating%20bandwidth%20of%20the%20system>.
- [148] Malcolm E Leader. Understanding journal bearings. 2012.
- [149] N Lewis, S Cole, E Glossbrenner, and C Vest. Friction, wear, and noise of slip ring and brush contacts for synchronous satellite use. *IEEE Transactions on Parts, Hybrids, and Packaging*, 9(1):15–22, 1973.
- [150] Simon Lewis, Lionel Gaillard, René Seiler, Giorgio Parzianello, and Ronan LeLetty. Recent steps towards a common understanding of ball bearing load capacity. *ESA Special Publication*, 737:35, 2015.
- [151] Rui Li, Feng Guo, Chunxu Yu, Yu He, Zhuang Ye, and Shuai Yuan. Development and validation of a mechatronic solar array drive assembly for mini/micro-satellites. *Acta Astronautica*, 134:54–64, 2017.

- [152] Matthew Long, Allen Lorenz, Greg Rodgers, Eric Tapio, Glenn Tran, Keoki Jackson, Robert Twiggs, Thomas Bleier, and Stellar Solutions. A cubesat derived design for a unique academic research mission in earthquake signature detection. In *Proc. AIAA Small Satellite Conference*, 2002.
- [153] Bruce T Lundin. Report of the seasat failure review board. 1978.
- [154] Mohammed Chessab Mahdi, Adnan Falh Hassan, and Jaafer Sadiq Jaafer. New deployable solar panel array for 1u nanosatellites. 2006.
- [155] Matthew Marinella and Hugh Barnaby. Total ionizing dose and displacement damage effects in embedded memory technologies (tutorial notes-draft 1). 2013.
- [156] Michele Marino, Andrea Negri, Massimo Perelli, and Raffaele Palamides. Innovative solar array drive assembly for cubesat satellite. In *Proc. of the 40th Aerospace Mechanisms Symposium*, 2016.
- [157] F Landis Markley and John L Crassidis. *Fundamentals of spacecraft attitude determination and control*, volume 1286. Springer, 2014.
- [158] Masood Mayanbari and Yaser Kasesaz. Design and analyse space radiation shielding for a nanosatellite in low earth orbit (leo). pages 489–493, 2011.
- [159] Grant Munro, M Checkley, Tom Forshaw, and Rene Seiler. Preloaded bearing characteristics under axial vibration. 2013.
- [160] PA Mäusli, G Feusier, and V Gass. Rotating electrical joints with continuous metallic connections. *Proc. 10th ESMATS*, 2003.
- [161] Koji Nakaya, Kazuya Konoue, Hirotaka Sawada, Kyoichi Ui, Hideto Okada, Naoki Miyashita, Masafumi Iai, and Saburo Matunaga. Tokyo tech cubesat: Cute-i-design & development of flight model and future plan. In *21st International Communications Satellite Systems Conference and Exhibit*, page 2388, 2002.
- [162] S Nasir Adeli. Deployment system for the cubesail nano-solar sail mission. 2010.
- [163] Mike Passaretti and Ron Hayes. Development of a solar array drive assembly for cubesat. In *Proceedings of the 40th aerospace mechanisms symposium*, 2010.
- [164] Damon D Phinney. Slip ring experience in long duration space applications. 1986.
- [165] Jeannette Plante and Brandon Lee. Environmental conditions for space flight hardware – a survey. 2004.
- [166] Jeannette Plante and Brandon Lee. Environmental conditions for space flight hardware: a survey. 2005.
- [167] Michel Privat and Denis Schwander. Innovative contactless slip ring. 2007.
- [168] Jordi Puig-Suari, Clark Turner, and William Ahlgren. Development of the standard cubesat deployer and a cubesat class picosatellite. 1:1–347, 2001.
- [169] KR Rajagopal, M Krishnaswamy, Bhim Singh, and BP Singh. An improved high-resolution hybrid stepper motor for solar-array drive of indian remote-sensing satellite. *IEEE Transactions on Industry Applications*, 33(4):906–913, 1997.
- [170] Donald V Reames. Particle acceleration at the sun and in the heliosphere. *Space Science Reviews*, 90(3): 413–491, 1999.
- [171] Terence Rees, John M Standing, and Hawker Siddeley. Design and development of a solar array drive. In *NASA. Goddard Space Flight Center The 11 th Aerospace Mech. Symp. p 223-240(SEE N 79-21374 12-37)*, 1977.
- [172] Alejandro Rivera. Study of spacecraft deployables failures. 2021.
- [173] Fabio Santoni, Fabrizio Piergentili, Gian Paolo Candini, Massimo Perelli, Andrea Negri, and Michele Marino. An orientable solar panel system for nanospacecraft. *Acta Astronautica*, 101:120–128, 2014.

- [174] Fabio Santoni, Fabrizio Piergentili, Serena Donati, Massimo Perelli, Andrea Negri, and Michele Marino. An innovative deployable solar panel system for cubesats. *Acta Astronautica*, 95:210–217, 2014.
- [175] Noëmy Scheidegger, Mark Ferris, and Nigel Phillips. Bi-axial solar array drive mechanism: Design, build and environmental testing. 153, 2014.
- [176] Manfred Schneller. Target pointing of the bird spacecraft via ground in the loop attitude control. In *Proceedings on*. Citeseer, 2003.
- [177] Josh Schoolcraft, Andrew Klesh, and Thomas Werne. Marco: interplanetary mission development on a cubesat scale. pages 221–231, 2017.
- [178] ECSS Secretariat. Ecss-e-st-32-10c rev.1 - structural factors of safety for spaceflight hardware. 2009.
- [179] ECSS Secretariat. Ecss-e-st-33-01c rev.1 - mechanisms. 2017.
- [180] Patrick Senatore, Andrew Klesh, Thomas H Zurbuchen, Darren McKague, and James Cutler. Concept, design, and prototyping of xsas: A high power extendable solar array for cubesat applications. 2010.
- [181] W Shapio, F Murry, R Howorth, and R Fusaro. Space mechanisms lessons learned study: Volume i–summary. *NASA Technical Memorandum*, 107046, 1995.
- [182] Wilbur Shapiro, Frank Murray, Roy Howarth, and Robert Fusaro. Space mechanisms lessons learned study. volume 1: Summary. 1995.
- [183] Wilbur Shapiro, Frank Murray, Roy Howarth, and Robert Fusaro. Space mechanisms lessons learned study. volume 2: Literature review. 1995.
- [184] Wilbur Shapiro, Frank Murray, Roy Howarth, and Robert Fusaro. Space mechanisms lessons learned study. *Volume II-Literature Review*, 1995. URL <https://core.ac.uk/download/pdf/42779861.pdf>.
- [185] Joseph E Shigley, Charles R Mischke, and Thomas Hunter Brown Jr. *Standard handbook of machine design*. McGraw-Hill Education, 2004.
- [186] Doug Sinclair and Jonathan Dyer. Radiation effects and cots parts in smallsats. 2013.
- [187] Emanuele A Slejko, Anna Gregorio, and Vanni Lughì. Material selection for a cubesat structural bus complying with debris mitigation. *Advances in Space Research*, 67(5):1468–1476, 2021.
- [188] Alexander Slocum. Power transmission elements ii. URL https://dspace.mit.edu/bitstream/handle/1721.1/36391/2-007Spring-2003/NR/rdonlyres/Mechanical-Engineering/2-007Design-and-Manufacturing-ISpring2003/AB038E9F-29E8-4525-B914-10AC734962EA/0/Topic6ScrewsandGears_GW.pdf.
- [189] Arturo Solís-Santomé, Guillermo Urriolagoitia-Sosa, Beatriz Romero-Ángeles, Christopher Rene Torres-San Miguel, Jorge J Hernández-Gómez, Isaac Medina-Sánchez, Carlos Couder-Castañeda, Jesús Irán Grageda-Arellano, and Guillermo Urriolagoitia-Calderón. Conceptual design and finite element method validation of a new type of self-locking hinge for deployable cubesat solar panels. *Advances in Mechanical Engineering*, 11(1):1687814018823116, 2019.
- [190] Philip Swenson, Grant Thomas, Richard Cobb, Jonathan Black, and Eric Swenson. Development and design of an afit cubesat demonstrating deployable technology. In *51st AIAA/ASME/ASCE/AHS/ASC Structures, Structural Dynamics, and Materials Conference 18th AIAA/ASME/AHS Adaptive Structures Conference 12th*, page 2906, 2010.
- [191] Cal Poly SLO The CubeSat Program. Cubesat design specification rev. 14. 2020.
- [192] Power transmission reference guide. Know which gear is more efficient?, 2016. URL <http://maxpowergears.com/know-gear-efficient/>.
- [193] Power transmission reference guide. Using gears to change the inertia ratio of a motor-driven system, 2020. URL https://issuu.com/wtwhmedia/docs/power_transmission_reference_guide_may_2020/s/10474688.

- [194] Turtogtokh Tumenjargal and Mengu Cho. Standardized, flexible interface design for a cubesat bus system. 2019.
- [195] Jose E Velazco and Jaime Sanchez de la Vega. Q4—a cubesat mission to demonstrate omnidirectional optical communications. pages 1–6, 2020.
- [196] Aleksandar Vencel, Vlada Gašić, and Blaža Stojanović. Fault tree analysis of most common rolling bearing tribological failures. 174(1):012048, 2017.
- [197] E Videira, C Lebreton, SD Lewis, and L Gaillard. Design, assembly and preloading of ball bearings for space applications—lessons learned and guidelines for future success. 2013.
- [198] Nathan K Walsh. Development of a deployable 3u cubesat solar panel array. *FELLOWSHIP REPORTS*, page 59, 2010.
- [199] Meng-Hui Wang and Mu-Jia Chen. Two-stage fault diagnosis method based on the extension theory for pv power systems. *International Journal of Photoenergy*, 2012, 2012.
- [200] Q Jane Wang and Yip-Wah Chung. *Encyclopedia of tribology*. Springer, 2013.
- [201] James Richard Wertz, Wiley J Larson, Douglas Kirkpatrick, and Donna Klungle. *Space mission analysis and design*, volume 8. Springer, 1999.
- [202] Sasha Weston, Cameron S Miller, Joshua E Ingersoll, Bruce D Yost, Elwood Agasid, Roland Burton, Roberto Carlino, Gregory Defouw, Andres Dono Perez, Arif Goktug Karacalioglu, et al. State of the art: Small spacecraft technology. 2018.
- [203] J Jaap Wijker. *Spacecraft structures*. Springer Science & Business Media, 2008.
- [204] Jason M Wilkenfeld, Roland E Leadon, and Charles E Mallon. Radiation effects in satellite cables. 1978.
- [205] Brian Wood, Paul Joachim Schüngel, Guido Sutter, and Andrew Skulicz. Lessons learnt from the root cause investigation on the sad-lp solar array drive mechanism. 2007.
- [206] I Yasar, AYKUT Canakci, and F Arslan. The effect of brush spring pressure on the wear behaviour of copper-graphite brushes with electrical current. *Tribology International*, 40(9):1381–1386, 2007.
- [207] Han Yuan, Jean-Christophe Fauroux, Frédéric Chapelle, and Xavier Balandraud. A review of rotary actuators based on shape memory alloys. *Journal of Intelligent Material Systems and Structures*, 28(14): 1863–1885, 2017.
- [208] Yongjie Zhang and Bin Hu. Research on space wireless drive mechanism based on wireless measurement and control network technology. 677(4):042119, 2019.



Appendix

A.1. COTS SADA for Mini & MicroSats

Company	Name of SADM	Output Step angle (deg)	Mass (kgs)	Avg Holding torque (Nm)	Slipring Power transfer
Moog	Type-1	0.0375	1.16	8.4	30 rings at 2A
Moog	Type-2	0.02	3.5	11	34 rings at 3.2A
Moog	Type-3/5	0.0075	5	45.2	26 rings at 6A
Moog	Type-5	0.0075	5	45.2	16 rings at 1A
RUAG Space	SEPTA-24	0.00625	3.5	11	24 lines at 6.2A up to 110V
RUAG Space	SEPTA-31	0.01	3.6	≥ 10.6	24 lines at 1.65A & 55V
RUAG Space	SEPTA-32	0.01	4.4	≥ 10.6	20 lines at 3A & 55V
RUAG Space	SEPTA-33	upto 0.002055	4.25	≥ 10	10 lines at 4A & 55V
RUAG Space	SEPTA-41	0.015	1.7	≥ 0.05	11 lines at 1.65A & 33V
Honeybee Robotics	SmallSat SADM	0.0042	3.1	24	34 lines at 3A
Honeybee Robotics	MicroSat SADM	0.0018	0.9	>1	16 lines at 1.1A
Thales Alenia	ATV SADM	0.12	3	-	8 lines at 3.5A upto 100V
Thales Alenia	GEO SADM	0.12	4.5	-	20 lines at 7.5A upto 100V
Thales Alenia	Low power SADM	0.12	3.5	-	8 lines at 5A upto 120V
Sierra Nevada Corp	C14-750 W	0.0625	1.6	14	30 rings at 2A

Table A.1: Commercially available single axis articulation SADM for Mini/Micro-satellites

A.2. CubeSat structure standard data-sheets

A.2.1. Random vibration loads

Table 2.4-3
Generalized Random Vibration Test Levels
Components (ELV)
22.7-kg (50-lb) or less

Frequency (Hz)	ASD Level (g^2/Hz)	
	Qualification	Acceptance
20	0.026	0.013
20-50	+6 dB/oct	+6 dB/oct
50-800	0.16	0.08
800-2000	-6 dB/oct	-6 dB/oct
2000	0.026	0.013
Overall	14.1 G_{rms}	10.0 G_{rms}

The acceleration spectral density level may be reduced for components weighing more than 22.7-kg (50 lb) according to:

	<u>Weight in kg</u>	<u>Weight in lb</u>	
dB reduction	$= 10 \log(W/22.7)$	$10 \log(W/50)$	
ASD(50-800 Hz)	$= 0.16 \cdot (22.7/W)$	$0.16 \cdot (50/W)$	for protoflight
ASD(50-800 Hz)	$= 0.08 \cdot (22.7/W)$	$0.08 \cdot (50/W)$	for acceptance

Where W = component weight.

The slopes shall be maintained at + and - 6dB/oct for components weighing up to 59-kg (130-lb). Above that weight, the slopes shall be adjusted to maintain an ASD level of $0.01 \text{ g}^2/\text{Hz}$ at 20 and 2000 Hz.

For components weighing over 182-kg (400-lb), the test specification will be maintained at the level for 182-kg (400 pounds).

Figure A.1: Qualification random vibration loads from NASA GEVS [108]

A.2.2. 12U structure

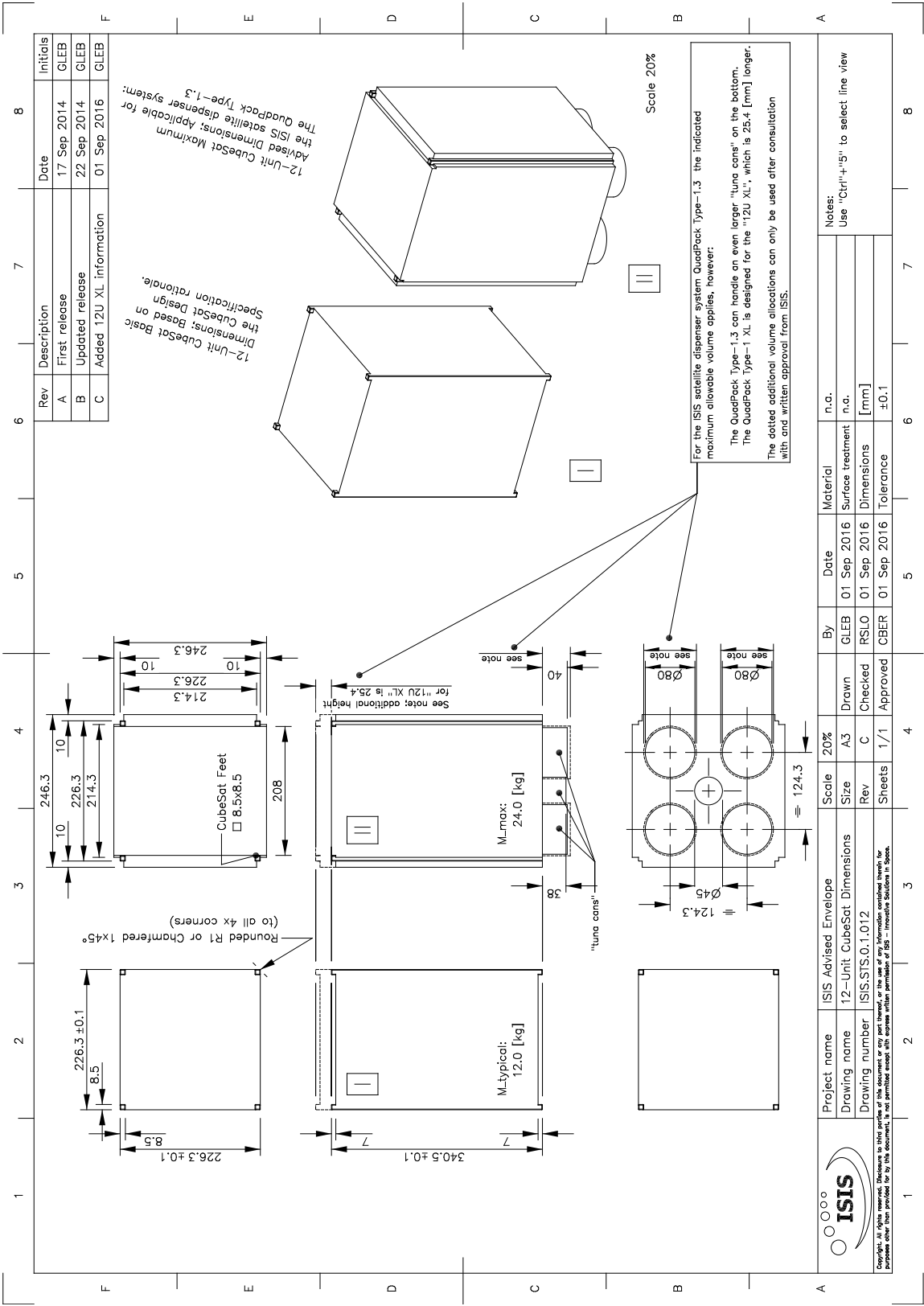
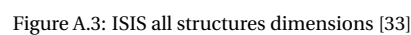


Figure A.2: ISIS 12 U data sheet [32]



A.3. SPENVIS Radiation simulation results

A.3.1. SAA Passover

Simulation parameters			
Coordinate generators	Spacecraft trajectories	Number of mission segments	1
		Mission duration	5 years
		Satellite orientation	1 axis parallel to velocity vector
		Orbit type	General
		Orbit specification	South Atlantic anomaly
		Trajectory duration	30 days
		Altitude (circular orbit)	800 km
		Inclination (deg)	55
		RAAN	0
		Argument of pericenter	0
Radiation sources & effects	Trapped proton & electron fluxes	Proton model	AP-8
		Electron model	AE-8
		Model version	Solar maximum
		Threshold flux for exposure(/cm2/s) - protons	1
		Threshold flux for exposure(/cm2/s) - electrons	1
		Confidence level [%]	50
	Solar particle mission fluences	Solar particle model	ESP-PSYCHIC (total fluence)
		Ion range	H to U
		Confidence level [%]	80
		Magnetic shielding	default
	Galactic cosmic ray fluxes	Ion range	H to U
		GCR model at 1 AU	ISO-15390 standard model
		Solar activity data	Solar Minimum (May 1996)
		Magnetic shielding	default
	Ionizing dose for simple geometries	Dose model	SHIELDOSE-2Q
		Shielding configuration	centre of Al spheres
		Shield composition	Aluminium
		Target material	Silicon

Figure A.4: Simulation parameters of orbit through SAA (referred from [20])

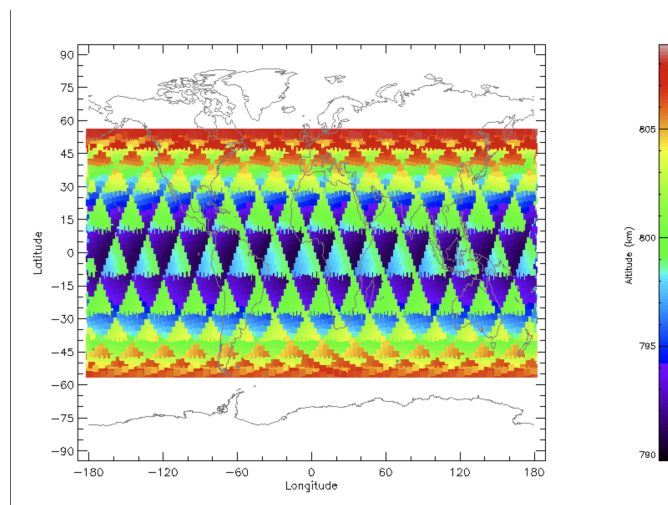


Figure A.5: Ground track of orbit through SAA

Aluminium			
Total absorber thickness (mm)	Total mission dose (rad)	Trapped electrons (rad)	Trapped protons (rad)
1.00E-04	2.34E+07	4.67E+06	1.80E+07
2.00E-01	1.36E+06	1.33E+06	1.87E+04
4.00E-01	3.69E+05	3.55E+05	1.16E+04
6.00E-01	1.56E+05	1.46E+05	8.87E+03
8.00E-01	9.09E+04	8.24E+04	7.36E+03
1.00E+00	6.36E+04	5.63E+04	6.43E+03
1.20E+00	4.81E+04	4.16E+04	5.81E+03
1.40E+00	3.82E+04	3.22E+04	5.37E+03
1.60E+00	3.13E+04	2.57E+04	5.01E+03
1.80E+00	2.62E+04	2.10E+04	4.76E+03
2.00E+00	2.23E+04	1.73E+04	4.55E+03
2.50E+00	1.54E+04	1.10E+04	4.10E+03
3.00E+00	1.11E+04	7.10E+03	3.78E+03
3.50E+00	8.42E+03	4.63E+03	3.58E+03
4.00E+00	6.58E+03	3.02E+03	3.37E+03
4.50E+00	5.36E+03	1.96E+03	3.24E+03
5.00E+00	4.50E+03	1.24E+03	3.12E+03
5.50E+00	3.88E+03	7.67E+02	2.99E+03
6.00E+00	3.50E+03	4.71E+02	2.91E+03

Table A.2: Aluminium thickness required for different radiation doses in orbit with SAA passover

Titanium			
Total absorber thickness (mm)	Total mission dose (rad)	Trapped electrons (rad)	Trapped protons (rad)
1.00E-04	2.97E+07	5.79E+06	2.30E+07
0.1198	1.22E+06	1.18E+06	2.16E+04
2.40E-01	3.08E+05	2.90E+05	1.33E+04
3.60E-01	1.36E+05	1.24E+05	1.01E+04
4.79E-01	8.30E+04	7.31E+04	8.38E+03
5.99E-01	5.90E+04	5.05E+04	7.30E+03
7.19E-01	4.49E+04	3.73E+04	6.59E+03
8.39E-01	3.57E+04	2.88E+04	6.08E+03
9.59E-01	2.91E+04	2.28E+04	5.66E+03
1.08E+00	2.42E+04	1.83E+04	5.38E+03
1.20E+00	2.05E+04	1.48E+04	5.14E+03
1.50E+00	1.40E+04	9.00E+03	4.62E+03
1.80E+00	1.01E+04	5.56E+03	4.26E+03
2.10E+00	7.70E+03	3.46E+03	4.02E+03
2.40E+00	6.11E+03	2.14E+03	3.79E+03
2.70E+00	5.09E+03	1.30E+03	3.64E+03
3.00E+00	4.41E+03	7.75E+02	3.50E+03
3.30E+00	3.93E+03	4.58E+02	3.36E+03
3.60E+00	3.64E+03	2.69E+02	3.27E+03

Table A.3: Titanium thickness required for different radiation doses in orbit with SAA passover

Iron			
Total absorber thickness (mm)	Total mission dose (rad)	Trapped electrons (rad)	Trapped protons (rad)
1.00E-04	4.10E+07	6.26E+06	3.34E+07
6.86E-02	1.16E+06	1.12E+06	2.31E+04
1.37E-01	2.87E+05	2.69E+05	1.41E+04
2.06E-01	1.30E+05	1.17E+05	1.07E+04
2.74E-01	8.07E+04	7.04E+04	8.78E+03
3.43E-01	5.76E+04	4.89E+04	7.63E+03
4.12E-01	4.40E+04	3.62E+04	6.88E+03
4.80E-01	3.49E+04	2.79E+04	6.33E+03
5.49E-01	2.84E+04	2.19E+04	5.89E+03
6.17E-01	2.36E+04	1.75E+04	5.59E+03
6.86E-01	1.99E+04	1.41E+04	5.33E+03
8.57E-01	1.35E+04	8.37E+03	4.79E+03
1.03E+00	9.72E+03	5.04E+03	4.41E+03
1.20E+00	7.42E+03	3.05E+03	4.16E+03
1.37E+00	5.92E+03	1.83E+03	3.92E+03
1.54E+00	4.98E+03	1.08E+03	3.76E+03
1.71E+00	4.37E+03	6.26E+02	3.61E+03
1.89E+00	3.94E+03	3.63E+02	3.46E+03
2.06E+00	3.68E+03	2.10E+02	3.37E+03

Table A.4: Iron thickness required for different radiation doses in orbit with SAA passover

Tantalum			
Total absorber thickness (mm)	Total mission dose (rad)	Trapped electrons (rad)	Trapped protons (rad)
1.00E-04	1.20E+08	1.47E+07	1.02E+08
3.24E-02	7.31E+05	6.74E+05	4.76E+04
6.47E-02	2.03E+05	1.71E+05	2.77E+04
9.71E-02	1.07E+05	8.33E+04	2.05E+04
1.29E-01	7.09E+04	5.24E+04	1.65E+04
1.62E-01	5.12E+04	3.56E+04	1.42E+04
1.94E-01	3.91E+04	2.53E+04	1.26E+04
2.27E-01	3.09E+04	1.84E+04	1.15E+04
2.59E-01	2.50E+04	1.35E+04	1.07E+04
2.91E-01	2.09E+04	1.01E+04	1.01E+04
3.24E-01	1.77E+04	7.55E+03	9.56E+03
4.04E-01	1.27E+04	3.74E+03	8.51E+03
4.85E-01	1.00E+04	1.86E+03	7.76E+03
5.66E-01	8.53E+03	9.31E+02	7.29E+03
6.47E-01	7.56E+03	4.65E+02	6.84E+03
7.28E-01	6.99E+03	2.34E+02	6.54E+03
8.09E-01	6.57E+03	1.19E+02	6.27E+03
8.90E-01	6.21E+03	6.06E+01	5.99E+03
9.71E-01	6.00E+03	3.08E+01	5.82E+03

Table A.5: Tantalum thickness required for different radiation doses in orbit with SAA passover

A.3.2. Heliosynchronous orbit

Simulation parameters			
Coordinate generators	Spacecraft trajectories	Number of mission segments	1
		Mission duration	5 years
		Satellite orientation	1 axis parallel to velocity vector
		Orbit type	Heliosynchronous
		Trajectory duration	30 days
		Altitude	400 km
Radiation sources & effects	Trapped proton & electron fluxes	Proton model	AP-8
		Electron model	AE-8
		Model version	Solar maximum
		Threshold flux for exposure(/cm2/s) - protons	1
		Threshold flux for exposure(/cm2/s) - electrons	1
		Confidence level	50 %
	Solar particle mission fluences	Solar particle model	ESP-PSYCHIC (total fluence)
		lon range	H to U
		Confidence level [%]	80
		Magnetic shielding	default
	Galactic cosmic ray fluxes	lon range	H to U
		GCR model at 1 AU	ISO-15390 standard model
		Solar activity data	Solar Minimum (May 1996)
		Magnetic shielding	default
	Ionizing dose for simple geometries	Dose model	SHIELDOSE-2Q
		Shielding configuration	centre of Al spheres
		Shield composition	Aluminium
		Target material	Silicon

Figure A.6: Simulation parameters of heliosynchronous orbit (referred from [186])

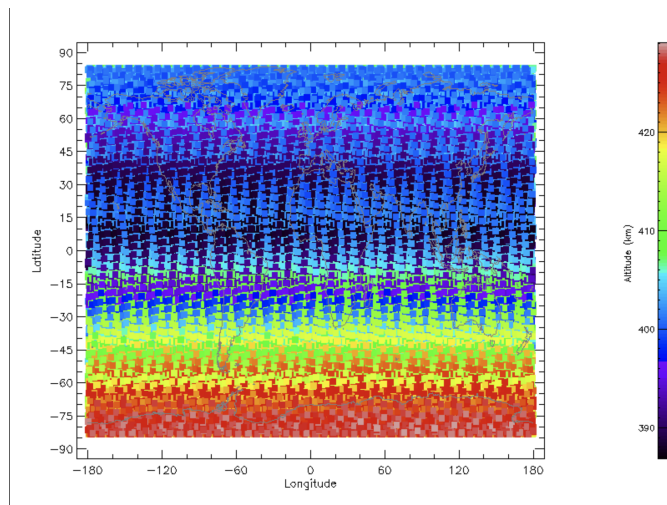


Figure A.7: Ground track of heliosynchronous orbit

Aluminium			
Total absorber thickness (mm)	Total mission dose (rad)	Trapped electrons (rad)	Trapped protons (rad)
1.00E-04	8.11E+06	8.90E+05	6.13E+05
2.00E-01	1.97E+05	1.70E+05	3.06E+02
4.00E-01	8.18E+04	6.83E+04	2.22E+02
6.00E-01	4.72E+04	3.83E+04	1.88E+02
8.00E-01	3.22E+04	2.57E+04	1.67E+02
1.00E+00	2.39E+04	1.89E+04	1.54E+02
1.20E+00	1.87E+04	1.45E+04	1.45E+02
1.40E+00	1.51E+04	1.16E+04	1.40E+02
1.60E+00	1.23E+04	9.37E+03	1.35E+02
1.80E+00	1.03E+04	7.70E+03	1.31E+02
2.00E+00	8.71E+03	6.38E+03	1.29E+02
2.50E+00	5.84E+03	4.05E+03	1.21E+02
3.00E+00	4.02E+03	2.60E+03	1.16E+02
3.50E+00	2.89E+03	1.69E+03	1.11E+02
4.00E+00	2.11E+03	1.10E+03	1.07E+02
4.50E+00	1.59E+03	7.15E+02	1.05E+02
5.00E+00	1.23E+03	4.58E+02	1.02E+02
5.50E+00	9.70E+02	2.90E+02	9.89E+01
6.00E+00	8.02E+02	1.81E+02	9.72E+01

Table A.6: Aluminium thickness required for different radiation doses in a LEO Heliosynchronous orbit

Titanium			
Total absorber thickness (mm)	Total mission dose (rad)	Trapped electrons (rad)	Trapped protons (rad)
1.00E-04	1.04E+07	1.12E+06	7.83E+05
1.20E-01	1.94E+05	1.61E+05	3.52E+02
2.40E-01	7.94E+04	6.35E+04	2.54E+02
3.60E-01	4.62E+04	3.57E+04	2.14E+02
4.79E-01	3.16E+04	2.40E+04	1.89E+02
5.99E-01	2.34E+04	1.75E+04	1.74E+02
7.19E-01	1.82E+04	1.34E+04	1.64E+02
8.39E-01	1.45E+04	1.05E+04	1.58E+02
9.59E-01	1.18E+04	8.36E+03	1.52E+02
1.08E+00	9.76E+03	6.74E+03	1.48E+02
1.20E+00	8.14E+03	5.47E+03	1.45E+02
1.50E+00	5.34E+03	3.30E+03	1.36E+02
1.80E+00	3.65E+03	2.03E+03	1.30E+02
2.10E+00	2.62E+03	1.26E+03	1.25E+02
2.40E+00	1.92E+03	7.83E+02	1.20E+02
2.70E+00	1.47E+03	4.82E+02	1.17E+02
3.00E+00	1.16E+03	2.93E+02	1.14E+02
3.30E+00	9.41E+02	1.76E+02	1.11E+02
3.60E+00	8.02E+02	1.05E+02	1.09E+02

Table A.7: Titanium thickness required for different radiation doses in a LEO Heliosynchronous orbit

Iron			
Total absorber thickness (mm)	Total mission dose (rad)	Trapped electrons (rad)	Trapped protons (rad)
1.00E-04	1.47E+07	1.21E+06	1.14E+06
6.86E-02	1.92E+05	1.58E+05	3.73E+02
1.37E-01	7.88E+04	6.19E+04	2.66E+02
2.06E-01	4.60E+04	3.50E+04	2.23E+02
2.74E-01	3.15E+04	2.36E+04	1.97E+02
3.43E-01	2.34E+04	1.72E+04	1.81E+02
4.12E-01	1.81E+04	1.30E+04	1.70E+02
4.80E-01	1.44E+04	1.02E+04	1.64E+02
5.49E-01	1.17E+04	8.07E+03	1.57E+02
6.17E-01	9.60E+03	6.45E+03	1.53E+02
6.86E-01	7.98E+03	5.19E+03	1.50E+02
8.57E-01	5.19E+03	3.07E+03	1.41E+02
1.03E+00	3.53E+03	1.84E+03	1.34E+02
1.20E+00	2.53E+03	1.11E+03	1.29E+02
1.37E+00	1.85E+03	6.72E+02	1.24E+02
1.54E+00	1.43E+03	4.02E+02	1.21E+02
1.71E+00	1.14E+03	2.38E+02	1.17E+02
1.89E+00	9.34E+02	1.40E+02	1.14E+02
2.06E+00	8.05E+02	8.20E+01	1.12E+02

Table A.8: Iron thickness required for different radiation doses in a LEO Heliosynchronous orbit

Tantalum			
Total absorber thickness (mm)	Total mission dose (rad)	Trapped electrons (rad)	Trapped protons (rad)
1.00E-04	4.35E+07	2.36E+06	3.48E+06
3.24E-02	2.04E+05	1.32E+05	7.36E+02
6.47E-02	8.51E+04	5.15E+04	5.06E+02
9.71E-02	5.06E+04	2.90E+04	4.13E+02
1.29E-01	3.44E+04	1.89E+04	3.58E+02
1.62E-01	2.49E+04	1.30E+04	3.25E+02
1.94E-01	1.89E+04	9.29E+03	3.04E+02
2.27E-01	1.48E+04	6.75E+03	2.91E+02
2.59E-01	1.17E+04	4.96E+03	2.78E+02
2.91E-01	9.58E+03	3.69E+03	2.69E+02
3.24E-01	7.96E+03	2.76E+03	2.63E+02
4.04E-01	5.30E+03	1.37E+03	2.46E+02
4.85E-01	3.78E+03	6.91E+02	2.33E+02
5.66E-01	2.94E+03	3.51E+02	2.23E+02
6.47E-01	2.32E+03	1.79E+02	2.14E+02
7.28E-01	1.95E+03	9.12E+01	2.08E+02
8.09E-01	1.67E+03	4.66E+01	2.02E+02
8.90E-01	1.45E+03	2.37E+01	1.95E+02
9.71E-01	1.30E+03	1.20E+01	1.92E+02

Table A.9: Tantalum thickness required for different radiation doses in a LEO Heliosynchronous orbit

A.3.3. Polar orbit

Simulation parameters			
Coordinate generators	Spacecraft trajectories	Number of mission segments	1
		Mission duration	5 years
		Satellite orientation	1 axis parallel to velocity vector
		Orbit type	General (Specific for polar orbit)
		Trajectory duration	30 days
		Altitude (circular orbit)	800 km
		Inclination (deg)	98
		RAAN	0
		Argument of pericenter	0
		True anomaly	0
Radiation sources & effects	Trapped proton & electron fluxes	Proton model	AP-8
		Electron model	AE-8
		Model version	Solar maximum
		Threshold flux for exposure(/cm2/s) - protons	1
		Threshold flux for exposure(/cm2/s) - electrons	1
		Confidence level	50 %
	Solar particle mission fluences	Solar particle model	ESP-PSYCHIC (total fluence)
		Ion range	H to U
		Confidence level [%]	80
		Magnetic shielding	default
	Galactic cosmic ray fluxes	Ion range	H to U
		GCR model at 1 AU	ISO-15390 standard model
		Solar activity data	Solar Minimum (May 1996)
		Magnetic shielding	default
	Ionizing dose for simple geometries	Dose model	SHIELDOSE-2Q
		Shielding configuration	centre of Al spheres
		Shield composition	Aluminium
		Target material	Silicon

Figure A.8: Simulation parameters of polar orbit

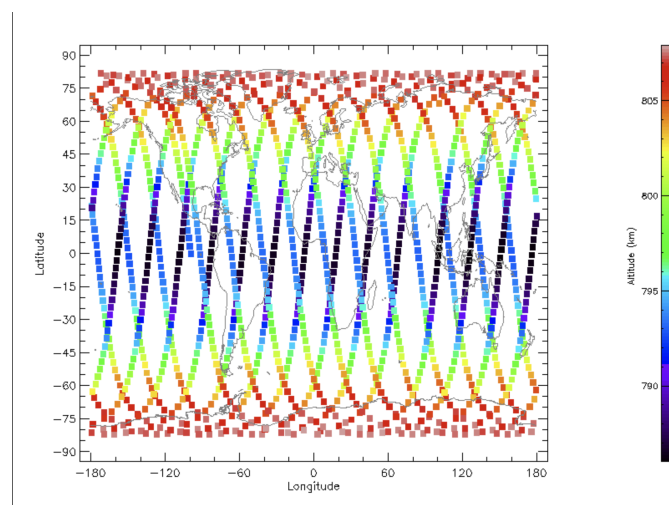


Figure A.9: Ground track of polar orbit

Aluminium			
Total absorber thickness (mm)	Total mission dose (rad)	Trapped electrons (rad)	Trapped protons (rad)
1.00E-04	2.50E+07	3.92E+06	1.37E+07
2.00E-01	1.11E+06	1.06E+06	1.22E+04
4.00E-01	3.44E+05	3.20E+05	7.85E+03
6.00E-01	1.62E+05	1.46E+05	6.16E+03
8.00E-01	1.00E+05	8.74E+04	5.19E+03
1.00E+00	7.17E+04	6.13E+04	4.59E+03
1.20E+00	5.48E+04	4.59E+04	4.18E+03
1.40E+00	4.36E+04	3.58E+04	3.89E+03
1.60E+00	3.56E+04	2.86E+04	3.64E+03
1.80E+00	2.97E+04	2.33E+04	3.48E+03
2.00E+00	2.51E+04	1.92E+04	3.33E+03
2.50E+00	1.70E+04	1.20E+04	3.02E+03
3.00E+00	1.20E+04	7.68E+03	2.80E+03
3.50E+00	8.89E+03	4.96E+03	2.65E+03
4.00E+00	6.78E+03	3.22E+03	2.51E+03
4.50E+00	5.40E+03	2.07E+03	2.41E+03
5.00E+00	4.43E+03	1.31E+03	2.32E+03
5.50E+00	3.73E+03	8.12E+02	2.23E+03
6.00E+00	3.30E+03	4.99E+02	2.18E+03

Table A.10: Aluminium thickness required for different radiation doses in a LEO polar orbit

Titanium			
Total absorber thickness (mm)	Total mission dose (rad)	Trapped electrons (rad)	Trapped protons (rad)
1.00E-04	3.19E+07	4.92E+06	1.76E+07
1.20E-01	1.02E+06	9.64E+05	1.41E+04
2.40E-01	3.01E+05	2.73E+05	9.01E+03
3.60E-01	1.47E+05	1.28E+05	7.04E+03
4.79E-01	9.38E+04	7.91E+04	5.91E+03
5.99E-01	6.76E+04	5.56E+04	5.21E+03
7.19E-01	5.17E+04	4.14E+04	4.74E+03
8.39E-01	4.10E+04	3.20E+04	4.40E+03
9.59E-01	3.33E+04	2.53E+04	4.12E+03
1.08E+00	2.75E+04	2.02E+04	3.93E+03
1.20E+00	2.30E+04	1.63E+04	3.76E+03
1.50E+00	1.54E+04	9.77E+03	3.41E+03
1.80E+00	1.09E+04	5.97E+03	3.15E+03
2.10E+00	8.11E+03	3.68E+03	2.98E+03
2.40E+00	6.26E+03	2.27E+03	2.82E+03
2.70E+00	5.10E+03	1.37E+03	2.71E+03
3.00E+00	4.31E+03	8.21E+02	2.61E+03
3.30E+00	3.75E+03	4.85E+02	2.50E+03
3.60E+00	3.41E+03	2.85E+02	2.44E+03

Table A.11: Titanium thickness required for different radiation doses in a LEO polar orbit

Iron			
Total absorber thickness (mm)	Total mission dose (rad)	Trapped electrons (rad)	Trapped protons (rad)
0.00E+00	4.48E+07	5.33E+06	2.57E+07
6.86E-02	9.78E+05	9.21E+05	1.50E+04
1.37E-01	2.87E+05	2.57E+05	9.52E+03
2.06E-01	1.43E+05	1.22E+05	7.40E+03
2.74E-01	9.20E+04	7.67E+04	6.19E+03
3.43E-01	6.64E+04	5.40E+04	5.44E+03
4.12E-01	5.08E+04	4.02E+04	4.94E+03
4.80E-01	4.03E+04	3.09E+04	4.58E+03
5.49E-01	3.26E+04	2.43E+04	4.28E+03
6.17E-01	2.69E+04	1.93E+04	4.08E+03
6.86E-01	2.24E+04	1.55E+04	3.90E+03
8.57E-01	1.49E+04	9.06E+03	3.53E+03
1.03E+00	1.05E+04	5.40E+03	3.26E+03
1.20E+00	7.81E+03	3.24E+03	3.08E+03
1.37E+00	6.06E+03	1.93E+03	2.91E+03
1.54E+00	4.98E+03	1.14E+03	2.80E+03
1.71E+00	4.26E+03	6.63E+02	2.69E+03
1.89E+00	3.75E+03	3.84E+02	2.58E+03
2.06E+00	3.44E+03	2.22E+02	2.52E+03

Table A.12: Iron thickness required for different radiation doses in a LEO polar orbit

Tantalum			
Total absorber thickness (mm)	Total mission dose (rad)	Trapped electrons (rad)	Trapped protons (rad)
0.00E+00	1.32E+08	1.19E+07	7.83E+07
3.24E-02	7.20E+05	6.09E+05	3.08E+04
6.47E-02	2.35E+05	1.79E+05	1.86E+04
9.71E-02	1.30E+05	9.16E+04	1.41E+04
1.29E-01	8.67E+04	5.80E+04	1.16E+04
1.62E-01	6.25E+04	3.94E+04	1.01E+04
1.94E-01	4.74E+04	2.78E+04	9.04E+03
2.27E-01	3.71E+04	2.00E+04	8.32E+03
2.59E-01	2.97E+04	1.47E+04	7.72E+03
2.91E-01	2.45E+04	1.09E+04	7.33E+03
3.24E-01	2.07E+04	8.10E+03	6.98E+03
4.04E-01	1.44E+04	3.97E+03	6.25E+03
4.85E-01	1.09E+04	1.97E+03	5.73E+03
5.66E-01	9.05E+03	9.85E+02	5.40E+03
6.47E-01	7.75E+03	4.92E+02	5.08E+03
7.28E-01	6.98E+03	2.47E+02	4.86E+03
8.09E-01	6.40E+03	1.25E+02	4.67E+03
8.90E-01	5.91E+03	6.29E+01	4.46E+03
9.71E-01	5.62E+03	3.16E+01	4.34E+03

Table A.13: Tantalum thickness required for different radiation doses in a LEO polar orbit

A.4. Rotary actuator

A.4.1. Motor trade-off

Name of motor	Company	Diameter (mm)	Length (mm)	Nominal torque (mNm)	Peak torque (mNm)	Maximum power output (mW)	Operational temperature (C)		Non-operating temperature (C)	Space-grade lubrication	Total requirements met	
							-40	70			125	Desirable
Motor requirement												
DM0620-0130/0080	Faulhaber	6	14.65	0.25	0.39	65.00	-35.00	70.00	-30.00	130.00	No	6
		8	19.8	0.65	1.00	112.80	-30.00	70.00	-30.00	130.00	No	5
		10	22.4	1.6	2.40	170.00	-35.00	70.00	-30.00	130.00	No	5
		6	20.5	15	0.39	65.00	-20.00	70.00	-35.00	130.00	No	6
MaalonDrive HighAcc 6mm - Type 3												
MaalonDrive Space 8mm - Type 3	Micromotion GmbH	8	27.9	3	1.00	110.00	-20.00	70.00	-35.00	130.00	Yes	5
		3.4	4.7	0.025	0.04	11.76	-10.00	50.00	-25.00	60.00	No	3
		4.3	5.4	0.05	0.09	27.44	-10.00	50.00	-25.00	60.00	No	3
		5	5.7	0.08	0.14	37.68	-10.00	50.00	-25.00	60.00	No	3
SMH6-F20	Minebea Mitsumi	6	7.6	0.15	0.40	78.40	-10.00	50.00	-25.00	60.00	No	4
SMH8-F20	Minebea Mitsumi	8	9.8	0.65	0.70	215.00	-10.00	50.00	-25.00	60.00	No	3
ZWBMD003003-5	Zhaowei	3.4	15.00	4.9	14.71	12.60	-10.00	85.00	-	-	No	5
ZWBMD004004-625	Zhaowei	4	23.1	6.86	19.61	20.76	-20.00	85.00	-	-	No	5
Piezo-electric motors												
PI-U-622	PI	10	20 x 20	5	-	-	-	-	-	-	-	0
PI-U-651	PI	14	116 x 116	30	-	-	-	-	-	-	-	0
PT1C60-800S	PT-Japan	20	60 x 60	-	-	-	-	-	-	-	-	0
PI-Q-632	PI	8	36 x 36	6	-	-	-	-	-	-	-	0
XPT-A-25-109	Xeryon	15	40 x 31	4	-	-	-	-	-	-	-	0

Table A.14: Motor selection trade-off

A.4.2. Motor data-sheet



Stepper Motors

0,25 mNm

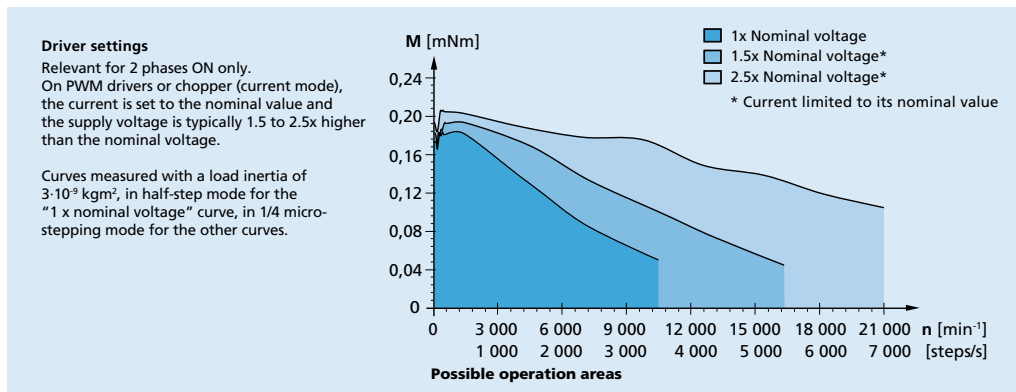
Two phase with Disc Magnet,
20 steps per revolution

Series DM0620

Values at 20°C	DM0620	0130	0080	0040	
Nominal current per phase (both phases ON)		0,13	0,08	0,04	A
Boosted current per phase (both phases ON)		0,26	0,16	0,08	A
Nominal voltage per phase (both phases ON)		2	3	6	V
Phase resistance		13,6	30	120	Ω
Phase inductance (1 kHz)		2	4,5	18,5	mH
Holding torque (at nominal current in both phases)		0,25	0,25	0,25	mNm
Holding torque at boosted current		0,39	0,39	0,39	mNm
Residual torque, typ.		0,03	0,03	0,03	mNm
Back-EMF amplitude		0,53	0,83	1,6	V/k step/s
Electrical time constant	0,15				ms
Rotor inertia	$0,5 \cdot 10^{-9}$				kgm ²
Step angle (full step)	18				°
Angular accuracy	±5				%
Angular acceleration, max.	$780 \cdot 10^3$				rad/s ²
Resonance frequency (at no load)	110				Hz
Thermal resistance	15 / 96,6				K/W
Thermal time constant	3,2 / 120				s
Operating temperature range	-35 ... +70				°C
Winding temperature, max.	+130				°C
Shaft bearings ^{1) 2)}	sintered bearing (Bearing code: SB)	ball bearings, preloaded (Bearing code: 2R)			
Shaft load max.:					
– with shaft diameter	1	1			mm
– radial at 5 000 min ⁻¹ (3 mm from bearing)	0,3	3			N
– axial at 5 000 min ⁻¹	0,5	0,5			N
– axial at standstill	0,5	5,8			N
Shaft play:					
– radial	0,02	0,012			mm
– axial	0	0			mm
Housing material	aluminium, black anodized				
Mass	1,1				g
Magnet material	NdFeB				

¹⁾ Special lubricant options available on request.

²⁾ 2 preloaded ball bearings available on request for vacuum / low temperature (bearing code: RC).

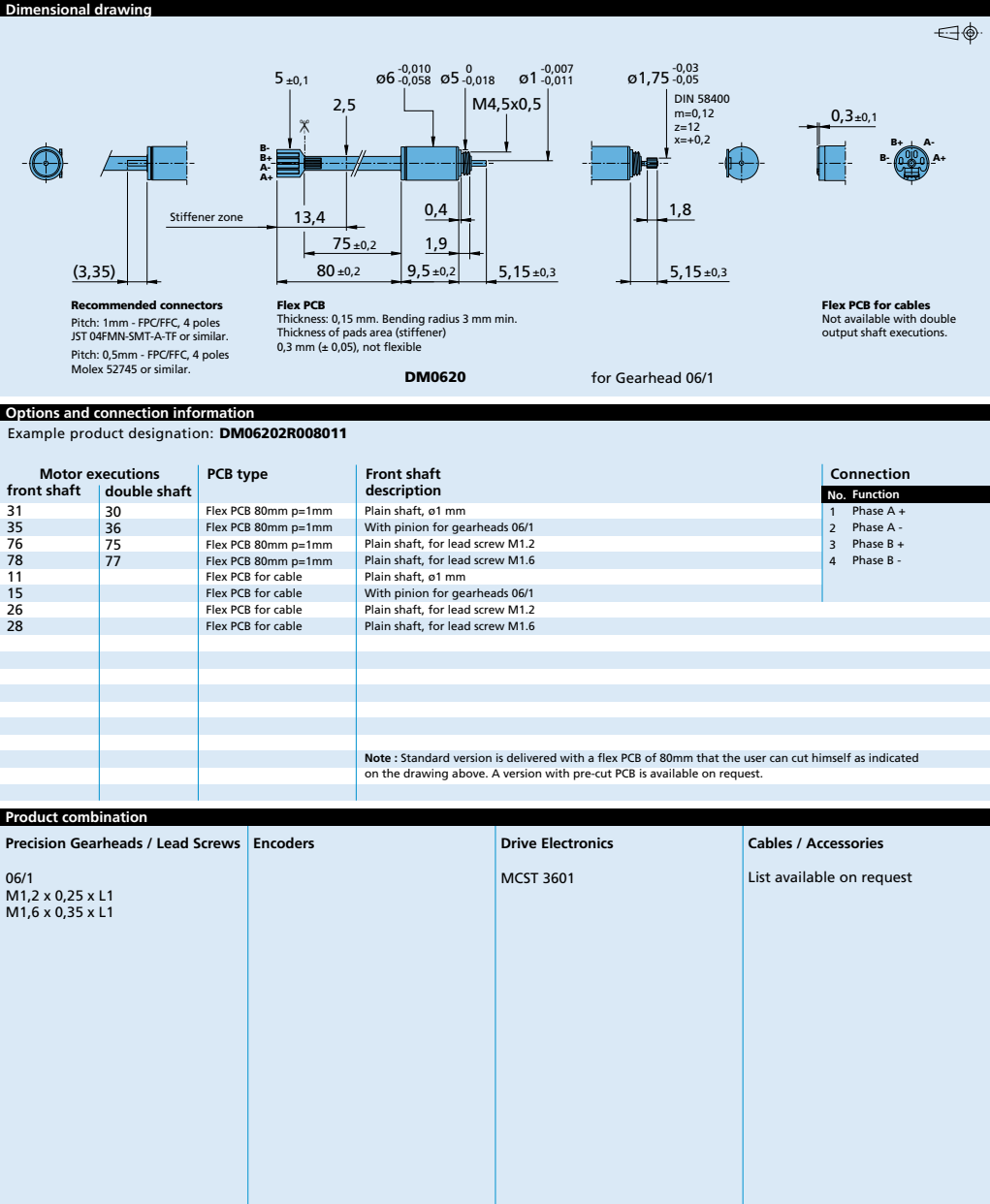


For notes on technical data and lifetime performance refer to "Technical Information".

Edition 2020 Feb. 18

© DR. FRITZ FAULHABER GMBH & CO. KG
Specifications subject to change without notice.

Figure A.10: DM0620-datasheet



For notes on technical data and lifetime performance refer to "Technical Information".
Edition 2020 Feb. 18

© DR. FRITZ FAULHABER GMBH & CO. KG
Specifications subject to change without notice.

Figure A.11: DM0620-datasheet

A.5. Gearbox datasheet

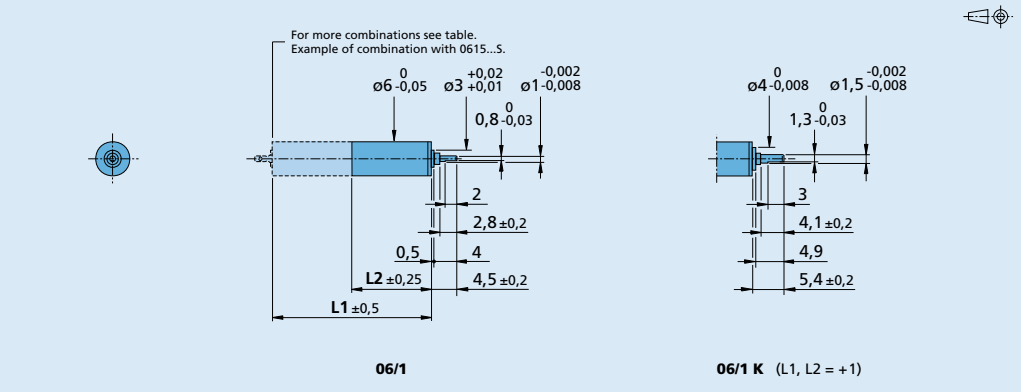


Planetary Gearheads

25 mNm

For combination with
DC-Micromotors
Brushless DC-Motors
Stepper Motors

Series 06/1		06/1		06/1K			
Housing material		steel		steel			
Geartrain material		steel		steel			
Recommended max. input speed for:							
– continuous operation		8 000 min ⁻¹		8 000 min ⁻¹			
Backlash, at no-load		≤ 3 °		≤ 3 °			
Bearings on output shaft		sintered bearings		ball bearings			
Shaft load, max.:							
– radial (3,5 mm from mounting face)		≤ 0,5 N		≤ 5 N			
– axial		≤ 0,5 N		≤ 3 N			
Shaft press fit force, max.		≤ 3,5 N		≤ 5 N			
Shaft play							
– radial (3,5 mm from mounting face)		≤ 0,06 mm		≤ 0,06 mm			
– axial		≤ 0,1 mm		≤ 0,05 mm			
Operating temperature range		- 30 ... + 100 °C		- 30 ... + 100 °C			
Technical data							
Number of gear stages		1	2	3	4	5	6
Continuous torque		mNm	25	25	25	25	25
Intermittent torque		mNm	35	35	35	35	35
Mass without motor, ca.		g	2	2,8	3,4	4	4,4
Efficiency, max.		%	90	80	70	60	55
Direction of rotation, drive to output		=	=	=	=	=	=
Reduction ratio (exact)		4:1	16:1	64:1	256:1	1 024:1	4 096:1
L2 [mm] = length without motor		9,2	11,9	14,6	17,3	20,0	22,7
L1 [mm] = length with motor		24,2	26,9	29,6	32,3	35,0	37,7
0615C...S		23,8	26,5	29,2	31,9	34,6	37,3
0620C...B		29,2	31,9	34,6	37,3	40,0	42,7
DM0620...35		18,7	21,4	24,1	26,8	29,5	32,2



For notes on technical data and lifetime performance refer to "Technical Information".
Edition 2020 Feb. 18

© DR. FRITZ FAULHABER GMBH & CO. KG
Specifications subject to change without notice.

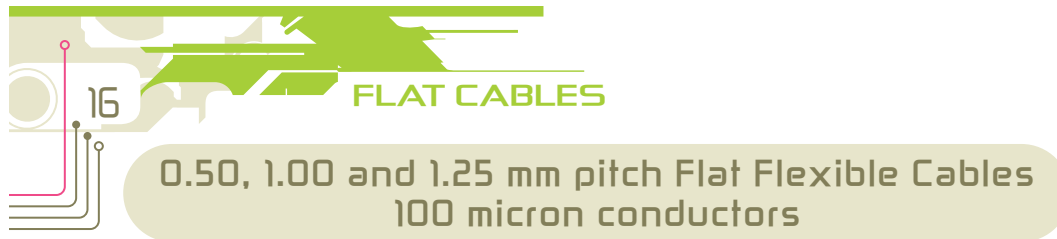
A.6. Bevel gear calculation formulas

Gear parameter	Formula
Shaft angle	θ_{shaft}
Reference cone angle of pinion	$\delta_1 = \tan^{-1} \left(\frac{\sin \theta_{shaft}}{\frac{T_2}{T_1} + \cos \theta_{shaft}} \right)$
Reference cone angle of driven gear	$\delta_2 = \theta_{shaft} - \delta_1$
Cone distance	$R_{cone} = \frac{d_2}{2 \sin \delta_2}$
Face width	$w_{face} < \frac{R_{cone}}{3}$
Addendum distance of driven gear	$d_{add-2} = 0.54m + 0.46 \frac{z_1 \cos \delta_2}{z_2 \cos \delta_1}$
Addendum distance of pinion	$d_{add-1} = 2m - d_{add-2}$
Dedendum distance	$d_{ded} = 2.188m - d_{add}$
Dedendum angle	$\theta_{ded} = \tan^{-1} \left(\frac{d_{ded}}{R_{cone}} \right)$
Addendum angle of driver	$\theta_{add-1} = \tan^{-1} \left(\frac{d_{add-1}}{R_{cone}} \right)$
Addendum angle of driven gear	$\theta_{add-2} = \tan^{-1} \left(\frac{d_{add-2}}{R_{cone}} \right)$
Tip angle of gears	$\theta_{tip} = \delta + \theta_{add}$
Root angle of gears	$\theta_{root} = \delta - \theta_{ded}$

Table A.15: Formulas for gear sizing [81, 185]

A.7. Flat flexible cable datasheet

A.7.1. FFC datasheet



Standard versions

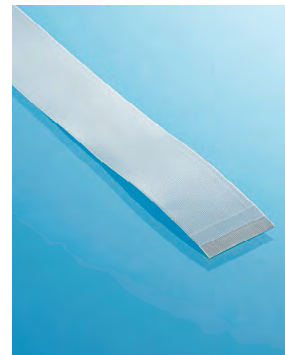
General characteristics

Temperature rating: up to 105°C.

Voltage rating: up to 60V AC.

Conductor

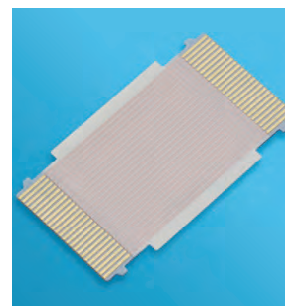
Pitch (mm)	Width (mm)	Max conductor resistance (Ω /km) at 20°C	Conductor thickness (mm)
0.50	0.30 ± 0.02	730	0.10 ± 0.015
1.00	0.70 ± 0.03	300	0.10 ± 0.015
1.25	0.80 ± 0.03	280	0.10 ± 0.015



0.50 MM PITCH STANDARD FLAT FLEXIBLE CABLE

Conductor plating

Tin	0.4 μ m mini
Gold	0.3 μ m Ni mini / 0.05 μ m Au



0.50 MM PUNCHED FLAT FLEXIBLE CABLE

Insulation

Polyester insulation with flame retardant adhesive.

White colour.

Connection schemes

With ZIF connectors

Reinforcement tape: Polyester K code.
Blue colour.



Hot bar soldering

Reinforcement tape: Polyimide H code.
Natural colour (amber).



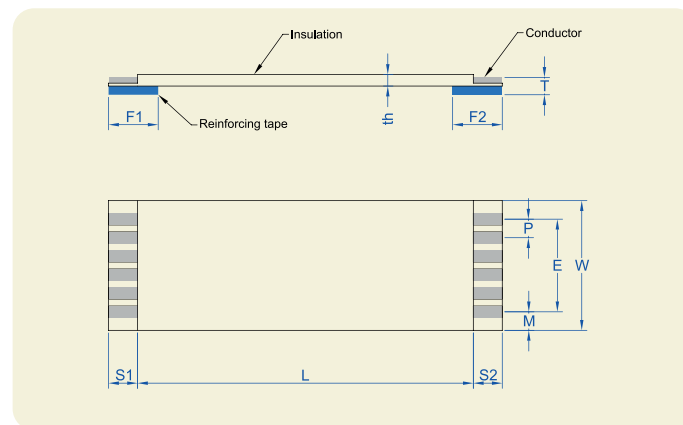
Manual soldering

Code for the end: T.
F1 ; F2 = 2.50 mm.



0.50, 1.00 and 1.25 mm pitch Flat Flexible Cables 100 micron conductors

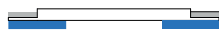
General drawing



Processing forms

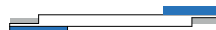
Type A

Reinforcements at both ends,
on the same side.



Type D

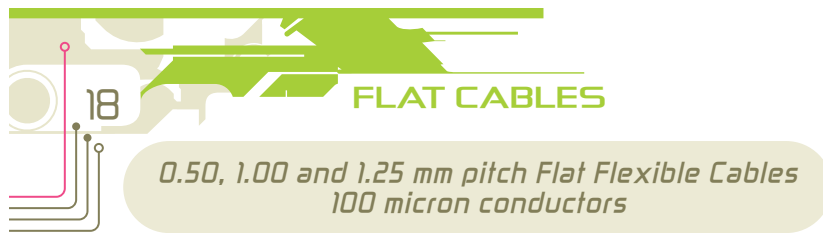
Reinforcements at both ends,
on opposing side.



Dimensions

Pitch: P (mm)	0.50 ± 0.05	1.00 ± 0.08	1.25 ± 0.10
Number of conductors: N	6 to 80	4 to 60	4 to 60
Span: E (mm)	$(N-1) \cdot 0.50 \pm 0.07$	$(N-1) \cdot 1.00 \pm 0.15$	$(N-1) \cdot 1.25 \pm 0.15$
Width: W (mm)	$(N+1) \cdot 0.50 \pm 0.06$	$(N+1) \cdot 1.00 \pm 0.10$	$(N+1) \cdot 1.25 \pm 0.15$
Margin: M (mm)	0.50 ± 0.12	1.00 ± 0.20	1.25 ± 0.20
Strip length: S1-S2 (mm)	2.00 to 10.0 ± 0.80 (standard value: 4 mm)		
Reinforcement length: F1-F2 (mm)	6.00 to 20.0 ± 2.00 (standard value: 8 mm)		
Insulated length: L (mm)	20 to 60 ± 2 61 to 100 ± 3 101 to 200 ± 4		
Thickness at end of cable: T (mm)	0.30 ± 0.05 (only for ZIF connectors)		
Cable thickness: th (mm)	0.25 typical		

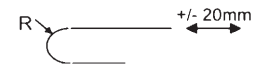
Figure A.14: FFC-datasheet-2 [79]



Electrical properties

	Testing conditions	Pitch		
		0.50	1.00	1.25
Dielectric Test (V AC) - Min	Conductor to conductor, during 1 minute	200	400	500
Current rating (A) - Max	FFC at 23°C Allowable temperature rise: 40°C	0.55	1.25	1.40
Insulation resistance (MΩ.m min)	Conductor to conductor	10 at DC 200V	10 at DC 400V	10 at DC 500V
Continuity test	DC 3.0 V at 0.1mA	Passed	Passed	Passed
Impedance cond/cond balanced method (typical value)	FFC without shielding at 1MHz	130 Ω	120 Ω	130 Ω
Capacitance cond/cond balanced method (typical value)	FFC without shielding at 1KHz	62 pF/m	50 pF/m	30 pF/m

Other properties

	Testing conditions	Characteristics	
Heat resistance	136°C, 168 hours	Dielectric test Insulation resistance	Passed Passed
Thermal shock	(-55°C x 30 min → 25°C x 5 min → 85°C x 30 min → 25°C x 5 min) x 25 cycles	Dielectric test Insulation resistance	Passed Passed
Cold coiling	-40°C, 96 hours The sample is initially wound on a mandrel of 3 mm	At room temperature: Visual inspection Dielectric test Insulation resistance	Passed Passed Passed
Wear by abrasion	Test following EN3475-503 Weight: 500 g Speed: 60 cycles/min Abrasion tool: Ø = 0.50 mm	Dielectric test Insulation resistance: After 10 000 cycles	Passed
Flame resistance	UL 758	VW-1	Passed
Folding	The specimen shall be folded manually at 180°	Continuity after more than 20 times	Passed
Moisture resistance	60°C, 95% RH, 96 hours	Dielectric test Insulation resistance	Passed Passed
Flex-life (typical values)	speed 100 cycles /min Flex-life tests are performed at 23°C. 	Radius 10 mm	100 000 cycles

axon
cable & interconnect

© 2009 - AXON'CABLE - RELEASED SEPTEMBER 2020 / G
FLAT FLEXIBLE CABLES AND FLAT CABLE ASSEMBLIES - www.axon-cable.com



Figure A.15: FFC-datasheet-3 [79]

A.7.2. FPC manufacturer specifications

Single layer FPC stackup		
Thickness		
<div>0.08mm</div> <div>0.1mm</div> <div>0.13mm</div> <div>0.16mm</div>		
top coverlay	PI	25um
	Adhesive	25um
top copper layer	Copper	18um(Finished Copper thickness 18um)
	Adhesive	13um
	PI	25um dielectric constant 3.3~3.5 (The DK value is not absolute and will vary depending on the base material's models and thickness.)
Total thickness		106um

(a) 18 micrometer trace thickness

Single layer FPC stackup		
Thickness		
<div>0.08mm</div> <div>0.1mm</div> <div>0.13mm</div> <div>0.16mm</div>		
top coverlay	PI	25um
	Adhesive	25um
top copper layer	Copper	35um(Finished Copper thickness 35um)
	Adhesive	20um
	PI	25um dielectric constant 3.3~3.5 (The DK value is not absolute and will vary depending on the base material's models and thickness.)
Total thickness		130um

(b) 35 micrometer trace thickness

Single layer FPC stackup		
Thickness		
<div>0.08mm</div> <div>0.1mm</div> <div>0.13mm</div> <div>0.16mm</div>		
top coverlay	PI	12.5um
	Adhesive	50um
top copper layer	Copper	70um(Finished Copper thickness 70um)
	Adhesive	0um
	PI	25um dielectric constant 3.3~3.5 (The DK value is not absolute and will vary depending on the base material's models and thickness.)
Total thickness		157.5um

(c) 70 micrometer trace thickness

Figure A.16: PCB Way's FPC stackup for different trace thicknesses [41]

Bend radius (flexibility):

Single-layer:	$6 \times \text{circuit thickness (minimum)}$
Double-layer:	$12 \times \text{circuit thickness (minimum)}$
Multilayer:	$24 \times \text{circuit thickness (minimum)}$

Circuit thickness is approximately 0.006" per layer.

Figure A.17: Bending radius of FPC [83]

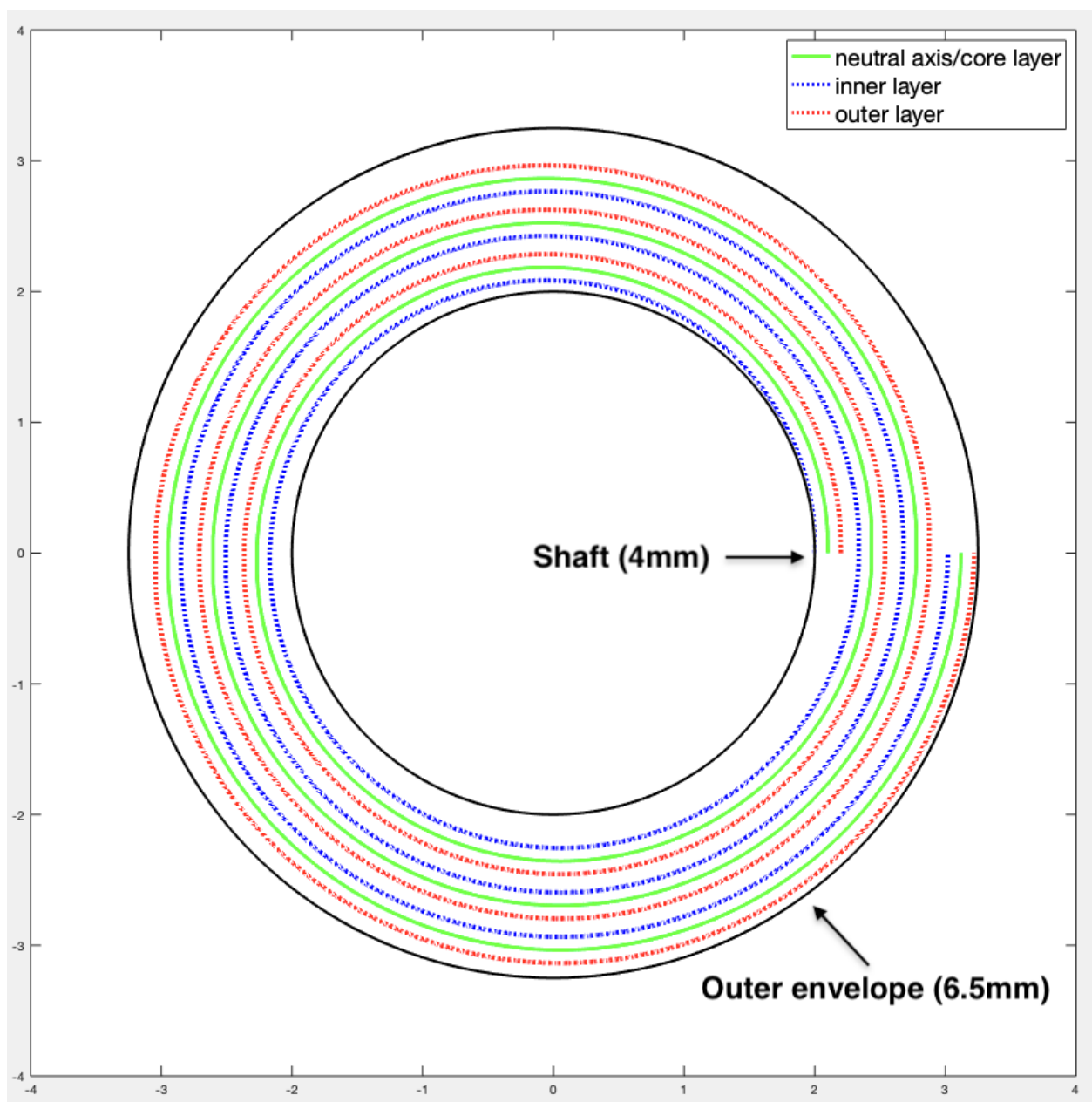


Figure A.18: Flex-wrap schematic with 3 spiral turns

A.8. Sleeve bearing service life & datasheet

	Material	Service-life [h]	Dimensions [mm] ?		
			d1	b1	d2
<input type="radio"/>	J350	609,789	4	4	5.5
<input checked="" type="radio"/>	Z	92,072	4	4	5.5
<input type="radio"/>	C500	15,603	⚠	-	-
<input type="radio"/>	A500	12,421	4	4	5.5
<input type="radio"/>	A350	10,610	4	4	5.5

(a) page-1

	Material	Service-life [h]	Dimensions [mm] ?		
			d1	b1	d2
<input type="radio"/>	A350	10,610	4	4	5.5
<input type="radio"/>	X6	5,075	⚠ 5	⚠ 5	7
<input type="radio"/>	L500	2,403	⚠	-	-
<input type="radio"/>	L350	1,993	4	4	5.5
<input type="radio"/>	T500	286	4	4	5.5

(b) page-2

Figure A.19: Iglidur service life [59]

Figure A.20: Z material bearing data-sheet - 1[61]



Long service life under extreme conditions

Resistant to wear and impact even at high loads and temperatures

Extremely high compressive strength coupled with high flexibility enables iglidur® Z bearings to attain their prominent properties in association with soft shafts, edge loads and impacts. At the same time the bearings are suitable for temperatures up to +250°C.

- Excellent wear resistance especially with high loads
- High temperature resistance
- Suitable for very high loads
- Suitable for high surface speeds
- Suitable for high edge pressures
- Lubrication-free
- Maintenance-free

Typical application areas

- Construction machinery industry
- Mechanical engineering
- Textile industry
- Aerospace engineering
- Glass industry

Descriptive technical specifications

Wear resistance at +23°C	-	+
Wear resistance at +90°C	-	+
Wear resistance at +150°C	-	+
Low coefficient of friction	-	+
Low moisture absorption	-	+
Wear resistance under water	-	+
High media resistance	-	+
Resistant to edge pressures	-	+
Suitable for shock and impact loads	-	+
Resistant to dirt	-	+

Online product finder
www.igus.eu/iglidur-finder

Online service life calculation
www.igus.eu/iglidur-expert

Technical data

General properties		Testing method
Density	g/cm³	1.40
Colour		brown
Max. moisture absorption at +23°C and 50% rh.	% weight	0.3
Max. moisture absorption	% weight	1.1
Coefficient of friction, dynamic, against steel	μ	0.06 – 0.14
pV value, max. (dry)	MPa · m/s	0.84
Mechanical properties		
Flexural modulus	MPa	2,400
Flexural strength at +20°C	MPa	95
Compressive strength	MPa	65
Max. recommended surface pressure (+20°C)	MPa	150
Shore D hardness		81
Physical and thermal properties		
Max. application temperature long-term	°C	+250
Max. application temperature short-term	°C	+310
Min. application temperature	°C	-100
Thermal conductivity	W/m · K	0.62
Coefficient of thermal expansion (at +23°C)	K⁻¹ · 10⁻⁵	4
Electrical properties		
Specific contact resistance	Ωcm	> 10¹¹
Surface resistance	Ω	> 10¹¹

Table 01: Material properties

In addition to iglidur® X, iglidur® Z is among the best-selling iglidur® high-temperature materials. Specifically worth noting is the outstanding wear behaviour under extreme conditions (high loads and temperatures).

Resistance to weathering

iglidur® Z plain bearings are continuously resistant to weathering. The material properties are only slightly affected. Possible discolorations are only superficial.

Moisture absorption

Under standard climatic conditions, the moisture absorption of iglidur® Z plain bearings is approximately 0.3% weight. The saturation limit in water is 1.1% weight.

Vacuum

In vacuum, any present moisture is released as vapour. Use in vacuum is only possible with dehumidified iglidur® Z bearings.

Radiation resistance

Plain bearings made from iglidur® Z are resistant up to a radiation intensity of 1 · 10⁶ Gy.

Mechanical properties

With increasing temperatures, the compressive strength of iglidur® Z plain bearings decreases. Diagram 02 shows this inverse relationship. The maximum recommended surface pressure is a mechanical material parameter. No conclusions regarding the tribological properties can be drawn from this.

iglidur® Z is suitable for both medium and – due to its high heat resistance – high speeds. Diagram 03 shows the elastic deformation of iglidur® Z at radial loads. At the maximum recommended surface pressure of 150MPa the deformation is about 5.5% at room temperature.

Surface pressure, page 41

Figure A.21: Z material bearing data-sheet - 2 [61]

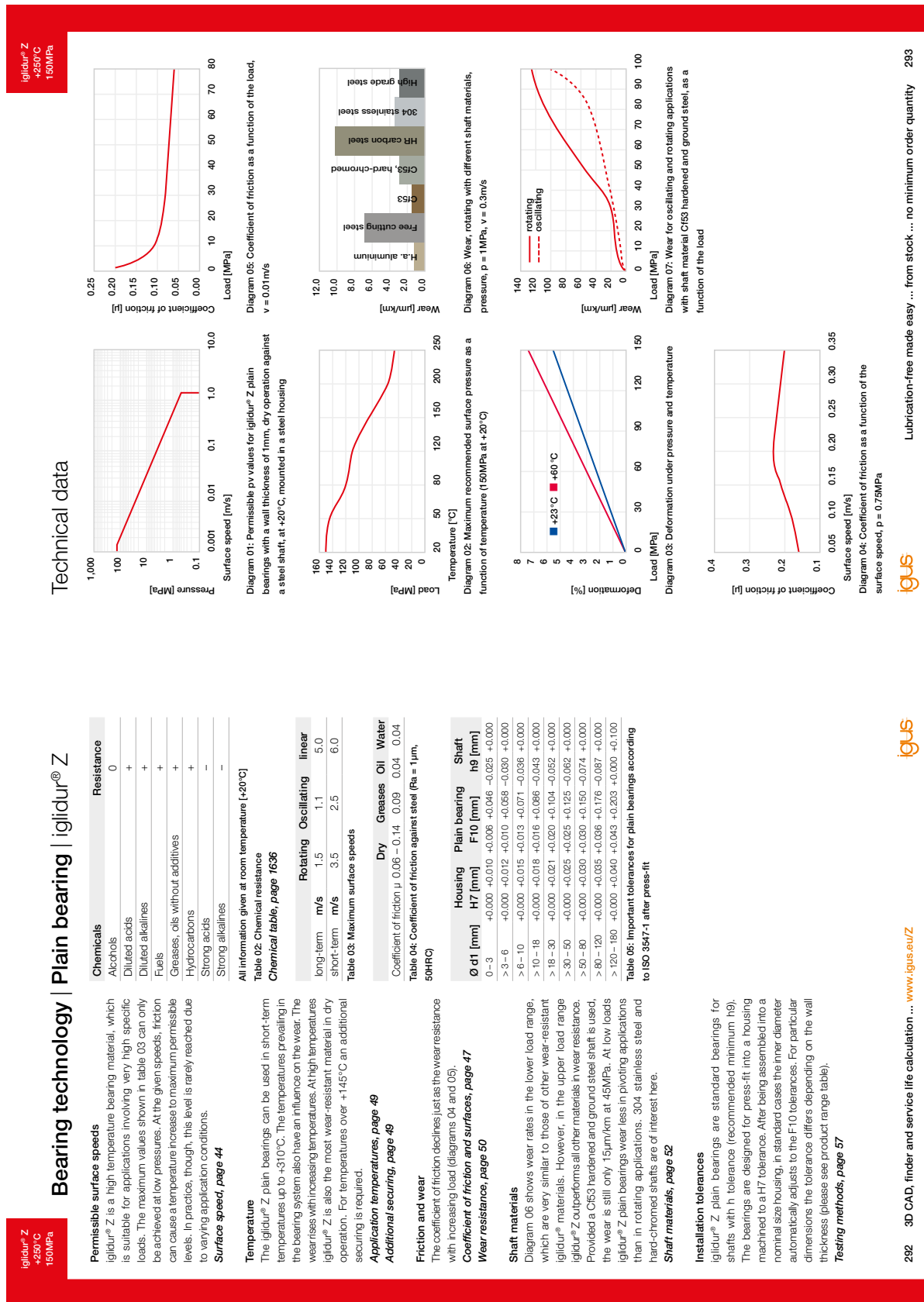
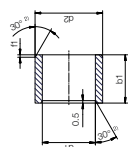


Figure A.22: Z material bearing data-sheet - 3 [61]

Bearing technology | Plain bearing | iglidur® Z

Sleeve bearing (form S)



^{a)} Thickness < 0.6mm: Chamfer = 20°

Chamfer in relation to d1

d1 [mm] Ø 1-6 | Ø 6-12 | Ø 12-30 | Ø > 30 | f1 [mm] 0.3 | 0.5 | 0.8 | 1.2



Order example: **ZSM-0405-04** – no minimum order quantity.



Z iglidur® material **S** Sleeve bearing **M** Metric **Ø4** Inner Ø **Ø1** **Ø5** Outer Ø **Ø2** **Ø4** Total length **b1**

d1	d1 Tolerance ^{a)}	d2	b1	h13	Part No.	d1	d1 Tolerance ^{a)}	d2	b1	h13	Part No.
4.0	4.0	5.5	4.0	5.5	ZSM-0405-04	14.0	14.0	16.0	15.0	16.0	ZSM-1416-25
4.0	4.0	5.5	6.0	5.5	ZSM-0405-06	15.0	15.0	17.0	15.0	17.0	ZSM-1517-15
4.0	4.0	5.0	8.0	5.0	ZSM-0405-08	15.0	15.0	17.0	20.0	17.0	ZSM-1517-20
5.0	5.0	7.0	5.0	7.0	ZSM-0507-05	15.0	15.0	17.0	22.0	17.0	ZSM-1517-22
5.0	5.0	7.0	9.0	7.0	ZSM-0507-09	15.0	15.0	17.0	25.0	17.0	ZSM-1517-25
5.0	+0.010	7.0	10.0	7.0	ZSM-0507-10	16.0	16.0	18.0	12.0	18.0	ZSM-1618-12
6.0	+0.058	8.0	6.0	8.0	ZSM-0608-06	16.0	16.0	18.0	15.0	18.0	ZSM-1618-15
6.0	6.0	8.0	8.0	8.0	ZSM-0608-08	16.0	16.0	18.0	20.0	18.0	ZSM-1618-20
6.0	6.0	8.0	10.0	8.0	ZSM-0608-10	16.0	16.0	18.0	25.0	18.0	ZSM-1618-25
6.0	6.0	8.0	12.0	8.0	ZSM-0608-12	18.0	18.0	20.0	15.0	20.0	ZSM-1820-15
6.0	6.0	10.0	6.0	10.0	ZSM-0610-06	18.0	18.0	20.0	20.0	20.0	ZSM-1820-20
8.0	8.0	10.0	6.0	10.0	ZSM-0810-06	18.0	18.0	20.0	24.0	20.0	ZSM-1820-24
8.0	8.0	10.0	8.0	10.0	ZSM-0810-08	18.0	18.0	20.0	25.0	20.0	ZSM-1820-25
8.0	8.0	10.0	10.0	10.0	ZSM-0810-10	20.0	20.0	23.0	10.0	23.0	ZSM-2023-10
8.0	+0.013	10.0	12.0	10.0	ZSM-0810-12	20.0	20.0	23.0	15.0	23.0	ZSM-2023-15
10.0	+0.071	12.0	8.0	12.0	ZSM-1012-08	20.0	20.0	23.0	20.0	23.0	ZSM-2023-20
10.0	10.0	12.0	10.0	12.0	ZSM-1012-10	20.0	20.0	23.0	25.0	23.0	ZSM-2023-25
10.0	10.0	12.0	12.0	12.0	ZSM-1012-12	20.0	20.0	23.0	30.0	23.0	ZSM-2023-30
10.0	10.0	12.0	15.0	12.0	ZSM-1012-15	20.0	20.0	23.0	35.0	23.0	ZSM-2023-35
10.0	10.0	12.0	20.0	12.0	ZSM-1012-20	22.0	22.0	25.0	10.0	25.0	ZSM-2225-10
12.0	12.0	14.0	8.0	12.0	ZSM-1214-08	22.0	22.0	25.0	15.0	25.0	ZSM-2225-15
12.0	12.0	14.0	10.0	12.0	ZSM-1214-10	22.0	22.0	25.0	20.0	25.0	ZSM-2225-20
12.0	12.0	14.0	12.0	12.0	ZSM-1214-12	22.0	22.0	25.0	25.0	25.0	ZSM-2225-25
12.0	+0.016	14.0	15.0	12.0	ZSM-1214-15	22.0	22.0	25.0	30.0	25.0	ZSM-2225-30
12.0	+0.086	14.0	20.0	12.0	ZSM-1214-20	24.0	24.0	27.0	15.0	27.0	ZSM-2427-15
13.0	13.0	15.0	10.0	13.0	ZSM-1315-10	24.0	24.0	27.0	20.0	27.0	ZSM-2427-20
13.0	13.0	15.0	20.0	13.0	ZSM-1315-20	24.0	24.0	27.0	25.0	27.0	ZSM-2427-25
14.0	14.0	16.0	15.0	14.0	ZSM-1416-15	24.0	24.0	27.0	30.0	27.0	ZSM-2427-30
14.0	14.0	16.0	20.0	14.0	ZSM-1416-20	25.0	25.0	28.0	15.0	28.0	ZSM-2528-15

^{a)} After press-fit. Testing methods, page 57

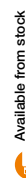
294 3D CAD, finder and service life calculation ... www.igus.eu/Z



Product range

d1	d1 Tolerance ^{a)}	d2	b1	h13	Part No.	d1	d1 Tolerance ^{a)}	d2	b1	h13	Part No.
25.0	25.0	28.0	20.0	25.0	ZSM-2528-20	40.0	40.0	44.0	40.0	44.0	ZSM-4044-40
25.0	25.0	28.0	25.0	25.0	ZSM-2528-25	40.0	40.0	44.0	47.0	44.0	ZSM-4044-47
25.0	25.0	28.0	30.0	25.0	ZSM-2528-30	40.0	40.0	44.0	50.0	44.0	ZSM-4044-50
25.0	25.0	28.0	48.0	25.0	ZSM-2528-48	45.0	45.0	50.0	20.0	50.0	ZSM-4550-20
25.0	25.0	30.0	20.0	25.0	ZSM-2530-20	45.0	45.0	50.0	30.0	50.0	ZSM-4550-30
26.0	26.0	30.0	34.0	26.0	ZSM-2630-34	45.0	+0.025	50.0	40.0	50.0	ZSM-4550-40
28.0	+0.020	32.0	20.0	28.0	ZSM-2832-20	45.0	+0.125	50.0	50.0	50.0	ZSM-4550-50
28.0	+0.104	32.0	25.0	28.0	ZSM-2832-25	50.0	50.0	55.0	20.0	55.0	ZSM-5055-20
28.0	28.0	32.0	30.0	28.0	ZSM-2832-30	50.0	50.0	55.0	30.0	55.0	ZSM-5055-30
28.0	28.0	34.0	29.0	28.0	ZSM-2834-29	50.0	50.0	55.0	40.0	55.0	ZSM-5055-40
30.0	30.0	34.0	20.0	30.0	ZSM-3034-20	50.0	50.0	55.0	50.0	55.0	ZSM-5055-50
30.0	30.0	34.0	25.0	30.0	ZSM-3034-25	50.0	50.0	55.0	60.0	55.0	ZSM-5055-60
30.0	30.0	34.0	30.0	30.0	ZSM-3034-30	55.0	55.0	60.0	60.0	60.0	ZSM-5560-60
30.0	30.0	34.0	40.0	30.0	ZSM-3034-40	60.0	+0.030	65.0	60.0	65.0	ZSM-6065-60
32.0	32.0	36.0	44.0	32.0	ZSM-3236-44	70.0	+0.150	75.0	70.0	75.0	ZSM-7075-70
32.0	32.0	36.0	20.0	32.0	ZSM-3236-20	80.0	80.0	85.0	60.0	85.0	ZSM-8085-60
32.0	32.0	36.0	30.0	32.0	ZSM-3236-30	80.0	80.0	85.0	80.0	85.0	ZSM-8085-80
32.0	32.0	36.0	40.0	32.0	ZSM-3236-40	85.0	+0.036	90.0	100.0	90.0	ZSM-8590-100
35.0	+0.025	39.0	20.0	35.0	ZSM-3539-20	85.0	+0.176	90.0	60.0	90.0	ZSM-8590-60
35.0	+0.125	39.0	30.0	35.0	ZSM-3539-30	85.0	85.0	100.0	60.0	100.0	ZSM-8590-60
35.0	35.0	39.0	40.0	35.0	ZSM-3539-40	100.0	+0.072	105.0	100.0	105.0	ZSM-100105-100
35.0	35.0	39.0	50.0	35.0	ZSM-3539-50	100.0	+0.212	105.0	100.0	105.0	ZSM-100105-100
40.0	40.0	44.0	15.0	40.0	ZSM-4044-15	120.0	+0.043	125.0	100.0	125.0	ZSM-120125-100
40.0	40.0	44.0	20.0	40.0	ZSM-4044-20	120.0	+0.203	125.0	100.0	125.0	ZSM-120125-100
40.0	40.0	44.0	30.0	40.0	ZSM-4044-30						

^{a)} After press-fit. Testing methods, page 57



Available from stock

Detailed information about delivery time online.

www.igus.eu/24



Online ordering

Including delivery times, prices, online tools

www.igus.eu/Z



Ordering note

Our prices are scaled according to order quantities, current prices can be found online.

Discount scaling

1 - 9	50 - 99	500 - 999
10 - 24	100 - 199	1,000 - 2,499
25 - 49	200 - 499	2,500 - 4,999

No minimum order value.

No low-quantity surcharges.

Free shipping within Germany for orders above €150.



Lubrication-free made easy ... from stock ... no minimum order quantity 295

Figure A.23: Z material bearing data-sheet - 4 [61]

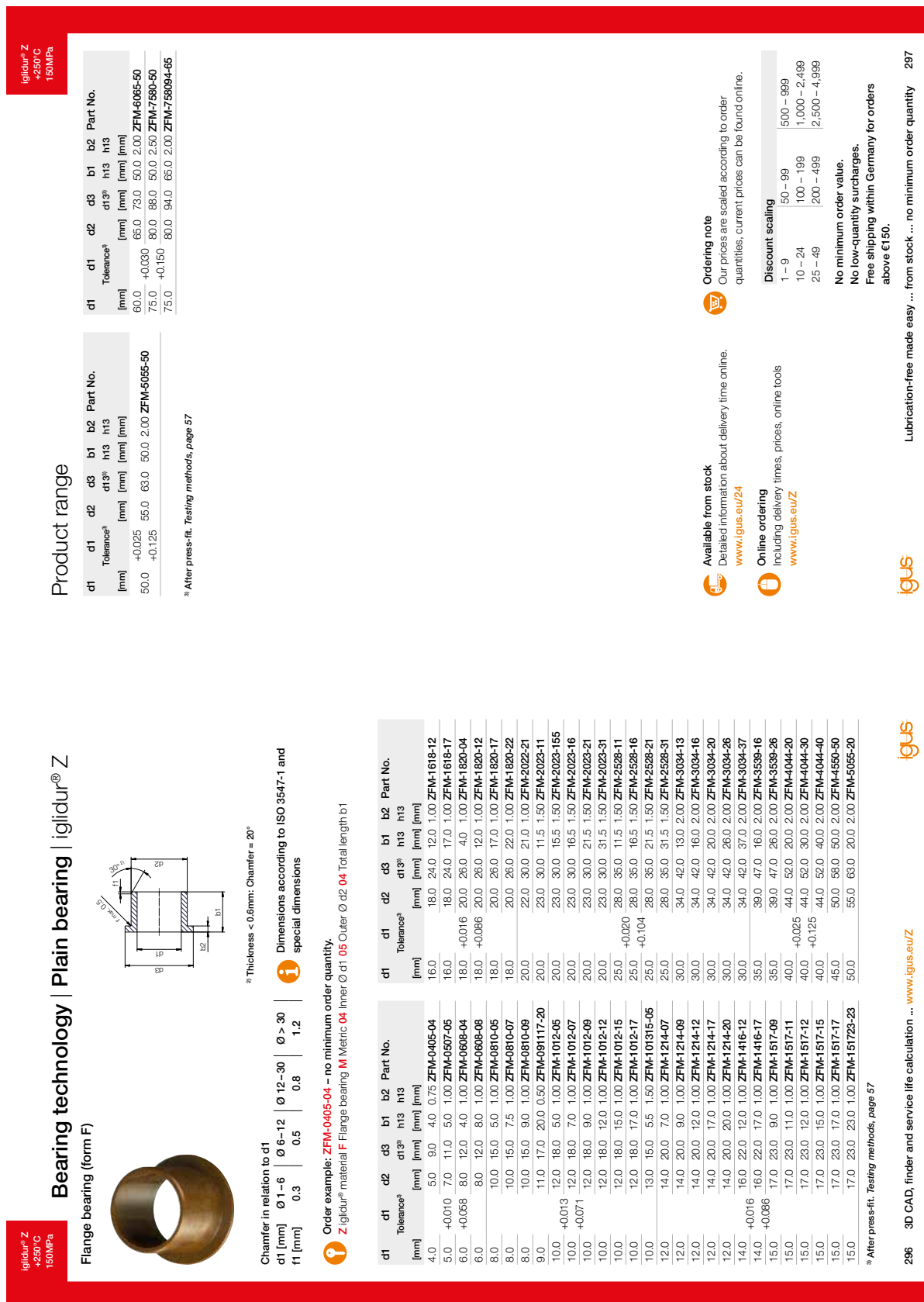


Figure A.24: Z material bearing data-sheet - 5 [61]

A.9. Interfaces

A.9.1. Mechanical interface

Lubricant	Nut Factor	
	Mean	Range
Cadmium Plating	0.194-0.246	0.153-0.328
Zinc Plate	0.332	0.262-0.398
Black Oxide	0.163-0.194	0.109-0.279
Baked on PTFE	0.092-0.112	0.064-0.142
Molydisulfide Paste	0.155	0.14-0.17
Machine Oil	0.21	0.20-0.225
Carnaba Wax (5% Emulsion)	0.148	0.12-0.165
60 Spindle Oil	0.22	0.21-0.23
As Received Steel Fasteners	0.20	0.158-0.267
Molydisulfide Grease	0.137	0.10-0.16
Phosphate and Oil	0.19	0.15-0.23
Plated Fasteners	0.15	
Grease, Oil, or Wax	0.12	

Figure A.25: Nut factors[103] [185]

Thread Size M	Tightening Torque		Head Side Tensile Strength	
	N · m		N/mm ²	
	CBSTSR	CBSTNR CBSTBR	CBSTSR	CBSTNR CBSTBR
M2	0.16	0.23	200	300
M2.5	0.35	0.46	350	460
M3	0.6	0.72		
M4	1.1	1.7		
M5	2.2	3.4		
M6	5	6.2		

Figure A.26: Space saving bolt tightening torque values [64]

A.9.2. Electrical interface

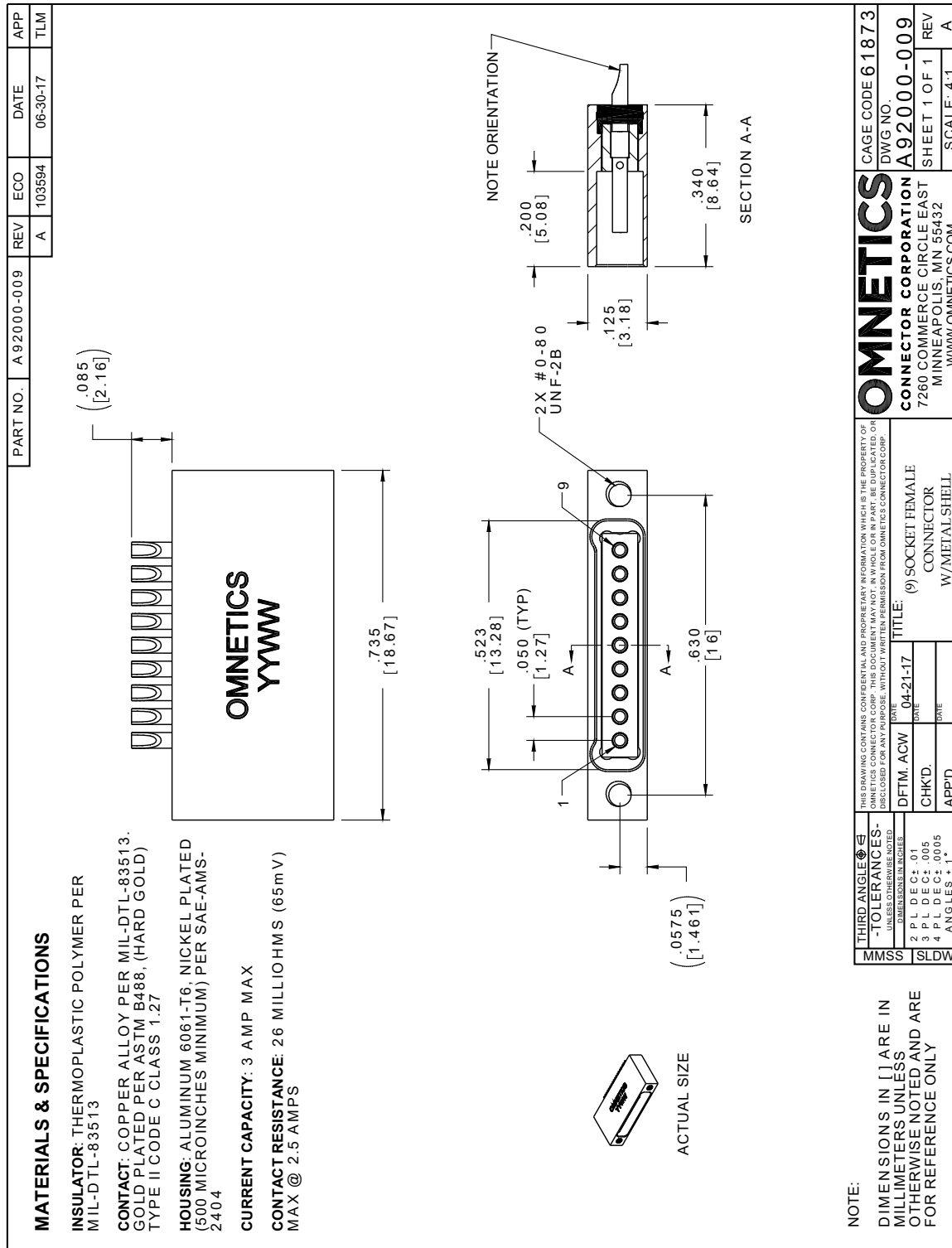


Figure A.27: Omnetics Micro-D 9 pin connector

A.9.3. Data interface

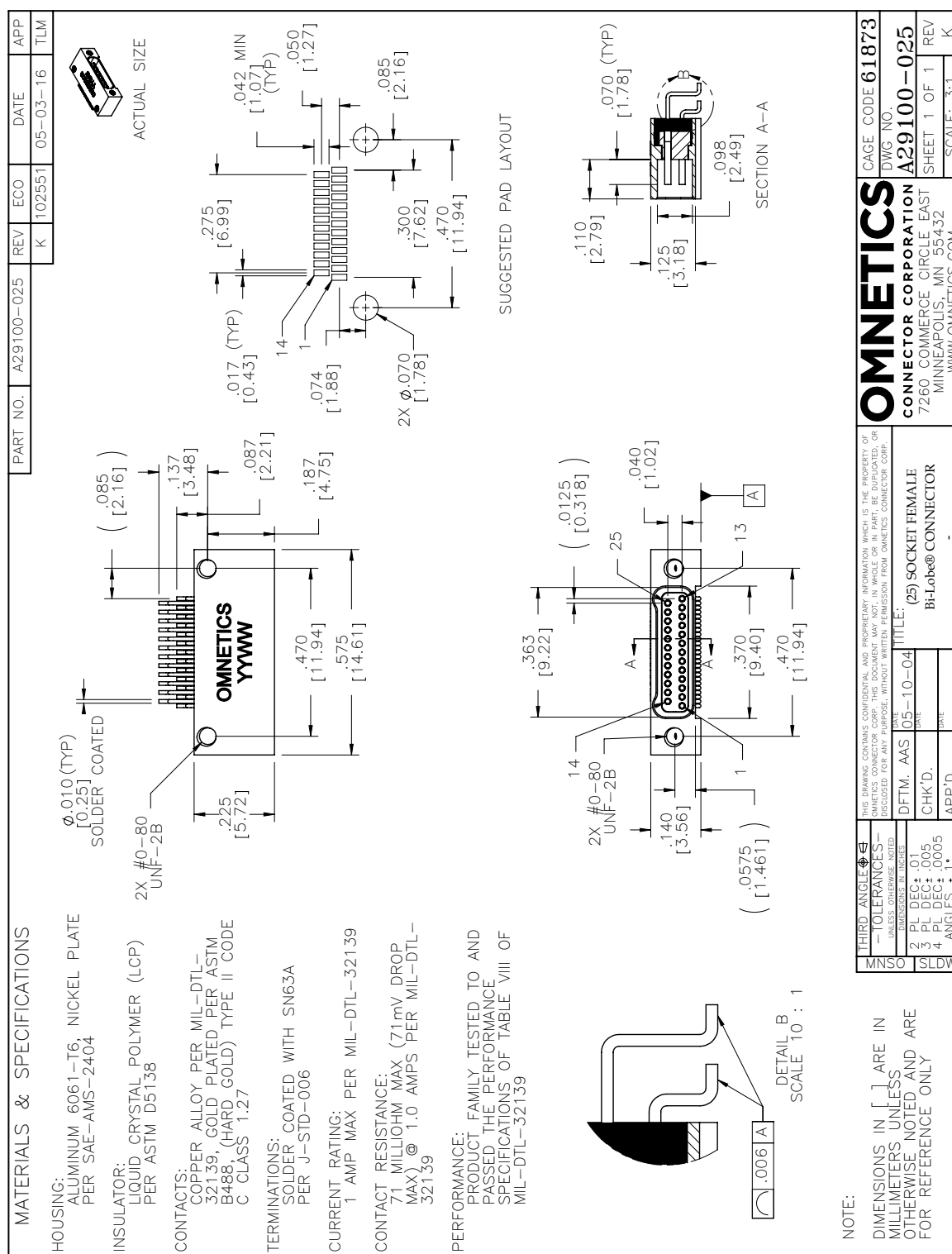


Figure A.28: Omnetics Nano-D 25 pin connector